Cobalt-Doped Zinc Oxide Thin Films as Model Fischer-Tropsch Nano-Catalysts Grown by Pulsed Electron Beam Ablation

By

Asghar Ali

A thesis submitted in partial fulfillment

of the requirements for the degree of

Doctor of Philosophy (PhD) in Natural Resources Engineering

The Faculty of Graduate Studies

Laurentian University

Sudbury, Ontario, Canada

THESIS DEFENCE COMMITTEE/COMITÉ DE SOUTENANCE DE THÈSE
Laurentian Université/Université Laurentienne
Faculty of Graduate Studies/Faculté des études supérieures

Title of Thesis Titre de la thèse	Cobalt-Doped Zinc Oxide Thin Films as Model Fischer-Tropsch Nano Catalysts Grown by Pulsed Electron Beam Ablation
Name of Candidate Nom du candidat	Ali, Asghar
Degree Diplôme	Doctor of Philosophy Science
Department/Program Département/Programme	Natural Resources Engineering
Date of Defence Date de la soutenance	December 05, 2017

APPROVED/APPROUVÉ

Thesis Examiners/Examinateurs de thèse:

Dr. Redhouane Henda
(Supervisor/Directeur de thèse)

Dr. Joy Gray-Munro
(Committee member/Membre du comité)

Dr. Nick Vayenas
(Committee member/Membre du comité)

Dr. Vassilios Kazakidis
(Committee member/Membre du comité)

Dr. Adrian Kital
(External Examiner/Examinateur externe)

Dr. Mazen Saleh
(Internal Examiner/Examinateur interne)

Approved for the Faculty of Graduate Studies
Approuvé pour la Faculté des études supérieures
Dr. David Lesbarrères
Monsieur David Lesbarrères
Dean, Faculty of Graduate Studies
Doyen, Faculté des études supérieures

ACCESSIBILITY CLAUSE AND PERMISSION TO USE

Abstract

The production of materials in thin film form with unique properties is of growing scientific and technological interest. Zinc oxide is a low cost, and environmentally benign wide band gap semiconductor, which makes it an excellent supporting material for nanoparticles with a plethora of potential applications. Upon doping with Co and other transition metals, ZnO exhibits room temperature ferromagnetic properties with enhanced performance and new functionalities when used in thin film devices. Zinc oxide-supported cobalt nano-composites are promising materials with desirable catalytic properties making it an interesting material for use as an efficient nano-catalyst in many important reactive processes such as Fischer-Tropsch synthesis (FTS), photocatalysis, hydrogen production and steam reforming.

Pulsed electron beam ablation (PEBA) has recently emerged as a potential technique for the fabrication of superior quality thin films. The production of well controlled nano-sized particulates is a characteristic feature of PEBA, which has a strong bearing on the surface morphology of the deposited films. In the current work, the potential of PEBA in the deposition of Co-doped ZnO thin films has been assessed and the critical process conditions that affect the growth of the thin films on different substrates have been thoroughly investigated. The main objective of the current work is to deposit Co-doped ZnO thin films via PEBA, and assess the potential of the deposited films as model nano-structured catalysts for the synthesis of green liquid fuels from syngas. PEBA has several advantages including modest requirements for vacuum, control of film thickness, easy set-up, low capital cost, reduced operation and maintenance costs, small footprint, enhanced efficiency, and relative safety (no toxic gases as in pulsed laser ablation or potential noxious by-products as in solvo-thermal routes) over other film preparation techniques.

In this project, Co:ZnO thin films have been synthesized from a single target on various substrates. Numerous process parameters have been assessed such as substrate material, deposition temperature, electron beam voltage, beam pulse frequency. Targets of varying cobalt loads viz., 5 w%, 10 w%, and 20 w% have been investigated as well. The effects of pre and post annealing on the physico-chemical properties of the thin films have also been studied. The deposited films have been characterized using complementary analytical techniques such as x-ray diffraction (XRD), x-ray photoelectron spectroscopy (XPS), scanning electron microscopy (SEM), energy dispersive x-ray (EDX), visible reflectance spectroscopy (VRS), and atomic force microscopy (AFM). Such comprehensive analyses have helped in assessing the quality of the films and in guiding the experimental strategy in the quest to find the optimal process conditions. Finally, the films have been evaluated for their potential as model nano-catalysts for Fischer-Tropsch synthesis in a 3-phase continuously-stirred tank slurry reactor (3-φ-CSTSR) using a Robinson-Mahoney stationary basket (RMSB). The results have been described in terms of activity and selectivity of the thin film nano-catalysts.

Acknowledgements

First of all, I would like to say that this work would not have been possible without the Support and Mercy of the Almighty Allah. Second, I want to express my deepest gratitude and supplications to my respected parents for all what they did for me. It provides me immense privilege to dedicate this thesis to them.

I would like to express my special thanks to Prof. Redhouane Henda for his constant intellectual stimulation, which kept me motivated to complete my PhD study successfully. I am grateful for his open-door policy, invaluable guidance, motivating discussions and sustained interest, and for the timely completion of this research project. It has been an honour for me to work under his supervision, and I appreciate his contributions of time, productive criticism to make my PhD experience productive and stimulating. I could not have imagined having a better mentor and advisor for my PhD study.

I would also like to give special thanks to the members of my thesis advisory committee: Prof. J. G. Munro, Prof. N. Vayenas, and Prof. V. Kazakidis. I would like to extend my sincere thanks to Prof. N. Abatzoglou and Dr. J. Aluha (Université de Sherbrooke) for their collaborating efforts to carry out Fischer Tropsch synthesis tests. I would like to thank to Prof. A. Chughtai (I.C.E.T. Univ. of the Punjab, Pak), Prof. J. Shepherd (Laurentian Univ.), Mr. A. L. Pinto (exchange student, Brazil), Mr. M. Mustafa (undergrad student), and Mr. H. Ylitalo (Technologist) for helping me with some aspects of the research project.

I want to thank my wife, Sana, and my son, Ahmad. They have made many sacrifices in achieving this milestone and were always around me for providing me with a loving environment and assistance. I would like to express my appreciation and gratitude to my brothers and sister for their prayers and moral support. Finally, I owe thanks to madam Yvonne Cholette, who spent a lot of her time with my wife and son to help them out in many ways during this tough time.

Table of Contents

List of Figures

List of Tables

List of Abbreviations

AFM	Atomic Force Microscope
Ar	Argon
BSE	Back Scatter Electron
CoO	Cobalt Oxide
Co^{o}	Metallic/Elemental Cobalt
CVD	Chemical Vapour Deposition
CZO	Cobalt-doped Zinc Oxide
DMSs	Dilute Magnetic Semiconductors
EDX	Energy Dispersive X-ray Spectroscopy
FID	Flame-Ionization Detector
fcc	Face Centered Cubic
FTS	Fischer Tropsch synthesis
GC	Gas Chromatograph
hcp	Hexagonal Close Packed
HRTEM	High Resolution Transmission Electron Microscopy
ITO	Indium Tin Oxide
NCs	Nano-composites
MBE	Molecular beam epitaxy
MOCVD	Metal Organic Chemical Vapor Deposition
PEBA	Pulsed Electron Beam Ablation
PLD	Pulsed Laser Deposition
rf	Radio Frequency
RHEED	Reflection High Energy Electron Diffraction
RMSB	Robinson-Mahoney Stationary Basket
RS	Rock salt
SE	Secondary Electron
SEM	Scanning Electron Microscope
SDD	Silicon Drift Detector
S-K	Stranski-Krastanov
S_{Ci}	Overall selectivity
TCD	Thermal Conductivity Detector

T_c	Curie temperature
THC	Transient Hollow Cathode
TOF	Turn Over Frequency
T SP	Temperature set point
V-W	Volmer-Weber
VRS	Visible reflectance spectroscopy
WZ	Wurtzite
XRD	X-ray diffraction
XPS	X-ray Photoelectron Spectroscopy
Z	Atomic number
ZB	Zincblende
ZnO	Zinc Oxide

Chapter 1: Literature review

1.1 Introduction

Nanotechnology describes the branch of science that studies and manipulates the properties of materials at dimension between approximately 1 and 100 nanometer. At nanoscale, particles exhibit unique properties, and products can be fabricated with significantly better properties than can be achieved by tailoring materials on bulk scale. The unique phenomena enable novel applications at nanoscale. Nanotechnology has revolutionized many areas such as electronics, renewable energy, environmental remediation, medicine, information technology and biotechnology among many others. The production of technologically important thin film nanoscale materials with unique properties is of growing scientific and technological interest. This interest stems from the fact that the behaviour of all devices based on thin film grown on selected surfaces are governed by atomic and molecular scale interactions at the interface created during film deposition processes. The fundamental nature of such interactions has proven to be particularly effective in the development of technologically important devices.

For sustainable development of energy sources worldwide, research is focused on alternative and clean fuels. The utilization of biomass, coal and other fuel sources rather than existing fossil fuels could offer more environmentally acceptable processes for energy production and will aid in preserving the limited supplies of fossil fuels. Canada has huge reserves of coal, with at least 7.3 billion short tons of recoverable coal reserves (Liming et al., 2008). Canada is also rich in biomass sources with an excess of 400×10^6 ha of forested land. Moreover, forest-harvest residue removal, disturbance isolation, and precommercial thinning might produce $20\text{-}33\times10^6$ mt/yr of feedstock for Canadian biorefineries (Mabee et al., 2006). Thus, both coal and biomass can be used for the production of synthesis gas, which can be

converted into liquid fuels coupled with Fischer Tropsch synthesis. The renewed interest is not only due to abundant reserves of coal, natural gas and biomass but also because of clean fuels and high value chemicals produced from FT process (Dry, 2002). Some advantages of FT synthetic diesel over petroleum-based diesel are as follows (Morales and Weckhuysen, 2006).

- Low content of sulphur and aromatic compounds
- High cetane number
- Low particulate formation
- Low SOx , NOx and CO emissions

Due to high cetane number FT diesel can either be used as a blending stock to upgrade the quality of petroleum diesel or it can be used in applications where high quality diesel is required.

Of particular interest is the development of thin film nano-catalysts for use in the production of clean energy. The aim of this research project is to prepare Co-doped ZnO thin-film nanocomposites via pulsed electron beam ablation, to characterize the deposited films through various spectroscopic and microscopic techniques, and, finally, to exploit them as a potential model catalyst for conversion of synthesis gas ($CO + H_2$) into liquid fuels via FTS. Synthesis gas can be obtained from gasification of FT feed stock materials containing carbon such as coal, natural gas, biomass, municipal waste and a natural or synthetic polymer (Boerrigter and Uil, 2002; Norbeck and park, 2008).

Several deposition techniques such as chemical vapour deposition (CVD), molecular beam epitaxy (MBE), sputtering, sol-gel, spray pyrolysis, electrodeposition and pulsed laser deposition (PLD) have been extensively assessed (See section 1.6) to prepare CZO thin films but each technique has various limitations. CVD method suffers with several drawbacks such as the

handling of hazardous chemicals caused by the use of toxic reagent gases. Further, it is hard to grow multicomponent material with well controlled stoichiometry by CVD (Palma and Lakhtakia, 2013). MBE requires high vacuum environment and suffers with high maintenance cost (Ptak, 2015; Palma and Lakhtakia, 2013). Sputtering is limited by lower deposition rate and low ionization efficiencies of plasma. It also often necessitates the use of cooling equipment by the heating of the substrates (Palma and Lakhtakia, 2013). Sol-gel method provides very least advantages over the conventional methods in the areas of cost, purity, homogeneity and safety (Tillotson et al., 2001). Spray pyrolysis suffers with many fatal disadvantages such as difficulty of controlling particle size (Kim S.G. et al., 2000), porosity in the deposited film (Lee et al., 2003) and low deposition efficiency, which causes a very poor economy of this technique (Siefert, 1984). The most challenging and common issue in electrodeposition is the nonuniformity of the films. Also, the growing electroplating film may consists of air bubbles, which results in voids in the final film (Losey and Kelly, 2008). Similar to other deposition techniques, PLD has also many limitations such as bombardment with high kinetic energy ablation particles in PLD is the key problem for epitaxial growth of high quality thin films (Xin et al., 2006) and consequently hill-and-valley like structures are formed on the target surface (Rong, 1995). PLD technique has less beam to target energy transfer efficiency (~ 3%) and it is failed to ablate materials having high optical transparency and reflectivity (Harshavardhan and Strikovski, 2005; Aga, et al., 2006). Thus, pulsed electron beam ablation (PEBA) method has been selected on the basis of the limitations found in previously studied techniques. Further, there is a dire need to assess alternative deposition method in the hope of preparing good quality CZO thin-films. The potential technique should allow for deposition of the film in a single step, should not have high operating and maintenance costs, and should be safe and has ability to scale

up. PEBA can be a potential technique by which high quality CZO thin film NCs can be prepared. As per literature review, so far PEBA has not been employed for the synthesis of CZO thin films.

1.2. Zinc Oxide (ZnO)

Transition metal oxides are a highly interesting group of materials for possessing of wide variety of structures and with diverse electronic, magnetic and optical properties. Among these ZnO is a well-known transition metal oxide for its interesting properties and applications (Ellmer et al., 2008). ZnO has attracted much attention, over the past years, due to its wide range of properties, depending on doping levels, including a range of conductivity from metallic to insulating, piezoelectricity, high transparency, wide-band gap semiconductivity, room-temperature ferromagnetism, and huge magneto-optic and chemical-sensing effects (Fan et al., 2013).

Zinc oxide (ZnO) is an oxidic compound, which naturally occurs as the rare mineral zincite. Zinc oxide is a semiconductor with a band gap of 3.37 eV, and large exciton binding energy of 60 meV at room temperature making it an attractive material for potential use in electronics, optoelectronics and laser technology (Yang, 2013; Radzimska and Jesionowski., 2014). ZnO can occurs as one (1D), two (2D) and three (3D) dimensional structures. ZnO provides one of the greatest groups of different particle structures among all the known materials (Radzimska and Jesionowski., 2014). The valency of Zn is +2 in ZnO, so it can be readily replaced by transition metals such as Mn, Fe, Co, N, V and Cr. Upon alloying with Co and other transition metals, ZnO exhibits both ferromagnetic and semiconducting properties to employ the spin state for information transfer or storage in innovative spinelectronic devices (Ellmer et al., 2008).

ZnO can be synthesized in different phases, thus widening its spectrum of technological applications. The different phases in which ZnO can be condensed in crystalline forms are hexagonal wurtzite (WZ), cubic zincblende (ZB), cubic rock salt (RS), hexagonal graphite-like and tetrapods among others (Perez et al., 2015). The wurtzite crystalline phase is stable at normal pressure and temperature, whereas other phases are stable under special conditions. ZnO hexagonal wurtzite crystal structure has lattice parameters a = 3.25 Å and c = 5.12 Å and Zn atoms are tetrahedrally coordinated to four O atoms (Pearton et al., 2005). Ashrafi and Jagadish, (2007) described that the atomic arrangement in zincblende and wurtzite structures are quite

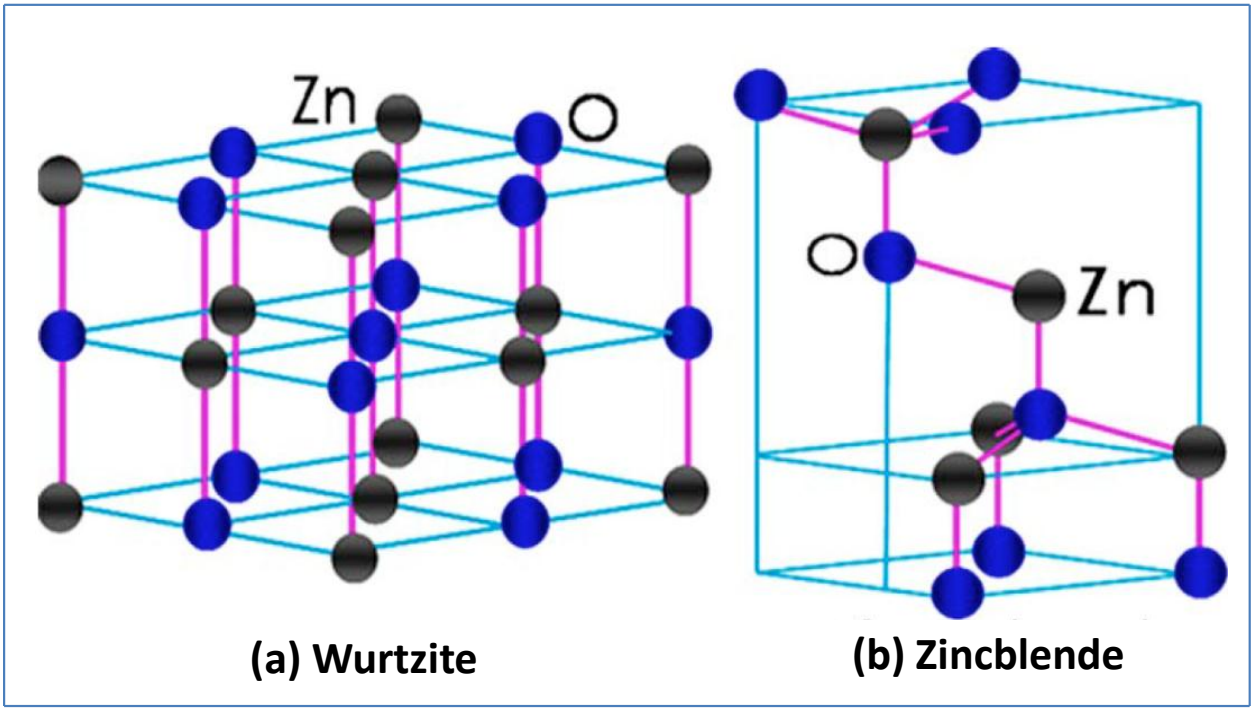

Figure 1.1: A schematic representation of ZnO crystal structures: (a) wurtzite and (b) zincblende. (Reprinted with the permission from: Ashrafi and Jagadish, 2007. © 2007, American Institute of Physics).

similar. Only the difference is in the angle of adjacent tetrahedral units, having values of 0^{o} and 60^{o} for wurtzite and zincblende phases, respectively. The crystal structures consist of alternating

planes of tetrahedrally coordinated Zn^{2+} and O^{2-} ions stacked alternately along the c-axis, as depicted schematically in Figure 1.1. The zincblende ZnO phase has a lower iconicity and the highest symmetry compatible with the existence of piezoelectric polarization as compared to wurtzite ZnO phase, which offers an attractive platform for exploring the features of excitonic systems.

1.3 Role of dopants in metal oxides

Doping is the process of adding some foreign substance into the semiconductor. These added foreign substances are known as dopants. Dopants may be cationic (addition of cation to metal oxide) such as Co, Cr, Fe, Ni etc., or anionic (addition of anion to metal oxide) such as C, N, S etc. (Ali et al., 2012). Usually doping is done in metal oxides to create tail states in the vicinity of the valence band, which leads to decrease in effective band gap. Actually, doping of metal oxides like TiO_2, ZnO with metal and/or transition metals increases the surface defects, which ultimately increases the surface area. These surface defects and increased surface area play an important role in the catalytic activities of metal oxides (Ullah and Dutta, 2008). Doping of metal oxide semiconductors causes the following key changes in the band gap electronic structures as summarized by Serpone, 2006.

- Increased localize dopant levels near the conduction and valence bands
- Band gap shrinkage due to broadening of the valence band
- Localized dopant levels and electronic transitions to the conduction band
- Electronic transitions from localized levels near the valence band to their corresponding excited states

Thus, dopants play a key role to achieve technologically important desired properties in the semiconductors.

1.4 Impact of Co-doping on ZnO properties

Co ions are systematically substituted Zn ions in optimal CZO thin films without changing the hexagonal wurtzite structure of ZnO (Ueda et al., 2001). Figure 1.2 depicts lattice structure of CZO thin film. Many attempts have been made to modify or improve the properties of ZnO by doping with different transition metals in order to achieve the multifunctional behavior (Su et al., 2011; Jaramillo et al., 2005). Antibacterial as well as photocatalytic activities of ZnO are enhanced upon doping with Co (Poongodi et al., 2015). Su et al., (2011), have shown that in homogeneous distribution of Co in the CZO films could improve the links of the grains

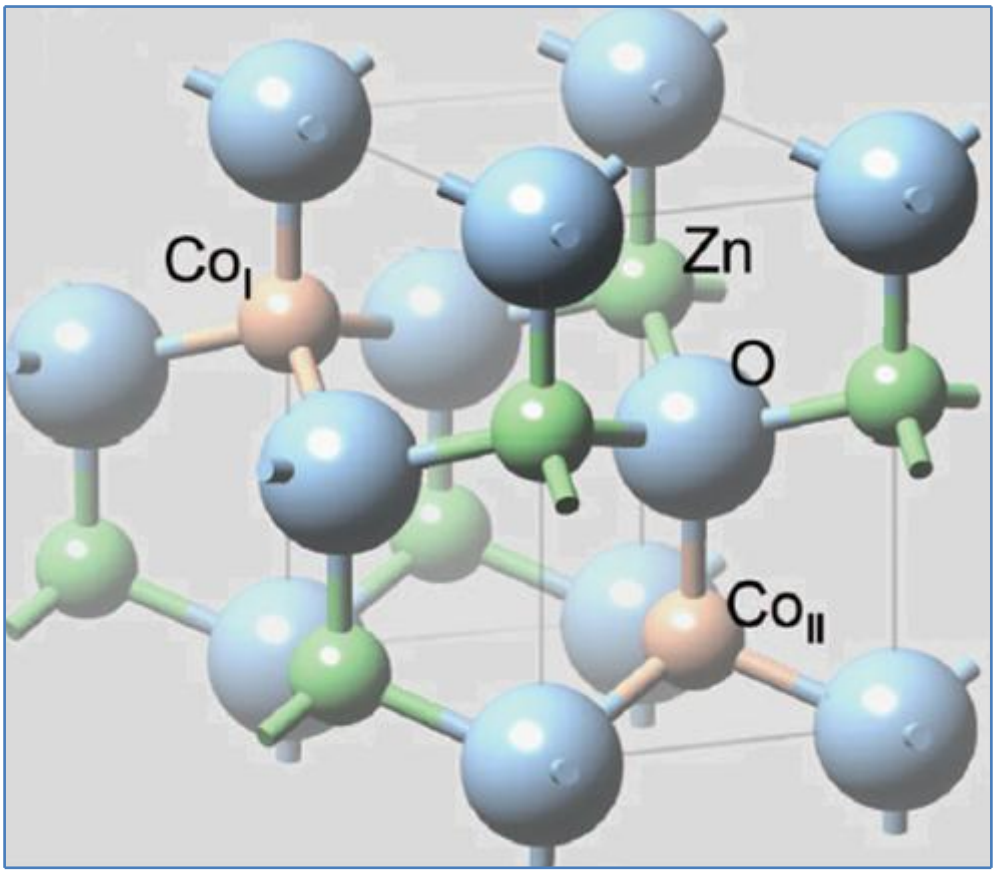

Figure 1.2: The lattice structure of (4 at. %) CZO thin film. (Reprinted with the permission from: Song et al., 2006. © 2006, the American Chemical Society).

and increase the carrier concentration of the films. The Co doping causes the turn-on field to increase by increasing the concentration of the Co dopant, which could be attributed to the band gap narrowing in the deposited films (Wang et al., 2011).

Similarly, Yang and Nie, (2009), depicted that the band gap decreases with increasing the Co doping level in ZnO. They found that spherical nanostructured film has band gap of 2.83 eV, whereas undoped ZnO has 3.11 eV band gap. Ullah and Dutta, (2008), described that Co doping results in hyperchromic shift in the optical absorption of ZnO, which is also attributed to narrowing of the band gap. These changes in ZnO caused by Co doping play a key role in photocatalysis.

Neogi et al., (2009), found that level of dopant strongly affects the morphological, structural and transport properties of CZO films. Xu et al., (2010), synthesized CZO powders with different Co compositions (0, 0.5, 1, 3 and 5 molar %). They found that films with 3% molar Co as a dopant exhibits a high photocatalytic activity to degrade Methyl Orange. Recently, Taabouche et al., (2014), described that Co doping results in a decrease of the grain size in ZnO thin films. They demonstrated that the grain size decreases from 37 to 31 nm when the Co concentration level increases from 0 to 5 % in the deposited films.

The magnetic, optical, electrical, structural and catalytical properties of CZO thin films are presented in detail in chapter 2. The deposited thin film NCs are characterized using numerous complementary analytical techniques such as X-ray diffraction (XRD), scanning electron microscope (SEM), Energy Dispersive x-ray spectroscopy (EDX), atomic force microscope (AFM), visible reflectance spectroscopy and X-ray photoelectron spectroscopy (XPS) will be described in chapter 3, and experimental results will be discussed in chapter 4-6. Thin film growth process and growth modes are discussed in the next section (1.5).

1.5 Thin film growth

Thin film deposition processes consist of essentially three main steps: (a) production of appropriate atomic, ionic or molecular species, (b) Transport of these species to the substrate, (c) condensation of these species on the substrate surface (Wasa et al., 2004). Thin film formation takes place step by step via nucleation and different growth processes. A sufficient number of vapour atoms and molecules condense on the substrate surface during the early stages of film growth. This step involving the formation of stable nuclei is called nucleation (Ohring, 2002). Initially, the adsorbed species are not in thermal equilibrium with the substrate, and, consequently, move over the substrate surface resulting in the formation of bigger clusters. Soon after nucleation, a uniform distribution of small clusters or islands is observed on the substrate surface. The next stage in the process of film formation involves merging of these islands by coalescence. The merging tendency to form larger size islands is called agglomeration, which is enhanced by increasing the surface mobility of the adsorbed species (Wasa et al., 2004). This process is extremely important for the growth of films with special properties. Solid-like coalescence of two islands results in grain boundaries between them, whereas liquid-like fusion results in the formation of new, large and boundary free islands. Ripening involves the redistribution of mass between different islands and with the passage of time the larger islands grow or ripen at the expense of smaller ones. (Ohring, 2002; Kaiser, 2002). Thin-film fabrication processes may be summarized as consisting of nucleation, formation of islands, and surface-diffusion controlled growth of islands to give a continuous film on substrate surface.

There are three basic growth modes of thin-film growth processes. These growth modes are: (a) island type, called Volmer-Weber(V-W) mode, (b) layer by layer type, called Frank-ven der Merwe mode, (c) Mixed (Layer plus island) type, called Stranski-Krastanov (S-K) mode.

Any of the three growth modes can occur depending on the interaction energies of the substrate atoms and adsorbed species. However, the S-K type of material growth is very common and has been observed in a number of metal-metal and metal-semiconductor systems (Ohring, 2002; Martin et al., 2010).

In the next section (1.6), the brief process description of different fabrication techniques employed to deposit CZO thin films is presented, and at the end of each growth technique some more experimental studies conducted using that specific technique have been summarized.

1.6 Co-doped ZnO thin film growth techniques

1.6.1 Chemical vapour deposition (CVD)

Chemical vapour deposition (CVD) is parent to a family of processes whereby high purity and high performance solid materials are deposited from vapours by a chemical reaction occurring on or in the vicinity of the heated surface. In CVD process, the substrate is exposed to one or more volatile precursors in order to produce desired deposits on the substrate surface. The resulting deposited material on the substrate is in the form of a thin film or single crystal. CVD technique ensures the production of uniform coatings and thin films with selective properties. This technique is employed in many thin film applications viz., dielectric, conductor, passivation layers, corrosion and heat resistant coatings and microelectronics. Other applications include preparation of solar cells, high temperature materials and more recently carbon nanotubes (Carlsson and Martin, 2010).

Deposition temperature, pressure, reactant gas concentration and gas flow rate are the key parameters required to control and monitor during film growth. The deposition process can be broadly categorized into thermally activated, ultrasonic assisted, plasma assisted and laser assisted CVD. In general the key steps in a typical CVD process include transport of active gaseous species to the reaction chamber, adsorption and reaction of the species on the substrate

surface followed by diffusion, nucleation and growth of thin film on the substrate. Finally, the by-products and unreacted gaseous precursors are transported away from the deposition chamber. During deposition it is necessary to keep all parts of the deposition chamber at least as hot as the vapour source; otherwise vapours will condense on any relatively cold surface (Palma and Lakhtakia, 2013; Collins, 2012; Bryant, 1977).

Tuan et al., (2004), have grown CZO thin films on Al_2O_3 (012) substrates by metal organic chemical vapor deposition (MOCVD) technique. They found that high concentration of Co was uniformly incorporated into the films and the film thickness was achieved in the range of 40-600 nm. The deposited films showed weak ferromagnetism with a curie temperature (T_c) of at least 350 K. The Co oxidation state was found to be +2 and there was no evidence for the formation of secondary phases such as metallic Co and CoO. They concluded that the magnetic properties depend strongly on the conductivity, which is greatly improved by vacuum annealing and oxygen vacancies.

Similarly, Zukova et al., (2007), managed to deposit $Zn_{1-x}Co_xO$ films on sapphire (1102) substrates at a temperature of 550^oC using pulse-injection metal organic chemical vapor deposition (PI-MOCVD). The thickness of the deposited films varied from 59 nm to 102 nm in which Co^{2+} ions replace Zn^{2+} without disrupting ZnO lattice. The magnetic moments were decreased for large Co levels in the films, for x = 0.01 a magnetic moment of 18.9 μB/Co and 6.5 μB/Co for x = 0.02 was measured. All the grown films except for x = 0.2, were found to be magnetic at room temperature. It was concluded that this giant moment (18.9 μB/Co) and the observed decrease in saturation moment with increasing Co concentration is not due to the formation of metallic Co clusters (supported by XPS and XRD measurements), instead the magnetic behaviour of grown films is truly intrinsic.

Khare et al., (2006), prepared $Zn_{0.98}Co_{0.02}O$ on c-plane sapphire substrate at a deposition temperature of 400^{o}C and 500^{o}C using ultrasonic-assisted solution chemical vapour deposition (UASCVD) technique. The films grown at 400^{o}C exhibited strong ferromagnetic signals at room temperature. Through annealing the films under different oxidation atmospheres and in the absence or presence of Zn vapours, it was observed that ferromagnetism was not linked to conductivity, and small level of Zn_i defects play a key role in producing ferromagnetic signals in the deposited films.

1.6.2 Molecular Beam Epitaxy (MBE)

Molecular beam epitaxy (MBE) allows ultra-thin films to grow epitaxially by interaction of several atomic or molecular beams on the top of the substrate surface with a good control of thickness and stoichiometry. The deposition process takes place under ultra-high vacuum condition (typically below 10^{-10} Torr). Thus, MBE process is considered a refined form of evaporation in which ultra-pure targets are heated to their sublimation point in effusion cells, also called Knudsen cells to produce molecular beams, which are directed toward a single crystalline substrate. These molecular beams in the vicinity of substrate may react chemically with each other or with other gaseous species followed by deposition as a thin film on the substrate (Palma and Lakhtakia, 2013).

Various pumping technologies including cryopumps, ion pumps and turbo molecular pumps are employed to maintain ultra-high vacuum in a MBE system. The materials condensing on the substrate surface may be desorbed, incorporate into the growing film or segregate on the substrate surface to form islands. The substrate is often heated and rotated continuously to improve the homogeneity and uniformity of the deposited film. During deposition, the growth process can be monitored and precisely controlled with feedback from reflection high energy

electron diffraction (RHEED). High film growth control and in situ characterization are the main advantages of MBE. High maintenance cost and low growth rate are the disadvantages of this technique.

Lu et al., (2010) attempted to deposit $Zn_{0.95}Co_{0.05}O$ single crystalline films on a plane sapphire substrate at 400^{o}C using molecular beam epitaxy (MBE) system with a base pressure of 5 x 10^{-10} Torr. They showed that the films as grown exhibit high resistivity and non-ferromagnetic behaviour at room temperature and after annealing in Ar atmosphere or mixed gas Ar (95%)/H_2 (5%) the deposited films become ferromagnetic and good conductivity due to induced donor defects or free carriers. However, the films annealed in pure Ar atmosphere exhibit weak ferromagnetism (0.16 μB/Co) as compared to the films annealed in Ar/H_2 mixed gas (0.82 μB/Co). Both XRD and optical transmission spectrum analyses reveal the incorporation of Co^{2+} cations into wurtzite ZnO lattice. However, X-ray absorption studies clearly indicates the presence of metallic Co clusters in the films after thermal annealing in Ar/H_2 mixed gas. Similarly, Sati et al., (2007) and Liu et. al., (2013) also successfully synthesized CZO thin films using plasma assisted MBE and laser MBE, respectively, as explained in chapter 2 (see magnetic properties of CZO films).

1.6.3 Sputtering

Sputtering is a physical deposition process, which can be used to grow thin films on the substrate surface. Sputtering has the capability of fabricating high melting point materials, which are difficult to deposit by thermal evaporation process. The target is generally made of a metal or alloy disk. The particles are ejected from the target surface by a nonthermal evaporation process. The ejected particles are the source of thin film (Wasa, 2012).

In a typical sputtering process, cathode made of target material is bombarded with atom

sized energetic particles. The bombardment process leads to the ejection or sputtering of the target atoms. The ejected atoms form a plasma consisting of vapour flux, which may then condense on a substrate surface as a thin film. The secondary electrons are also emitted from the target surface, which play an important role in maintaining the plasma (Kelly and Arnell, 2000). Sputtering has been used to make dielectric, semiconductor, magnetic, superconducting oxide materials, as well as catalysts and protective coatings. The most widely configurations for sputtering deposition to generate plasma are the direct-current (DC) configuration, the radio frequency (r.f.) configuration and the magnetron assisted configuration (Fan et al., (2013; Palma and Lakhtakia, 2013).

Song et al., (2007), used rf magnetron sputtering to deposit (6 at. %) CZO thin films on Al_2O_3 substrates at room temperature and 573 K. The films growth rate was approximately 3.6 nm/min and the films were ~105 nm thick. They described that the combination of growth rate and substrate deposition temperature are the key parameters in determining the crystallinity of the deposited films. They concluded that the structural defects in the films play a key role in the room temperature ferromagnetism. Furthermore, they concluded that high temperature annealing results in evolution of the local Co cluster, which most likely accounts for the transition from ferromagnetism to paramagnetism in the deposited thin films. Similarly, Sakuma et al., (2010), deposited CZO films using a low-energy process of gas flow sputtering, and measured the chemical state of CZO film using XPS. They described that the peak position for metallic Co, including Co nano clusters, is 778.1-778.5 eV. The Co 2p XPS spectra revealed the possibility of the existence of CoO clusters in CZO thin films.

1.6.4 Sol-Gel

The sol-gel process enables the deposition of solid materials as thin film, at much lower

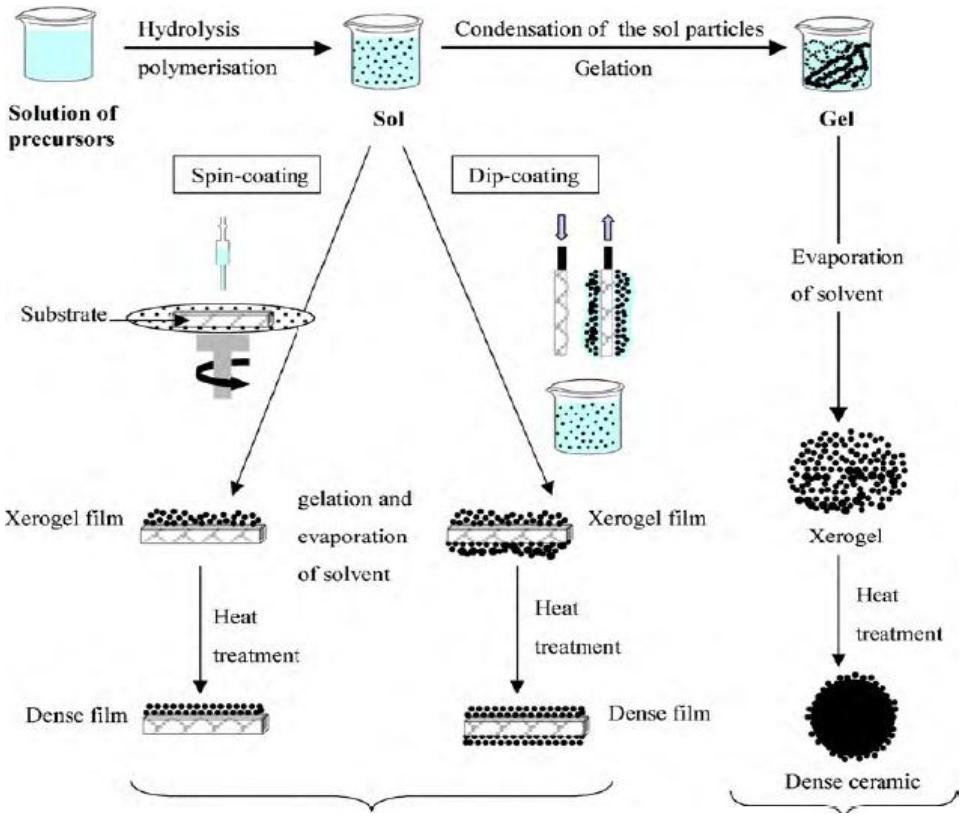

Figure 1.3 : Overview showing two synthesis examples by the sol–gel method; (a) films from a colloidal sol; (b) powder from a colloidal sol transformed into a gel. (Reprinted with the permission from: Znaidi L., 2010. © 2010, Elsevier Science).

temperature than by traditional methods of thin film deposition. The process is shown schematically in the Figure 1.3. Coatings of different materials such as glass, ceramic, metal and plastic etc. on substrates by sol-gel technique are useful to create new properties or to change the existing properties of the substrate, which are needed for developing various kinds of devices. This method allows the fabrication of thin films on the substrates that are non-heat resistant and is used mainly for the synthesis of materials based on the transformation of precursors into an oxide network by hydrolysis and condensation (Znaidi L., 2010; Sakka, 2013). The commonly used precursors for sol-gel synthesis process are organoalkoxysilanes and metal alkoxides. A possible way to synthesize the desired nanoscopic thin film is to control the hydrolysis and

condensation of precursors during sol-gel process (Ferreira et al., 2011). Fabrication of thin films and powder by sol-gel process involves three main steps. These steps are as follows: precursor solution preparation and deposition of sol on the substrate surface by a suitable technique followed by the heat treatment of the deposited film (Znaidi, 2010).

Park et al., (2004), prepared $Zn_{1-x}Co_xO$ thin films by sol-gel method. The prepared films were thermally annealed at 600^oC for 10 min in a reduced oxygen pressure at 10^{-2} Torr. They observed that the structure, while temperature-dependent, is affected by the level of Cobalt doping in CZO films. Below a threshold Cobalt loading of x = 0.12, the properties of CZO are practically similar to those of ZnO as Zinc atoms are substituted by Cobalt counterparts. Beyond the threshold value, the secondary phases such as metallic Cobalt and Cobalt oxides appear in CZO films. Further, they also emphasized that heat treatment at 600^oC of CZO film under reduced oxygen partial pressure results in the formation of metallic Co inclusions in CZO films.

Lee et al., (2002), fabricated $Zn_{1-x}Co_xO$ with different Co levels ($0 \leq x \leq 0.30$) on (0001) Al_2O_3 substrates by sol-gel technique. The prepared films were dried at 300^oC in air for 10 s and the films were annealed in O_2 environment at a temperature of 700^oC for 1 min. The thickness of the films was found to be 200-250 nm. The XPS measurements revealed that the films with $x > 0.25$ exhibit a secondary phase (CoO) but the measurements ruled out the presence of metallic Co clusters. They observed high temperature ferromagnetism in the films above 350 K and suggested that ferromagnetism strongly depends on the technical methods used for the preparation of the films.

Recently, Poongodi et al., (2015), successfully deposited CZO nanostructured thin films with different concentrations (0 w%, 5 w%, 10 w% and 15 w%) on glass substrates by sol-gel technique. The deposited films were dried at 100^oC for 10 min in order to evaporate the residue

solvents in the films. The coated films with the desired thickness were annealed in air at 400^{o}C for two hours. The XRD results revealed that the thin films exhibit hexagonal wurtzite structure. The results of energy dispersive x-ray (EDAX) analysis and XPS showed that Co was doped into ZnO structure. They demonstrated that the CZO compared to the undoped ZnO thin films exhibit enhanced photocatalytic activity under visible light for the degradation of methylene blue dye. It was concluded that this improved photocatalytic degradation activity of CZO is due to high charge separation efficiency and reactive oxygen species generation which enhanced the antibacterial activity of CZO thin films.

1.6.5 Spray pyrolysis

Spray pyrolysis is a technique in which thin film is deposited by spraying a solution on a heated substrate surface as shown schematically in the Figure 1.4. This technique is very simple and relatively inexpensive, particularly with regard to equipment cost, than many other film deposition techniques. This technique has the capability of fabricating a large variety of films such as dense, thin, porous as well as multilayered films on a variety of substrates and, is particularly useful for large area application (Perednis and Gauckler, 2005). A spray pyrolysis system mainly consists of stationary or moving spraying nozzle, precursor solution, substrate holding plate, gas/air compressor, substrate heater and thermocouple and liquid and gas flow meters. During deposition, fine droplets of the precursor solution reach the substrate surface mostly using air as a driving gas where the constituents react to form a chemical compound. The deposition process involves products other than the desired compound. Thus, the chemical reactants are selected carefully such that the undesired products are volatile at the deposition temperature. The spray rate, droplet size, carrier gas, nozzle-substrate distance, substrate temperature, ambient atmosphere, substrate or nozzle motion and cooling rate after deposition

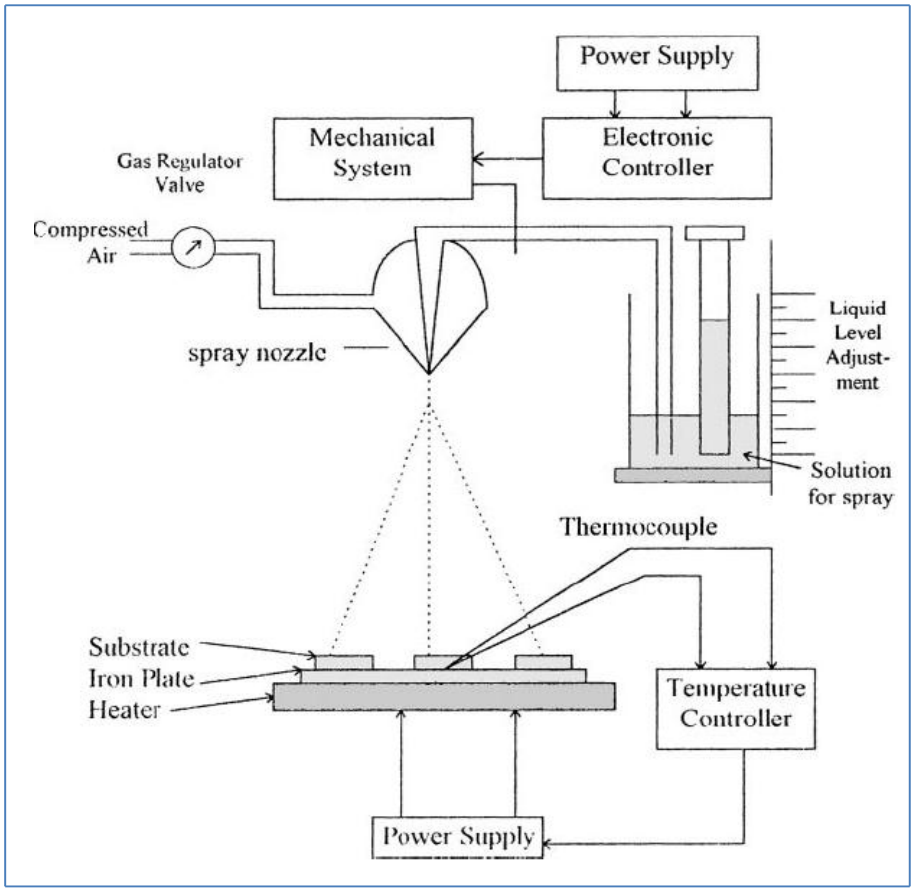

Figure 1.4: Schematic set-up for spray pyrolysis technique. (Reprinted with permission from: Patil, 1999. © 1999 Elsevier Science).

affect the quality of the deposited films (Patil, 1999).

Belghazi et al., (2009), successfully synthesized ZnO and $Zn_{1-x}Co_xO$ thin-films ($0 \leq x \leq 0.09$) on glass substrates at a temperature of 450^{o}C using spray pyrolysis technique. The glass substrates were cleaned in ethanol followed by rinsing in distilled water and subsequently dried before deposition. During deposition, the solution flow rate was fixed at 2.6 ml/min and the thickness of the films was about 300 nm. It was found that the Co^{2+} ions were well substituted for the Zn^{2+} ions into the ZnO matrix without damaging ZnO wurtzite structure. The deposited films were found to be paramagnetic at low temperature magnetization measurements and there was no sign of ferromagnetism and secondary phases.

Benramache et al., (2012), fabricated transparent conducting CZO thin films on glass substrates applying ultrasonic spray technique. The deposition was carried out at different deposition temperatures of 300^{o}C, 350^{o}C and 400^{o}C with a deposition time of 120 s. All the deposited films exhibit preferential growth along (002) plane. The maximum crystallite size value of the film deposited at 350^{o}C was found to be 55.46 nm. The optical gap and activation energy measurements reveal that the films deposited at 350^{o}C exhibit n-type semiconducting behaviour. They described that deposition temperature has strong bearing on electrical conductivity and energy band gap of the deposited film. The electrical conductivity of the films increases with temperature viz., 7.424 Ω (300^{o}C), 7.547 Ω (350^{o}C) and 6.743 Ω (400^{o}C). Similarly, energy band gap of CZO films increases from 3.351 eV to 3.362 eV as the deposition temperature increases from 300^{o}C to 350^{o}C.

Acosta et al., (2009), successfully fabricated ZnO and CZO thin films on Si (100) substrates at temperatures of 450^{o}Cand 500^{o}C using chemical spray technique, and the Co concentration was varied as 3%, 8% and 16% for each temperature. They concluded that electrical resistivity of the CZO thin films was found to improve when Co was incorporated into the starting solution. They observed the lowest resistivity value 5 x 10^{-3} Ωcm for CZO films. Rutherford backscattering spectrometry (RBS) measurements revealed that the Co concentration in the deposited films increases with the deposition temperature as well as with depth. No extra secondary phases related to Co have been detected in the deposited films.

1.6.6 Electrodeposition

Electrodeposition is a surface modification technique to improve the surface characteristics and is widely used for the growth of thin films. Materials are deposited near ambient conditions at much higher flow rates. The essential elements of the process are a

workpiece to be coated (cathode), a counter electrode (anode), current source and electrolyte solution that contains the metal ions (Losey and Kelly, 2008).

The electrodeposition technique involves the deposition of metal ions over the conducting surface by means of electrolysis. The steps involved in the electrodeposition process are presented schematically in Figure 1.5. The cathode is the conducting surface on which deposition takes place. During electrolysis, reduction and oxidation reactions occur at the cathode and anode respectively. During deposition, the hydrated ions are deposited as adatoms at the cathode surface. The incorporation and surface diffusion of adatoms lead to the formation of a film on the cathode surface (Jayakrishnan, 2012).

Manouni et al., (2009), managed to deposit polycrystalline $Zn_{1-x}Co_xO$ thin films with different Co concentrations (x = 0.01, 0.07, 0.08 and 0.17) on glass coated indium tin oxide

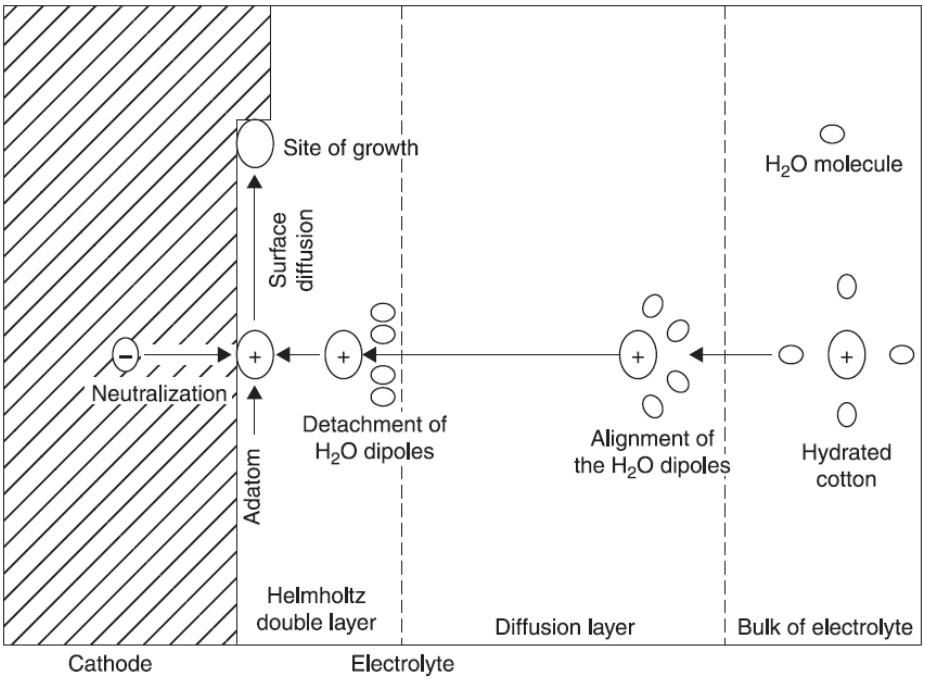

Figure 1.5: Schematic representation of steps in the electrodeposition process. (Reprinted with permission from: Jayakrishnan, 2012. © 2012, Woodhead Publishing Limited).

(ITO) substrates applying cathodic electrodeposition technique. Before the deposition, the substrates were cleaned in an ultrasonic acetone bath for 15 min and rinsed in distilled water followed by air drying. During deposition, the solution temperature was fixed at 90^{o}C and deposition potential was maintained at - 0.09 V. After deposition the films were annealed at 400^{o}C in air atmosphere for one hour. The thickness of the film was found to be in the range of 520 to 850 nm. All the films exhibit hexagonal wurtzite structure which reflects that Co doping (up to 17 w%) does not affect the crystal structure of ZnO. The crystal quality was improved by annealing as evidenced by Raman measurements. XPS and optical transmission spectroscopies confirm the incorporation of Co^{2+} cations in substitution sites of Zn^{2+} in ZnO wurtzite structure. Furthermore, for the films with x> 0.10 XPS spectra confirms that metallic Co and O are adsorbed in the surface of the deposited films, which disappear with moderate annealing.

Wang et al. (2011) grew CZO thin films on ITO glass substrates using electrodeposition. The films deposition were carried out at 80^{o}C for 10 min followed by washing with distilled water in order to remove the Co^{2+} and Zn^{2+} left from the surface of the deposited films. They demonstrated that Co loudening of (x = 0.0, 0.15) does not change the crystal structure of deposited ZnO films. The macroscopic field-emission characteristics of the prepared films were examined and indicate that Co doping causes band gap narrowing in the deposited films. Similarly, Tortosa et al., 2008 deposited CZO film via electrodeposition. They measured the chemical state of the films by XPS, and described that the energy peak at around 779 eV is associated with non-oxidized metallic cobalt in CZO films.

1.6.7 Pulsed laser deposition

Pulsed laser deposition (PLD) has been widely used as a technique for the fabrication of thin film of simple and complex oxides. The PLD technique is conceptually simple, in which a pulsed laser beam lead to the rapid ablation of material from a target and results in an energetic

plasma plume, which eventually condenses on the substrate surface (Christen and Eres, 2008). However, various mechanisms such as ablation, plasma plume formation and propagation as well as nucleation and growth involved in the PLD technique are rather complex in contrast to the simplicity of the technique. The idea of utilizing high power density of laser beam for material processing has been tested since 1960 (Strikovski et al., 2010) but was not used as a growth technique of choice until the late 1980 (Martin et al., 2010). Since then, this technique has been used extensively for the growth of high temperature cuprates and complex oxides.

In PLD, the deposition is achieved by vaporization of the materials using an external energy source (laser), which makes it a more versatile material growth process. A typical PLD system consists of a vacuum chamber equipped with pumps, target holder and rotator, substrate heater, holder and rotator, various pressure gauges, controllers and other instruments which control the deposition process of the system (Fan et al., 2013). A high energy pulsed laser hits the target surface and results in localized heating and vaporization of the target, producing a plasma plume consisting of atoms, ions and neutrals above the target surface. The plasma expands away from the target surface directed towards substrate, and condenses on the substrate surface as thin film. The most commonly laser used in PLD is KrF excimer (248 nm, typically 20-35 ns pulse duration. Successful material growth has also been achieved using ArF (193 nm) and XeCl (308 nm) excimers (Christen and Eres, 2008).

The stoichiometric removal of material from a solid target is the most important factor in the success of PLD. However, stoichiometric removal of the material from the target does not necessarily lead to the growth of stoichiometric materials because all the elements do not incorporate into the growth surface at the same rate. Some elements can re-sputter and more volatile elements may re-evaporate from the growth surface (Martin et al., 2010). The target

material is typically a solid source but liquid sources such as organic liquids have also been investigated successfully for material growth (Rong, 1995).

Karamat et al., (2010) synthesized and characterized both bulk and thin films of cobalt doped zinc oxide. Thin films were grown using 12,000 laser pulses on substrates of Al_2O_3 at a temperature of 375±5^oC in different N_2 pressure through PLD. They showed that ferromagnetic behaviour of CZO films is intrinsic based on substitution of Co into the ZnO matrix and donor defects, and the electrons also play an important role in enhancing film ferromagnetism. Ferromagnetism significantly depends on the growth pressure of background gas (nitrogen). They found that there is an increase in defects in the thin films grown at higher pressure. These defects may be in the form of Zn interstitials and oxygen vacancies, and suppress ferromagnetism in the films. They concluded that the presence of Co^{2+} ions is an important source of ferromagnetic behaviour in the deposited film.

Peng et al. (2005) deposited epitaxial and textured $Zn_{1-x}Co_xO$ (x = 0.15-0.25) thin films on polished c-plane sapphire substrates using dual beam pulsed laser deposition. A KrF excimer laser (248 nm, 10 Hz) was used to deposit the films and irradiated on two separate targets viz., Co and ZnO. The resulting film thickness was about 100-200 nm and deposition was carried out at 650^oC and a pressure of 5 x 10^{-5} Torr. It was found that the films exhibit wurtzite structure having similar lattice parameters to that of ZnO. They demonstrated that more impurity levels are developed within the band gap when more Zn is replaced by Co and, consequently, more defects are produced in the films. Furthermore, they described that an increase in the dopant level leads to an increase in band gap of the deposited films. Chemical state of the films were evaluated using XPS. The Co $2p_{3/2}$ peak attributed to Co-Co bonding is located in the range of 778.1-3 eV, whereas the peak corresponding to Co-O bonding is located at 780 eV. The

intensity of the peaks increases as the Co concentration increases. In order to find out the effect of Co concentration, a spectrum for x = 0.41 was also introduced. The excessive Co content results in the occurrence of a dominant peak at 778 eV, demonstrating the existence of metallic Co precipitates in the $Zn_{1-x}Co_xO$ thin film.

Opel et al., 2008 fabricated epitaxial $Zn_{0.95}Co_{0.05}O$ thin films on a single crystalline, c-axis oriented ZnO (0001) substrates at temperature between 3000°C and 6000°C in Ar atmosphere at a pressure of 4×10^{-3} mbar. They showed that the deposited films exhibit room temperature ferromagnetic behaviour which clearly stems from nanometric sized metallic Co precipitates. The XRD spectrum reveals a peak at $2\Theta = 44.2^{o}$, which agrees well with what is expected for reflection of (111) face centered cubic (fcc) metallic Co phase or the (0002) reflection of hexagonal closed pack (hcp) metallic Co phase. Further, they concluded that the formation and growth of these metallic Co nano scale particles can be controlled by co-doping and growth conditions. Su et al., (2011) deposited CZO films on c-sapphire using PLA. They concluded that formation of secondary phases in CZO films strongly depends on the substrate temperature. Above threshold value of deposition temperature (800°C), strong signals from metallic Co appear in CZO films as per XPS measurements. On the other hand, the formation of metallic Co in CZO films (40-400 nm) have been reported in a narrow temperature range of 450°C (Dorneles et al, 2006). They deposited films on sapphire substrate using PLA technique.

Samanta et al., (2006), managed to synthesize CZO thin films on Al_2O_3 (0001) substrates using PLD. The growth of highly c-axis oriented thin films with an approximate thickness of 800 nm was carried out using an excimer laser (KrF, 248 nm, 10 Hz) with laser energy of 2.5 J/cm^2. The deposition temperature and background pressure were maintained at 650°C and 10^{-6} Torr, respectively. The distance between target and substrate was maintained at 5 cm and the

deposition time was 17 min. It was concluded that the ferromagnetic properties of the films are intrinsic due to substitution of Co into ZnO lattice. The substitution of more than 10 w% of Co results in the formation of a new phase, $ZnCo_2O_4$, which is antiferromagnetic and, therefore, reduce the ferromagnetic properties of the deposited films.

Wang et al., 2012, fabricated $Zn_{0.95}Co_{0.05}O$ thin films on a c-plane sapphire substrate through the use of pulsed KrF excimer laser with a wavelength of 248 nm, energy 200 mJ and a frequency of 10 Hz. The growth chamber was kept at 10^{-4} to 5 Pa in ambient oxygen gas for 15 min with a substrate temperature of 500^{o}C resulting in 200-300 nm thick films. The deposited films exhibited room temperature ferromagnetism and had c-axis orientation. It was found that there existed a single phase of wurtzite structure CZO when the films were grown under lower oxygen pressure (< 1.3 Pa) at 500^{o}C. At higher oxygen pressure (1.3 Pa and above), the deposited films comprised of cubic CoO secondary phase. It was shown that the magnetic behaviour is directly related to the presence of intrinsic defects, particularly Zn and oxygen vacancies, and Zn interstitials.

Yang et al., (2013), grew CZO thin film NCs via PLD on sapphire (0001) substrates with a KrF excimer laser (248 nm, 10 Hz, 3 J/cm^2). The deposition chamber was kept at a base pressure of 4 x10^{-4} Pa with a substrate-target distance of 40 mm and substrate temperature of 300-700^{o}C. The substrate and target holders were rotated at 5 rpm in opposite direction in order to obtain uniformly deposited films with a thickness of about 280 nm. All the prepared films possessed hexagonal structure of ZnO, which exhibited room temperature ferromagnetism and secondary phases like metallic Co inclusions: CoO and Co_3O_4 were not detected in the films. The crystalline quality and lattice structure of the samples were found to be strongly dependent on the deposition temperature. It was observed that the average grain size of the prepared thin films

increased with increasing temperature from 25-39 nm for the 300-500^{o}C temperature range and then decreased with the increase in deposition temperature.

Taabouche et al., (2014), fabricated pure ZnO and CZO (Co: 3, 5 %) thin films on a glass substrate at a temperature of 450^{o}C using PLD. Glass substrates were chemically cleaned using methanol and deionized water before deposition. All the films exhibited high crystalline quality hexagonal wurtzite structure. KrF excimer laser (248 nm, 25 ns, 2J/cm^2) with a pulsed repetition rate of 5 Hz was used to carry out film deposition. The deposition chamber was initially evacuated at 5 x 10^{-3} Pa. The incident angle of laser beam on a rotating target was set to 45 degree. The oxygen pressure in the deposition chamber was maintained at 1 Pa. The grain size was found to be dependent on Co doping level in ZnO matrix. The grain size decreases from 37 to 31 nm when the Co concentration level increases from 0 to 5 % in the deposited films. Moreover, they showed that the optical band gap varies from 3.23 to 3.37 eV when the Co doping level increases from 0 to 5 at. %. Similarly, Negi et al., 2014, reported the growth of epitaxial Co films from ZnO target pellets containing 60 % Co concentration (with Co (II) and Co (III) at 24 % and 36 %, respectively) using PLD. In the film deposition process, extremely slow growth rate (2 Hz) was applied and the tail region of the plume was used, which allowed the growth of metallic Co films. The inhomogeneity of the plasma plume is schematically presented in Figure 1.6. Thin films of Co: ZnO grow in the central regions (region B), whereas in the extreme tail regions (A) only metallic Co films grow. Moreover, between regions A and B, mixed phases encompassing Co metal, Co oxides (CoO, Co_3O_4) and Co: ZnO are formed. The thin films showed ferromagnetic behaviour with a large carrier concentration of ~1.3 x 10^{22} cm^{-3}. TEM and HRTEM imaging confirms the presence of hexagonal close packed (hcp) metallic Co in the prepared films.

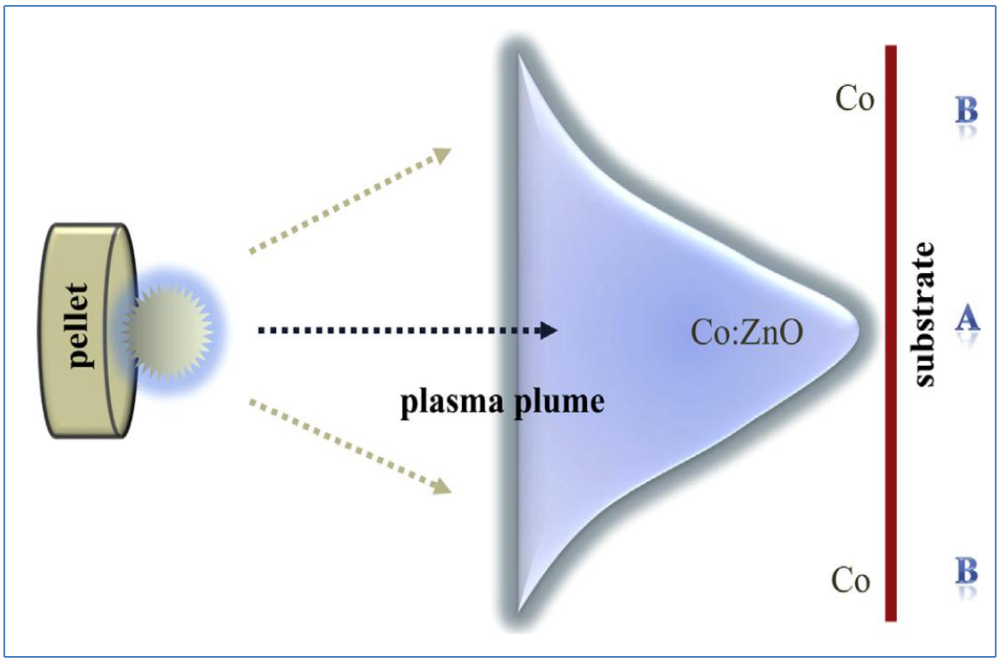

Figure 1.6: Schematic representation of the composition variation of CZO plasma plume upon laser ablation. The tail part of the plasma deposits Co metal on the substrate. (Reprinted with the permission from: Negi et al., 2014. © 2014, Elsevier Science).

Ivill et al., (2008) investigated the crystal structure and phase analysis of CZO thin films using XRD in Bragg-Brentano geometry. They used a step size of 0.02^{o} and time 1.25s per step for each scan. The primary peaks (002) obtained in XRD pattern for a series of films grown at400^{o}C correspond to the wurtzite ZnO indicating good texture with the c-plane of the sapphire substrate. A small peak was consistently observed at around $2\Theta = 44.4^{o}$ in the films containing 15% and 30% Co concentration, and occasionally seen in the films containing lower Co concentration (5%).This peak does not correspond to any ZnO or substrate peaks and has very low intensity with only few hundred counts above background. They also found that the Co phases strongly depend on the growth temperature, at higher deposition temperature Co precipitates out as CoO. The CoO phase begins to form at 500^{o}C along with metallic Co for the films grown in vacuum. Further, the CoO phase becomes prominent at 600^{o}C, while the metallic

Co phase disappears at this temperature. The metallic Co precipitation appears for higher doping levels at around $2\Theta = 44.4^{o}$. From the literature survey we can see that the focus is on the presence of secondary phases in CZO films.

1.6.8 Pulsed electron beam ablation

Pulsed electron beam ablation (PEBA) has been employed in the fabrication of high quality thin film devices for over a period of twenty years. This relatively novel technique has gained much attention for its advantages over other thin-film deposition techniques. Christiansen and Schultheiss, (1979), developed the pseudo spark discharge, which opened up the way for a number of studies on pulsed electron beams in many fields including thin film deposition. Due to poor reliability of the pseudo spark electron beam used in early devices, thin-film deposition via pulsed electron beam has been hardly studied. Hobel et al. (1990) successfully deposited superconducting YBaCuO thin films on ZrO_2(Y) and $SrTiO_2$ substrates by pseudo spark ablation. Schultheiss and Hoffman discovered in 1990 that such pseudo spark produces a magnetically self-pinched electron beam with maximum current density of 10^6 A/cm^2 and pulsed duration of 100 ns. The magnetically self-pinched electron beam was observed when the current exceeds 10 A. The diameter of the electron beam at the anode, depending on the current density, was found to be between 0.1 mm and 0.5 mm (Schultheiss and Hoffmann, 1990).

Later, Jiang et al. (1994) developed a new discharge, so called channel spark, which is quite similar to pseudo-spark discharge with nearly same pulsed width and beam diameter. However, they observed that with a shorter channel spark chamber the beam self-pinching is much more stable relatively to the bean generated from a pseudo spark discharge. More importantly, it has been demonstrated that the efficiency of energy transfer from beam to target is nearly 30% in channel spark against a pseudo spark efficiency of about 4%.

In PEBA, transient hollow cathode (THC) develops a well-focussed electron flow with large current densities in the range of 10-100 kA/cm^2 (Venkatesan et al., 2005). When a high power electron beam is incident on the target surface, it results in the rapid evaporation of the target material. Eventually non-equilibrium heating is produced and the ablation process is initiated. The energetic electrons lose energy as they penetrate into the target surface and collide through inelastic collisions with the electrons of the target atoms. After covering a short distance, the energetic electrons experience strong Coulomb scattering and diffuse into the material rather than move in a straight path. This effect helps to confine the entire dissipated energy of the pulsed electron beam within the range of 1-2 μm (Harshavardhan and Strikovski, 2005).

A pre-discharge trigger circuit, which controls the discharge voltage is used to ignite the plasma. When a sufficiently intense beam propagates in a background gas, a self-pinching force develops as the beam ionizes the background gas and produces conducting plasma. This plasma plume, which consists of neutral atoms, ions and electron, expands in the direction of maximum pressure gradients and is the primary precursor source material for thin film growth on the substrate. The plasma plume range (L_o) is controlled by the ratio of the number of ablated atoms (N_o) to the gas pressure (P) as follows (Strikovski et al., 2010).

$$L_o \propto \left(\frac{N_o}{P}\right)^{0.33} \qquad (1.1)$$

The rate of deposition depends mainly on the discharge voltage, density and thermodynamic properties of the target material, and the distance between the target and substrate. Thin film structure is influenced by the substrate temperature and material as well. The physical parameters such as heat and mass distribution, atoms and ions velocity, as well as angular distribution of the plasma plume species play an important role in thin film deposition (Muller et al., 1995; Nistor et al., 2011).

PEBA and PLD are considered to be sister technologies in thin film deposition on the basis of pulsed forms of energy, although the physics involved is not the same. PEBA has become alternative to PLD as a means of producing high quality thin films. In PLD, the mechanism of target ablation is governed by high energy photons, whereas in PEBA it is governed by energetic electrons. PEBA offers several unique advantages over PLD such as high beam to target energy transfer efficiency (~ 30%) and the ability to ablate materials having high optical transparency and reflectivity (Aga, et al., 2006). Furthermore, PEBA does not require toxic gases to operate. Mathis and Christen (2007) described that PEBA yields higher deposition rates than PLD because in the latter case, the plasma plume strongly absorbs laser light and restricts the amount of energy reaching the target surface. In PEBA, the plasma plume interacts less strongly with the incident electrons and, consequently, the target absorbs more energy, which results in higher ablation per pulse.

1.7. Nano-catalysts

The properties of the macro materials are changed when they are reduced to nano scale. Nano-catalysts are more effective than conventional catalysts as extremely small sizes (Typically 10-80 nm) yield a high surface area-to-volume ratio. They acquire unique properties that are not found within their macroscopic counterparts. Due to these properties nano-catalysts are more versatile and effective than bulk catalysts (Chaturvedi et al. 2012).

1.7.1 Application of Nano-catalysts

Catalytic behavior is strongly dependent on the nature of the materials as well as size of the materials. The colloidal and supported nanocatalysts have been used to catalyze numerous types of reaction such as oxidation, cross coupling, electron transfer, fuel cells and hydrogenation reactions are among many others (Narayanan and El-Sayed, 2005). Nanocatalysts with their

enhanced unique properties find wide spread applications in several processes (Chaturvedi et al. 2012; Mohamed et al., 2012), which are schematically presented in the Figure 1.7. Metallic nanoparticles have also attracted much attention due to their optical, magnetic, electrical and catalytic properties, as well as their application in catalysis and many other chemical processes (Gual et al., 2012). Co-doped ZnO is a perfect candidate to produce suitable nano composite for numerous such applications. Properties (Magnetic, optical, electrical, magnetic and catalytic) and

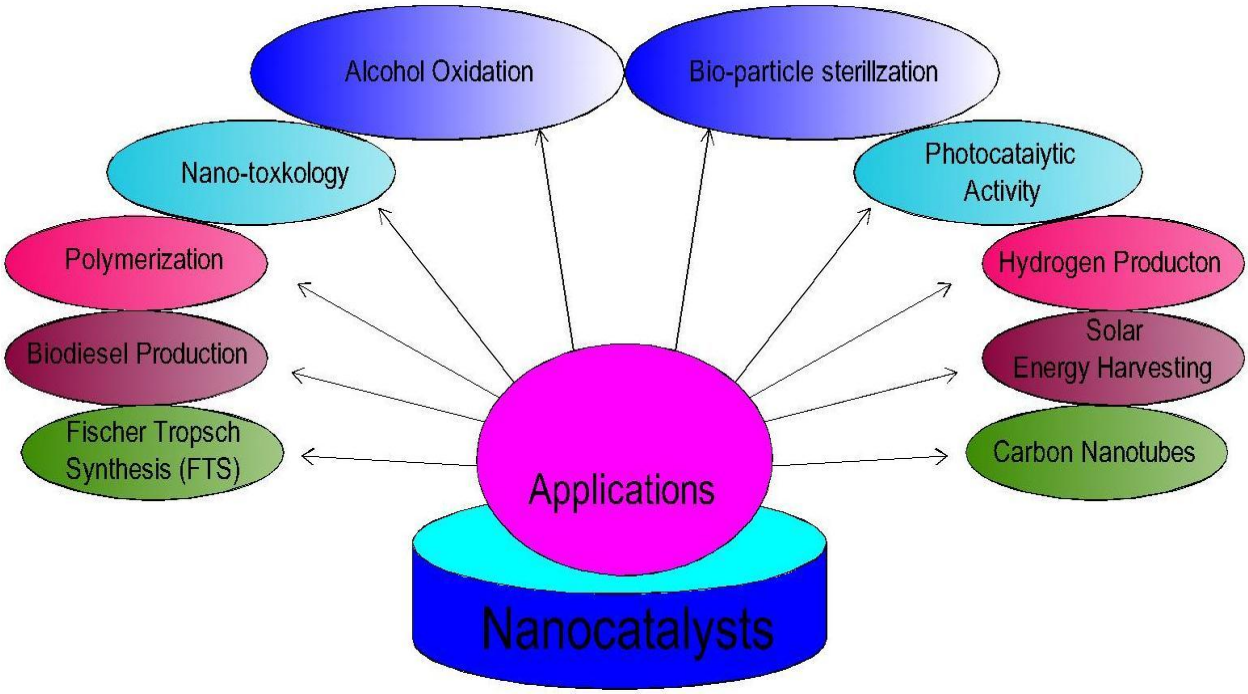

Figure 1.7: Schematic diagram of major applications of nano catalysts.

applications of CZO have been described in chapter 2, section 2.2-6.

1.7.2 Selection of support material

The choice of support material for FT-catalysts is of paramount importance, which is dependent on several considerations like metal dispersion and reducibility effect, strong metal support interaction, surface area, pore volume and stability of active phases under FTS operating conditions. Co based catalysts supported on different support materials like ZnO (Wang et al., 2012,

Pan and Bukur, 2011; Adesina et al., 1996), SiO_2 (Okabe et al., 2004; Gnanamani et al. 2013), Al_2O_3 (Karaca et al. 2011), Carbon nano fiber (Bezemer et al. 2006; Breejen et al. 2010) have been studied to carry out FTS. But for pilot and commercial scale FTS only titian, silica, alumina, aluminate and zinc oxide have been investigated (Rytter and Holmen, 2016). ZnO supported Co catalysts have many important features such as they are more resistant to oxidation caused by water produced as a by-product of FT reaction. Consequently, the catalyst is able to maintain its activity over a long period of time (Clarkson et al., 2012). One other attractive feature of ZnO supported Co catalysts is their tolerance of carbon dioxide (CO_2), which make them potential catalyst for FTS (Freide et al., 2004). Moreover, ZnO has also been reported to promote FT-reaction by improving structural and catalytic properties of the catalysts (Jahangiri et al., 2014). ZnO has been used as a support material as well as promoter (co-catalyst) for FT-reaction. Hence, ZnO has been selected as a support material for Co based FT-catalyst for this research project.

1.7.3 Selection and preparation of FT-catalyst

FT is a well-established catalytic process in which synthesis gas is converted into liquid transportation fuels (Jahangiri et al., 2014). The most common practical catalysts are Fe and Co, although Ni and Ru have also been used since the discovery of the process (Dalai and Davis, 2008). Nickel catalyst under FTS operating conditions produces much more methane and forms volatile carbonyl resulting in continuous loss of metal. The ruthenium catalyst is the most active one but it is very expensive due to limited reserves in the world. Thus Co and Fe based FT catalyst are the practical choices for FTS. Fe catalyst is less expensive than Co catalyst but has lower activity and has less resistant to deactivation as compared to Co catalyst at the operating condition of FT plants. The water gas shift reaction is more significant on iron catalyst than on Co (Tsakoumis et al., 2010). While, the activities of Co and Fe based FT-catalysts are comparable and they display similar chain growth capabilities at relatively low temperature (473-523 K), the productivity at

higher conversion is superior using Co based nanocatalysts (Gual et al., 2012). Based on its advantages, Co based FT catalysts has been selected for this study.

Preparation of FT-catalysts has been investigated by various methods viz., incipient wetness impregnation (IWI) (Xiaoping et al., 2007; Vasireddy et al., 2010; Tavasoli et al., 2008; Yuanyuan et al., 2009; Liu et al., 2007), sol-gel (Okabe et al.,2004), and co-precipitation (Wan et al., 2007) have been investigated. There are many steps involved in the preparation of FT-based catalyst by these wet chemical methods. The principal stages in the preparation of Co-based FT catalysts include deposition of cobalt on a suitable support material, decomposition/calcination of cobalt precursor followed by activation/reduction process (Khodakov et al., 2007). Commercially available ZnO supported Co based FT catalysts prepared by wet chemical methods have major issues which include inappropriate particle size distribution, and, due to low surface area of ZnO several impregnation steps necessitate obtaining a reasonable amount of cobalt loading on the support surface (Baijense and Rekkel, 2009). So, it is imperative to assess alternative synthesis techniques in the hope of preparing high quality CZO thin film nano-catalyst in a single step. PEBA can be a potential technique. This technique is very suitable for the production of nano sized materials as it has the ability to control the particle size during deposition (Mathis and Christen, 2007).

1.7.4 FT process conditions and product analysis

The FT process is preferably carried out at a temperature of 180-280°C, more preferably 190-240°C, and preferably at a pressure of 5-50 bar, more preferably 15-35 bar, generally 20-30 bars. The ratio of hydrogen to carbon monoxide in the syngas is preferably 2:1 by volume in FTS (Freide and Hardy, 2009). The synthesis process involves the hydrogenation of CO to ultra-clean liquid fuels and high value chemical products. In FT reaction both saturated and unsaturated

hydrocarbons are produced. FTS is an exothermic reaction (Jess et al., 1999).

$$CO + 2H_2 \rightarrow -(CH_2)- + H_2O \qquad \Delta H = -152\ KJ/mol \qquad (1.2)$$

In this highly exothermic polymerization reaction, a number of desirable paraffins, olefins and alcohols, and undesired products like aldehyde, ketones, acids, esters, carbons etc. are obtained (Dalai and Davis, 2008).This indicates that it is highly complex reaction. Main reactions taking place in FT process can be summarized as (Equations 1.3-1.9) follows (Dalai and Davis, 2008; Jahangiri et al., 2014; Jess et al., 1999).

- Desired reactions

(a) Paraffins

$$n\,CO + (2n+1)\,H_2 \rightarrow C_nH_{2n+2} + nH_2O \qquad (1.3)$$

(b) Olefins

$$nCO + 2nH_2 \rightarrow CnH_2n + nH_2O \qquad (1.4)$$

(c) Alcohols

$$nCO + n2H_2 \rightarrow CnH_{2n+1}OH + (n-1)H_2O \qquad (1.5)$$

- Undesired reactions

(a)Water-gas shift reaction

$$CO + H_2O \leftrightarrow CO_2 + H_2 \qquad (1.6)$$

(b) Boudouard reaction

$$CO + CO \leftrightarrow C + CO_2 \qquad (1.7)$$

(c) Bulk oxide & carbide formation

$$yCO + xM\ (\text{Metallic catalyst}) \rightarrow MxOy + yC \qquad (1.8)$$

$$yCO_2 + xM\ (\text{Metallic catalyst}) \rightarrow MxOy + yCO \qquad (1.9)$$

In FT product analysts, CO conversion % and selectivity of liquid hydrocarbons are important parameters in term of evaluation of FT-catalyst performance. The empirical relations for calculating CO conversion (%) and selectivities are as follows (Aluha et al., 2015; Song and Li, 2006).

$$Co conversion(\%) = \frac{CO_{in} - CO_{out}}{CO_{in}} \bullet \frac{Ar_{in}}{Ar_{out}} \bullet 100 \qquad (1.10)$$

Selectivity towards various FT products has been determined by assuming that CO is converted into both gaseous and liquid products. Raw figures of gas concentration (%) for gaseous products (C_o, C_1, C_2, C_3, C_4) have been collected by GC. The CO conversion (%) has been calculated using equation 1.10. Let total CO conversion to gaseous phase be denoted by C. Then C = C_o, C_1, C_2, C_3, C_4, where C_o, C_1, C_2, C_3, C_4 are the concentrations of gaseous products, viz., CO_2, CH_4, C_2, C_3, C_4 respectively as per GC analysis. The total CO conversion into liquid products will be equal to 100-C. The selectivity of each liquid product (S_i) has been calculated from the peak area (A_i) obtained in GC analysis for each product, and then divided by the total area of all the peaks corresponding to C_{5+} and higher liquid hydrocarbons. Thus,

$$S_i = \frac{A_i}{A_5 + A_6 + A_7 + A_8 ..... A_n} \qquad (1.11)$$

The overall selectivity (S_{Ci}) of each liquid hydrocarbon can be calculated as follows.

$$S_{Ci} = \frac{S_i}{100}(100 - C) \qquad (1.12)$$

Where C_i is the liquid phase hydrocarbon product corresponding to i number of carbon atoms

1.8 Motivation

Zinc oxide is not only low cost, wide band gap semiconductor but also an environmentally benign, which makes it an excellent supporting material for nanoparticles with a

plethora of potential applications. Cobalt metal is quite expensive and with low abundance, which calls for the use of Co more effectively on the nanoscale. In the past few decades Co-doped ZnO thin films have been fabricated using a variety of deposition techniques. In the present work, synthesis of Co-doped ZnO thin films has been carried out using pulsed electron beam ablation (PEBA). This constitutes one of the motivations for this work. To the best of our knowledge, no study on the synthesis and characterization of Co-doped ZnO thin films has been carried out using PEBA so far. Furthermore, Cobalt doped ZnO has excellent catalytic properties, especially when doped with Co in hexagonal (hcp) structure. Co/ZnO has been investigated as a potential catalyst to carry out Fischer Tropsch synthesis (FTS), which is a well-established catalytic process for the conversion of the synthesis gas ($Co + H_2$) into liquid fuels of different grades and compositions and high value chemicals for commercial applications (Pan and Bukur et al., 2011; Gnanamani et al., 2013).

For sustainable development of energy sources worldwide, research has focused on alternative and clean fuels. The utilization of biomass, coal and other fuel sources rather than existing fossil fuels could offer more environmentally acceptable processes for energy production and will aid in preserving the limited supplies of fossil fuels. Canada is rich in biomass sources and also has huge reserves of coal. Thus, both coal and biomass can be used for the production of synthesis gas which can be converted into liquid fuels coupled with Fischer Tropsch synthesis. Of particular interest is the development of thin film nano-catalysts for use in the production of renewable fuels via FTS. There is no information in the open literature, though, indicating CZO thin film application in Fischer-Tropsch synthesis.

1.9 Research Objectives

Due to many drawbacks encountered in the growth of CZO thin films via numerous

techniques as discussed earlier (Section 1.1), there is a need to use alternative deposition techniques, which should be versatile/flexible, scalable, low cost, and energy-efficient in order to produce high quality CZO thin films in a single step process. For the present research work, CZO thin films deposition has been carried out using PEBA method in order to meet such technological challenges and requirements. The main objectives of this research work are to:

1- Assess the potential of PEBA technique in the deposition of CZO thin films from a synthetic target (Co:ZnO) containing 20 w% Co, on sapphire (0001), Si (100), pyrex and crystal quartz substrates under different process conditions.

2- Investigate the deposition of CZO thin films from single target (Co:ZnO) with different Co loads (5 w%, 10 w% and 20 w%) on sapphire (0001) and Si (100) substrates.

3- Optimize critical process conditions such as deposition temperature, substrate material, accelerating voltage, pulsed repetition rate, target-substrate distance and electron beam tube tip-target distance.

4- Investigate the effects of pre-processing (annealing of substrates) and post-processing (annealing of deposited CZO thin films).

5- Characterize the chemical composition, structure, surface morphology and thickness of the resulting CZO thin film nano-composites by using various experimental techniques such as x-ray photoelectron spectroscopy (XPS), x-ray diffraction (XRD), scanning electron microscopy (SEM), Energy dispersive x-ray spectroscopy (EDX), atomic force microscopy (AFM), and visible reflectance spectroscopy (VRS).

6- Investigate the potential of deposited CZO thin films as a nano structured model catalyst for the synthesis of substituted liquid fuels from syngas via FTS.

Chapter 2: Properties and applications of Co-doped ZnO thin films nanocomposites

2.1 Introduction

Doping of Co into (substitutional and interstitial sites of) zinc oxide structure results in interesting structural, optical, electrical, magnetic and catalytic properties in CZO thin-films, which are described in the section 2.2-6. The applications of CZO thin-films in various fields are given in the section 2.7.

2.2 Structural properties

The structural properties of Co-doped ZnO thin films strongly depend on the growth parameters (Ivill, 2008), film thickness (Benramache et al., 2014) and Co doping concentration (Caglar, 2013). Thermodynamically, the formation of Co_3O_4 and CoO phases are expected at lower deposition temperature but not the Co^o phase as shown in Figure 2.1. Metallic cobalt phase is thermodynamically metastable, but it gains some structural stability from ZnO lattice. X-ray diffraction (XRD) is one of the simple and powerful tools to investigate different structural properties such as strain state, grain size, phase composition, epitaxy, preferred orientation and structural defects (Brabazon and Raffer, 2015; Gürbüz et al., 2015).

The crystalline quality of ZnO film decreases with increasing Co doping due to the degradation of crystallinity. The difference in the ion size between Co^{2+} (0.58 Å) and Zn^{2+} (0.60 Å) results in crystal defects during the occupation of the Zn^{2+} sites in the lattice by Co^{2+} ions. However, the lattice parameters of the films do not change significantly with the increase in Co concentration due to almost identical ionic radii of Co^{2+} and Zn^{2+}. The broadening of the diffraction peaks with increasing Co doping suggests the decrease in the crystallite size. The crystallite size decreases from 47 nm to 32 nm as Co concentration increases from 0 to 5% in

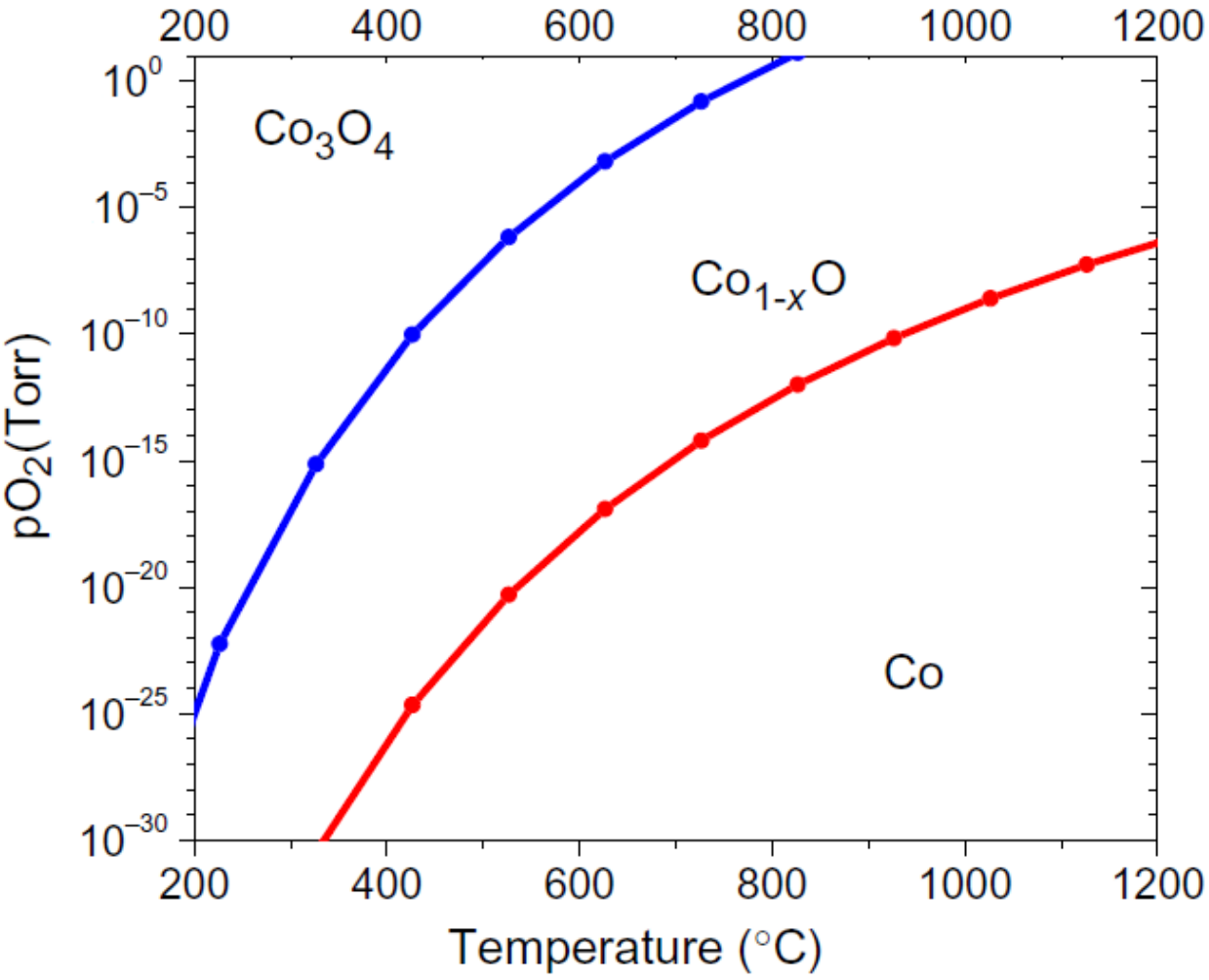

Figure 2.1: Phase diagram for cobalt and cobalt oxides (Reprinted with permission from: Ivill et al., 2008. © IOP Publishing Ltd and Deutsche Physikalische Gesellschaft).

ZnO films (Caglar, 2013). Moreover, crystal lattice distortion is also induced as a result of Co^{2+} incorporation into the ZnO lattice. The degree of crystal lattice distortion of the films increases with increasing Co contents despite of small difference between the ionic radii. There is a solubility limit of Co in the ZnO lattice at the given deposition conditions. A rough estimation indicates that a preferred crystallographic orientation is not observed any more around 20 at. % Co concentration in ZnO (Gürbüz et al., 2015). Moreover, the strain (ε) in the deposited films is the degree of deformation from ideal lattice. The crystal imperfection and distortion induce strain

in the films. The calculated strain values for all the films are negative and very small, which indicate small shrinkage resulting from Co doping for hexagonal crystal lattice. Furthermore, granular size and number of defects in deposited films are increased with higher concentration of Co. The strain (ε) and the crystallite size in CZO thin films also vary with film thickness.

Benramache et al. (2014) have reported that the crystallite size of CZO film increases from 27.34 to 56.42 nm as the film thickness increases from 192 to 569 nm and then decreased from 56.42 to 47.54 nm with increasing film thickness from 569 to 756 nm. The enhancement in the crystalline quality of the films is due to the improvement in crystallinity of the films. Whereas the decrease of the crystallite size after achieving the maximum (569 nm) value is due to the deterioration in the crystallinity of the films. Moreover, the mean strain (ε) decreases from - 0.207 to - 0.431% as the film thickness increases from 192 to 756 nm. This reduction in the mean strain is due to the enhancement of crystallinity or by the decrease of defects in the deposited films (Benramache et al., 2014). Higher Co doping level in ZnO results in an increase in the lattice parameter c, as the Co concentration increases from 0 to 3% the lattice parameter c increases from 5.223 Å to 5.24 Å respectively. This reveals that the unit cell is expanded by the Co^{2+} ions octahedral coordination with an ionic radius between 0.65 Å (low spin) and 0.745 Å (high spin) and, consequently the lattice parameter c is increased. The roughness of the nanostructured Co-doped ZnO also increases with Co concentration and reaches the maximum (2.572 nm) for 3 % cobalt concentration in ZnO: Co nanorods and decreases (2.521 nm) with further increasing of Co concentration, but higher than that of undoped ZnO (1.847 nm) (Salman and Abdullah, 2013).

The growth temperature affects the crystallite size of Co-doped ZnO thin film nano composite. The crystallite size varies with deposition temperature. The maximum crystallite size

(55.46 nm) obtained at 350^{o}C and then decreased to 39.61 nm for the deposition temperature of 400^{o}C (Benramache et al., 2012). Liu et al., (2013) also described that the deposition temperature has a strong effect on surface parameters of the deposited Co-doped ZnO thin film. They demonstrated that the root mean square roughness of CZO films deposited on sapphire increases from 1 nm to 2.2 nm as the temperature increases from 300^{o}C to 400^{o}C, then decreases to 1.7 nm as the temperature increases to 500^{o}C. The optimal CZO thin films possessed a hexagonal wurtzite structure of perfect ZnO crystal. Yang et al., 2013, described that residual film stress in the wurtzite structure of ZnO films included an intrinsic stress from thermal mismatch between film and substrate, and the intrinsic stress from film structure as well. Further, the thermal mismatch and Zn interstitials mainly induce intrinsic stress in the deposited CZO thin film NCs. The residual mean stress measurements provide additional structural information. A negative stress for the deposited films reveals compressive stress in CZO films. The lattice structure, crystalline quality and grain size of the Co-doped ZnO thin films strongly depend on the deposition temperature. The maximum grain size (39 nm) is obtained at a substrate temperature of 500^{o}C (Yang et al., 2013).

2.3 Optical properties

Optical properties mean the response of a material when exposed to electromagnetic radiation, particularly to visible light. Optical analysis of material is a means for investigating defect states, crystalline quality and formation of impurities band due to the incorporation of transition metals into the host materials (Callister, 2007).

Indication of Co substitution in the ZnO lattice can be inferred from the measurements of optical absorption which increases with substituted Co concentration. The increase in absorption band intensities with Co concentration reveals consistent incorporation of Co ions into ZnO

lattice. Further, if there are clear d-d transition lines in the optical transmission spectrum, it confirms Co has replaced Zn to form substitutional dopants (Kim et al., 2004). Ivill et al., 2008, described that the Co^{+2} is largely soluble in the ZnO lattice as ionic radii of Co^{+2} (0.058 nm) and Zn^{+2} (0.06 nm) are very similar. The optical absorption measurements shows three apparent absorption peaks at energies nearly 1.9 eV (651 nm), 2.0 eV (608 nm) and 2.2 eV (564 nm) in $Zn_{1-x}Co_xO$ films. These peaks are the characteristic d-d transition levels which are assigned Co^{+2} occupying tetrahedral lattice positions and confirms that the Co^{+2} is substituting in Zn lattice sites. Moreover, they showed that absorption from the Co^{+2} ions increases as Co concentration increases, which suggests that most of Co is dissolved in the Zn lattice (Ivill et al., (2008).

CZO thin films are transparent but have a slightly blue colour due to Co substitution but as the Co concentration increases, their transparency fades away and the colour becomes dark blue. (Ueda et al., 2001). The absorption bands originating from d-d transitions Co^{+2} of high spin states, are attributed to the charge transfer transitions between donor and acceptor ionization levels located within the band gap of the host ZnO lattice. The absorption band intensities are directly proportional to Co^{+2} ion concentration (Lim et al., 2003).The absorption edges of undoped ZnO and Co-doped ZnO (2 mole %) are 399 and 438 nm, which correspond to the band gap energies of 3.11 eV and 2.83 eV, respectively (Yang and Nie, 2009). This decrease in the band gap energy of Co-doped ZnO samples does not result from the chemical phase change. Instead, it can be attributed to Co related charge transfer transition. Thus, a large red shift of the band gap with increasing Co concentration was observed as shown in the Figure 2.2. On the other hand, few reports have been cited showing blue shifts in the band gap of CZO films. Peng et al., (2005) and Ivill et al., (2008) reported a blue shift of the absorption edges with increasing Co concentration indicating an increase in the band gap of the system. Similarly,

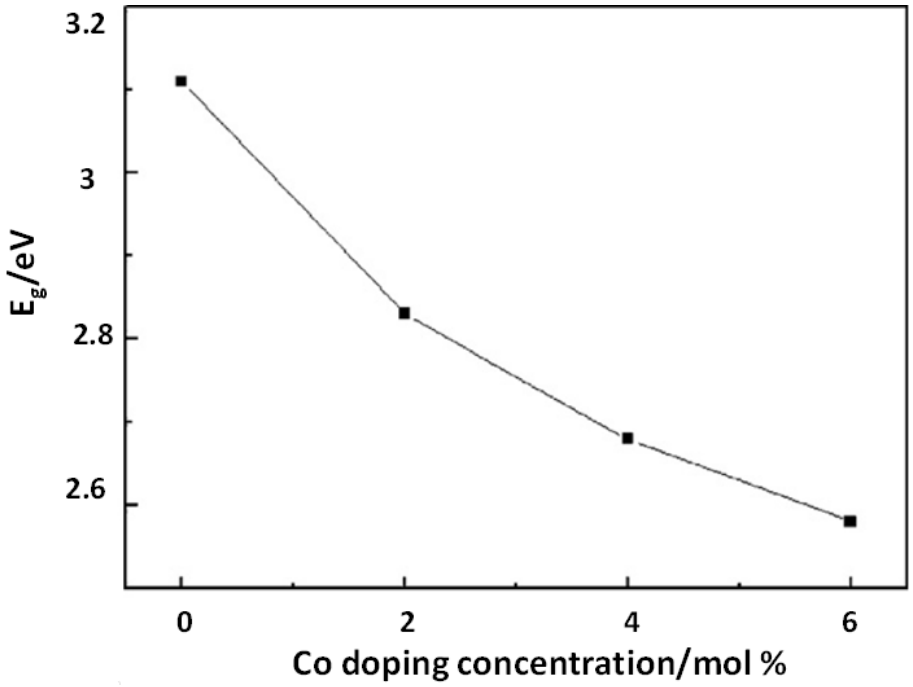

Figure 2.2: Effect of Co doping concentration on the energy band gap of Co-doped ZnO nano Composite. (Reprinted with the permission from: Young and Nie, 2009. © 2008, Elsevier Science).

Yoo et al., (2001) reported blue shifts in Al and Co-co-doped ZnO thin films which were proportional to carrier concentrations. Recently, Gürbüz et al., (2015) also reported blue shifts in CZO films which increase with dopant concentrations. The deposition temperature affects the optical band gap and transparency of the deposited films. The band gap increased from 3.351eV to 3.362 eV in CZO thin films when the film deposition temperature is increased from 300^{o}C to 350^{o}C. The strong transparency region is located between 400-800 nm and all the films have an average optical transparency over 62%–90% in the visible range (Benramache et al., 2012).

The refractive index is reduced in highly disordered films and reaches a minimum value (2.24) at the maximum substrate deposition temperature (400^{o}C), indicating that CZO films exhibits an n-type semiconducting nature (Benramache et al., 2012). The evaluation of refractive

indices of optical materials has a significant importance to design integrated optical devices such as switches, filters and modulators, etc. The average refractive index of undoped ZnO film was found to be 2.20, whereas with Co content it reaches ~2.67 (Caglar, 2013). The change in refractive index with doping also provides a means to modify the refractive index required for use in optical devices accordingly. Moreover, it is reported that the extinction co-efficient also increases slowly with Co contents in ZnO films. Actually, increase of film thickness with increasing Co doping will result in an increase in surface optical scattering and optical loss, which consequently induces the increase of extinction co-efficient (Caglar, 2013).

2.4 Electrical properties

The electrical properties of materials are important in material selection and process system designing. Various thin film based materials have diverse electrical behaviour and different electrical properties which play a crucial role in the efficient functioning of many important devices. For example; connecting wires require high conductivity; low resistivity is required in integrated circuits interconnections; thin film resistors need adequate charge carrier mobility as well as high on-off current ratio and protective coating need to have high insulation. Electrical conductivity measures the ability of the materials to conduct electric current and is the reciprocal of electrical resistivity. Generally, thin films as deposited have higher values of resistivity from their bulk metallic counterpart. More importantly, the excess resistivity in many metallic films is found to be inversely proportional to the grain size and film thickness (Machlin, 2006; Callister, 2007).

Gürbüz and his co-workers investigated the electrical properties of CZO (4.62 to 28.77 at. %.) thin films deposited on fused silica (SiO_2) at 125^{o}C via reactive electron beam deposition. Their measurements show that the electrical conductivity increases with an increase in Co

concentration except for films having higher Co concentrations (23.4 and 28.77 at. %). Both of these films having higher Co concentration but lower conductivity values exhibit a short range polycrystalline nature. Thus, conductivity depends on the Co concentration as well as on the crystalline structure quality of the thin films. The electrical conductivity was determined by taking the reciprocal of the measured resistivity (Gürbüz et al., 2015).

Benramache et al., 2012, showed, see Figure. 2.3, that the maximum conductivity value ($7.547\ \Omega\text{-cm})^{-1}$) is obtained at 350^{o}C, and the resistivity value of the film at this temperature is 0.1325 Ω-cm. The increase in the conductivity of the film can be explained by the displacement of electrons from the Co^{2+} ions into the substitutional sites of Zn^{2+}. The increase in the electrical resistivity of the film with the deposition temperature is due to an increase in potential barriers

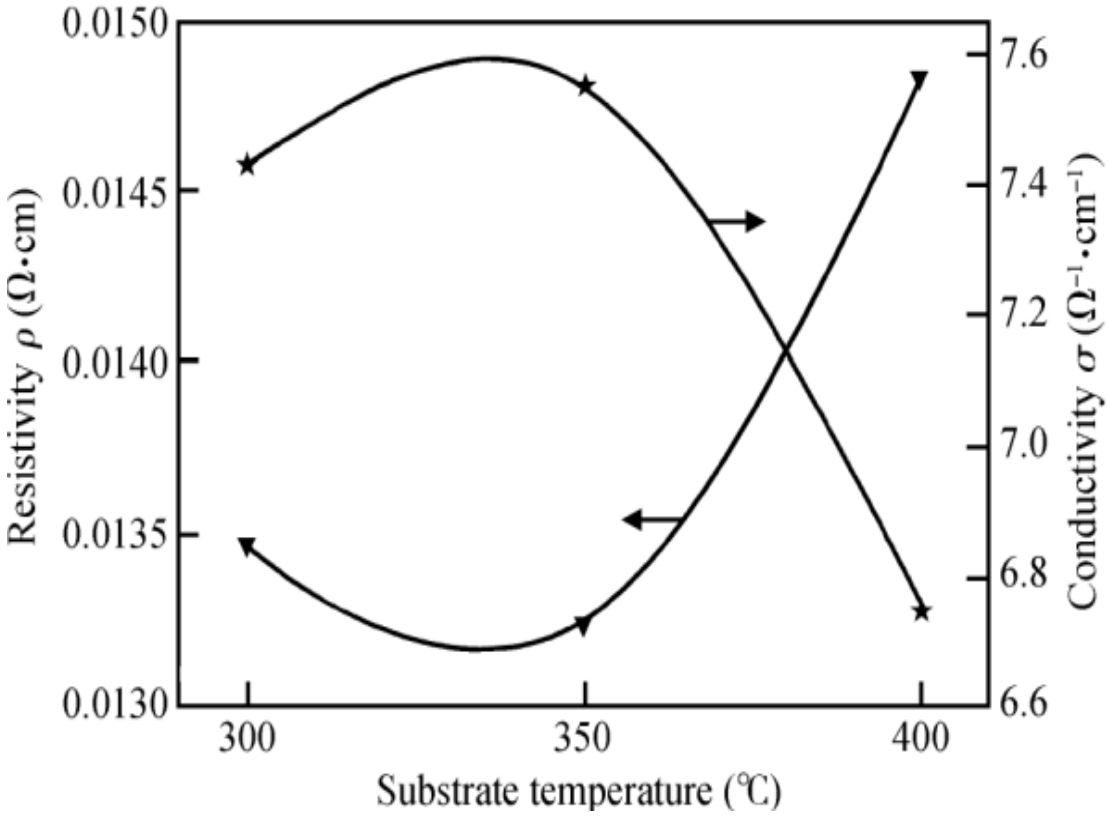

Figure 2.3: Variation of electrical resistivity and conductivity of Co-doped ZnO thin films at different substrate temperatures. (Reprinted with the permission from: Benramache et al., 2012. © 2010, Chinese Institute of Electronics).

barriers because the incorporated atoms of the dopant are segregated into the grain boundaries. After two years, Benramache et al., 2014, described a direct relation between the CZO film thickness and conductivity. Thus, the increase in electrical conductivity with increase in film thickness is due to the increase in carrier concentration in the deposited films.

Schmidt et al., (2007) showed that defects in the CZO thin films have strong effects on the electrical properties. The deep defects in the films depend on Co concentration as investigated by using deep level transient spectroscopy (DLTS). The concentration of deep defects was the largest for the films containing the highest (2 at. %) Co content, where the concentration of free charge carriers was also the largest.

Caglar, (2013), investigated the sheet resistance of CZO thin films with different Co contents using Van der Pauw method. There is a sharp increase in sheet resistance of CZO 1% film. This may be due to severe structural disorder and some scattering centers induced by Co substitution process. A slight decrease in sheet resistance was observed in the films at higher Co concentration which may be an indicator of the increase in the electron concentration with increasing Co content in spite of a significant deterioration in the crystal structure of ZnO films by Co doping.

2.5 Magnetic Properties and origin of ferromagnetism in Co-doped ZnO

Magnetic properties demonstrate the response of the material to the applied magnetic field. There are number of reports in open literature on the magnetic properties of CZO thin films but there is variation in observed ferromagnetism between different groups. The discrepancy in the observed results and their interpretation mainly stems from different film growth techniques, operating conditions and inadequate characterization. Some important properties of CZO and origin of ferromagnetism are presented as follows.

The magnetic properties of CZO thin films depend on the concentration of Co ions and carriers. Thin films with higher carrier concentration showed ferromagnetic characteristics with higher Tc, magnetization and metallic features. Moreover, the ferromagnetic behaviour is observed in CZO thin films which have carrier density as high as $1x10^{20}$ cm^{-3} (Ueda et al., 2001). The main factor responsible for ferromagnetism in CZO nano composite are the carrier induced magnetism, weak ferromagnetism of CoO, and the presence of metallic Co clusters. Hydrogen strongly affects the magnetic properties of Co: ZnO thin films. Hydrogen mediated spin-spin interaction can lead to high temperature ferromagnetism in CZO thin-film NCs. The Co-H-Co complex induces a strong ferromagnetic interaction between Co atoms, resulting in room temperature ferromagnetism in CZO films (Park and Chadi, 2005). On the other hand, Co clusters, which are several tens of nanometers and they occur close to the film surface and substrate-film interface. These ferromagnetic clusters initiate (mainly) ferromagnetism in CZO thin-films and a minor contribution from paramagnetic CZO matrix (Kim et al., 2004). $Zn_{1-x}Co_xO$ (x = 0.003 − 0.07) thin films grown by plasma-assisted MBE exhibit paramagnetic behaviour below the helium temperature and above helium temperature the thin-films become antiferromagnetic in nature (Sati et al.,2007).

Carrier concentration play, a key role in changing the magnetic properties of CZO thin film NCs. The increased concentration of the carrier in CZO film results in high temperature ferromagnetism, which can be realized by doping a small percentage of Al. The co-precipitation of Al with Co-doped ZnO samples show ferromagnetic behaviour even at 360 K (Liu et al., 2006). Similarly, room temperature ferromagnetism in Co and Cu doped ZnO is due to additional carriers resulting from Cu co-doping (Jayakumar et al., 2005).

The magnetic properties of CZO films are also strongly dependent on the growth

conditions and observed defects resulting from higher concentration of Co in the deposited films. Films deposited at 500^{o}C are found to be ferromagnetic whereas film, deposited at 800^{o}C are non-ferromagnetic, whatever the oxygen pressure was maintained during deposition. Similarly, Gacic et al. (2007) also presumed that defects in the base materials induced by Co doping and/or defects at the film substrate interface are responsible for the observed ferromagnetism in CZO thin-films.

On the one hand, it has been reported that films fabricated at 500^{o}C with 5% Co doping exhibits weak ferromagnetic signals (0.1emu/cm^{3}) under a magnetic field of 100 Oe, whereas films deposited with 10% Co doping do not show at all any magnetic signals under the same magnetic field (Fouchet et al., 2006). On the other hand, it has been described that the magnetic properties of CZO also depend on the doping level of Co in the deposited films. Magnetization data taken at 300 K for a series of films grown at 400^{o}C with different Co doping concentrations reveals that the films grown with 2 and 5% cobalt show weak magnetic signals and their hysteresis curves are not well developed, whereas films fabricated with 30 % Co exhibit clear hysteresis curves and show ferromagnetic behaviour up to 300 K. During growth, the pressure also affects the ferromagnetic behaviour of the CZO thin films. Higher pressures lead to a decrease in ferromagnetic signals significantly (Ivill et al., 2008). The film with 30% Co doping prepared under vacuum shows ferromagnetic behaviour, whereas films grown under O_2 pressure of 0.02 mTorr exhibit weak ferromagnetic signals. Cobalt phases in CZO thin films are also crucial in elucidating the magnetic properties of films. Cobalt clusters with a size of ~5 nm can provide room temperature large magnetization along with ferromagnetic behaviour (M = 770 G for a concentration of metallic Co equal to 9%, that is1.75 μ_B/Co atom) (Bardeleben et al. 2008).

Karamat et al.,2010, showed that the ferromagnetic behaviour of CZO films is intrinsic

based on substitution of Co into the ZnO matrix and donor defects, and electrons also play important role in enhancing the ferromagnetic signature. Ferromagnetism significantly depends on the growth pressure of ambient nitrogen. Films fabricated at higher pressure showed increased defects. These defects may be in the form of Zn interstitial and oxygen vacancies, which suppressed the ferromagnetism in CZO films. Karamat et al. (2013) investigated the magnetic properties of bulk as well as thin film of CZO samples, and revealed similar results whereby the presence of cobalt with Co^{2+} valence states in wurtzite ZnO matrix is responsible for the ferromagnetic nature of CZO films. Wei et al. (2009) described that the substitution of Co atoms and local structural distortion are interpreted as the origin of intrinsic weak room temperature ferromagnetism in the prepared thin films. Moreover, oxygen vacancies around Co atoms also play a key role in room temperature ferromagnetism in CZO thin films.

The magnetic properties of CoO mainly rely on intricate combination of metal dopants and material defects such as oxygen vacancies. Higher Co doping leads to the formation of secondary phases or metallic Co clusters in the resulting films. Thus, the magnetic properties strongly depend on film growth parameters and Co doping concentrations (Aravind et al., 2014).

2.6 Catalytic Properties

Metallic nanoparticles have attracted much attention due to their optical, magnetic, electrical and catalytic properties, as well as their application in catalysis and many other chemical processes. In general, the properties of metallic nanoparticles are size dependent, so it is vital to control their size in order to achieve monolayer assembly of the particles which exhibit the desired features. In addition, it is also essential to control their structure and organization during the growth process. Since, a large portion of atoms in nano particles are exposed to the surface, their physico-chemical properties are strongly influenced by the nature of surface

species (Gual et al., 2012). As nanocatalysts, metallic nanoparticles show a great potential because of their extremely small size (typically 10-80 nm) yielding a high surface to volume ratio and their unique properties, which are not found in their macroscopic counterparts (Chaturvedi et al. 2012). Cobalt is a well-established catalysts for FTS, and ZnO has been used as a support for Co based FT-catalysts in numerous previous investigations (Wang et al., 2012, Pan and Bukur, 2011; Adesina et al., 1996). Thus, the properties of Co, which are more critical for FT process, are briefly summarized as follows.

Oxides-supported cobalt (Co^{o}) nanocomposites are significantly important materials with excellent catalytic properties in FTS or hydrogenation of unsaturated organic feed stocks (Liu et al., 2015). In FT reaction, the activities of Co and Fe based FT-catalysts are comparable and they display similar chain growth capabilities at relatively low temperature (ca. 473-523 K), however, the productivity at higher conversion is superior using Co based nanocatalysts (Gual et al., 2012). Generally, a catalyst is subjected to a pre-treatment before the reaction in order to bring the catalyst into an active form for the reaction. The cobalt based-FT catalyst is almost always reduced with hydrogen or carbon monoxide at a temperature of 673-823 K to the zero-valent metallic state (Pan and Bukur et al., 2011). Depending on the activation temperature and the composition of reducing atmosphere, different cobalt phases can be formed, which eventually affect the catalytic properties of the catalyst.

The catalyst containing the hexagonal close packed (hcp) metallic phase has higher cobalt dispersion compared to face centered cubic (fcc) cobalt phase. During FT reaction, the catalyst containing cobalt hcp metallic phase exhibits higher syngas conversion into liquid fuels on a catalyst weight basis as well as shows less methane selectivity compared to the fcc phase-containing catalysts under similar reaction conditions (Gnanamani et al., 2013). A comparison of

the activity of hcp and fcc cobalt phases is summarized in Table 2.1. The structural changes in the catalyst significantly affects the performance in FT reaction. Depending on the operating conditions, the metallic nanoparticles can undergo sintering, carbidization, and fcc-hcp phase transformations. The hydrocarbon selectivity is almost similar with Co-based FT catalysts containing fcc and hcp cobalt phases. However, hcp phase exhibits higher cobalt sites yield in FT reaction, so catalytic-cobalt hcp phase seems to be more active than cobalt fcc phase. The higher turnover frequency of cobalt hcp phase is based on the spherical morphology, and the porous structure of cobalt hcp nano particles may be the possible reasons for higher activity of catalysts containing hcp cobalt phase. Under the reaction conditions hcp phase is stable and no transformation of cobalt hcp into cobalt fcc phase was observed. Furthermore, the cobalt hcp phase can be generated in the Co-based FT catalysts by consecutive CO and H_2 treatments (Sadeqzadeh et al., 2011).

Table 2.1: Comparison of the activity of cobalt hcp and fcc phases at similar operating conditions (T = 493 K, P = 1.99 MPa, H_2/CO = 2/1, syngas flow rate: 3.0 sl/h/g cat.) (Gnanamani et al., 2013).

Catalysts	Time on stream (TOS) (h)	CO conversion (%)	Selectivity of CH_4 (%)	Selectivity of C_{5+} (%)	Turn over frequency (TOF) (s^{-1})
Co-hcp	16	63.1	3.5	88.2	0.095
	450	55.5	4.2	90.2	0.068
Co-fcc	13	45.1	6.4	86.1	0.092
	492	32.1	7.2	82.9	0.049

Decreasing particle size to nanometric scale results in tremendous increase in the surface area on which reaction takes place. The metallic nanoparticles have abundant defect sites, which provide higher activities due to lower activation barrier for the reactant molecules (Gual et al., 2012). Cobalt metal is quite expensive and with low abundance, which calls for the use of Co more effectively on the nano scale. However, for too small particle size a drop in activity was observed by Breejen et al., 2010. Their investigations reveal that the optimum Co particle size to carry FT reaction is 4.7 ±0.2 nm; below this particle size TOF decreases very sharply as presented in Figure. 2.4. The turn over frequency (TOF) for CO hydrogenation is independent of Co particle size for catalysts with size larger than 6 nm. But both the activity and selectivity are affected for Co particle size smaller than 6 nm. When the particle size decreases from 16 to 2.6 nm, at a pressure of 35 bar TOF decreases from 23 x 10^{-3} to 1.4 x 10^{-3} s^{-1} and C^{+5} hydrocarbon selectivity decreases from 85 to 51 wt. % (Bezemer et al., 2006). Therefore, it is

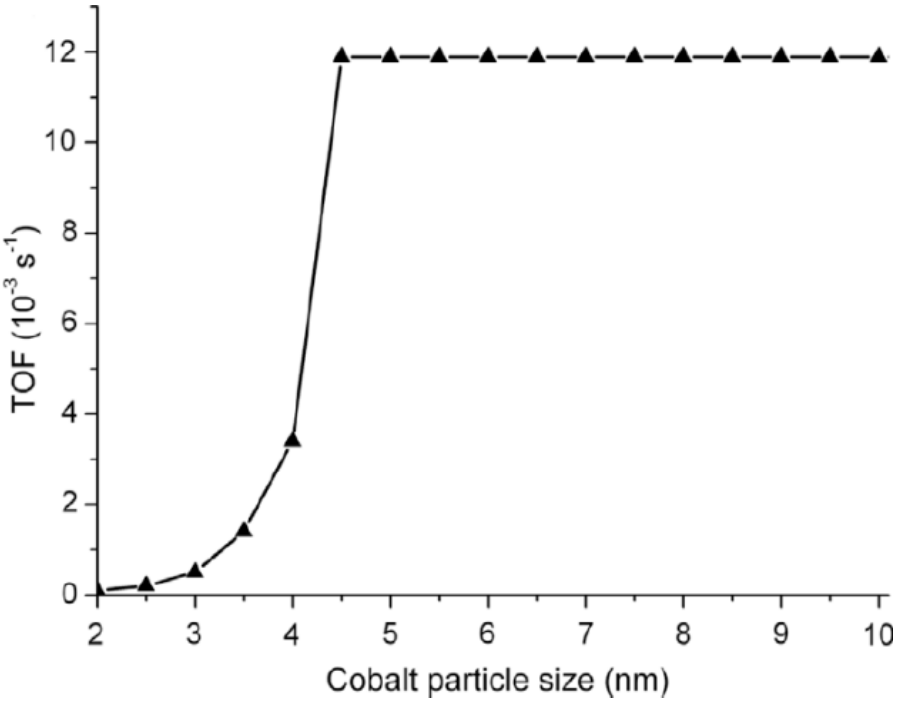

Figure 2.4: Estimated intrinsic TOF as function of Co particle. (Reprinted with the permission from: Breejen et al., 2010. © 2010, Elsevier Science).

argued that one should aim for Co-based FT catalyst with average particle size close to the optimum values of 6-8 nm. Similar observations have been reported by Barbier et al., (2001). According to them, TOF in FTS increases with increasing Co particle size, first very sharply in the particle size range of 4-6 nm and then more slowly from 6 to 9 nm. Further, Karaca et al., (2011), described that normally FT reaction takes place on cobalt sites located on the surface of cobalt metallic nanoparticles in the range of 6-30 nm. The catalyst containing metallic cobalt particles smaller than 4-5 nm are expected to re-oxidize to CoO during realistic FT reaction conditions and results in the deactivation of the catalyst. These observations reveal that the particle size of cobalt based FT-catalyst is very critical in order to attain high selectivity and activity in FTS.

Metal dispersion (percent exposed) is also an important property of the catalysts. FT cobalt based carbon supported catalyst produces large amount of lighter hydrocarbons, whereas moderately dispersed 10-15% Co/Al_2O_3 produces heavier hydrocarbons. But if 10% Co/Al_2O_3 is reduced at elevated temperature, then higher hydrocarbons are produced (Reuel and Bartholomew 1984). These investigations reveal that reduction property of Co based FT-catalyst is also important to achieve desired FT-product range of hydrocarbons. Gnanamani et al., 2013, reported higher dispersion (5.06 %) for Co (hcp) phase than that of Co (fcc) phase (3.8%) and found that the TOF is about the same for both phases during the initial period of FTS, however, after aging Co (hcp) may show a slightly higher TOFs relative to Co (fcc). In this case, higher activity of Co (hcp) is due to higher dispersion of Co metallic particles. The dispersion (D) percent can be calculated as follows (Pan and Bukur, 2011).

$$Dispersion\ (\%) = [\frac{Number\ of\ Co_0\ atoms\ on\ the\ surface}{Total\ number\ of\ Co_0\ atoms}]x100 \qquad (2.1)$$

The oxidation of metallic Co results in the deactivation of the catalyst and lead to reduce the reaction rates of FTS. During FT reaction, water is produced as a by-product which oxidizes the metallic Co. The nano-sized material is less resistant to oxidation than that of bulk crystalline materials but in recent years, research indicated that the oxidation of bulk or surface metallic Co is not a significant deactivation mechanism for Co-based FT catalysts with an average particle size of ≥2 nm (Jahangiri et al., 2014).

2.7 Applications of Co-doped ZnO

Dilute magnetic semiconductors (DMSs) are attracting much interest for their potentials in spintronics (spin based information processing technologies). Ferromagnetic DMSs with high Curie temperature (T_c) well above room temperature are required for spintronics applications (Kittilstved et al., 2006). CZO is a perfect candidate to produce suitable nano composites for numerous such applications as illustrated in the review of literature. CZO thin-films have low resistivity and good optical band gap energy at low temperature and are transparent in the visible regions. Therefore, CZO thin-film NCs have wide spread applications in the field of transparent conductors, semiconductors, ferromagnetism, solar cells and piezoelectronics. Cobalt doped ZnO is considered as an important material due to its high conductivity, high optical transparency as well as lower material cost (Benramache et al., 2012). These reasons have led to increasing interest to develop high quality CZO thin-film nano composites.

Other highly active research fields where Co-doped ZnO has gained intense interest are dye-sensitized solar cells (Hirano and Kozuka, 2003), Hydrogen (H_2) production (Jaramillo et al., 2005), steam reforming (Llorca et al., 2004) and Fischer Tropsch synthesis (FTS) (Wang et al., 2012, Pan and Bukur, 2011; Adesina et al., 1996) as well as photocatalysis (Yang and Nie, 2009; Poongodi et al., 2015).

Chapter 3: Experimental methods

3.1 Introduction

In this chapter, a description of the experimental methods used in the present work is given. First, a detailed account of the deposition method is given followed by brief description of the complementary analytical techniques used for the characterization and testing of the deposited films.

3.2 PEBA experimental set up

Channel-spark PEBA system, equipped with a pulsed electron beam source (PEBS-20, Neocera Inc., USA), has been used for the deposition of Co:ZnO thin films. A simplified schematic diagram of PEBA system is presented in Figure 3.1. A snapshot of the turnkey system

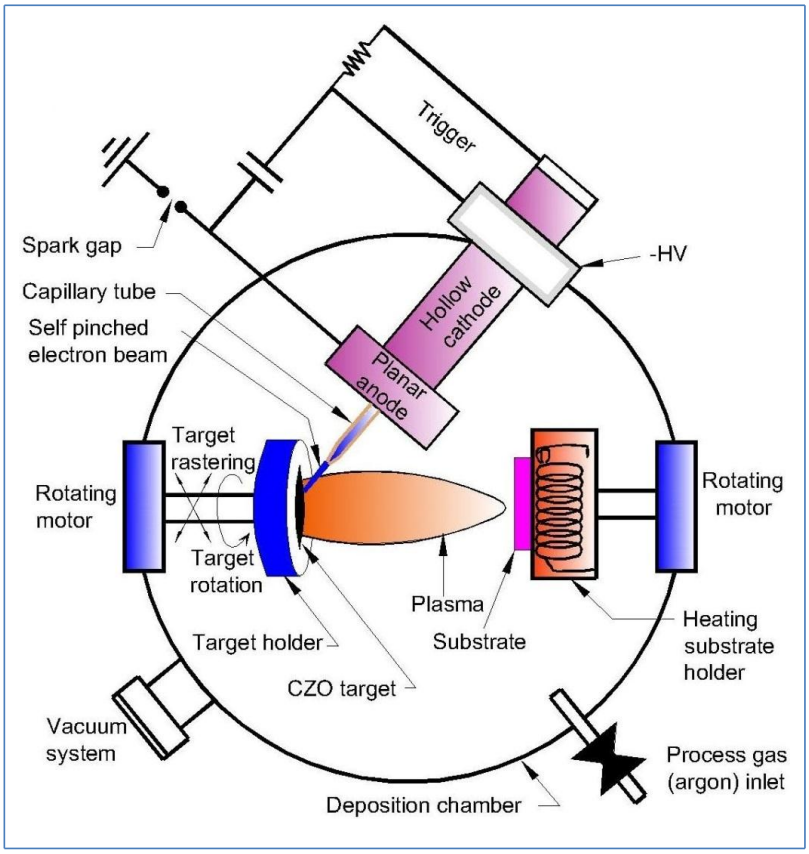

Figure 3.1: A simplified schematic diagram of PEBA system (Ali et al., 2017).

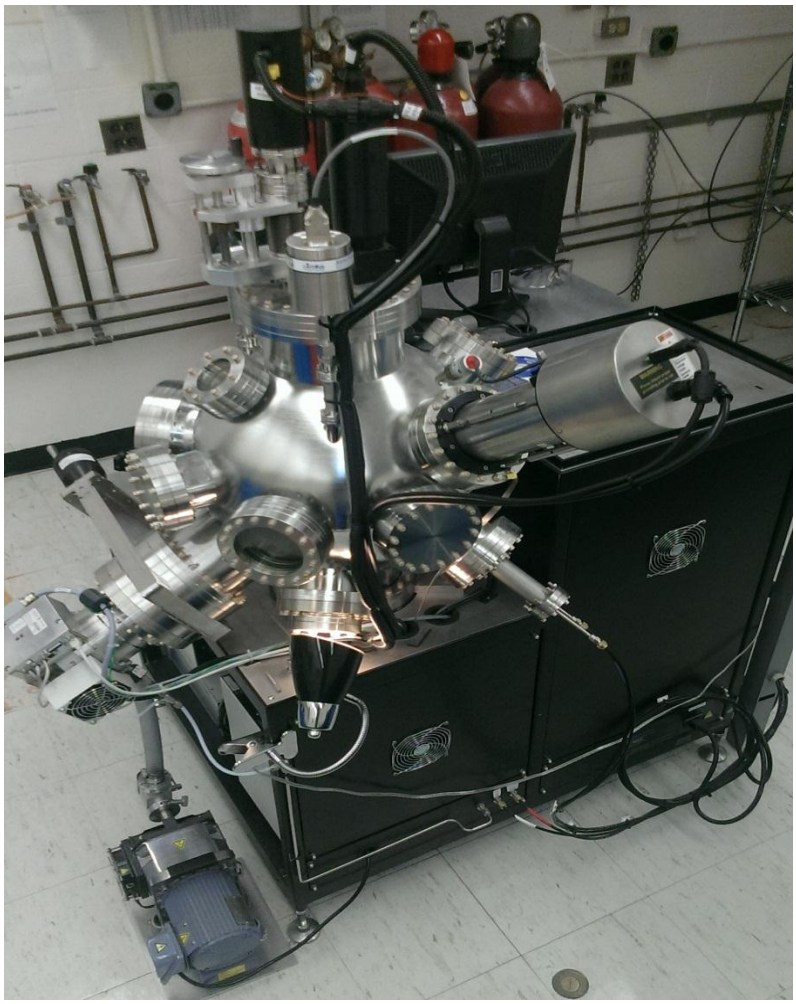

Figure 3.2: A snapshot of Neocera PEBA system used in this work.

used to carry out deposition of CZO thin films is shown in the Figure 3.2. The electron beam source is characterized by a short pulse (~100 ns), high fluence (max. ~10 J/cm^2), high beam current (~1 kA), and low energy electrons (10–20 KeV).

PEBA system is composed of a stainless steel chamber, which is pumped by a combination of rotary and turbo molecular pumps to achieve a pre-deposition pressure in the order of 10^{-6} Torr. The major components of the system are pulsed electron beam generator comprising of a hollow cathode, a trigger and a capillary tube. The tube is positioned at an angle of 45^{o} relative to the target mounted on a target holder. The target is rotated around its centre

axis during ablation. The target rotation helps to keep uniform and smooth ablation and as well as improve the film thickness homogeneity. Similarly, the substrates are mounted onto a stainless steel block (substrate holder) which is fixed on a rotating disk. The substrate holder can be removed from the rotating disk to mount the samples. The stainless steel block is large enough and a total of four different substrates, with lateral dimensions of 10 mm x 10 mm, can be easily mounted onto it to provide access to the growth of thin film.

3.3 Growth procedure

A typical growth procedure consists of two steps, cleaning and preparation of substrates and target, and film deposition.

3.3.1 Substrate cleaning and preparation

The substrate viz., c-sapphire, Si (100), pyrex or crystal quartz, used for the growth of CZO thin-film nano-composites were sonically successively cleaned using an ultrasonic cleaner (Cole-Parmer 8890, USA), as presented in Figure 3.3, in acetone and methanol at 50^{o}C for 30 minutes followed by rinsing in deionized water. Once the substrate degreasing process is finished, they were immediately placed into an air tight wafer carrier tray in order to reduce any surface contamination. The stainless steel block (substrate holder) was also cleaned before mounting the substrates onto it. The block was polished to clean the surface using a hand grinder as presented in the Figure 3.4. The substrate holder was rinsed in acetone and methanol followed by rinsing in deionized water. Once the cleaning procedure of substrate holder is finished, the substrates were attached to the block using a special glue (Leitsilber 200 silver paint, Ted Pella Inc.) and allowed to dry on hot plate at a temperature of 50^{o} C for 30 min.

3.3.2 Thin film deposition

After cleaning, the substrates are attached to the substrate holder and mounted inside the

Figure 3.3: A snapshot of ultra-sonic bath used for degreasing the substrates.

Figure 3.4: Experimental setup for hand grinder used to clean substrate holder and target.

deposition chamber. The deposition chamber is closed and pumped down to achieve a low pressure of ~10^{-6} Torr and a deposition temperature of interest. Before initiating deposition the target was pre-ablated for at least 3000 pulses at 2 Hz, 12 kV in order to remove oxides and other impurities from the target surface. Thin film deposition was carried out at pre-determined deposition temperature, background gas (Ar) pressure, electron beam frequency and accelerating voltage. A plasma plume, which is a mixture of atoms, ions and nuturals, is generated as a result of electron bombardment of the target. The ionized plasma hits the substrate surface, as schematically shown in Figure 3.5-a, leading to the formation of congruent CZO thin-films under judiciously selected process conditions. A snapshot of a typical run is schematically shown in Figure 3.5-b.When the deposition process was completed then the samples were removed from the system and stored in an air tight wafer carrier tray until needed for characterization.

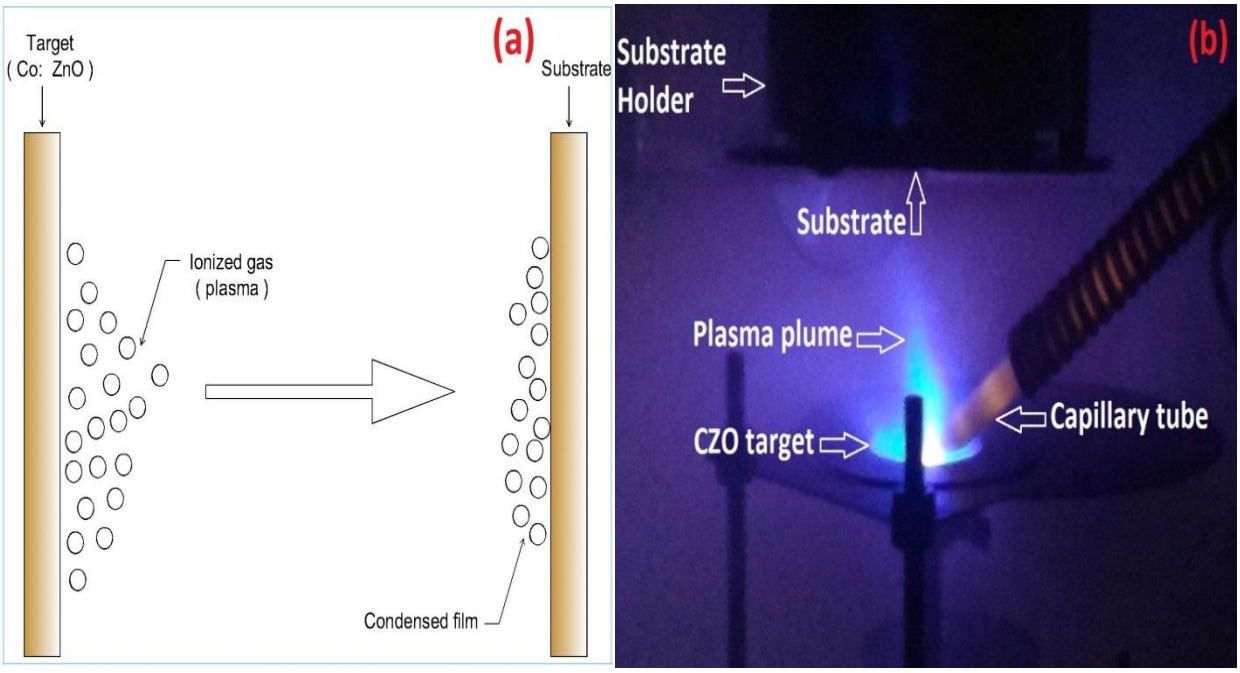

Figure 3.5: (a) Schematics of transfer of atoms from target to substrate (Plume propagation), (b) Snapshotof real plasma plume expansion during a typical deposition run.

All the deposited CZO thin films are transparent with a slight cobalt blue colour as shown in the Figure 3.6. It is not easy to have an appreciation of film color on silicon substrate (see Figure 3.6-c)s as the substrate has a dark grey color and is not transparent in the visible-wavelength range but on pyrex, c-sapphire and crystal quartz the bluish green color can be clearly appreciated, as shown in the Figures 4.30(a), 4.30(b) and 4.30(d) respectively. Further,

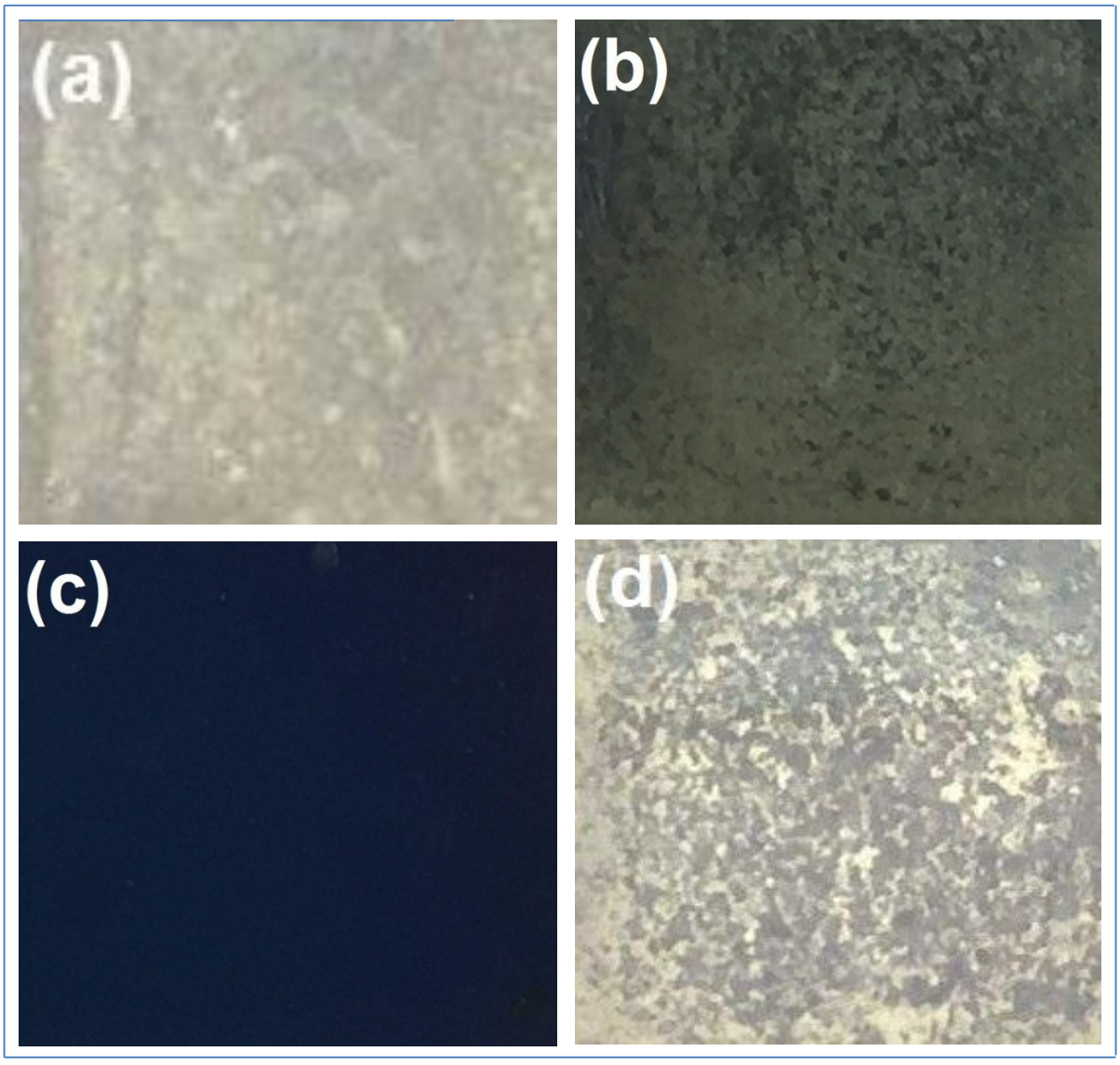

Figure 3.6: Snapshots of CZO thin film NCs deposited on (a) pyrex, (b) c-sapphire, (c) Si (100), and (d) crystal quartz.

it has been found that Co concentration increases in the films the bluish green colour becomes darker. These observations are coherent with Ueda et al., 2001.The specification of the substrates used in this study has been presented in the Table 3.1, whereas all the process conditions used for CZO thin-film deposition have been summarized in Table 3.2.

Table 3.1: Specifications of the substrates used in all experiments.

Substrate	Specification	Source
c-sapphire	Sapphire (Al_2O_3) substrate <0001>, one side polished, Dimensions: 10 mm x 10 mm x 0.5 mm.	University wafer, USA
Si(100)	Silicon substrate <100>, one side polished, Dimensions: 10 mm x 10 mm x 0.5 mm.	University wafer, USA
Pyrex	Pyrex substrate, one side polished, Dimensions: 10 mm x 10 mm x 0.5 mm.	University wafer, USA
Crystal quartz	Crystal quartz substrate, one side polished, Dimensions: 10 mm x 10 mm x 0.5 mm.	University wafer, USA

3.4 Heat treatment of substrate and films (Pre- and post-processing)

The term annealing denotes heat treatment process which consists of three steps viz., heating a material to a specified temperature, Dwelling at that temperature for certain time, and finally cooling down to initial conditions. The aim of pre-processing (annealing of substrate) and post-processing (annealing of thin-films) is to achieve desired morphological and microstructural properties in the materials.

Annealing process is usually divided into three distinct stages namely recovery, recrystallization, and grain growth. Recovery is usually defined as the restoration of physical

Table 3.2: Process parameters of all series.

Pulse repetition rate (Hz)	Number of pulses	Deposition temperature (^{o}C)	Background argon (Ar) pressure (mTorr)	Accelerating voltage (kV)	Substrate
First Series [(As-grown; $Zn_{1-x}Co_xO$ (x = 0.2)]					
2	3000	350^{o}C-450^{o}C	3	14	Si(100)
Second Series [(As-grown; $Zn_{1-x}Co_xO$ (x = 0.2)]					
2	3000	350^{o}C-800^{o}C	3	15, 16	Si(100)
Third Series [(As-grown; $Zn_{1-x}Co_xO$ (x = 0.2)]					
1, 2, 4, 8	3000	450^{o}C	3	16	Si(100), c-sapphire
Fourth Series [(As-grown; $Zn_{1-x}Co_xO$ (x = 0.2)]					
2	3000	450^{o}C	3	16	Si(100), c-sapphire, Quartz, Pyrex
Fifth series [(Post-heat treatment; $Zn_{1-x}Co_xO$ (x=0.2)]					
4	3000	350^{o}C-450^{o}C	3	15, 16	Si(100)
Sixth Series [(Pre-heat treatment; $Zn_{1-x}Co_xO$ (x = 0.05, 0.1, 0.2)]					
1	3000	350^{o}C-450^{o}C	3	16	Si(100), c-sapphire

properties, and is characterized with removal of internal stresses and crystal defects. Recrystallization is the stage in which strain free grains nucleate and grow to replace those deformed by internal stresses. Recrystallization is evident by a decrease in the hardness and increase in the ductility of the material. Grain growth stage is characterized with progressive growth and coarsening of grains. Annealing under high temperature in the presence of oxygen oxidizes the substrates surface and leads to smoothing out of the surface defects [Adegbuyi, 2009; Wadhwa and Dhaliwal, 2008]

Materials may be pre-annealed to eliminate the impurities or to increase the energy on the substrate surface. The latter case is driven by stimulating the molecules on the substrate surface. Higher surface energy may result in improved nucleation and consequently better growth of the films [Davis, 1992]. Further, it has been reported that pre-annealing of the substrate results in terrace and step morphology, which may be the origin of nucleation sites for film growth [Ribic and Bratina, 2017]. Thermal treatment of substrates at high temperature potentially removes the intrinsic stresses and the processes of softening, recrystallization and grain growth [Ohring, 2002]. Similarly, post-annealing is considered an effective approach to achieve desired properties in as-grown film. The effects of pre (post) thermal treatment of substrate (film) on structural and morphological properties of CZO films NCs will be discussed in chapters 5 and 6, respectively.

Thermal treatment was performed in a Horizontal Split Tube (HST) furnace (Carbolite, USA) equipped with a vacuum system. Figure 3.7 shows a simplified diagram of the heat treatment system used in this work. Prior to pre-annealing, the substrates were subjected to cleaning in ultra-sonic bath in acetone and methanol at 50^{o}C for 30 minutes followed by rinsing in deionized water. The substrates (4 maximum) were put in a quartz boat (MTI Corporation,

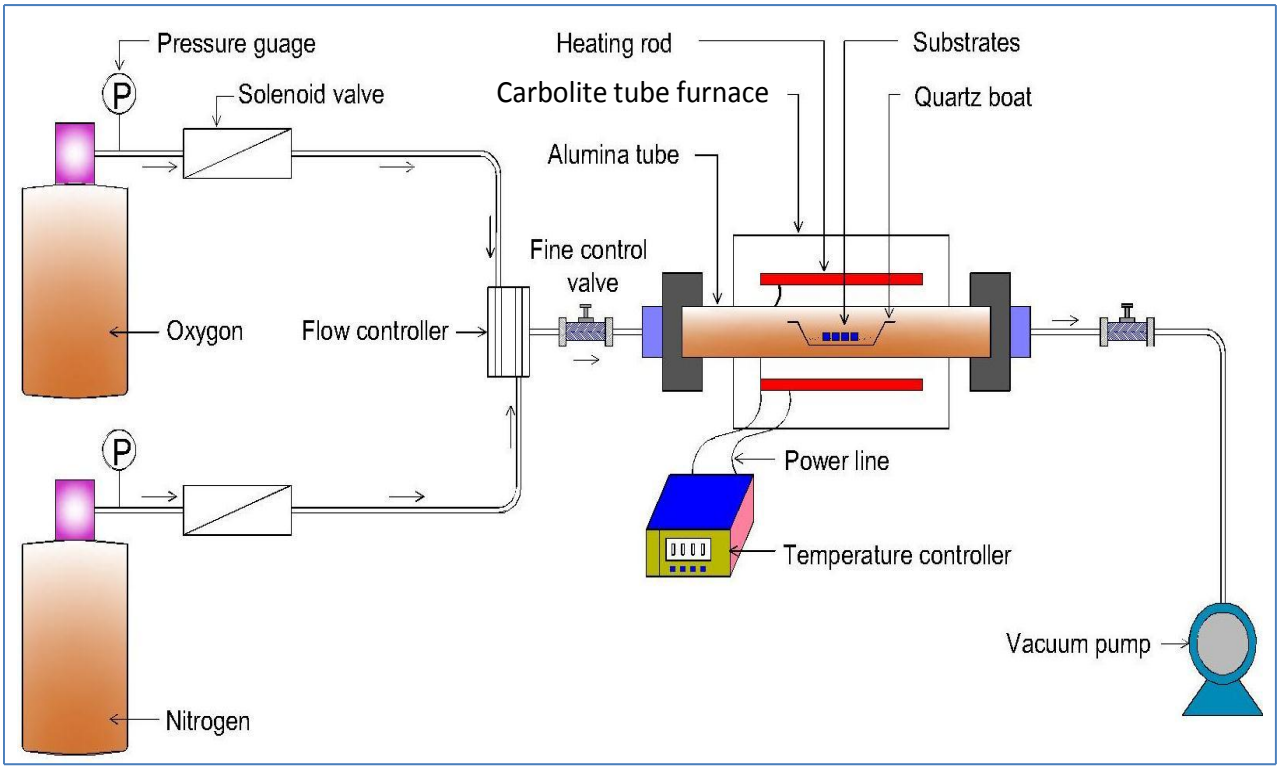

Figure 3.7: Schematic diagram of heat treatment system.

USA), having dimension of 100 mm L x 17 mm W x 10 mm H, and laid horizontally carefully in the center of ~100 mm diameter alumina tube of the furnace. The pre-annealing temperature was set to either 400^{o}C or 600^{o}C with a ramping up/down rate of 4^{o}C/minute. The substrates were annealed under reduced oxygen (99.999%, Praxair) pressure for one hour. The annealing process mainly consists of three steps. The first step is ramping up from room temperature until the set point temperature (400^{o}C, 600^{o}C or 1100^{o}C) is achieved. The second step is dwelling for one hour at the set point (SP) temperature followed by ramping down back to room temperature. However, for post annealing at 1100^{o}C, an intermediate dwelling step at a temperature of 600^{o}C for one hour was introduced as shown in Figure 3.8. When room temperature was reached, nitrogen gas was used for purging in order to bring the system back to ambient pressure.

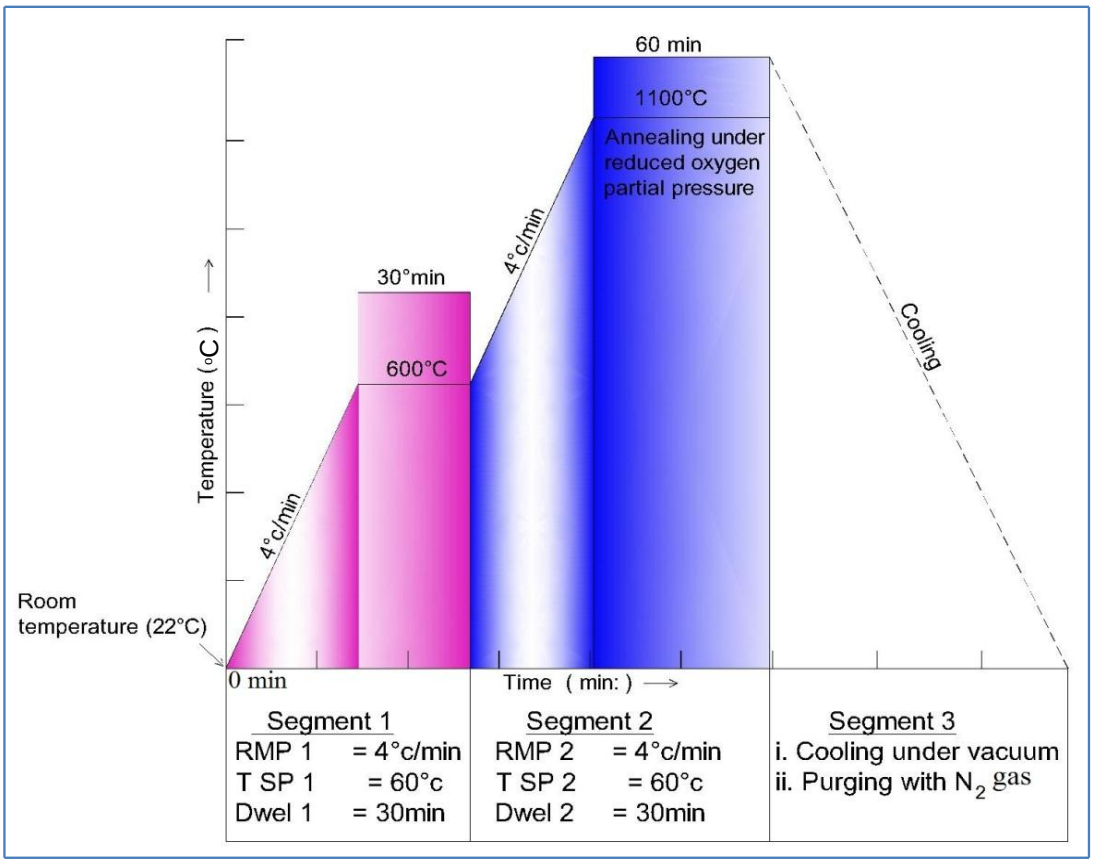

Figure 3.8: Schematics of the Segments/steps involved during heat treatment.

3.5 Fischer Tropsch synthesis

Under catalyst testing, the deposited thin-films have been evaluated for their FTS activity and selectivity in a 3-phase continuously-stirred tank slurry reactor (3-φ-CSTSR) using the Robinson-Mahoney stationary basket (RMSB) reactor configuration. The schematic of the experimental setup is shown in Figure 3.9. Typically, about 10 g of the supported Co-ZnO material containing 20 w% Co was loaded into RMSB reactor and reduced in situ in high purity hydrogen (N4.5) flowing at a rate of 160 $cm^3.min^{-1}$ with the temperature set at 673 K (400^oC) for 3 h. Subsequently, the reactor was cooled to ambient temperature under the flow of H_2 after which, a solvent, i.e., 150 cm^3 of squalane ($C_{30}H_{62}$) was introduced in the reactor. The pre-treated catalyst was then tested at a pressure of 2 MPa using synthesis gas composed of 60% H_2

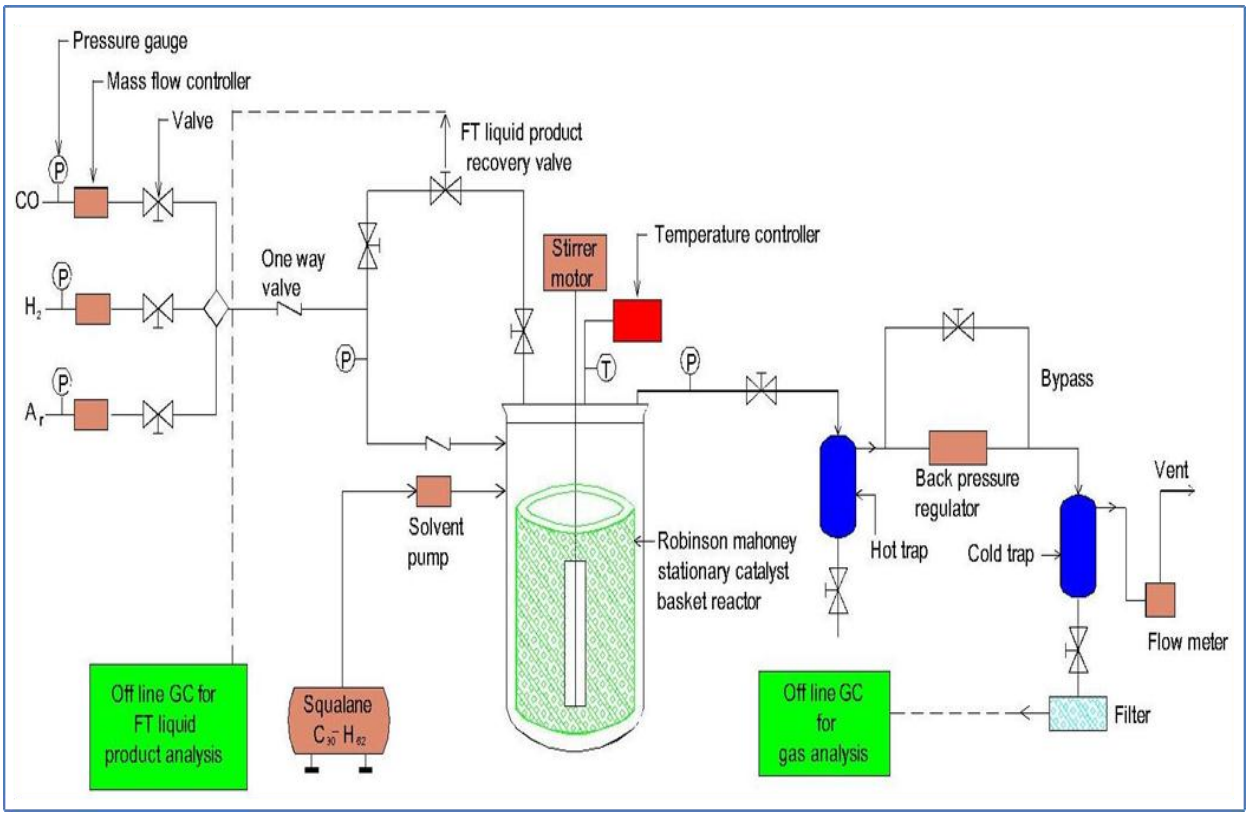

Figure 3.9: Schematic diagram of the experimental setup used for Fischer Tropsch synthesis tests.

and 30% CO, and balanced in Ar (H_2:CO volume ratio = 2) flowing at a rate of 280 $cm^3.min^{-1}$. A constant stirring speed of 2000 rpm was kept throughout the reaction. After certain time intervals of about 1 h, 6 h or 24 h of continuous flow, both inlet and outlet valves of the reactor were closed to convert the system into batch mode and the pressure is registered for about 3 h, after which, the reaction was returned into the continuous flow mode for 120 h.

Two offline Varian CP-3800 gas chromatographs (GCs) were used to analyzed the FT gas phase and liquid phase products. The GC for gas phase analysis was equipped with two thermal conductivity detectors (TCDs) and one flame-ionization detector (FID). One of the TCDs was dedicated to analyzing H_2 only, while the second one was used for analyzing the other gases. The Helium (He) gas was employed as the carrier gas for the general TCD in which the

column sequence consists of Hayesep T (CP81072), followed by Hayesep Q (CP81073), and then Molsieve 13X (CP81071), whereas the setup for the H_2 TCD consists of Hayesep Q (CP81069) with a Molsieve 5A (CP81025), and N_2 was used as the carrier gas. The FID was in series with the general TCD. He was used as the carrier gas in the liquid phase GC which was equipped with FID fitted with a low-polarity GC column 100–2000 DB-1HT (Agilent Technologies Inc.), of dimensions 30 (L) 0.32 cm (I.D.), and 0.1 cm (DF) and suited for working in the temperature range of 213–673 K.

3.6 Complementary characterization techniques and related physics

3.6.1 X-ray diffraction

X-ray diffraction (XRD) is a powerful technique to study the crystalline nature of materials. This technique has the ability to identify and quantify the different phases present in thin films **(**Ingham, 2014**)**. Identification of different structural properties such as strain state, grain size, phase composition, epitaxy, preferred orientation and defect structure are quite possible through the use of this versatile technique (Brabazon and Raffer, 2015). Moreover, changes in crystalline structure caused by external influences such as incorporation of impurities and heat treatment can be monitored. This technique has remarkable features such as the non-destructive in character and simple sample preparation. (Ohring, 2002).

X-rays are a form of electromagnetic radiation which are highly energetic and have short wavelengths on the order of the atomic spacing for solids. When a beam of x-rays hits the solid surface, a portion of the beam will be scattered by the electrons of atom or ion located in the beam's path. Diffraction through constructive interference occurs when the path difference between the reflected beams is equal to the whole number (n) multiple of the wave length. This X-ray diffraction condition is described by Bragg's law as follows (Callister, 2007).

$$n\lambda = d_{hkl}Sin\Theta + d_{hkl}Sin\Theta \quad (3.1)$$

$$n\lambda = 2\, d_{hkl}Sin\Theta \quad (3.2)$$

Where n is the order of reflection (an integer), λ is the wave length of X-rays, Θ indicates the X-ray scattering angle and, d_{hkl} is the inter-planar spacing. For constructive interference Bragg's law must be satisfied, otherwise interference will be non-constructive in nature which results in a very low intensity of diffracted beam (Callister, 2007). A typical diffractometer consists of X-ray tube (source of radiation), a monochromator to select the wave length, slits to adjust the beam shape, sample and detector. A diffractometer is an apparatus used to determine the angle of diffraction (Saravanan and Rani, 2012 ; Callister, 2007).

3.6.2 XRD measurements of thin films

The extension of XRD to thin films has not been used use vigorously due to two reasons: First, with typical incident angle, the path length of X-rays through the film is too short to produce diffracted patterns of sufficient intensity and, second, transmission electron microscopy (TEM) has the ability to provide similar diffraction information (Ohring, 2002). X-ray scattering from thin film can be weak if the film structure is disordered (Mannsfeld et al., 2009). However, now a days highly intense X-rays are produced routinely from sources such as rotating anode and powerful conventional tube. When these x-rays sources are coupled with powerful detection schemes, they make it possible to measure even submonolayer thick films.

For current work, the crystalline structure and phase formation of CZO films have been determined using a bench top x-ray diffractometer (Rigaku MiniFlex 300/600, USA) equipped with SC-70 detector. The system has been operated using a step width (size) of $2\Theta = 0.02^{o}$ and scan speed of 1^{o}/min at 40 kV and 15 mA. The diffraction patterns have been collected over the 2Θ range of 30^{o}-85^{o} using theta/2-theta Bragg-Brentano configuration.

3.6.3 Scanning Electron Microscopy

Scanning electron microscopy (SEM) is used to examine and record the surface topography of the films. The instrument is versatile and can provide useful structural information about the surfaces of the sample (Ohring, 2002). The signals resulting from electron beam-specimen interaction provide information about external texture, chemical composition, crystalline structure and orientation of the sample materials. The conventional SEM techniques can image an area approximately 1 cm to 5 μm of the sample surface having a magnification range of 20X to approximately 30,000X, and a spatial resolution of 50–100 nm (Saravanan and Rani, 2012). Moreover, point analysis on the sample is particularly useful in quantitative or semi-quantitative determination of chemical composition, crystal orientation and crystal structure as well. The sample must be conductive or coated with a conductive medium. Non-conducting samples appear bright as the rastering electron beam build up the charge on the sample surface (Collins, 2012). A typical SEM electron beam is produced by an electron gun located at the top of the microscope. The resulting electron beam is focussed through a series of electron magnetic lenses and scanning coils before it impinges on the sample surface placed in a high vacuum chamber.

Commonly, two types of detectors are employed in SEM to scan the sample surface, namely, the secondary electron (SE) detector and backscatter electron (BSE) detectors. The SE detector is the primary detector present in all SEMs. It is used to detect low energy (<50 eV) electrons emitted from the surface of the specimen in response to interaction with the electron beam. These inelastically scattered SEs escape within only a few nanometers and contain information about the surface topography of the specimen (Paredes,2014). The most common type of BSE is composed of several semiconductors and used to detect high energy elastically scattered electrons that encompass essentially the same energy as that of incident (primary) electrons. The elements with higher atomic number (Z) are denser and consequently produce

more backscattered electron as compared to the elements with lower Z. Thus, the regions containing heavier elements appear brighter than low density elements (Paredes,2014; Ohring,2002). BSE images can be used for phase determination in multiphase specimens, whereas diffracted backscattered electron detectors are used to examine microfabric and crystallographic orientation in many materials (Saravanan and Rani, 2012).

When high energy electrons impinge upon the specimen, the characteristic X-rays are emitted from the irradiated area. The energy of the emitted X-rays is directly related to the orbitals of the elements from which they are emitted. Thus, the atoms can be identified by the analysis of energy spectrum of the X-rays, and the concentration of atoms can be determined by a count of the number of X-rays emitted. It is possible to create an elemental distribution image called X-ray map, by accumulating the characteristic X-rays emitted from the surface of the specimen. (Michler, 2008; Ohring, 2002; Paredes, 2014). The detection of low energy X-rays is vital in order to characterize the nanoscale particles. Energy dispersive X-ray (EDX) use traditionally electron beam energies of 20 KeV to excite the core levels of the specimen. The silicon drift detector (SDD) has opened the way to characterize the nanoscale particles in the SEM. The EDX technique has much improved in the recent year due to the introduction of SDD (Gomati and Walker, 2014).

For current work, the surface morphology of the films has been investigated with scanning electron microscope equipped with energy dispersive X-ray (FEI Quanta FEG 250, USA). SEM was operated at 10 kV under high vacuum. EDX has been used to determine chemical composition of CZO thin films NCs.

3.6.4 Atomic Force Microscopy

Atomic force microscopy (AFM) has been widely used to investigate the surface properties and structure of the materials in nanometric scale thin films. Flexibility, a large number of

potential signals and its various operating modes make it a powerful tool for thin film characterization. These features also make it more versatile for a variety of materials such as conductors, insulators, hard, soft, organic and inorganic. Moreover, with AFM it is also possible to measure geometrical morphology, adhesion, friction, surface impurities, elasticity, type of different spots of the surface, distribution of surface electrical charges and polarity of various electrical points on the surface (Aliofkhazraei and Ali, 2014). AFM provides additional advantages and capabilities for generating images with a resolution of sub nanometer, which is higher than SEM and comparable to transmission electron microscopy (TEM). However, AFM has its own limitations such as the small imaging dimension and relatively slow imaging speed (Jalili and Laxminarayana, 2004).

AFM utilizes a sharp tip across a sample surface while monitoring the tip sample interaction to reconstruct 3D surface topography. The sharp tip is located at the end of a flexible cantilever, which is able to move across the samples surface by piezoelectric actuators. The cantilever-tip system is the heart of AFM, which determine, the quality of the measurements. The cantilever is typically made of silicon (Si) or silicon nitride (Si_3N_4), and between 50 and 200 mm long and only a few micrometers thick, which make them flexible and durable enough to hold the tips on their ends. The tip is only a few micrometers (~3 μm) long and often less than 10 nm in diameter at the end (Hilal et al., 2006; Aliofkhazraei and Ali 2014).

AFM has four primary modes of operation namely contact mode, non-contact mode, tapping or intermittent mode, and profile imaging mode. The contact mode is the most direct AFM imaging mode and is commonly used for rigid surfaces. The second mode, non-contact, is mostly used for soft materials, which can be deformed easily and the samples neither damaged nor contaminated by contact. During scanning of the sample, the cantilever is held at a very

small distance (5-10 nm) away from the surface and oscillated at a resonant frequency. The tip is attracted by the force like van der Walls forces or any other long range forces, which extends well above the surface. The third mode is intermittent, dynamic or tapping mode, which is the hybrid of the preceding modes in which the cantilever is vibrated at a distance close to the contact imaging mode. The fourth profile imaging mode can be used to have topographic information of sticky surfaces (Hilal et al., 2006; Brabazon and Raffer, 2015; Jalili and Laxminarayana 2004).

For current work, surface topography of CZO thin film NCs have been evaluated by atomic force microscope (Anasys Instruments, USA). AFM was operated in contact mode with a scan speed of 0.2-0.5 Hz.

3.6.5 X-ray photoelectron spectroscopy

X-ray photoelectron spectroscopy (XPS) has its fundamental origin from photoelectric effect, explained by Einstien in 1905. The photoelectric effect had become a powerful tool for studying the composition and electronic structure of matter since the late 1950, and, later on, Kai Siegbahn received the Nobel Prize for the development of high resolution XPS in 1981 (Fadley, 2010). High energy photons, which are in the range of X-rays, are required to remove inner shells electron.

XPS is the single most versatile technique widely used for surface analysis in many fields of study such as microelectronics, environmental chemistry, and heterogeneous catalysis. XPS provides information regarding chemical oxidation states, atomic composition, and electronic structure of the sample under investigation. This technique is also useful for quantitative analysis of ultrathin films of materials. The technique can be used to determine surface composition and electronic environment, and is non-destructive in many cases. Since the topmost atomic layers of

the materials (≤ 100 Å) are analyzed by XPS, the technique is very useful to investigate the interfacial phenomena at the solid-solid and solid-gas boundaries (Chusuei and Goodman, 2003).

When a substance is irradiated with a photon of sufficient energy, photoelectrons and auger electrons are emitted. XPS measures the kinetic energy distribution of these emitted electrons from the core levels of the elements constituting a solid. The difference between the energy of the primary photon (hυ) and the kinetic energy of the photoelectron (KE_P) is defined as core electron binding energy (BE_X = hυ - KEp). The measured binding energy is a characteristic of each element and can be used to identify the elements in the sample under investigation (Seyama et al., 2013; Stucki and Banwart, 1980).

XPS measurements are conducted under ultra-high vacuum (≤ 10^{-5} to 10^{-9} Torr). However, recent advancement in XPS instrumentation has enabled operation in the 1-5 Torr pressure regime (Chusuei and Goodman, 2003). A typical XPS consists of an X-ray source, an electron energy analyzer and a photo electron detector. Several factors need to be considered in order to select a suitable X-ray source including the energy resolution of the X-rays, energy of photons and ease of application of the material to an anode surface. Commonly used X-ray sources are Al Ka (1486.6 eV) and Mg Ka (1253.6 eV). The energy resolution of photoelectrons can be improved by eliminating satellite spectra using monochromatic X-rays with a narrow line width (Seyama et al., 2013). The ejected electrons are transferred to the energy analyzer through the lens system where they are separated according to their kinetic energy. The various types of analysers are employed including cylindrical electrostatic hemispherical, and spherical mirrors. The photoelectrons are detected by devices such as channel plates and electron multipliers (Stucki and Banwart ,1980).

For current work, Chemical composition and chemical state of the deposited films have

been determined by XPS (Thermo Fisher Scientific, UK) K-Alpha system at a take-off angle of 90^{o} relative to the surface. XPS survey scan spectra have been acquired in a high pass energy, low point-density (energy) scanning mode. The high pass energy is used to maximize sensitivity of the instrument. XPS Co $2p_{3/2}$ spectra, which are used to calculate the elemental composition and to determine the chemical state composition, have been acquired in a low pass energy (i.e., high energy resolution) mode, with a high point density on the energy axis (0.1 eV). The low pass energy yields the energy resolution that is required to better conclude on chemical state information.

3.6.6 Visible reflectance spectroscopy

Visible reflectance spectroscopy (VRS) is a well-established technique for measuring thin film thickness. This technique provides information based on how light propagates in and reflects upon a portion of the material under investigation. It is one of the basic optical techniques for determining film thickness and is highly accurate, non-destructive and cost effective for measuring thickness of translucent and reflecting thin films. It relies on the interference of light from air-film surface and film-substrate surface, where the optical path difference is related to the film thickness of the specimen. During measurements the substrate is illuminated with visible light of fixed wavelength and the amount of light reflected from the substrate is detected and measured. Reflectivity measurements are routinely carried out in order to measure the thickness of the thin films on substrate. The deposited films have wavelength-dependent optical properties, the two optical constants viz., refractive index (n) and extinction co-efficient (k), serves as input to VRS if film thickness needs to be measured (Adams and Calif, 1990; Ohring, 2002).

During measurements, when light impinges on thin-film deposited on a substrate, both the

top and bottom surfaces of the film reflect light. The total amount of reflected light depends on the superposition of these two reflections. Moreover, these two reflections may add together constructively or destructively depending upon their phase relationship. The phase relationship is determined by the difference in optical path lengths of the two reflections. The resulting interference pattern can be used to determine the thickness of the film (Hind and Chomette, 2011). Typically, these reflectivity measurements are made in the visible part of the light spectrum. For relatively thick films, as the light interference takes place in the film, maxima and minima are observed in a plot of reflectivity versus wavelength. The film thickness can be measured indirectly from the wavelength position of these various extrema. However, in case of extremely thin films, maxima or minima may not be observed, and an absolute measurement of reflectivity must be made in order to measure film thickness. These absolute reflectivity measurements are usually carried out at wavelength in the range of 400-500 nm (Adams and Calif. 1990).

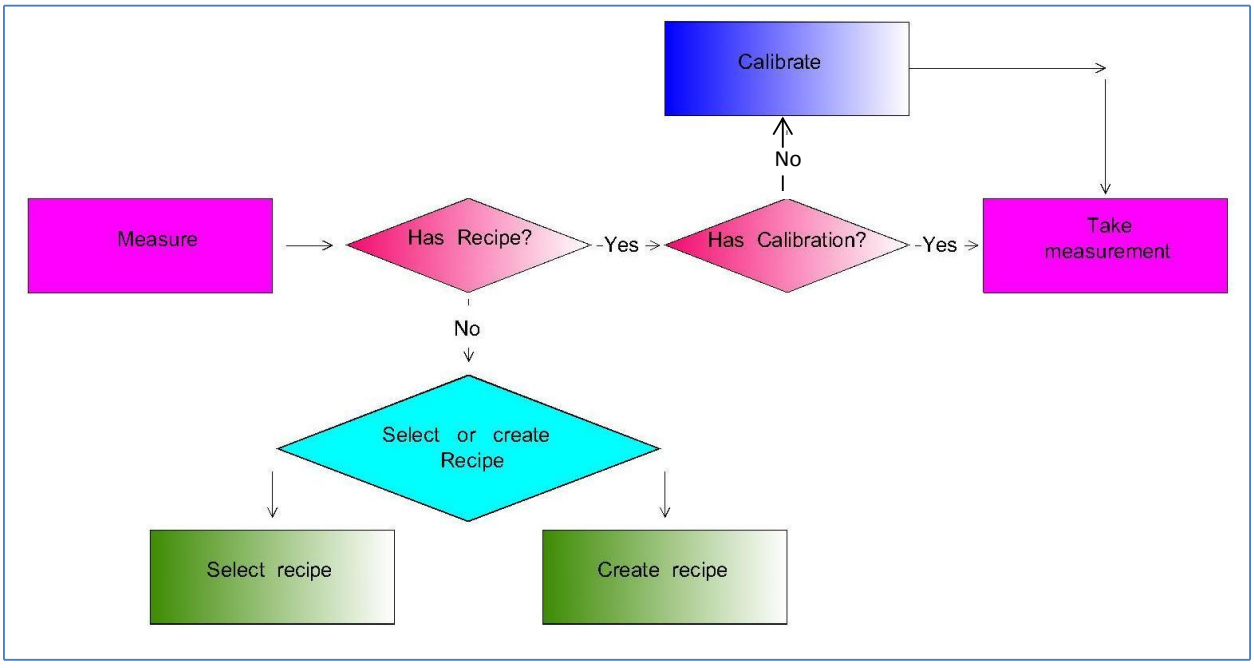

Figure 3.10: Schematic showing work flow of thickness measurement process.

For present work, M-probe series spectral reflectometer system (Semiconsoft, USA) has been used in order to measure the thickness of the deposited Co-doped ZnO thin films. The workflow of measurement process is presented schematically in the Figure. 3.10. A bare Si reference sample was used for reflectance calibration. It is also possible to use other well-known reference samples with a stable reflectivity. The reflectance data are obtained using a filmstack which is the optical model of the sample under investigation. The elements of the filmstack are ambient air, substrate, and layers that can be edited or modified according to nature of the sample in question. A built in modified Marquardt-Levenberg minimization scheme is employed to fit the experimental and estimated data. Basically, the built in numerical scheme compares the measured and simulated data, and infers the parameters of the filmstack based on the best fit.

Chapter 4: Chemical and morphological properties of as-grown Co-doped ZnO thin film nano-composites

4.1 Introduction

In this chapter, the effect of deposition temperature, accelerating voltage, pulse frequency and substrate materials on the chemical and morphological properties of the films have been evaluated systematically. The corresponding results are discussed in terms of film thickness, chemical composition, chemical state, morphology and structure (crystal phase) hereafter.

4.2. Effect of substrate temperature on the properties of Co-doped ZnO thin film

In the first series of CZO film deposition runs, we have deposited $Co_xZn_{1-x}O$ (x = 0.20) thin film NCs from a single target containing 20 w% Co on silicon (100). The films have been deposited at various temperatures (350^{o}C, 400^{o}C, 450^{o}C) and a pulse frequency of 2 Hz, under a background argon (Ar) pressure of ~3 mTorr and an accelerating voltage of 14 kV, see Chapter 3, Table 3.2. Complementary analytical techniques have been used to characterize the deposited films. The corresponding results and discussion are given next.

4.2.1 Film thickness

A typical cross section of the films deposited on silicon substrate, as per SEM investigations, is shown in Fig. 4.1-a. The average thickness of the films has been estimated to be ~38 nm. Film thickness has been averaged over 10 different points along SEM transversal cross section. Fig.4.1-b shows the reflectance response of VRS for the film deposited at 450^{o}C and 2 Hz. The measurements reveals that the thickness of the film is ~40 nm, which is in good accordance with SEM measurement (see Fig. 4.1-a). The deposition temperature (350^{o}C-450^{o}C) does not seem to have any significant effect on CZO film thickness deposited at a beam frequency of 2 Hz. The blue curve is the calculated (simulated) reflectance response of the films, whereas the red curve is the measured one. The experimental data have been fitted by means of

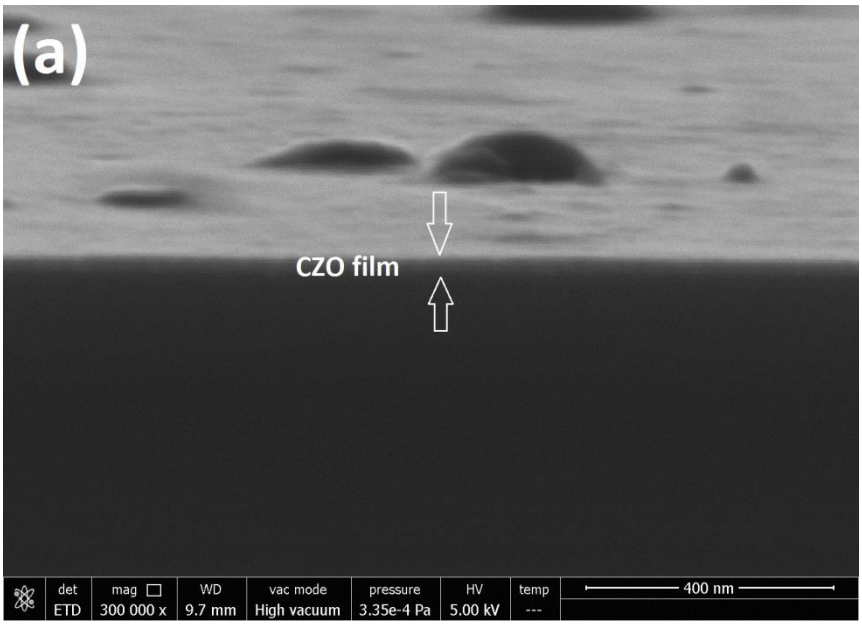

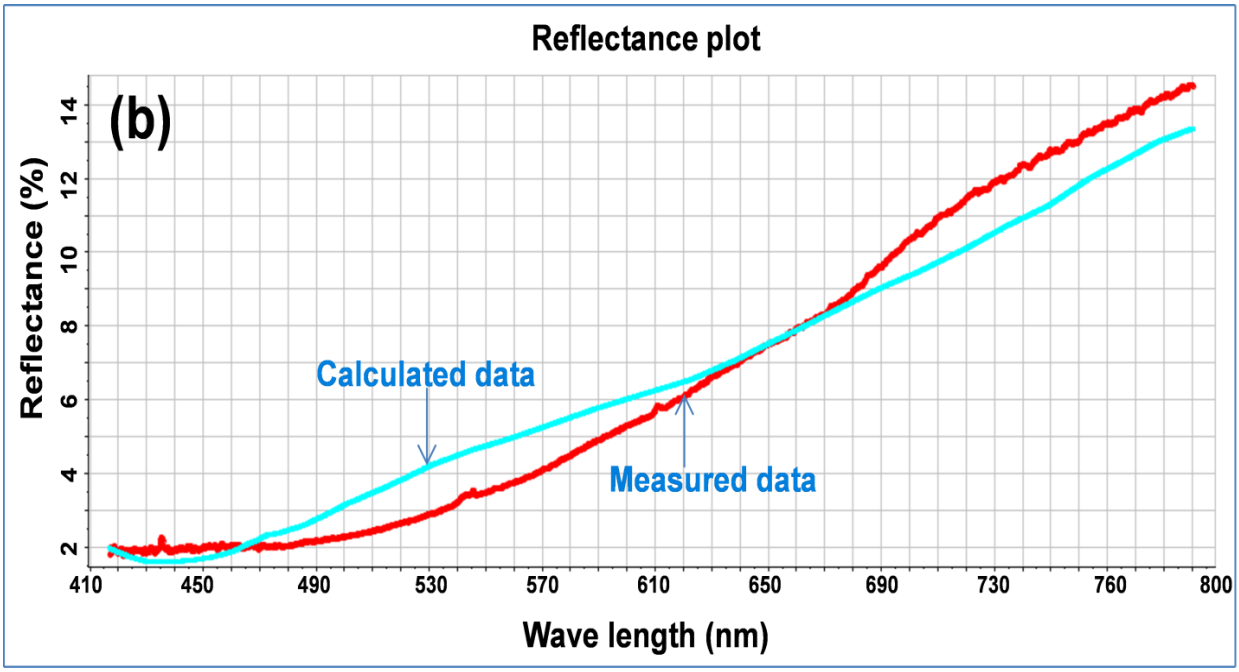

Figure 4.1: Typical SEM transversal sections of film deposited on Si at (a) 450^{o}C and 2 Hz. (b) Typical visible reflectance spectroscopic measurements of Co:ZnO film on Si under similar deposition conditions.

a modified Marquardt-Levenberg minimization scheme built in the accompanying software.

Basically, the thickness of the film is measured indirectly through the minimization of the difference between simulated and measured data. The fit between the two curves is quite good (max. relative error of 2 %).

4.2.2 Surface morphology

Surface morphology of the films has been assessed by SEM and AFM measurements. SEM images of Co-doped ZnO thin films deposited on Si (100) at 350^{o}C, 400^{o}C and 450^{o}C are presented in Figure 4.2. From SEM analysis, see Figure 4.2(a-c), the films consist of particles in globular form. The size of these globules is in the range of 20 to 400 nm. A closer look at the globules indicates that these grow out of many smaller nanoparticles, most likely by coalescence (Ohring, 2002). Figure 4.3, shows particle size distribution of the films deposited at various temperatures. The particle size of CZO film is directly measured from SEM images, see Figure 4.2(a-c). The data reveal that the films exhibit a higher proportion of nanoparticles whose size is in the range of 1-4 nm. The particle size of cobalt based FT-catalyst is very critical in order to attain high selectivity and activity in FTS. Metallic cobalt particles smaller than 4 nm are expected to re-oxidize to CoO during realistic FT reaction conditions, which results in the deactivation of the catalyst (Karaca et al., 2011). It has been found, based on SEM data that the deposition temperature affect the average globule size, which increases with temperature, viz., ~90 nm (350^{o}C), ~170 nm (300^{o}C) and ~178 nm (450^{o}C). Similar, observations have been recorded for the films deposited at a beam frequency of 4 Hz, and for the film deposited (at both frequencies, i.e., 2 Hz, 4 Hz) on c-sapphire under similar conditions (Ali et al., 2016). AFM images of films deposited on silicon (100) at 350^{o}C, 400^{o}C and 450^{o}C are presented in Figure 4.4. The data reveal that as the deposition temperature is increased, film roughness marginally increases, i.e., nearly 3.4 nm (350^{o}C), 3.7 nm (400^{o}C) and 5.3 nm (450^{o}C). As the temperature

increases from 350^{o}C to 450^{o}C, the number of globules decreases and their size increases (see Figure 4.2 and Figure 4.4). Similarly, AFM data have been recorded for the films deposited at a beam frequency of 4 Hz and for the films deposited on c-sapphire substrate under identical conditions (Ali et al., 2016). The increase in globule size with temperature can be explained in terms of the dependence of particle mobility (on the substrate) and surface diffusion transport on temperature. The driving force behind the growth of larger globules is due to the natural tendency to reduce the total surface energy of the system, resulting in higher mobility, and to diffusion-controlled mass transport, both of which increase with the deposition temperature

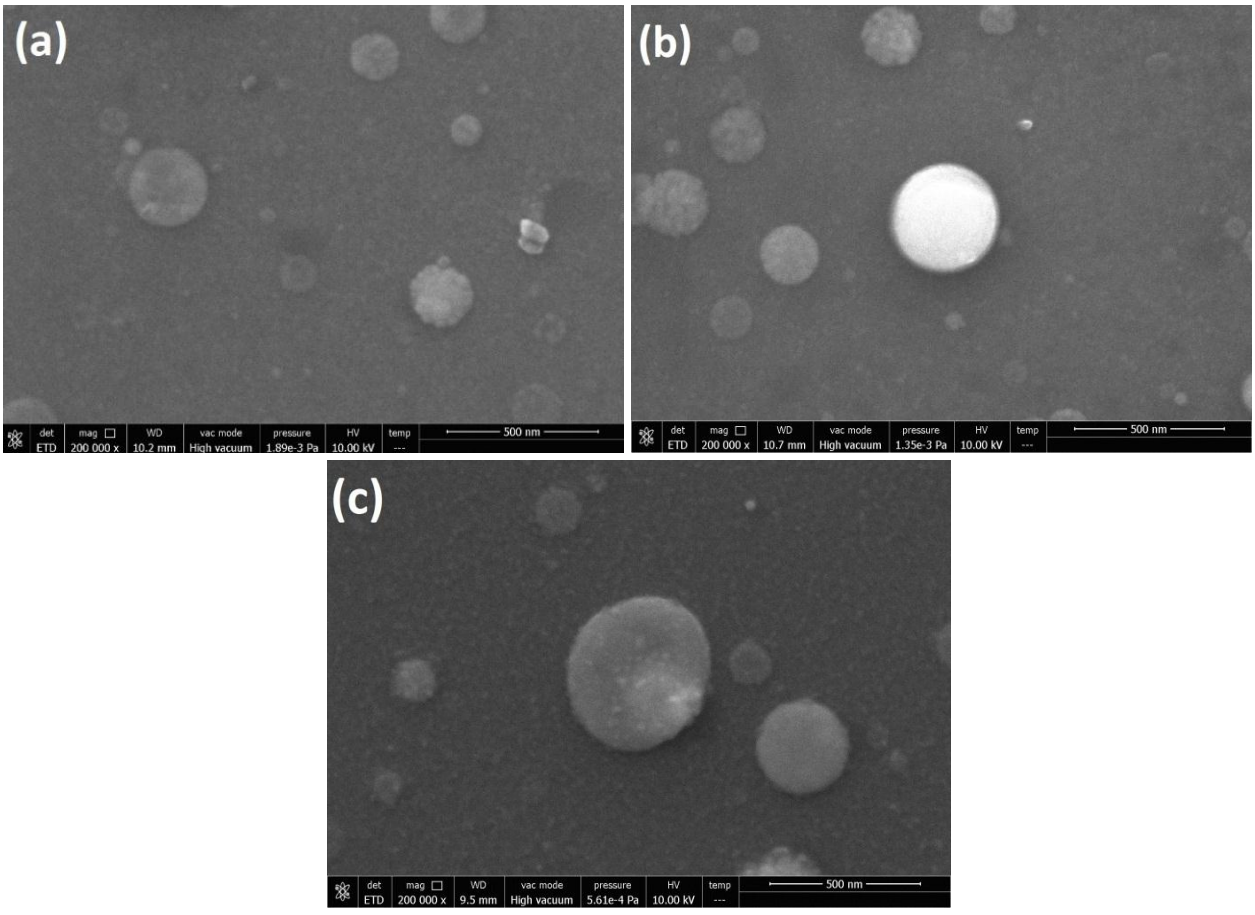

Figure 4.2: SEM images of Co-doped ZnO thin films on Si(100) 4 Hz and at (a) 350^{o}C, (b) 400^{o}C and,(c) 450^{o}C (Fiducial mark = 0.5 micron).

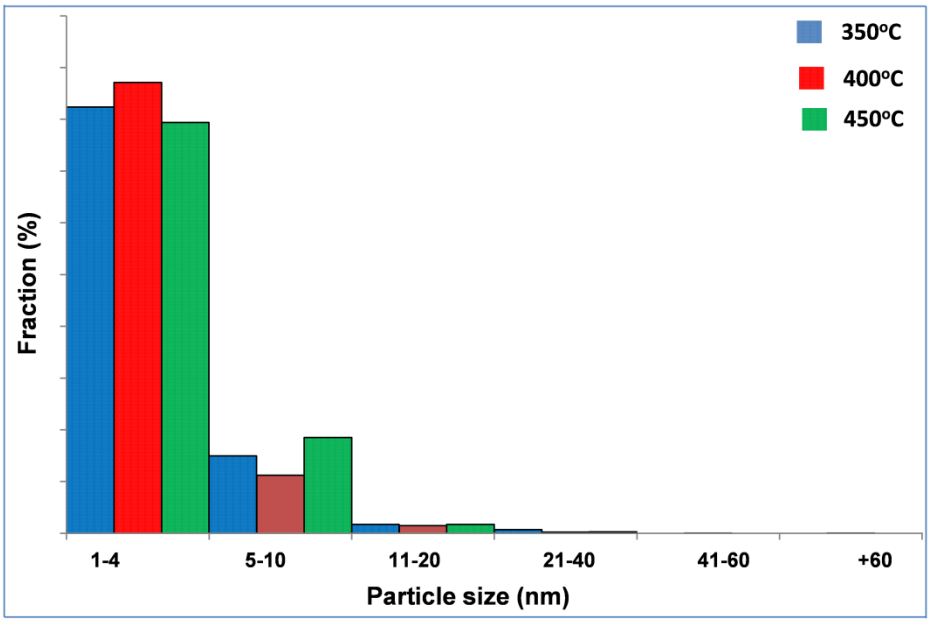

Figure 4.3: Particle size distribution of CZO films on Si measured directly from SEM images (Figure 4.2). The deposition temperature is indicated in the inset.

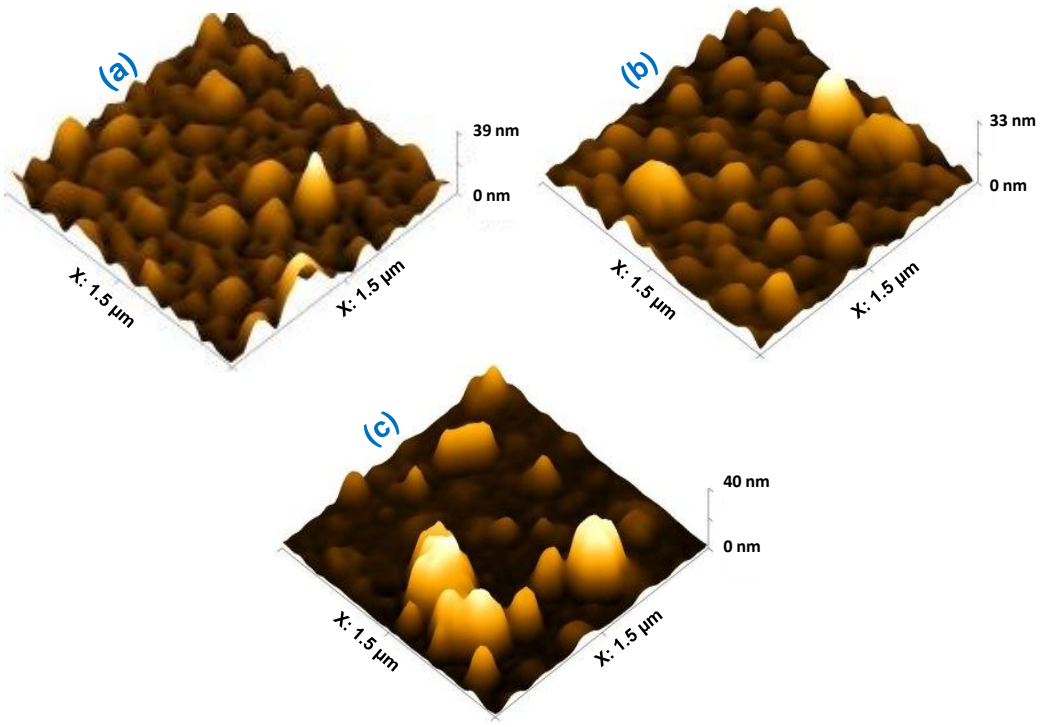

Figure 4.4: Topographs of CZO thin films on Si (100) 4 Hz and at (a) 350^{o}C, (b) 400^{o}C and,(c) 450^{o}C (Fiducial mark = 0.5 micron).

(Ohring, 2002; Liu et al., 2009). The combined effects result in larger size globules at the expense of smaller ones. The present AFM results are consistent with SEM measurements reported earlier.

4.2.3 Chemical composition and chemical state

Figure 4.5-a shows a SEM image of CZO film prepared on silicon (100) at 450^{o}C and 4 Hz, Figure 4.5-b depicts the corresponding EDX spectrum, which reveals the presence of O, Co and Zn, in the film, whereas SEM point analysis of the film indicates that deposition is congruent as the film contains ~20±5 % Co. Figure 4.5-c illustrates the distribution maps of O, Co and Zn in the deposited film. Further, it reveals that O and Zn are uniformly distributed in the films,

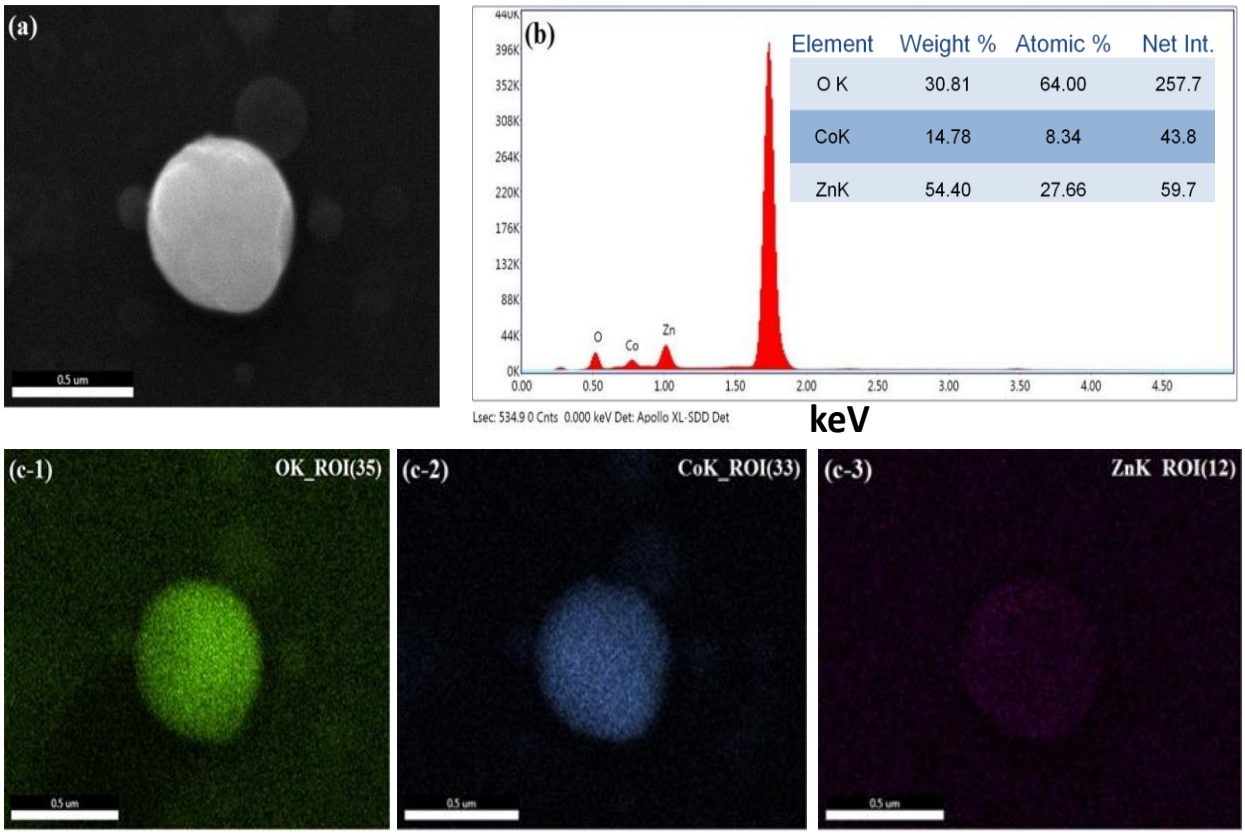

Figure 4.5: CZO film deposited on Si (100) at 4 Hz and 450^{o}C. (a) SEM image, (b) EDX spectrum, (c) Elemental mapping showing the distribution of (c-1) O, (c-2) Co and, (c-3) Zn in the deposited film (Fiducial mark = 0.5 micron).

whereas Co is concentrated in the globules, see Figure 4.5(c-2), which confirms the inhomogeneous distribution of Co in CZO films.

The chemical state of Co in the deposited films has been assessed by XPS measurements. The typical spectra of Co 2p of films grown on silicon at 350^{o}C, 400^{o}C and 450^{o}C are shown in Figure 4.6. The data have been collected with low energy resolution, as well as low point density on the energy axis. The former improves sensitivity, while the latter reduces acquisition time. The peaks are assigned as metallic (Co^{o}), Co2p$_{1/2}$, Co2p$_{3/2}$ (CoO) and shake-up satellite peaks (labeled 'sp'). The Co 2p$_{3/2}$ peak at the binding energy around 780.5 is attributed to Co^{+2} oxidation state (Ivill et al., 2008). The small shoulder (peak) at the low binding energy located at 778-779 eV is attributed to metallic Co (Peng et al., 2005; Tortosa et al., 2008). This low binding

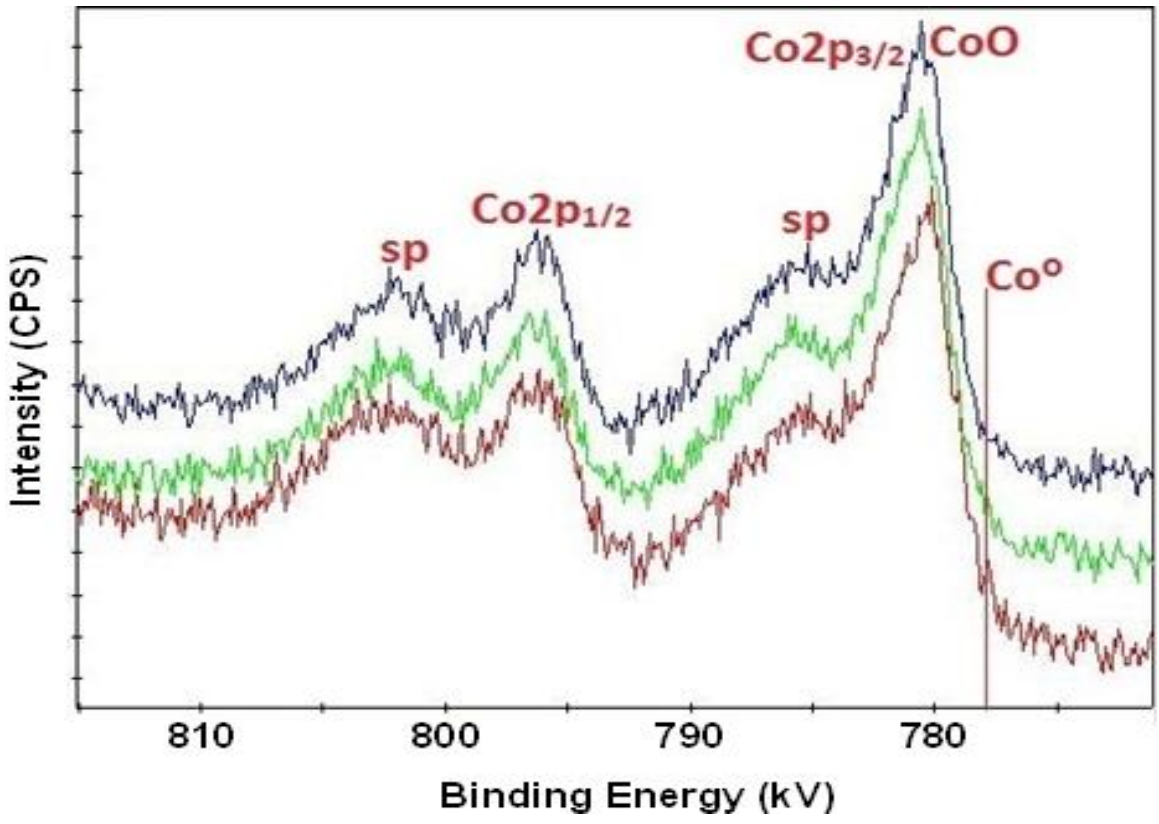

Figure 4.6: Co 2p XPS spectra of CZO films grown on Si at 4 Hz, and at 350^{o}C (Blue), 400^{o}C (Green) and 450^{o}C (Red).

energy peak is consistently found in most of the prepared films. The data indicate that a substantial portion of Co atoms are present in the films as Co^{+2} oxidation state and as Co^{+2} substituting Zn^{+2} lattice sites in ZnO.

4.2.4 Structure

The phase analysis of CZO films deposited at different temperatures is shown in Figure 4.7. Diffraction patterns of the films have been obtained using theta/2-theta Bragg-Brentano configuration to generate 30^{o}-80^{o} diffractograms. The characteristic peak at 2Θ ~34.43^{o} (002) is indicative of the presence of ZnO in the films (PDF card no.: 01-070-8070). The sharp and intense diffraction peak (002) reveals that the as-grown film has a preferential c-axis orientation. From the Figure 4.7, the structural analysis shows two peaks at 2Θ ~61.7^{o} (412) and 65.9^{o} (306) attributed to hcp metallic Co (PDF cardno.:01-070-2633).The data reveals that metallic Co content in the film increases as the deposition temperature increases.

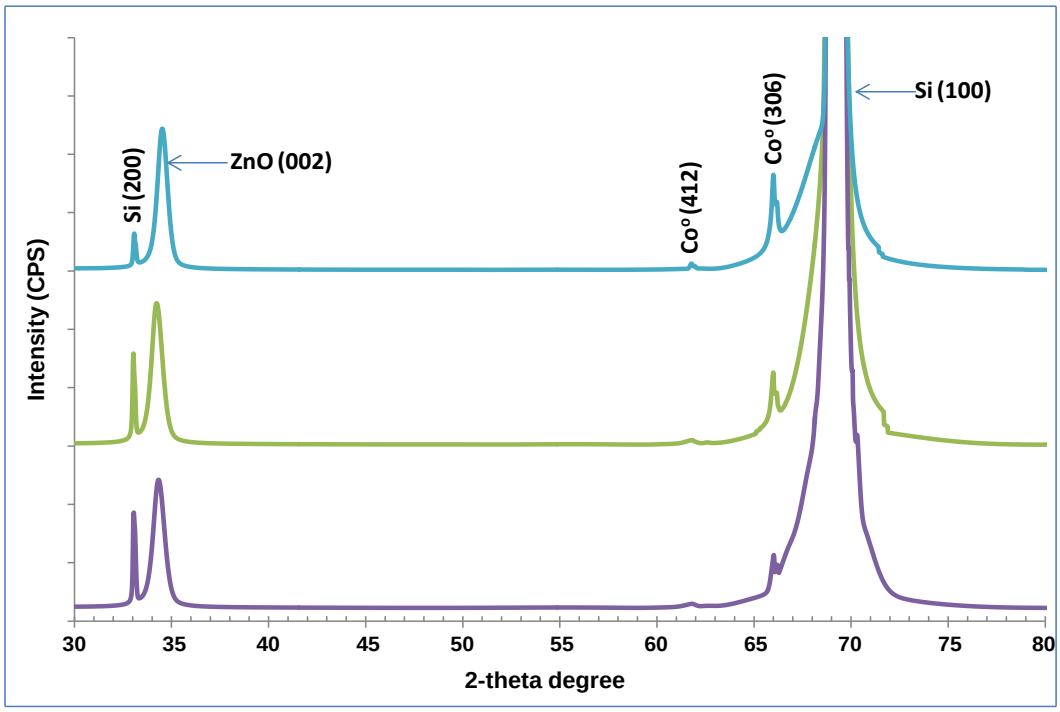

Figure 4.7: XRD patterns of CZO films deposited on Si at 4 Hz and 350^{o}C (bottom), 400^{o}C (middle), and 450^{o}C (top).

4.3 Effect of temperature and discharge voltage on the properties of Co-doped ZnO thin-films

In the second series of deposition runs, $Co_xZn_{1-x}O$ (x = 0.20) thin-films have been deposited from a single target (Co:ZnO containing 20 w% Co) on silicon. A few operation conditions viz., accelerating voltage (15 kV, 16 kV) and deposition temperature (350^oC-800^oC) were changed to elucidate their effects on the physico-chemical properties of the films. Other operating conditions such as pulse frequency, background Ar pressure, substrate-target distance and target-capillary tube tip distance were fixed at 2 Hz, ~3 mTorr, 5 cm and 0.25 cm respectively, see Chapter 3, Table 3.2.The corresponding results and discussion are given next.

4.3.1 Chemical composition and chemical states

The results of SEM-EDX measurements reveal that deposition is nearly congruent as the average Co content in the films is ~20 w%. Figure 4.8 shows line scans (dark green coloured straight line between two blue circles) of the elemental composition of the films produced at various temperatures and an accelerating voltage of 16 kV. EDX analysis, whose results are superimposed on SEM images in Figure 4.8 shows that the larger the globule size is, the higher the cobalt concentration is, and vice versa. The size of the globules lies in the range of 20 nm to 300 nm. The data, see Figure 4.8-c, confirm that films deposited at 800^oC consist of a predominately cobalt phase with Zn making up only 1-2 wt.%. This can be explained in terms of the boiling point of Zn nanoparticles (Viart et al., 2003). When film deposition is carried out at 800^oC (near the boiling point of Zn), Zinc is likely to have vaporized (re-evaporated from the film surface) due to its high vapor pressure. The calculated data, from EDX point analysis, of the elemental composition of the films produced at different values of temperature and electron beam accelerating voltage are listed in Table 4.1. The results show that the Co-rich globules contain ~15 - 43 wt.% cobalt and the distribution of Co atoms on the film surface is

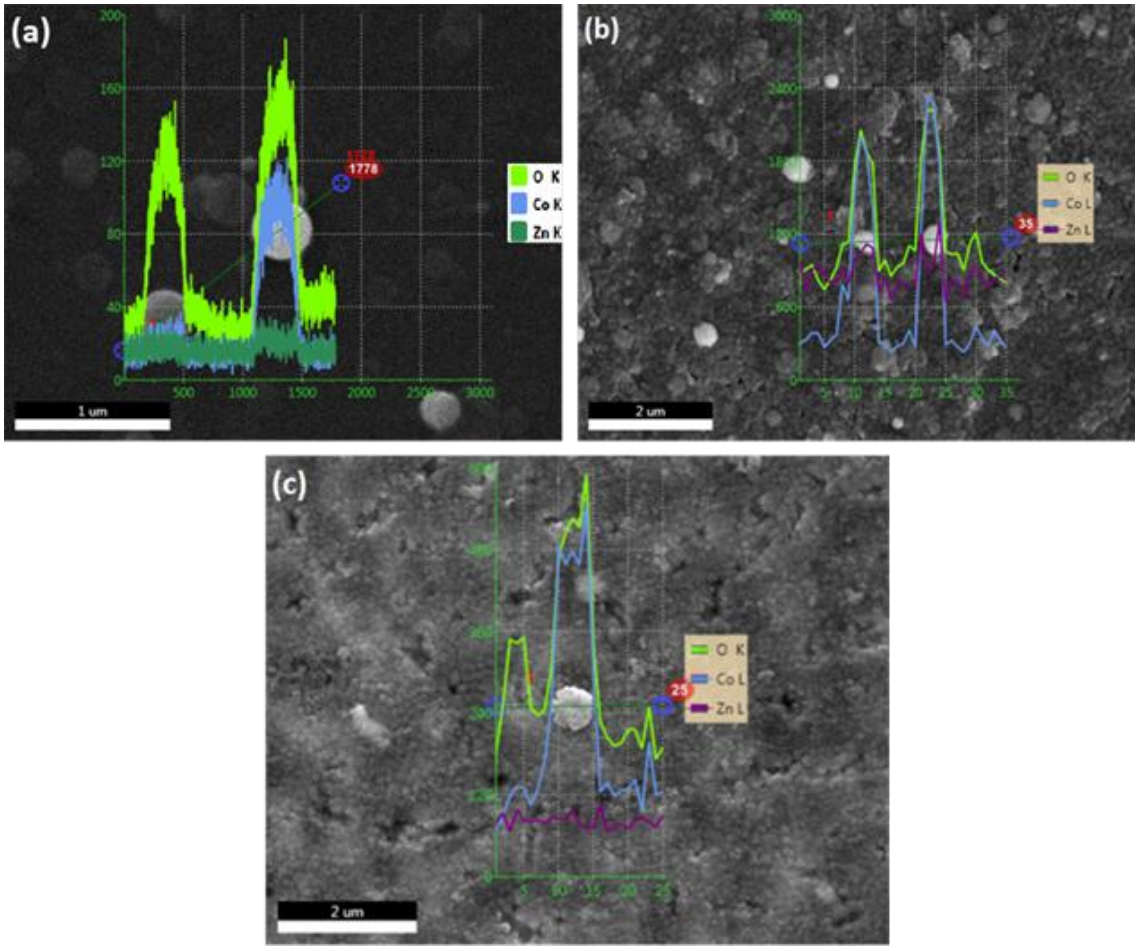

Figure 4.8: EDX line scans and their corresponding element profiles of the films produced at 16 kV and (a) 450^{o}C, (b) 600^{o}C, (c) 800^{o}C.

inhomogeneous.

The chemical state of Co in the deposited films has been investigated using XPS (with a detection limit from 0.001 at% to 0.005 at% for heavy metals). Figure 4.9 depicts XPS spectra of Co2p$_{3/2}$ peaks for CZO thin films deposited at various temperatures (350^{o}C-800^{o}C) and accelerating voltage values (15 kV and 16 kV). The data have been collected with low energy resolution, as well as low point density on the energy axis. The former improves sensitivity, while the latter reduces acquisition time. The deconvoluted XPS Co 2p$_{3/2}$ spectra reveal the presence of cobalt in Co^{o}, Co^{+2} and Co^{+3} valence states in the deposited films. The Co 2p$_{3/2}$ peak

Table 4.1: Elemental composition of the films as function of deposition temperature. and accelerating voltage (Ali et al., 2017).

Accelerating voltage (kV)	Deposition temperature (^{o}C)	Co weight (%)	Zn weight (%)	O weight (%)
15	350	14.78	54.40	30.81
	400	35.83	52.02	12.12
	450	42.54	23.02	34.44
16	350	17.02	52.46	30.52
	400	34.60	42.03	23.38
	450	40.96	38.80	20.29
	600	30.73	20.76	48.51
	800	24.06	1.80	74.14

at the binding energy around 780.5 eV is attributed to Co^{+2} oxidation state (Ivill et al., 2008). The small shoulder (peak) at the low binding energy located at around 778-779 eV is attributed to metallic Co (Co^{o}) (Peng et al., 2005; Tortosa et al., 2008). The energy peak at around 782.8-783.3 eV is assigned to Co^{+3} oxidation state (Zhou et al., 2008; Alves et al., 2017). As per XPS single spot analysis, at higher deposition temperature, the CZO films, overall, exhibit higher Co^{o} concentration, as shown in Figure 4.9. Further, XPS survey scan analysis reveals that, at relatively higher deposition temperature, Zn phase has disappeared from the films, resulting in Co-phase rich films, as shown in Figure 4.10, in agreement with EDX analysis. The data also show that a substantial fraction of Co atoms are present in +2 formal oxidation state in CZO films by substituting Zn^{+2} in ZnO lattice sites. The concentration of metallic Co appears to be in highest concentration in the films deposited at 600^{o}C, as shown in Figure 4.9-c.

4.3.2 Film Thickness

A typical transversal cross section of deposited films is shown in Figure 4.11-a. As per

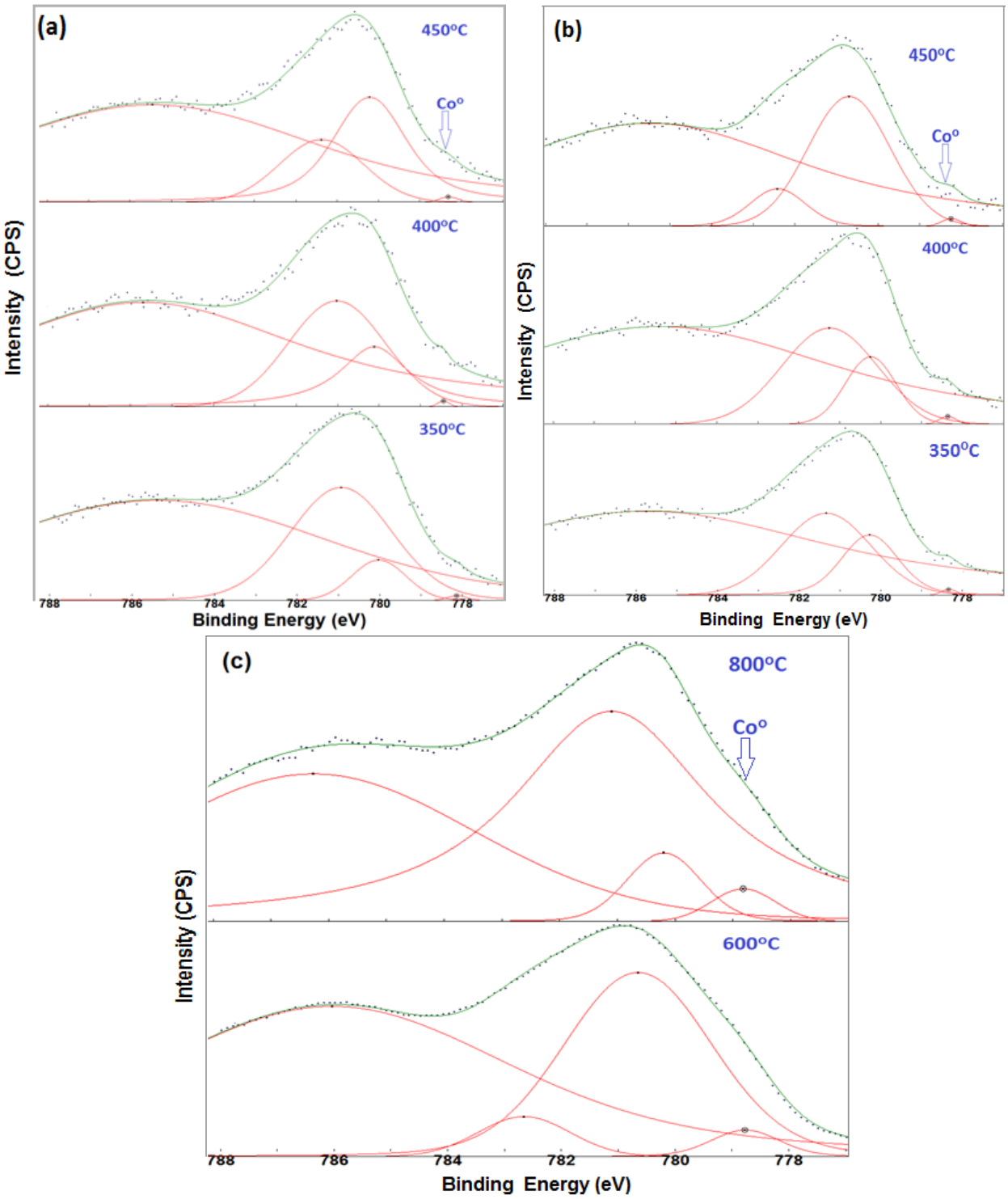

Figure 4.9: Typical XPS chemical binding spectra of Co $2p_{3/2}$ peaks (and their deconvolutions) of CZO films grown at different deposition temperatures (350°C-800°C) and accelerating voltages of (a) 15 kV and (b, c) 16 kV.

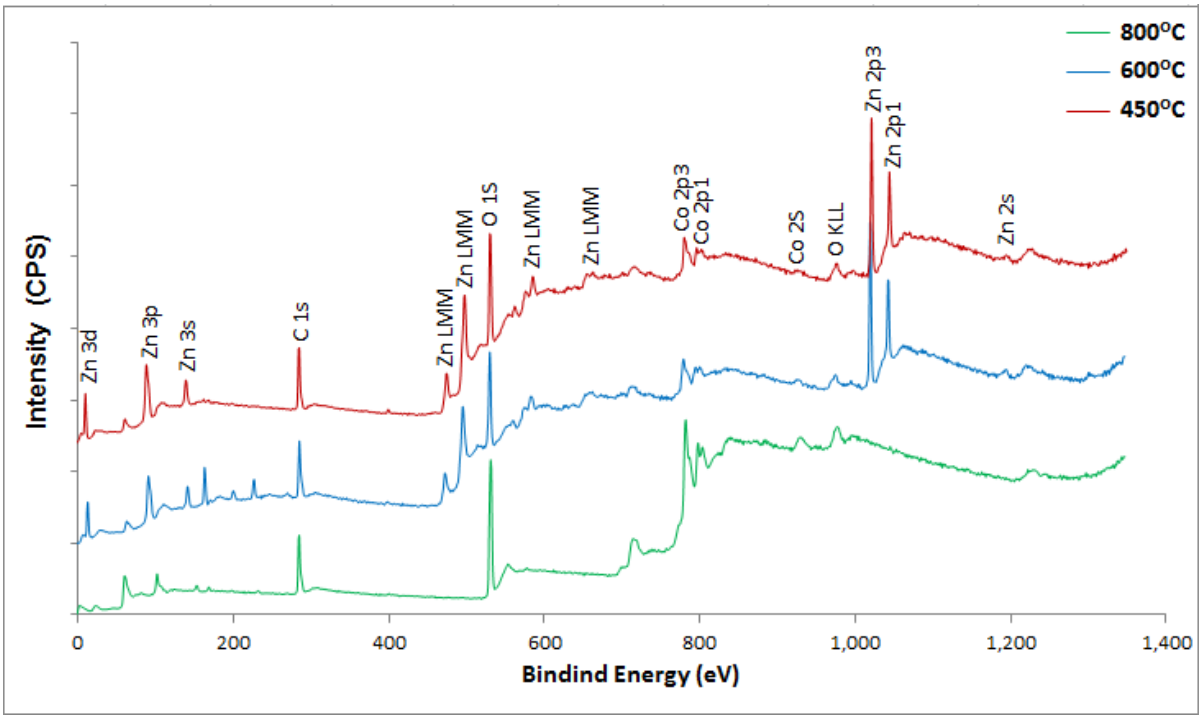

Figure 4.10: XPS survey scan spectra of CZO films deposited at electron beam accelerating voltage of 16 kV and at deposition temperatures of 450°C, 600°C and 800°C.

SEM measurements, the thickness of the film is in the range of 60-120 nm, which is in good agreement with the thickness, i.e., 111 nm, measured by VRS, as per Figure 4.11-b. The measurements confirm that the average film thickness increases with deposition temperature viz., ~60 nm (350°C) and ~120 nm (800°C). This may be explained in terms of surface morphology of the films. The higher the deposition temperature is, the higher the agglomerate on the surface is resulting in a thicker film at higher substrate temperature (800°C). The accelerating voltage (15 kV, 16 kV) does not have any considerable effects on film thickness. The deposited film thickness is indirectly measured through the minimization of the difference between measured and calculated data by means of a modified Marquardt-Levenberg built-in algorithm. The fit between measured and calculated reflectance curves is quite good, and any discrepancies are likely due to uncertainties in film optical properties, which are used as input to the algorithm.

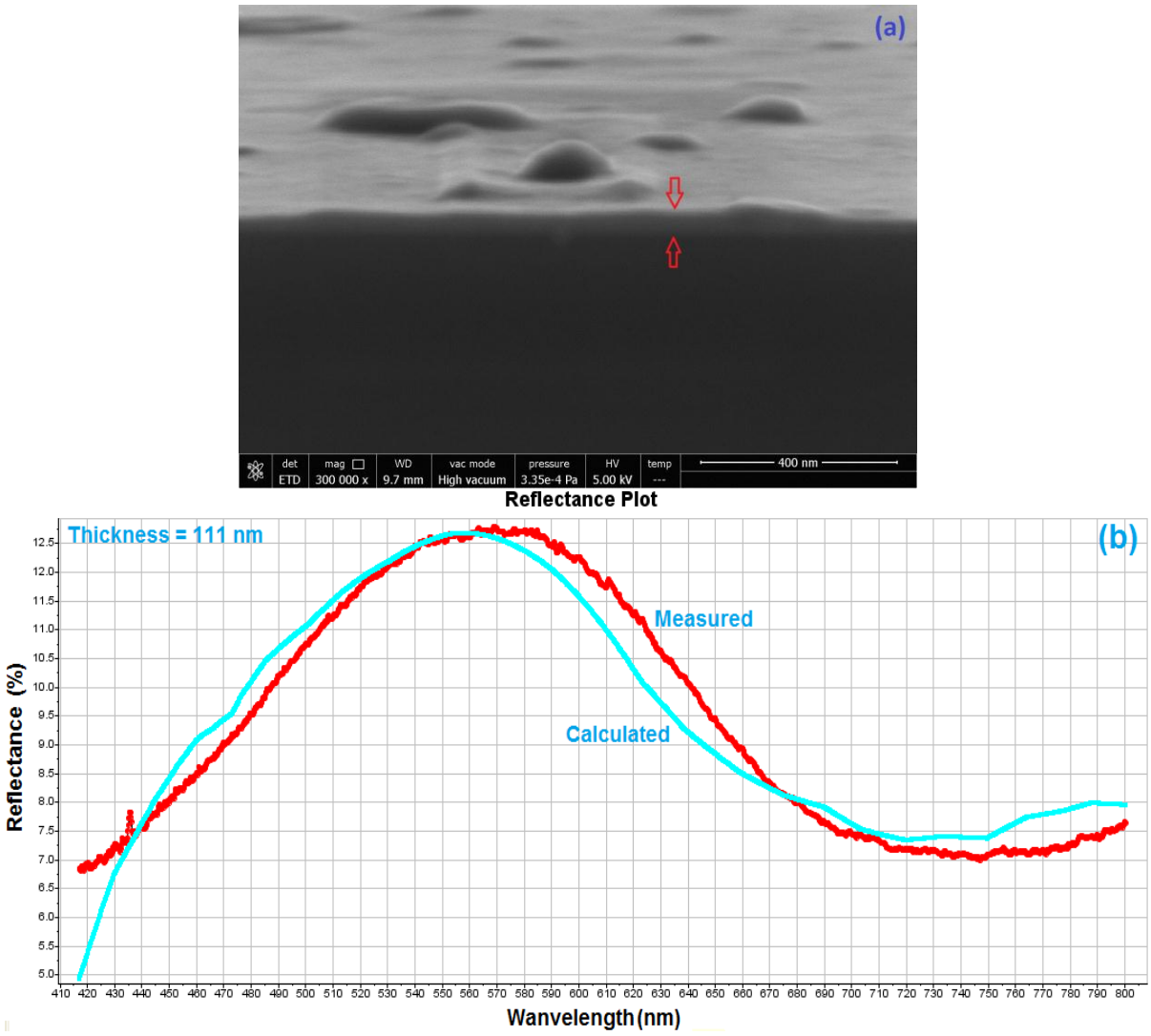

Figure 4.11: (a) Transversal cross section, and (b) visible reflectance spectroscopic measurement of film deposited at 400^{o}C and 15 kV.

4.3.3 Morphology

The deposited CZO thin films are transparent with a slight bluish green colour to them. Typical snapshot of the film has been shown in chapter 3 (see Figure 3.6). It is not easy to have an appreciation of film color on silicon substrates as the substrate has a dark grey color and is not transparent in the visible-wavelength range. Figure 4.12 shows typical SEM images of the films deposited at various temperatures and accelerating voltages. The films consist of many well-isolated globules whose size does not seem to be much affected by temperature when the latter is

varied from 350^{o}C to 450^{o}C, as illustrated in Figure 4.12(a-c) and Figure 4.12(d-f), at 15 kV and 16 kV, respectively. Film globule density appears to decrease then increase as temperature is increased from 350^{o}C to 450^{o}C for both voltage values, as shown in Figure 4.12 (a-f). Overall, films deposited at 16 kV have marginally larger globule size and higher density compared to films deposited at 15 kV. At 16 kV, and upon increasing the deposition temperature to 600^{o}C, the number of globules increases and the film exhibits a large number of small-size globules, which results in high globule density. The smaller globules seem to grow side by side forming a continuous layer of Co rich globules on the substrate surface, as shown in Figure 4.12-g. Under argon, the background gas used during deposition, the melting point of nano-sized Co particles has been reported to drop from 1495^{o}C (bulk value) to 650^{o}C (Homma et al., 2003). Accordingly, the high globule density at 600^{o}C may be attributed to cobalt particles melting and spreading over the film surface, as corroborated by EDX line scan analysis of Co in Figure 4.8-b. The cobalt particles disperse on the film surface owing to thermodynamic (the melting process) and kinetic (high surface mobility at high temperature) processes. For the film deposited at 800^{o}C, see Figure 4.8-c and Figure 4.12-h, the size of the globules is much smaller than it is at a lower temperature and the film mainly consisting of Co phase does not seem to be continuous (cracks, voids). This is likely due to high degree of re-evaporation under these deposition conditions as reported earlier, and thermal mismatch between Co (12.1 to 16.8 x 10^{-6} K^{-1}) (Donaldson and Beyersmann, 2012) and the underlying substrate (2.6 to 4.3 x 10^{-6} K^{-1}) (Watanabe et al., 2004). In addition, it is noted that at a lower deposition temperature (350^{o}C-450^{o}C) the Co-rich globules are sphere-like in shape, but as the growth temperature is further increased to 600^{o}C and 800^{o}C, tapered (faceted) Co-rich globules are formed in the films, as shown in Figure 4.8-b and Figure 4.12-g at 600^{o}C, and, Figure 4.8-c and Figure 4.12-h at 800^{o}C.

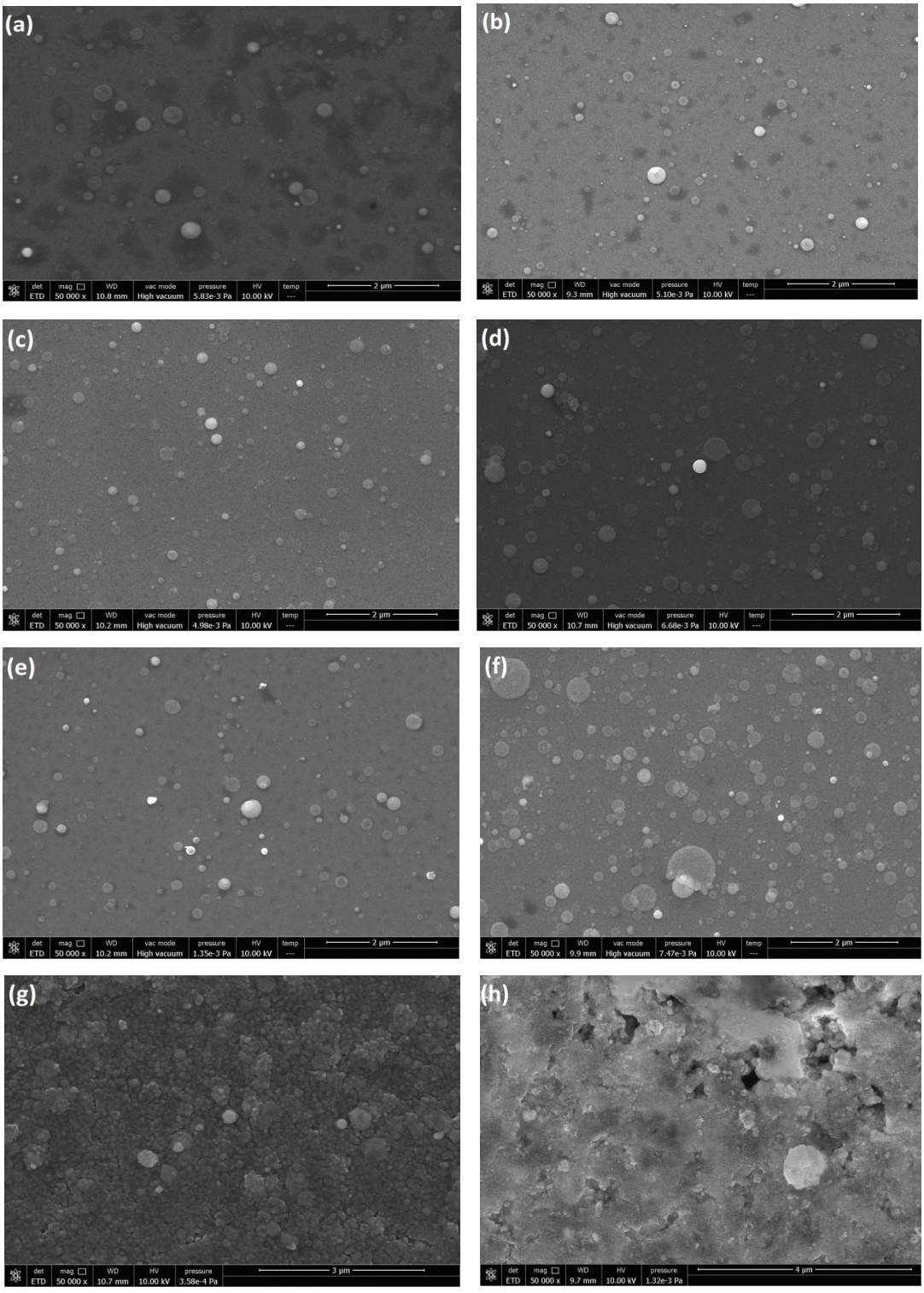

Figure 4.12: SEM images of deposited films as a function of accelerating voltage and temperature: 15 kV at (a) 350^{o}C, (b) 400^{o}C, (c) 450^{o}C, and 16 kV at (d) 350^{o}C, (e) 400^{o}C, (f) 450^{o}C, (g) 600^{o}C, (h) 800^{o}C.

As can be seen in Figure 4.8 and Figure 4.12, the films consist of globules dispersed over the surface which grow from many primitive nano-particulates. Based on SEM measurements, at both accelerating voltages, films exhibit a higher proportion of these primitive nanoparticles whose diameter is in the range of ~6-10 nm and no particle is found to be less than 5 nm in diameter. The particle size is directly measured from SEM images depicted in Figure 4.12. The formation of nanoparticulates is a characteristic of ablation-based deposition methods, viz., pulsed electron beam ablation and pulsed laser ablation (Mathis and Christen, 2007; Koren et al., 1989; Witanachchi et al., 1995). While the origin of nanoparticles in PEBA is still a subject of discussion, the number and size of nanoparticles has been found to depend on background pressure, which, in turn, affects the beam fluence delivered to the target, and on beam accelerating voltage, which affects the penetration depth of the electrons in the target (Mathis and Christen, 2007). The nanoparticulates may also be formed in the plasma during the transit of ablated species from the target to the substrate (Nistor et al., 2008).

The surface morphology of CZO films has been investigated by AFM as a function of deposition temperature and accelerating voltage. Surface roughness plays an important role in determining various physico-chemical properties of the thin films (Yang et al., 1996). Figure 4.13 (a-h) shows typical AFM images of CZO thin films, whereby the findings do not indicate drastic variations in film roughness (average arithmetic roughness ranges between ~3 nm and ~10 nm for all films) as the deposition temperature increases from 350^{o}C to 450^{o}C at both accelerating voltage values. However, roughness increases substantially, viz., ~19 nm to ~23 nm, as the temperature is increased from 600^{o}C to 800^{o}C, respectively (see Table 4.2). Films deposited at temperatures between 350^{o}C and 450^{o}C and for both accelerating voltage values appear to have globules on top of a smooth surface, as revealed in Figures 4.12 and 4.13. This

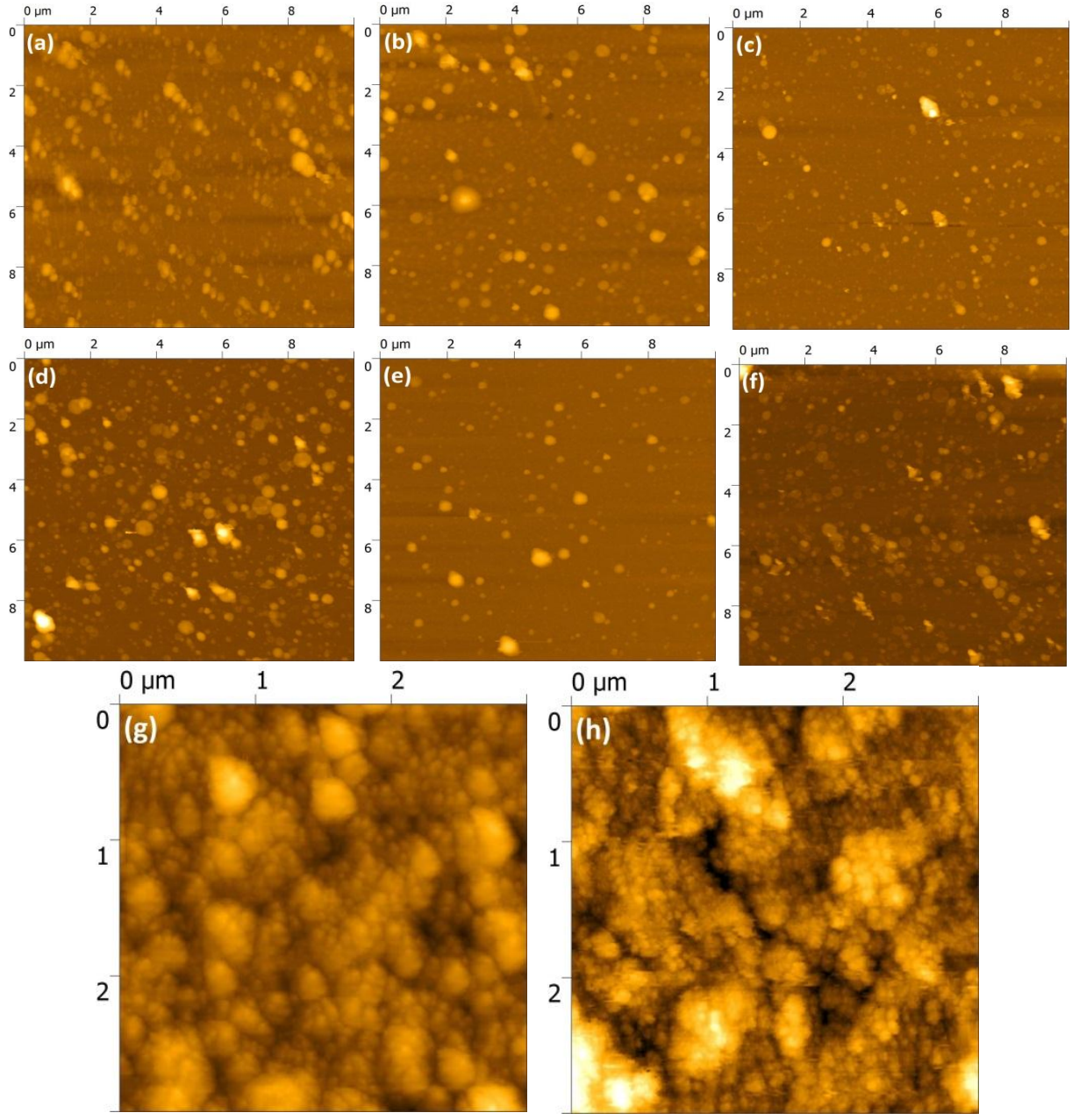

Figure 4.13: AFM topographic images of CZO films deposited on Si (100) substrates under argon as a function of accelerating voltage of 15 kV: (a) 350^{o}C, (b) 400^{o}C, (c) 450^{o}C, and 16 kV: (d) 350^{o}C, (e) 400^{o}C, (f) 450^{o}C, (g) 600^{o}C, and (h) 800^{o}C.

is akin to the Stranski-Krastanov growth model, i.e., single layer plus islands, albeit the thickness of the films in question is much larger than a single layer. The films deposited at higher

Table 4.2: Average arithmetic roughness (Ra, AFM) of CZO films deposited as a function of deposition temperature and accelerating voltage (AV). Bare substrate roughness: Ra = ~1 nm (Ali et al., 2017).

Temperature (^{o}C)	**AV (kV)**	**Ra (nm)**
350	15	7.38
400	15	5.91
450	15	3.91
350	16	8.71
400	16	3.02
450	16	10.2
600	16	19.01
800	16	22.90

temperature, i.e., 600^{o}C, show no smooth surface underneath the globules. The growth of these films appears to follow the Volmer-Weber model, i.e., from three dimensional islands. At 800^{o}C, film surface features seem to follow a different growth mode. The present AFM results are consistent with SEM measurements reported earlier.

4.3.4 Structure

The structure of the deposited films has been determined by XRD analysis using theta/2-theta Brag-Brentano configuration to generate 30^{o}-80^{o} diffractograms. Figure 4.14 shows XRD diffraction patterns of the films grown on Si (100) at an accelerating voltage of 16 kV. The two diffraction peaks, see Fig. 4.14-a, corresponding to 2Θ = 34.43^{o} (002) and 36.26^{o} (101) are indicative of the presence of ZnO in the films deposited at 400^{o}C-450^{o}C, whereas the film

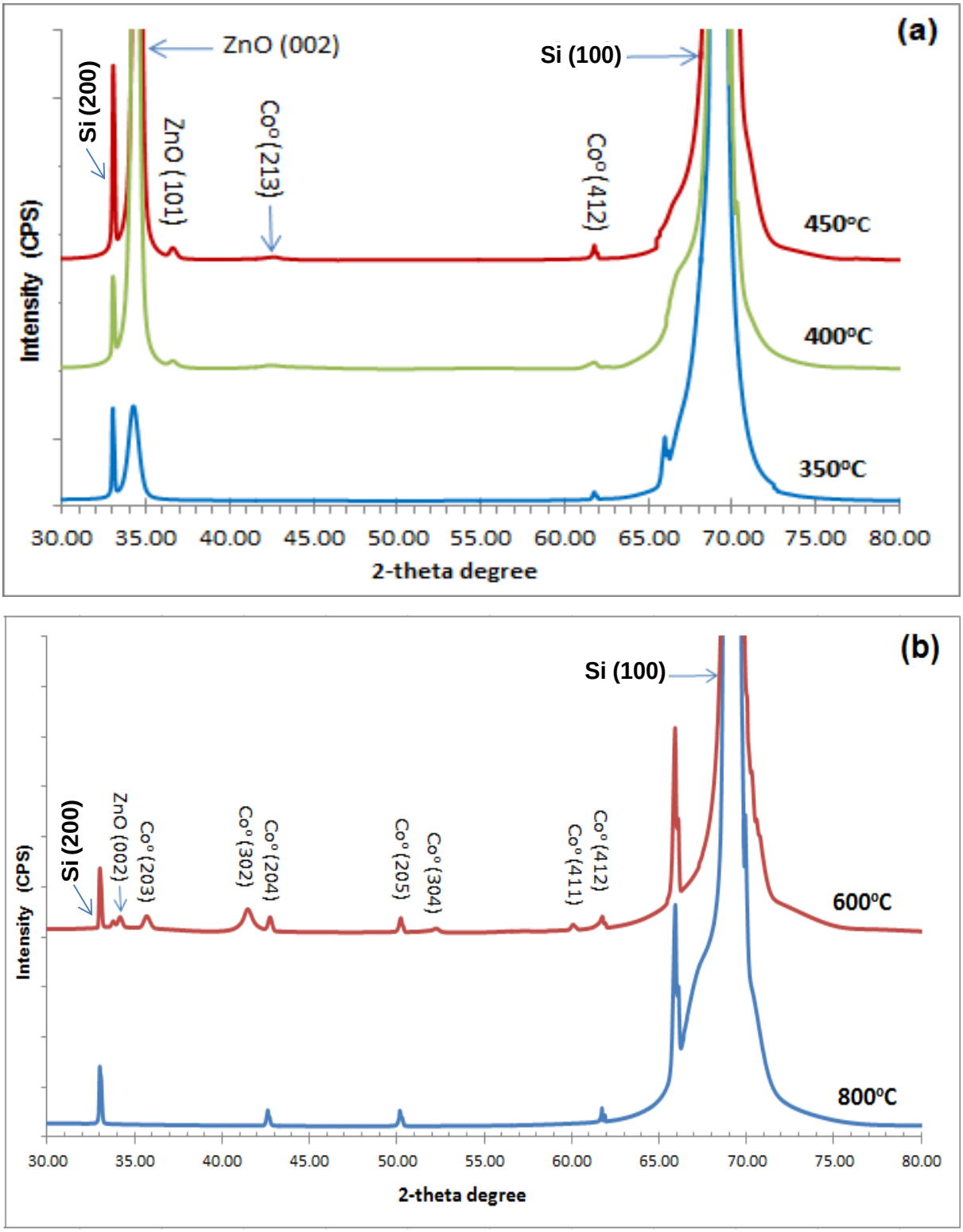

Figure 4.14: XRD patterns for CZO thin films deposited on Si (100) at an accelerating voltage of 16 kV and at (a) 350°C, 400 °C, 450°C, and at (b) 600°C and 800°C.

deposited at 350^{o}C shows one peak (002) only attributed to ZnO (PDF card no.: 01-070-8070). As temperature is increased from 350^{o}C to 450^{o}C, films are produced with conspicuous sharpness and intensity of the peak (002), i.e., c-plane orientation, as shown in Figure 4.14-a. From the latter figure, the structural analysis shows two peaks at 2Ɵ ~ 42.04^{o} (213) and ~61.7^{o}(412) attributed to hcp metallic Co (PDF card no.:01-070- 2633). Figure 4.14-b shows that films deposited at 600^{o}C consist of ZnO, albeit the intensity of the corresponding diffraction peak (002) is much smaller than in films deposited at lower temperatures. The cobalt phase in the same films is revealed through diffraction peaks at 2Ɵ ~ 35.7 (203), 41.4^{o} (302), 42.5^{o} (204), 50.1^{o} (205), 51.5^{o} (304), 59.6^{o} (411), and 61.7^{o} (412) corresponding to hcp metallic Co (PDF card no.:01-070-2633) (Hiu et al., 2002). Upon increasing the temperature to 800^{o}C, ZnO phase seems to disappear from the films, as shown in Fig. 4.14-b, and in accordance with EDX and XPS data. For films deposited at 800^{o}C, only three peaks have been detected that correspond to hcp metallic Co, viz., (204), (205) and (412).

4.4. Effect of beam frequency on structural and morphological characteristics of $Co_{0.2}Zn_{0.8}O$ thin films

In the third series of deposition experiments, $Co_xZn_{1-x}O$ (x = 0.20) thin films have been deposited on c-sapphire and Si (100) substrates. The films were grown from a single CZO target with 20 wt.% Co at various beam frequencies (1 Hz, 2 Hz, 4 Hz and 8 Hz). Other process parameters have been kept constant, viz., deposition temperature (450^{o}C), accelerating voltage (16 kV), target-substrate distance (5 cm), target-capillary tube tip distance(0.25 cm) and background gas (Ar) pressure (~3 mTorr) , see Chapter 3, see Table 3.2. The corresponding results and discussion are given next.

4.4.1 Chemical composition and chemical states

The compositional analysis, using EDX, of the films deposited at various beam frequencies is presented in Figure 4.15. Line scan (dark-green colored line ending with two blue circles) analysis (superimposed on SEM images in Figure 4.15) reveals the presence of O, Co and Zn in the films, and that the films consist of globules that are rich in Co and O. The more whitish the color of the globule is, the higher the cobalt concentration is relatively to oxygen concentration as shown in Figure 4.15-b. Point analysis performed by SEM-EDX confirms that deposition is nearly congruent (20±5%).

The near-surface chemical sataes in the films has been analyzed using XPS. Figure 4.16 depicts narrow scan XPS spectra of Co $2p_{3/2}$ peaks and their deconvolutions as a function of beam frequency. The data, as per Fig. 4.16, reveal that the peaks are well-fitted with the reported values of binding energies for Cobalt oxides and Co^{o}. The binding energy peak at 780.5 eV is assigned to Co^{+2} valence state (Ivill et al., 2008), and the small shoulder (peak) located at around778-779 eV is attributed to metallic Co (Co^{o}) (Peng et al., 2005; Tortosa et al., 2008).

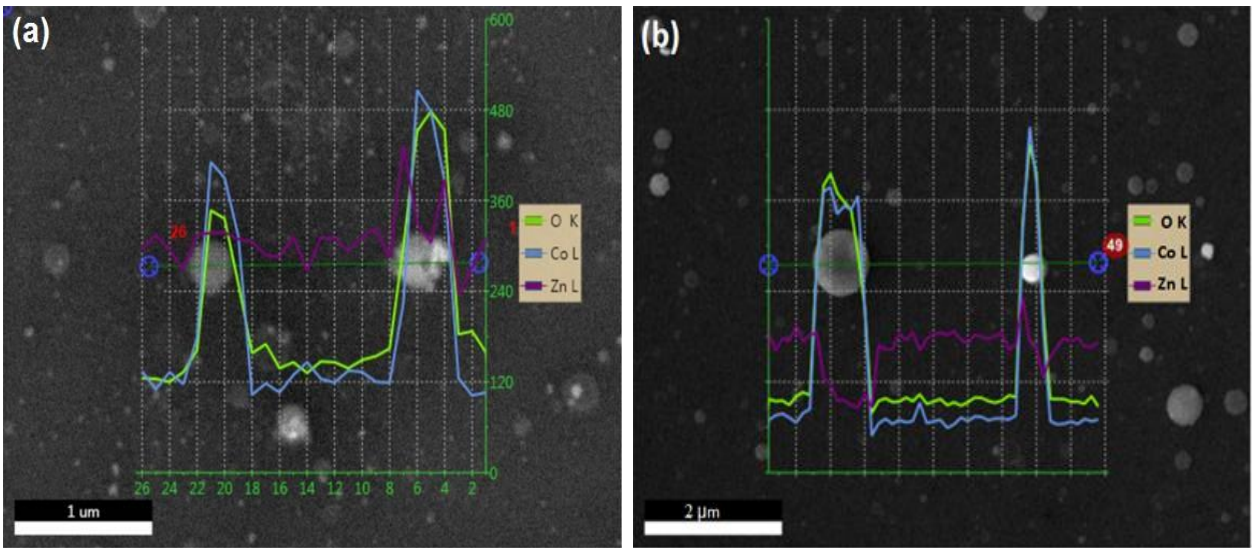

Figure 4.15: EDX line scans and their corresponding element profiles of the films deposited on Si at a beam frequency of (a) 1 Hz, (b) 8 Hz.

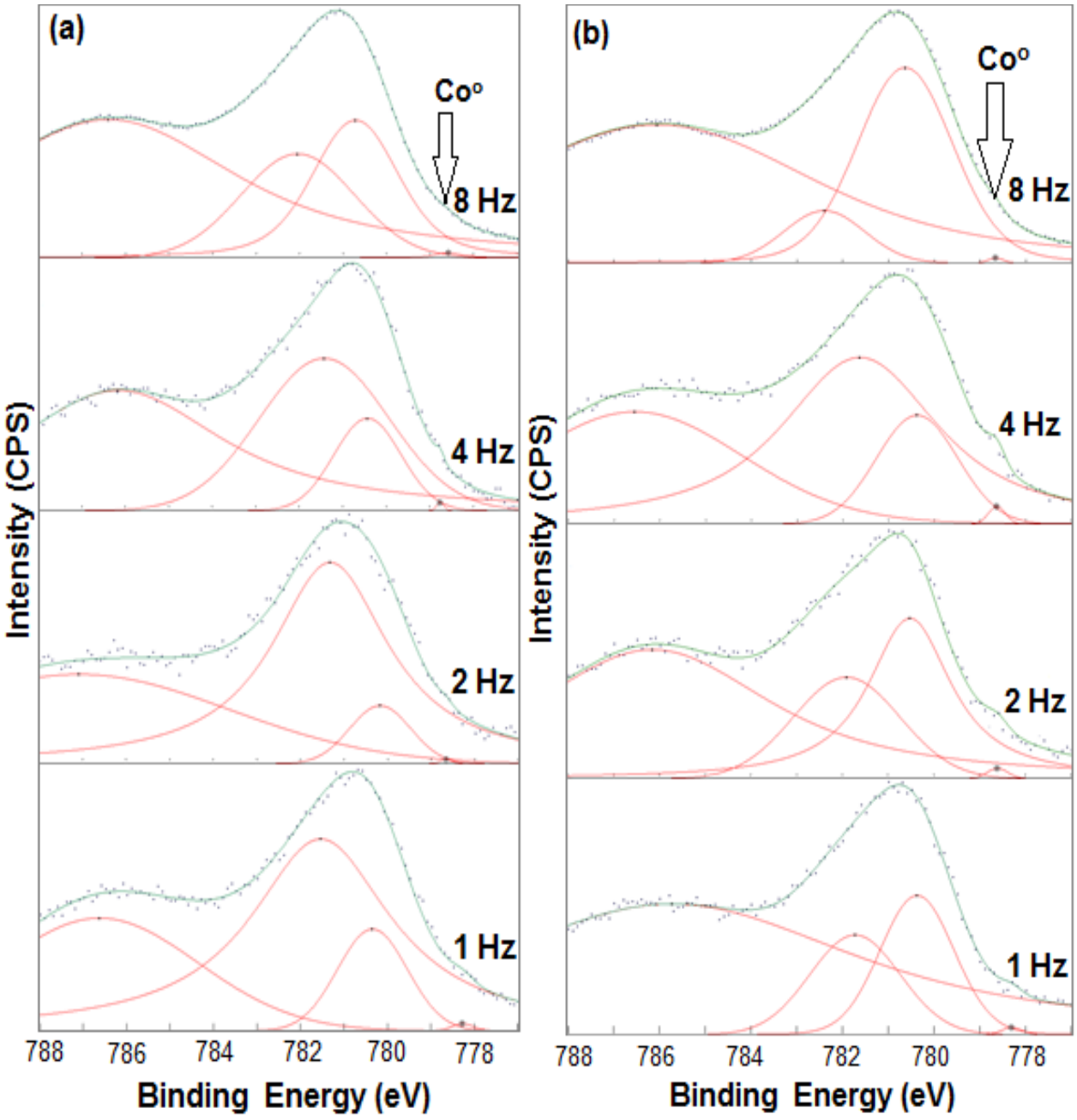

Figure 4.16: (a) Typical XPS narrow scan spectra of Co $2p_{3/2}$ peaks of the films deposited at various beam frequencies on (a) Si (100) and (b) sapphire (0001).

The peak at around 782.8-783.3 eV is attributed to Co^{+3} oxidation state (Zhou et al., 2008; Alveset al., 2017). The intensity ratio of Co^{+2} and Co^{+3} signals in the films changes because of the possibility of oxidation of Co^{+2} to Co^{+3}. The exact nature of the cobalt defect in the structure

cannot be unequivocally determined with XPS measurements (Zhou et al., 2008). The data indicate that a substantial portion of Co atoms are present in the films in +2 and +3 valence states. The beam frequency does not seem to strongly affect Co^{o} concentration in the films, but rather only marginally.

4.4.2 Film thickness

Figure 4.17(a-d) shows transversal cross-sectional SEM images of the deposited films on Si (100). As can be observed, the beam frequency affects the average film thickness, which increases as the beam frequency is increased, viz., 26 nm (1 Hz), 59 nm (2 Hz), 67 nm (4 Hz), 130 nm (8 Hz). Figure 4.18 depicts thickness measurement data, using VRS, of film deposited on Si at a frequency of 8 Hz. The red curve is the measured reflectance response of the film, whereas the blue curve is the calculated counterpart. The thickness is indirectly measured through the minimization of the difference between measured and calculated reflectance responses of the film by means of a modified Marquardt-Levenberg scheme. The estimated thickness (131 nm) as per VRS, is in good accordance with the average thickness (~130 nm) measured from SEM analysis, as shown in Fig. 4.17 (d). Film thickness has been averaged over 10 different points along SEM transversal cross section for each sample. A similar thickness trend has been observed for the films deposited on c-sapphire under the same deposition conditions in this study. This can be explained in terms of the time interval between two successive pulses hitting the target surface. At a high pulse frequency, the time interval between two pulses is shorter than at low pulse frequency, and, accordingly, the target is cooled down, between two consecutive pulses, less than at low frequency (where the time between two energy pulses is larger). In this case, i.e., at high frequency, heat accumulation in the target is increased resulting in lower ablation threshold at the next pulse. Accordingly, target heating by the next pulse starts at a higher temperature at a high repetition rate. Higher target ablation rate, higher

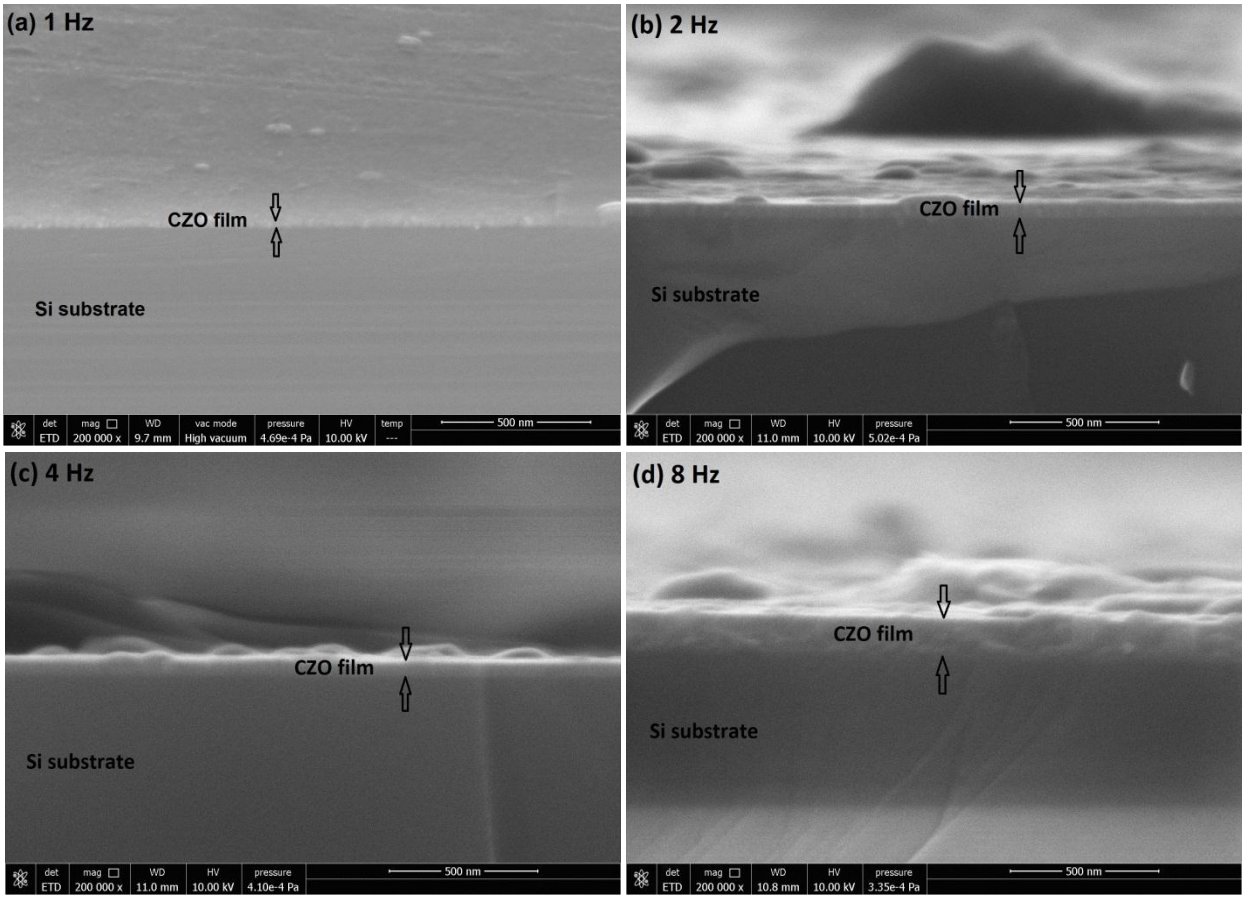

Figure 4.17: SEM cross-sectional images of CZO grown on Si at (a) 1Hz, (b) 2 Hz, (c) 4 Hz, and (d) 8 Hz.

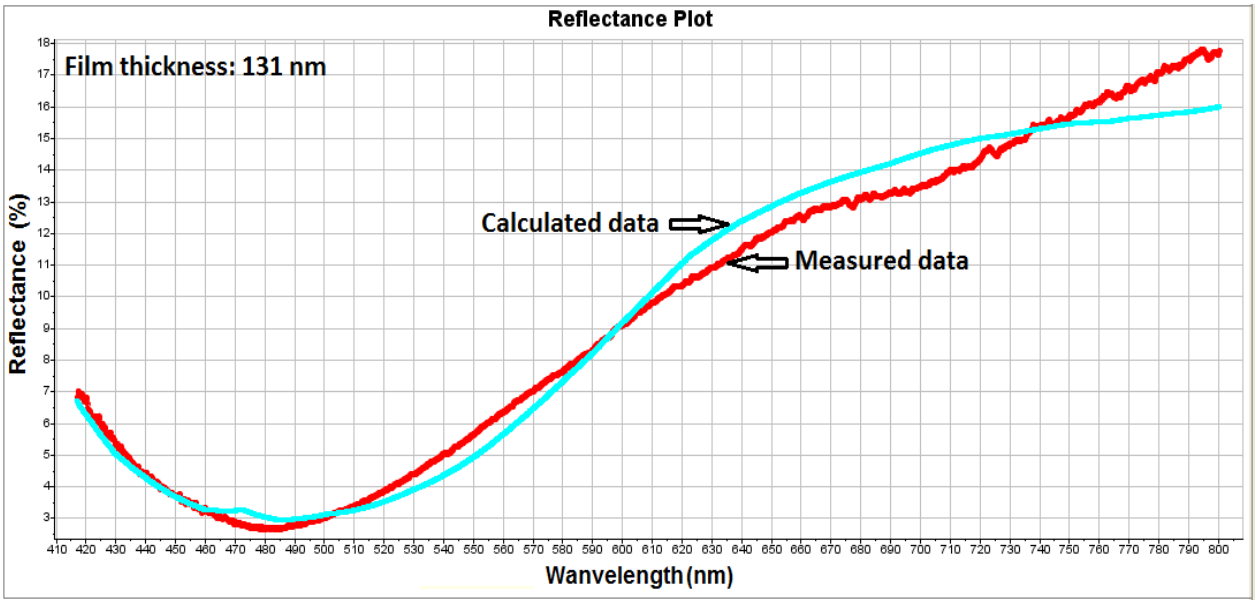

Figure 4.18: Visible reflectance spectroscopic measurements of the film deposited on Si at 8 Hz.

deposition rate and thicker films will ensue at a high beam frequency (Vanalakar et al., 2016).

4.4.3 Morphology

Figure 4.19 shows surface morphology of CZO films grown on Si at different beam frequencies as per SEM analysis. Various beam frequencies viz., 1Hz, 2Hz, 4 Hz and 8 Hz do not seem to have any effect on the film growth mode. Based on SEM observations, the growth of CZO films seem to follow the Stranski-Krastanov (S-K) growth model, i.e., layer plus islands. When the depositing atoms bond to the substrate relatively to bonding to one another, the deposited film follows the S-K growth mode as shown in Figure 4.19 (a-d).The beam frequency significantly affects the globule size of the deposited films. The data reveal that the average globules size is nearly 45 nm (1 Hz), 103 nm (2 Hz), 166 nm (4 Hz), and 115 nm (8 Hz) on silicon, and 78 nm (1 Hz), 112 nm (2 Hz), 137 nm (4 Hz), and 113 nm (8 Hz) on c-sapphire. The average globule density (relatively to same film area) is nearly 128 (1Hz), 54 (2 Hz), 20 (4 Hz), and 60 (8 Hz) on silicon, and 94 (1Hz), 69 (2 Hz), 28 (4 Hz), and 34 (8Hz) on c-sapphire. The observed dependence of globule size (and density) on beam frequency can be explained by considering the processes of nucleation, surface diffusion of adatoms and metal clustering by coalescence (Ohring, 2002). On the one hand, as beam frequency is increased, the number of atoms arriving onto the substrate surface increases, which eventually coalesce to form large-size globules by ripening of the smaller globules with the addition of more atoms either from the vapor phase (plasma) or by surface diffusion of neighboring atoms (Semaltianos, 2001). On the other hand, the adatoms can interact strongly with each other by chemisorption at high beam frequency (high deposition rate) with very little surface migration, which leads to a decrease in globule size similar to low beam frequency. Therefore, 4 Hz seems to be a critical beam frequency as it corresponds to the maximum(minimum) globule size (density).

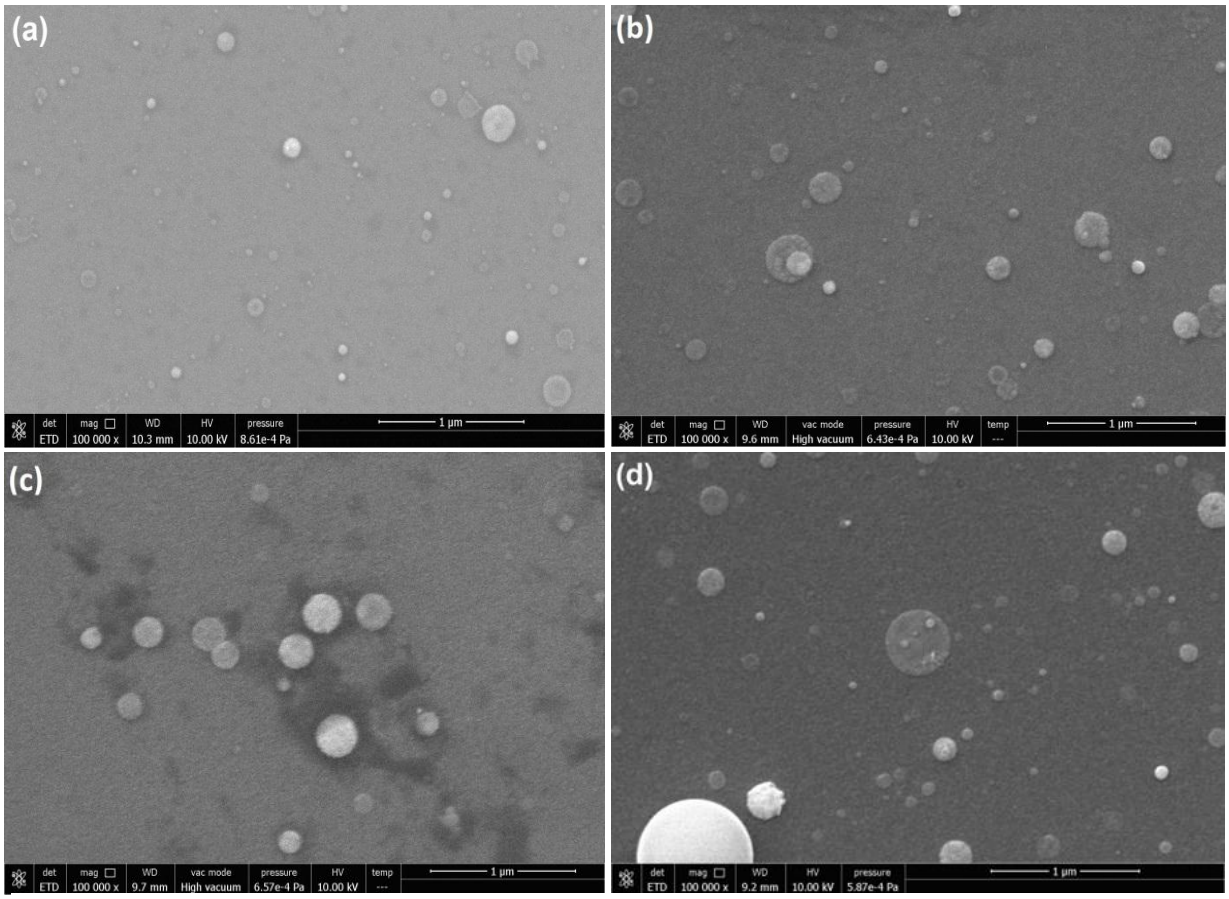

Figure 4.19: SEM surface images of CZO films deposited on Si (100) substrates at (a) 1 Hz, (b) 2 Hz, (c) 4 Hz, and (d) 8 Hz.

Figures 4.20 and 4.21 depict AFM topographic images of the films deposited on silicon and c-sapphire, respectively. Film roughness, based on arithmetic average value determined from AFM measurements, has been assessed as a function of beam frequency. The data reveal that as the frequency is increased, film roughness increases, i.e., nearly 2 nm (1 Hz), 4 nm (2 Hz), 6 nm (4 Hz), and 8 nm (8 Hz) on c-sapphire, and 1 nm (1 Hz), 8 nm (2 Hz), 8 nm (4 Hz), and 10 nm (8 Hz) on Si. At high beam frequency, i.e., high deposition rate, the density of nuclei on the substrate is higher, and the number of nuclei that coalesce to form large-size globules is higher resulting in higher film roughness (Semaltianos, 2001). Film roughening has also been reported to be caused by statistical fluctuations of the vapor flux impinging on the substrate during

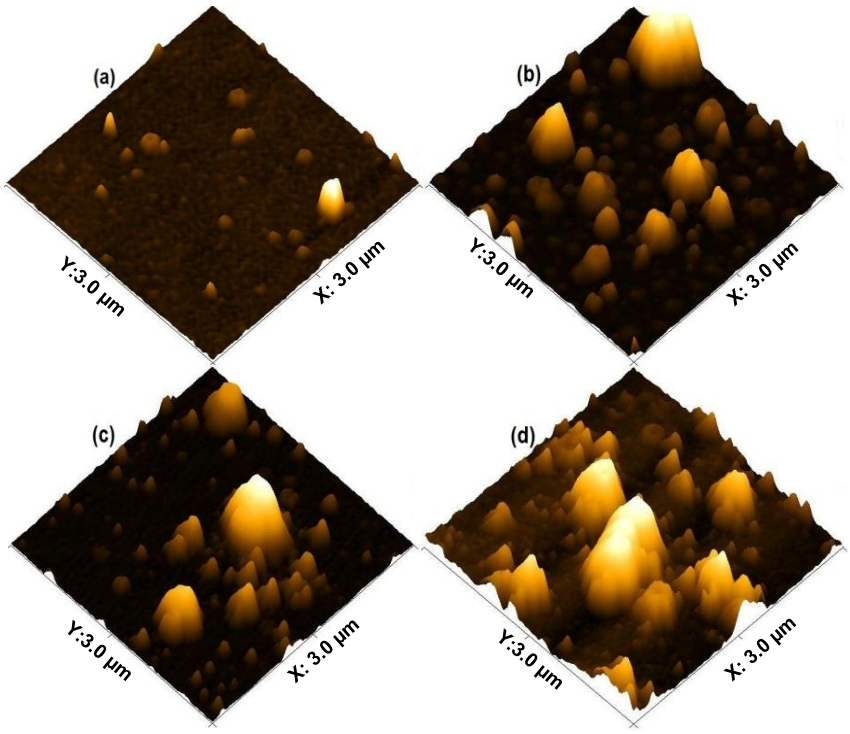

Figure 4.20: Topographs of films deposited on Si (100) at (a) 1 Hz, (b) 2 Hz, (c) 4 Hz, (d) 8 Hz.

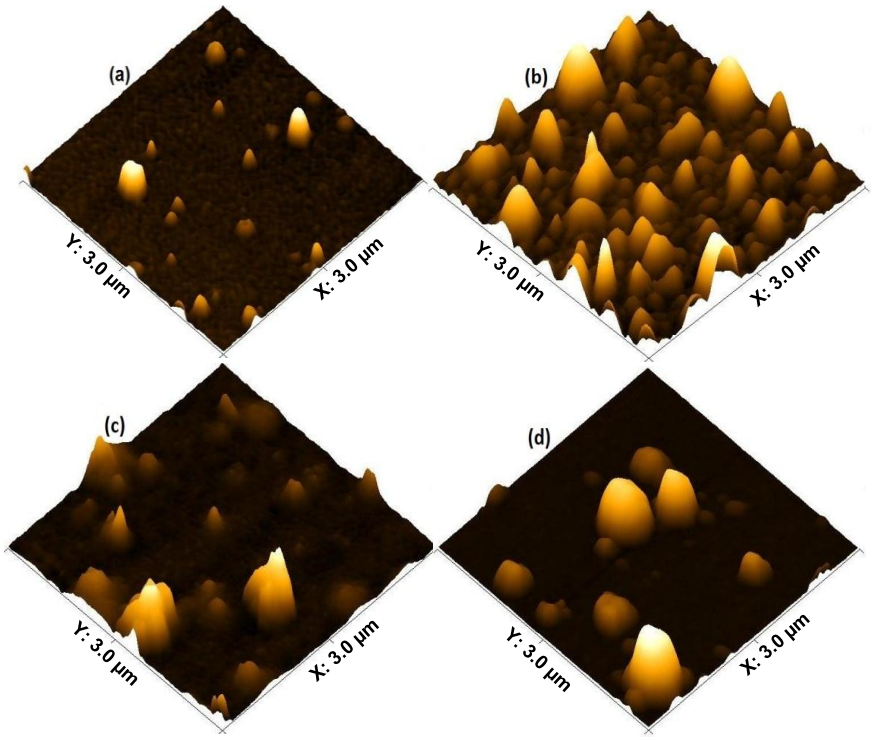

Figure 4.21: Topographs of films deposited on c-sapphire at (a) 1 Hz, (b) 2 Hz, (c) 4 Hz, (d) 8 Hz.

deposition (Zangwill, 1996). This phenomenon is likely to yield high film roughness with the increase in film thickness.

4.4.4 Structure

Figure 4.22 shows XRD patterns of the film deposited on Si (100) at beam frequencies of 1 Hz and 8 Hz. The characteristic peak of ZnO hexagonal wurtzite structure (002) can be observed at 2Θ ~34.43° for the film deposited at 1Hz, and the film deposited at a beam frequency of 8 Hz exhibits an additional peak (101) for ZnO at 2Θ ~36.26° (PDF card no.: 01-070-8070). One can notice that the film deposited at a beam frequency of 8 Hz has a higher and sharper diffraction peak at ~34.43°, indicating an improvement in (002) plane intensity relatively to the film deposited at low beam frequency, viz., 1 Hz. Thus, at higher beam frequency (8 Hz), the

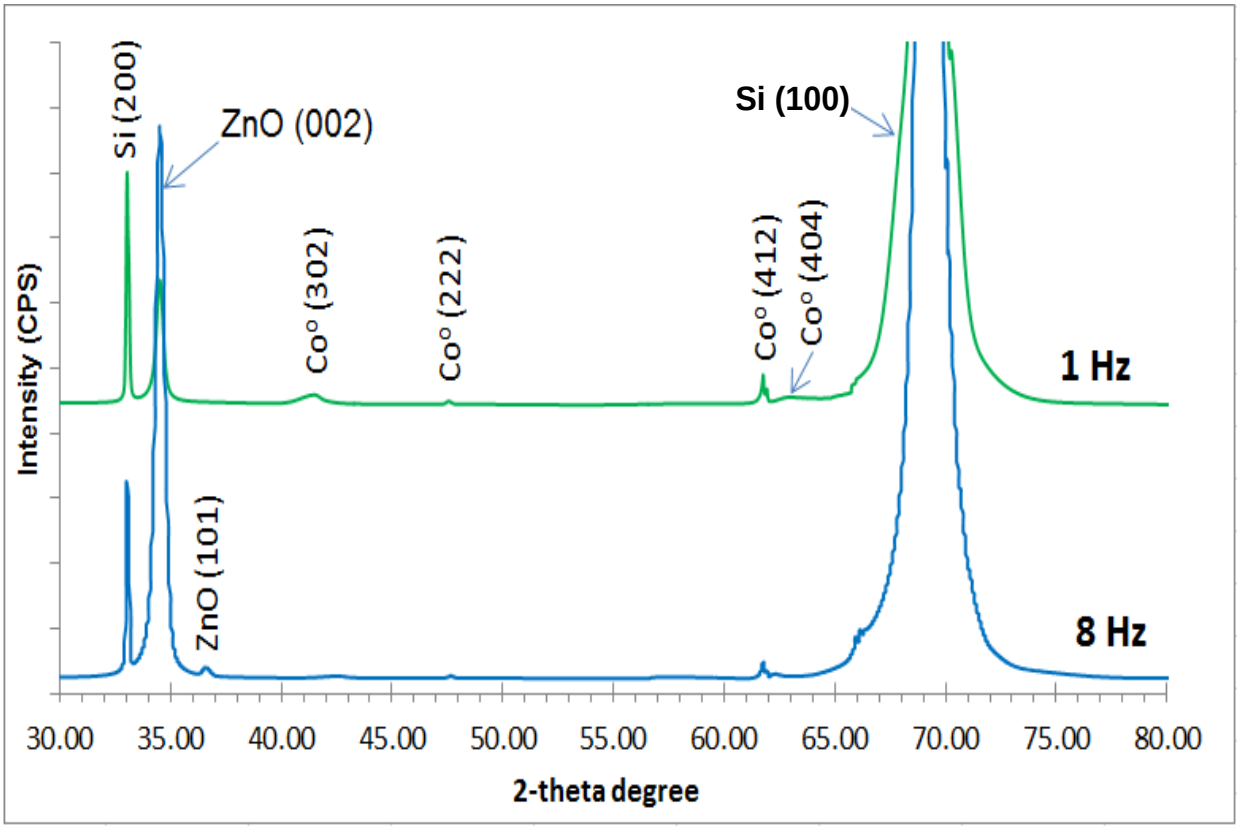

Figure 4.22: XRD patterns of films deposited on Si at beam frequencies of 1 Hz and 8 Hz.

sharper diffraction and higher intensity of the peak (002) correspond to higher degree of crystallinity in CZO film (Benramache et al., 2012; Prepelita et al., 2010). The beam frequency does not appear to affect Co hcp phase content in the films, which is in accordance with the findings of XPS measurements. The data, see Figure 4.21, reveal four diffraction peaks attributed to metallic Co at around $2\Theta = 41.6^{o}$, 47.1^{o}, 61.7^{o} and 62.6^{o}. The presence of theses peaks, viz., (302), (222), (412) and (404), agrees best with what is anticipated for hcp metallic Co (PDF card no.: 01-070-2633) (Hiu, et al., 2002). Diffraction peaks of CoO phase, which correspond to $2\Theta = 34.1^{o}$ (111), 68.31^{o} (311) and 71.8^{o} (222) (PDF card no.: 01-075-0419), are not readily visible in the diffraction patterns shown in Figure 4.21. The most likely reason for this is that these peaks overlap with some of the strong peaks attributed to ZnO, viz., plane (002), and Si, viz., plane (400). The experimental data hint at the potential of the deposited films as a model nano-catalyst in many chemical processes.

4.5 Effect of substrate materials on the properties of Cobalt-Doped Zinc Oxide thin films

In the fourth series of deposition experiments, we report on the deposition of $Co_xZn_{1-x}O$ ($x = 0.20$) thin film nano-catalysts on four different substrates, namely, Al_2O_3 (c-sapphire), silicon (100) (Si), SiO_2 (quartz) and pyrex. During deposition, the temperature ($450^{o}C$), accelerating voltage (16 kV), beam frequency (2 Hz), and background argon (Ar) pressure (~3 mTorr = 0.4 Pa) were kept constant, see Chapter 3, Table 3.2. The corresponding results and discussion are given next.

4.5.1 Chemical composition and chemical states

The near surface chemical composition of the films has been assessed by XPS. Figure 4.23 shows survey scans of the films grown on different substrates. Survey spectra have been

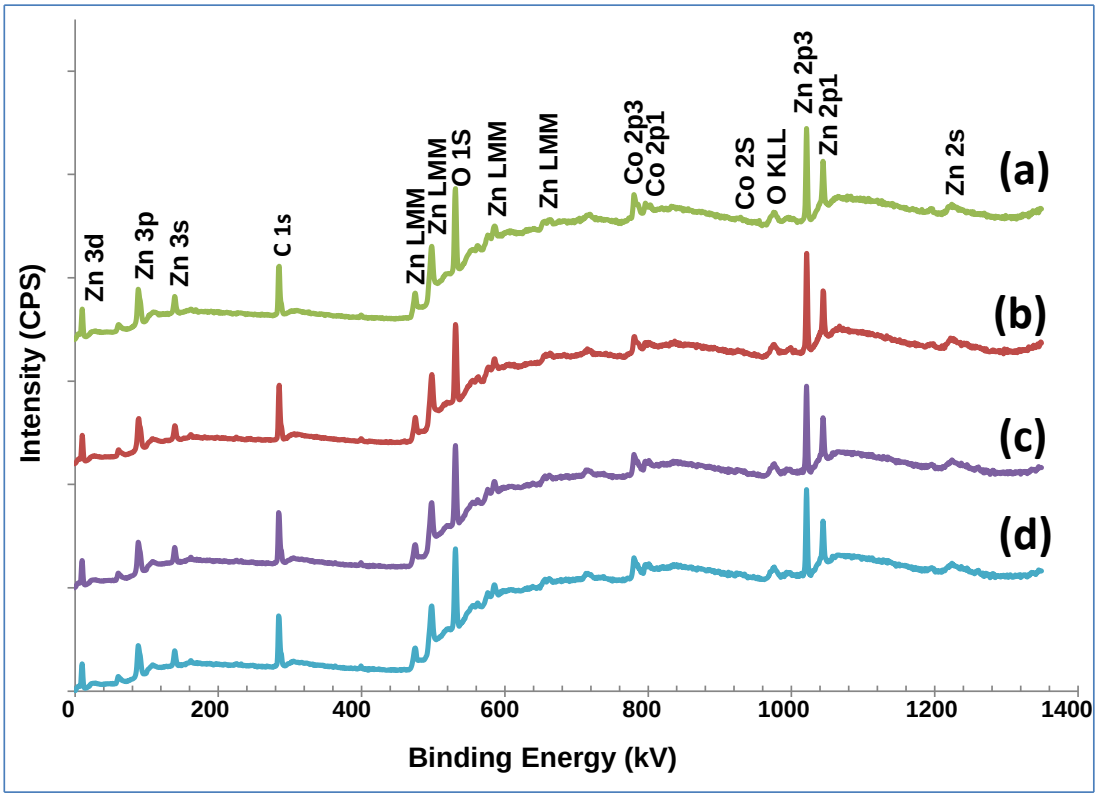

Figure 4.23: XPS spectra of films deposited on (a) c-sapphire, (b) quartz, (c) Si and (d) pyrex.

acquired in a high-pass energy and low point-density scanned mode. The high-pass energy, in this case, has been used to maximize the sensitivity of the instrument in order to get information about the surface species. The binding energy peaks in the scans confirm the presence of Co, Zn and O in the films. The scans do not show any noticeable differences between the films deposited on crystalline (c-sapphire, quartz, Si) and amorphous (pyrex) substrates as per Figures 4.23(a), 4.23(b), 4.23(c) and 4.23(d) respectively. Since XPS is an efficient technique that elucidates the secondary phases near the surface of thin films, Figure 4.24(a-d) shows high resolution XPS Co $2p_{3/2}$ spectra (and their deconvolution). The latter have been acquired in low-pass energy (i.e., high-energy resolution) mode with a high point density on the energy axis (0.1 eV). The high-energy resolution is essential in drawing conclusions on the chemical state

information of Co-ZnO thin films. The deconvoluted Co $2p_{3/2}$ spectra indicate that cobalt is present in three valence states, i.e., Co^{o}, Co^{2+} and Co^{3+} in the deposited films. The Co $2p_{3/2}$ peak at the binding energy around 780.5 eV is associated with oxidized Co (Co-O bonding) that is incorporated into ZnO structure in Co^{2+} valence state configuration (Ivill et al., 2008). The smaller shoulder (peak) at the lower binding energy side at around 778–779 eV is attributed to metallic Co (Co-Co bonding), which is neither oxidized nor incorporated into ZnO structure (Peng et al., 2005; Tortosa et al., 2008). The peak at around 782.8-783.3 eV is attributed to Co^{3+} oxidation state (Zhou et al., 2008; Alves et al., 2017). The intensity ratio of Co^{2+} and Co^{3+} signals in the films changes because of the possibility of oxidation of Co^{2+} to Co^{3+}. The exact nature of the cobalt defect in the structure cannot be unequivocally determined with XPS measurements (Zhou et al., 2008). The data indicate that a substantial fraction of Co atoms are present in the films in +2 and +3 valence states. The formation of metallic Co in Co-ZnO films could be attributed to the presence of oxygen vacancies in ZnO wurtzite structure or to smaller incorporation of oxygen during film growth (Tortosa et al., 20008).

As per EDX analysis, these nano-globules exhibit substantially higher Co content relatively to the film matrix. Quantitative EDX point analysis indicates that the deposited films are congruent with a composition close to that of the target material (20 ± 5% Co).

4.5.2 Film thickness

From VRS measurements, the thickness of the films is ~ 62 nm under the same deposition conditions. Figure 4.25 shows a typical reflectance response obtained from visible spectroscopy of Co-ZnO films deposited on c-sapphire. Film thickness is indirectly measured by means of a modified Marquardt - Levenberg built - in algorithm through minimization of the difference between measured and predicted data. The measured and calculated data are well fitted, and any

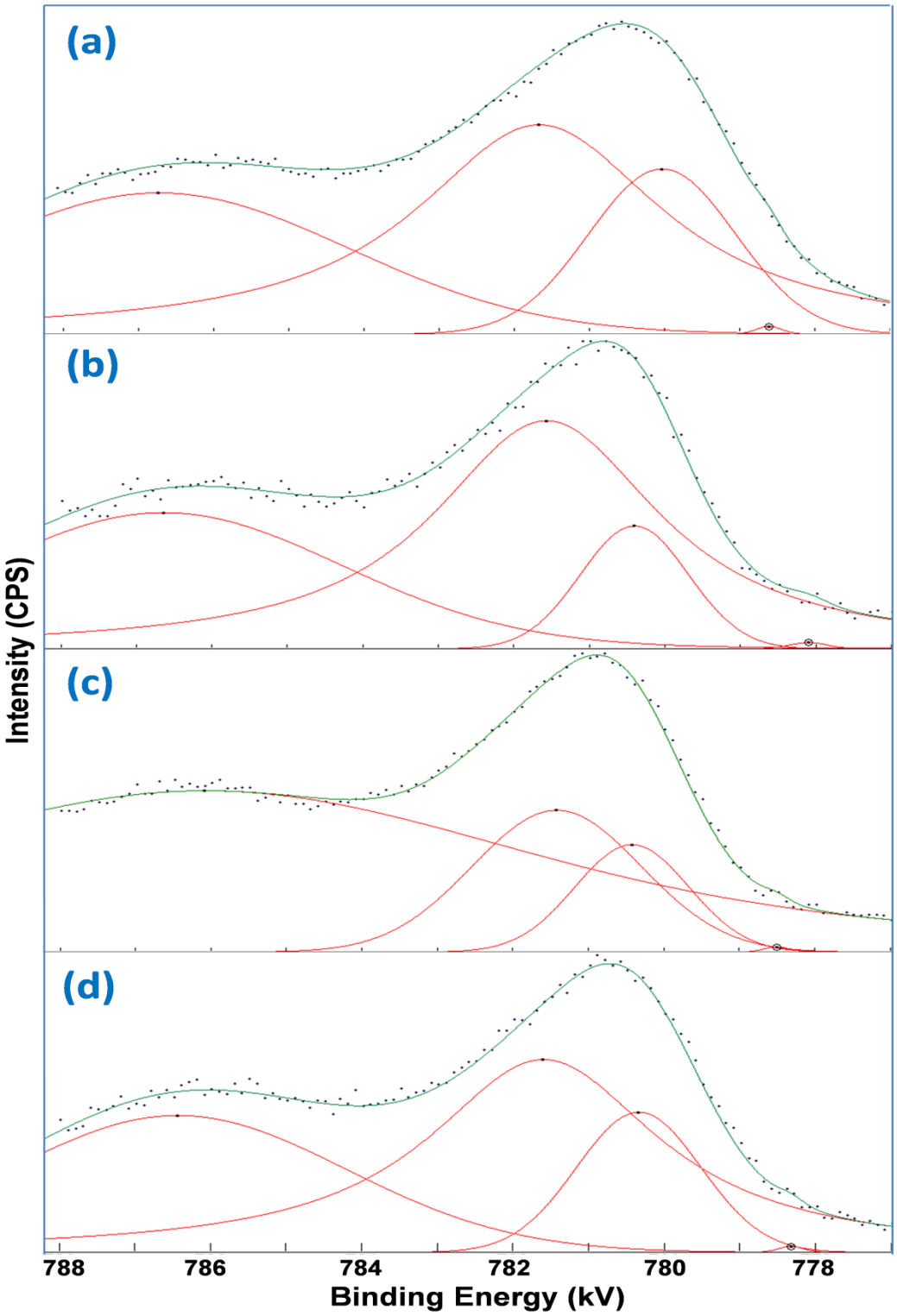

Figure 4.24: XPS chemical binding spectra of Co $2p_{3/2}$ peaks (and their deconvolution) of Co-ZnO films grown on (a) c-sapphire, (b) quartz, (c) silicon and (d) pyrex.

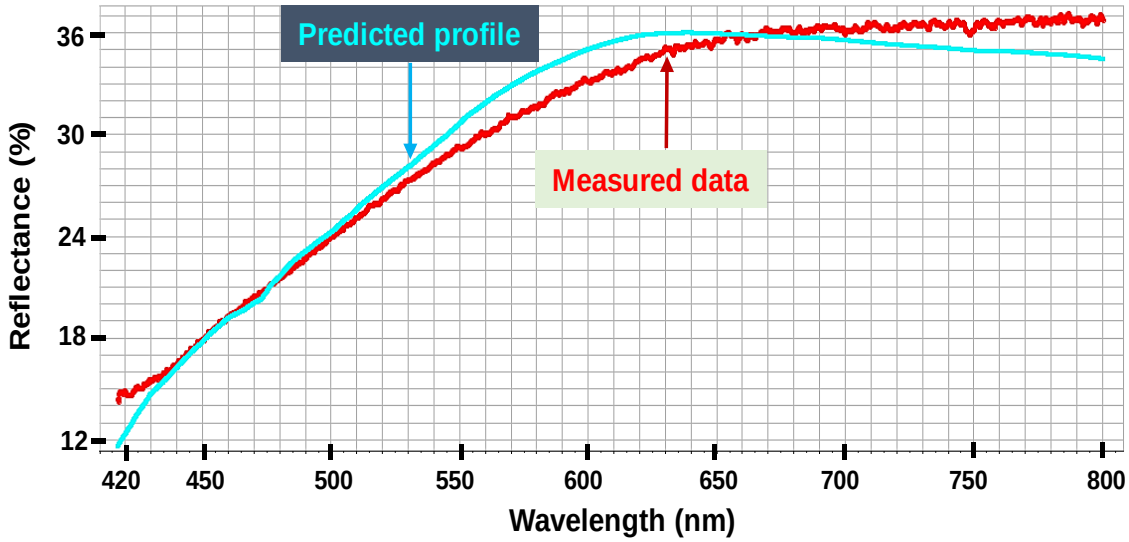

Figure 4.25: Typical Visible reflectance response of film deposited on Co-ZnO/Al_2O_3 catalyst.

discrepancies are most likely due to uncertainties in the film optical properties used as input to the algorithm.

4.5.3 Morphology

Figure 4.26 shows SEM images of Co-ZnO thin films deposited on various substrates. It can be clearly observed that the films consist of nano-sized globules, which are uniformly dispersed on the surface and whose size is in the range of ~ 20 nm-400 nm. A closer inspection of the nano-globules, as per the magnified square sections in Figure 4.26 (a-d), reveals that the latter consist of smaller (primitive) nano-particulates. The type of substrate does not seem to affect the size, shape and density of the nano-globules. The formation of these nano-globules depends on kinetic aspects, such as deposition flux, nucleation rate, and surface diffusion of neighboring atoms, in addition to thermodynamic factors, which require a decrease in the Gibbs free energy to form a solid. Based on SEM observations, the growth of Co-ZnO films on the four substrates seems to follow the Stranski-Krastanov (S-K) growth model, i.e., layer plus islands (see Figure 4.26, a-d). In S-K model, a few layers initially grow as the result of a large decrease

in Gibbs free energy when the depositing atoms bond to the substrate instead of bonding to one another and provided surface diffusion is fast. Due to lattice mismatch between the film and substrate, a build-up of strain causes the formation of 3D islands (nano-sized globules) on top of the initial layer to relax the strain. The formation of nanoparticulates is highly desirable to confer potential catalytic properties to Co-ZnO film nanocomposites. Particle size distribution is depicted in Figure 4.27 for the films deposited on the different substrates. The particle size has been directly measured on SEM images shown in Figure 4.26(a-d). The data

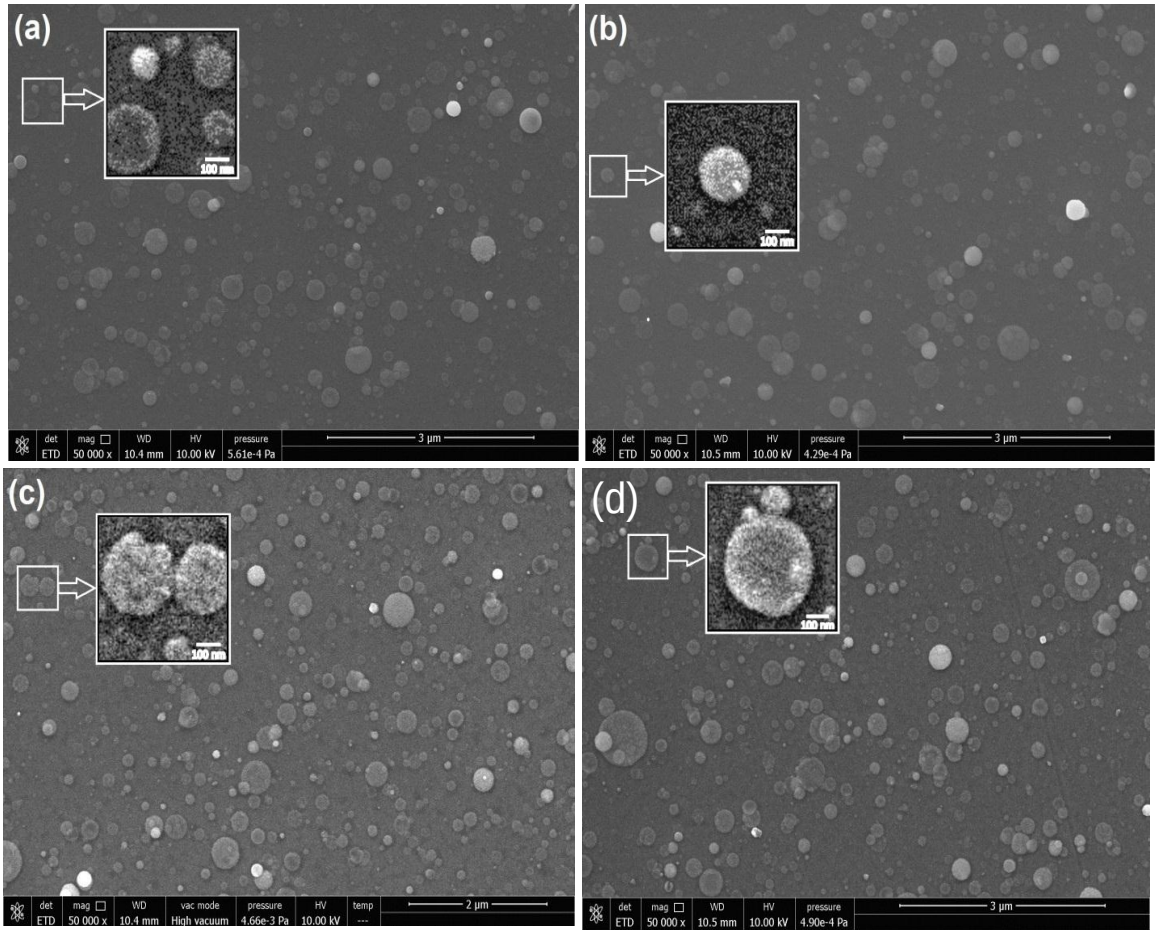

Figure 4.26: SEM images of Co-ZnO thin films deposited on different substrates: (a) Co-ZnO/pyrex, (b) Co-ZnO/SiO_2, (c) Co-ZnO/Al_2O_3 and (d) Si. Square areas are zoomed in and shown in the inset.

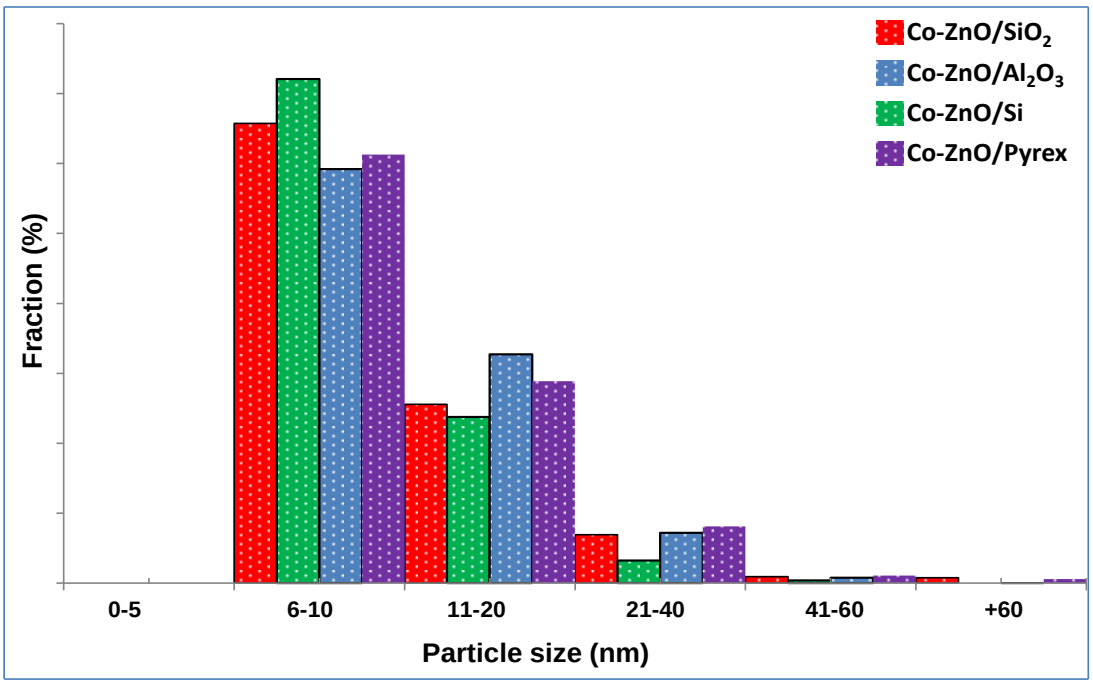

Figure 4.27: Particle size distribution of Co-ZnO films measured directly on SEM images shown in Figure 4.26(a-d).

reveal that the type of substrate has no significant effect on particle size distribution with the most frequent particle size in the range of 6-10 nm. The average particle size (relative to the same film area) on Si, quartz, c-sapphire and pyrex is nearly 10.8 nm, 11.1 nm, 9.5 nm and 11.3 nm respectively.

Film surface morphology and roughness have been characterized by AFM in contact mode over a scan area of 5 x 5 μm^2. The surface topography and roughness of Co-ZnO thin film nano-composites are important properties for catalytic applications, as they affect the physico-chemical properties of the films (Yildirim et al., 2016). AFM (2D and 3D) scans of surface morphology of Co-ZnO films on various substrates are shown in Figure 4.28. The bare substrates (not shown here) are very smooth with an average arithmetic roughness (Ra) of less than 1 nm. The data reveal that Ra of the films on pyrex, quartz, c-sapphire and Si is nearly 5.9 nm, 5.9 nm7.9 nm and 3.9 nm, as per Figures 4.28 (a), 4.28 (b), 4.28 (c) and 4.28 (d), respectively. AFM

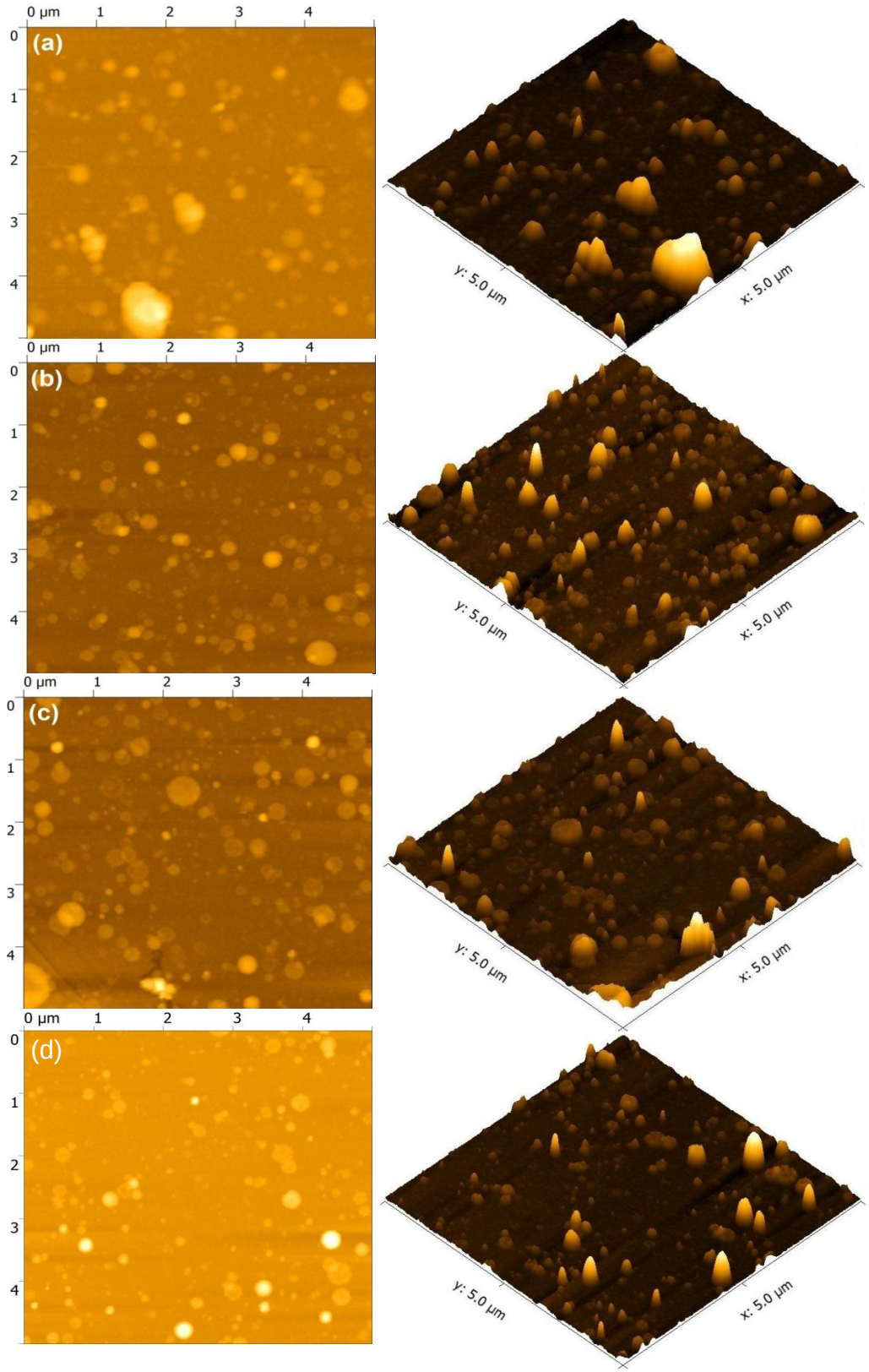

Figure 4.28: AFM images (2D, 3D) of films deposited on various substrates: (a) pyrex, (b) quartz, (c) c-sapphire and (d) Si.

images (Figure 4.28) reveal that Co-ZnO films consist of nano-globules that are well isolated from each other. These Co rich nano-particulates, when well distributed on the film surface that consists largely of ZnO, might be more favorable for exothermic reactions. Since FTS is a highly exothermic reaction, its potential to cause sintering for Co-based catalyst is relatively high (Tsakoumis et al., 2010). The matrix between these Co-rich nano-globules, however, may be useful in dissipating the heat released during FTS and in preventing the nano-catalyst from sintering, a process that results in potential catalyst deactivation.

4.5.4 Structure

The crystalline structure of the films has been determined by XRD analysis using theta/2-theta Brag-Brentano configuration. Figure 4.29 shows XRD patterns of Co-ZnO films deposited on Si, quartz, c-sapphire and pyrex substrates. The diffraction patterns of the films deposited on crystalline substrates (Si, Al_2O_3, SiO_2) show strong peaks corresponding to the respective substrate, i.e., the peak at $2\Theta \approx 69.14^o$ (100), see Figure 4.29-a, corresponding to Si (Hullavarad et al., 2009), the peak at $2\Theta \approx 41.68^o$ (0001), as shown in Figure 4.29-b, attributed to c-sapphire (Sbrockeya et al., 2012), and the peaks at $2\Theta \approx 49.58^o$ (112) and 69.75^o (202), see Figure 4.29-c, which are assigned to quartz (PDF card no: 00-011-0252). Three diffraction peaks, see Figure 4.29(a-d), corresponding to $2\Theta = 34.43^o$ (002), 36.26^o (101), and 72.6^o (004) are indicative of the presence of ZnO in Co-ZnO films (PDF card no. 01-070-8070). The sharp and intense diffraction peak (002) reveals that the deposited films have a preferential c-axis orientation. The structural analysis of the films deposited on Si, as shown in Figure 4.29-a, reveals three peaks corresponding to $2\Theta \approx 42.04^o$ (213), 61.7^o (412), and 77.03 (208) and attributed to hcp metallic Co (PDF card no. 01-070-2633). Two peaks associated with metallic Co appear at $2\Theta \approx 64.30^o$ (315) and 79.78^o (317) for films deposited on c-sapphire, while films deposited on quartz show

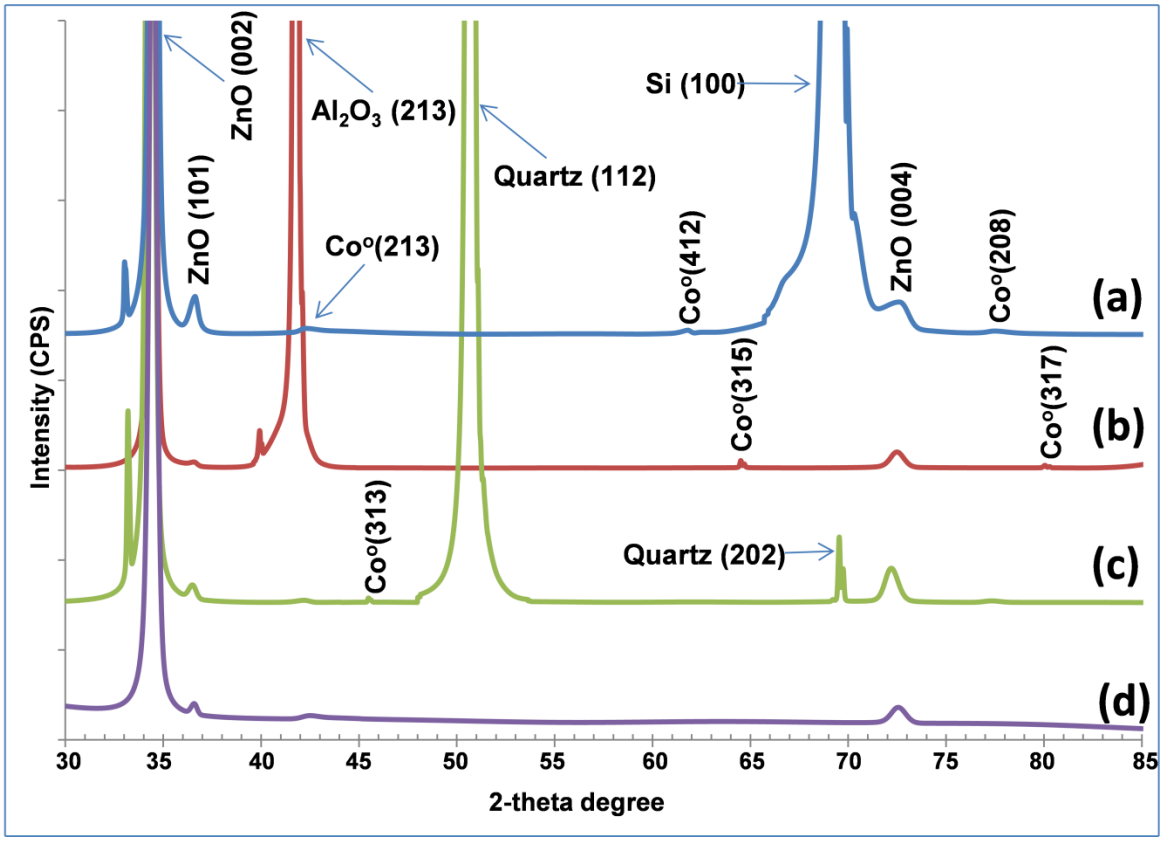

Figure 4.29: XRD patterns of CZO film deposited on (a) Si, (b) c-sapphire, (c) quartz, and (d) pyrex.

three reflections along the peaks corresponding to $2\Theta \approx 42.04^{o}$ (213), 45.53^{o} (310), and 77.03^{o} (208), which are indicative of the presence of hcp metallic Co in the film, as shown in Figure 4.29 (b, c). The diffraction pattern of the film deposited on pyrex shows only one peak corresponding to $2\Theta \approx 42.04^{o}$ (213) which reveals the presence of hcp metallic Co in the film (see Figure 4.29-d). The data indicate that CZO films deposited on crystalline substrates, viz., Si, c-sapphire and quartz, contain a higher metallic Co content relatively to the films deposited on amorphous pyrex substrate.

Chapter 5: Effect of post-processing on film properties

5.1 Introduction

In this chapter, as-grown $Co_xZn_{1-x}O$ (x = 0.20) thin-film NCs have been deposited on Si(100) substrate within the temperature range 350°C-450°C, at electron beam acceleration voltages of 15 kV and 16 kV and beam frequency of 4 Hz. The films have been subjected to heat treatment (post-processing) at either 400°C or 600°C for one hour. The corresponding results and discussion are given in the next sections in terms of chemical composition, chemical state, surface morphology and crystal structure.

5.1.1 Chemical composition and chemical states

The compositional analysis of CZO films has been obtained from EDX measurements and is presented in Figure 5.1. EDX line scan analysis (along the dark green line between two blue circles), superimposed on the respective SEM image, reveals the presence of Co, O and Zn in the films. It is worth noting that the films consist of nano-globules that are rich in Co (blue line) content, whereas Zn (purple line) is uniformly distributed throughout the films. The data reveal that annealing of as-grown CZO films under reduced oxygen pressure leads to a remarkable increase in oxygen content (green line) in the films, particularly for the films annealed at higher temperature (600°C), as shown in Figure 5.1-c. Point analysis by EDX shows that the nearly congruent films consist of Co-rich globules containing ~15-70 wt.% Co. The more whitish the color of the globule is, the higher the cobalt concentration is, as shown in Figure 5.1(a-c), which also confirms the unevenness of Co distribution in the film. The chemical state of Co in CZO films has been assessed by XPS. Figure 5.2 shows survey scans of as-grown films at 450°C and 16 kV, and the same films annealed at 400°C and 600°C. Survey spectra have been acquired in a high pass energy and low point-density scanned mode. The high-pass energy in this case is used

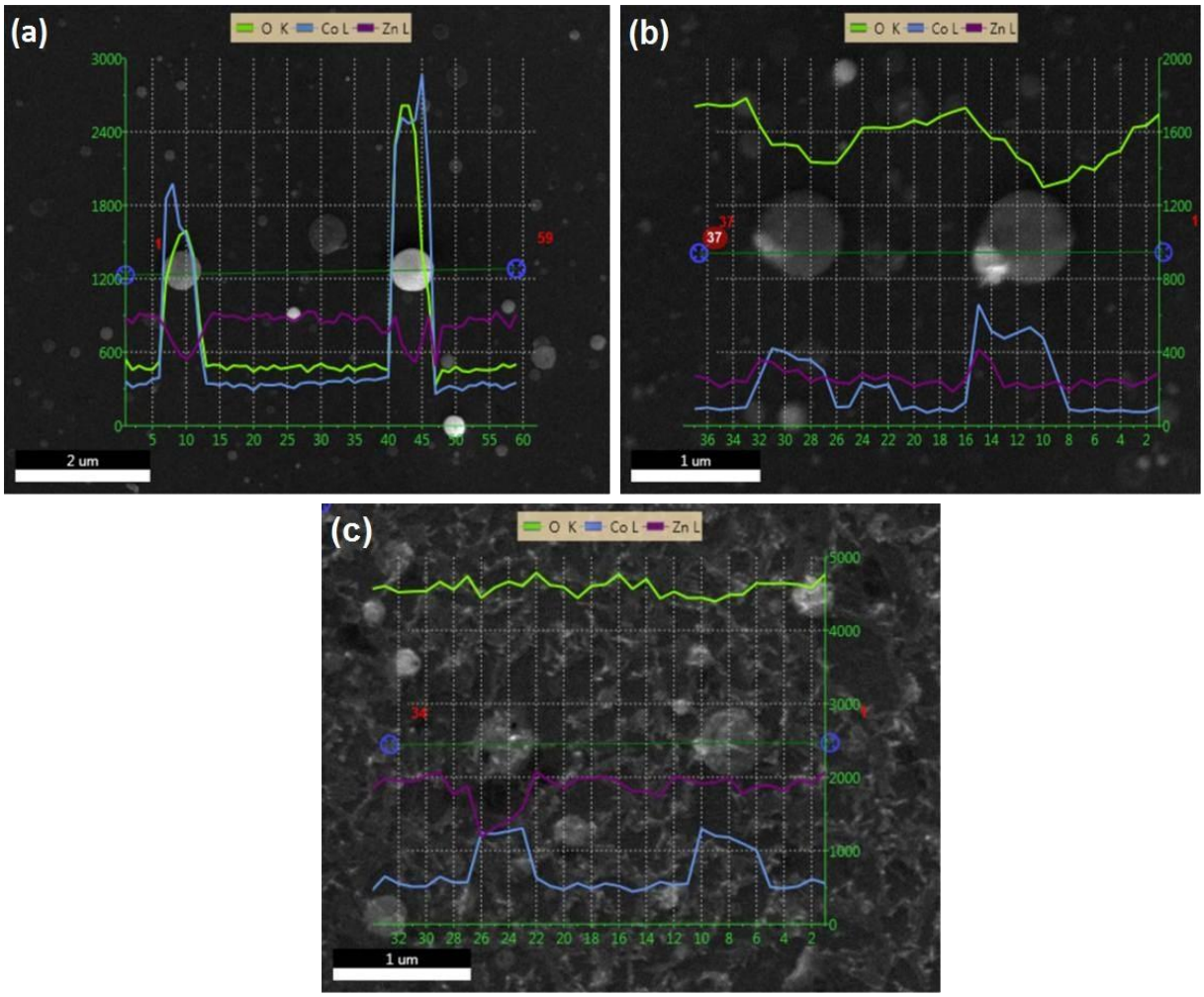

Figure 5.1: (a) EDX line scan analysis of as-grown film at 450^{o}C and 16 kV, and annealed at (b) 400^{o}C, and (c) 600^{o}C.

to maximize sensitivity of the instrument in order to get chemical information about the surface species. The survey spectra exhibit Co peaks in addition to the strong signals from zinc and oxygen. As can be observed, Zn $2p_3$ peak, which is associated with Zn-O bond in the film, shows a remarkable reduction in atomic concentration relatively to that of O 1s for the film annealed at higher temperature (600^{o}C). This result corroborates EDX data reported earlier. The survey scan spectra also reveal that annealing substantially affects the chemical composition of the film near the surface. The intensity of the peaks attributed to Zn significantly decreases, while the intensity of the peak associated with O increases (particularly at higher annealing temperature), relatively

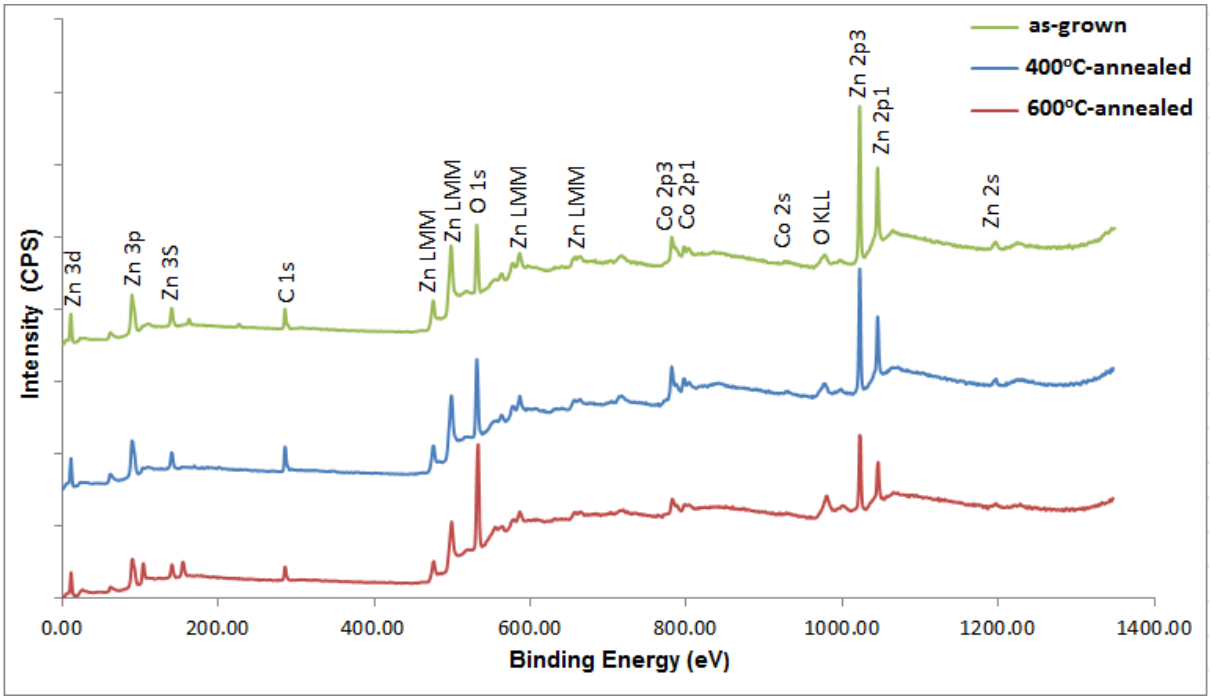

Figure 5.2: XPS survey scan spectra of as-grown CZO films at 450°C and annealed at 400°C and 600°C.

to their as-grown counterparts. This hints at the evaporation of metallic Zn nano-particles from the film surface as the latter are annealed at high temperature under reduced ambient oxygen pressure. Figure 5.3 (a, b) depicts spectra of Co $2p_{3/2}$ peaks, in as-grown films, which indicate that Co is present in three chemical states, viz., Co^{+2}, Co^{+3} (oxidized), and Co^{o} (non-oxidized) in the deposited films. The small shoulder (peak) at the low binding energy located at 778 -779 eV is attributed to metallic Co (Co^{o}) (Peng et al., 2005; Tortosa et al., 2008). The as-grown films at 450°C consist of higher metallic Co concentration for both accelerating voltages (15 kV and 16 kV) compared to the films deposited at 350°C and 400°C. The Co $2p_{3/2}$ peak at the binding energy around 780.5 eV is ascribed to Co^{+2} oxidation state (Ivill et al., 2008). The energy peak at around 782.8-783.3 eV is assigned to Co^{+3} oxidation state (Zhou et al., 2008; Alves et al., 2017). The intensity ratio of Co^{+2} and Co^{+3} signals in the films changes because of the possibility

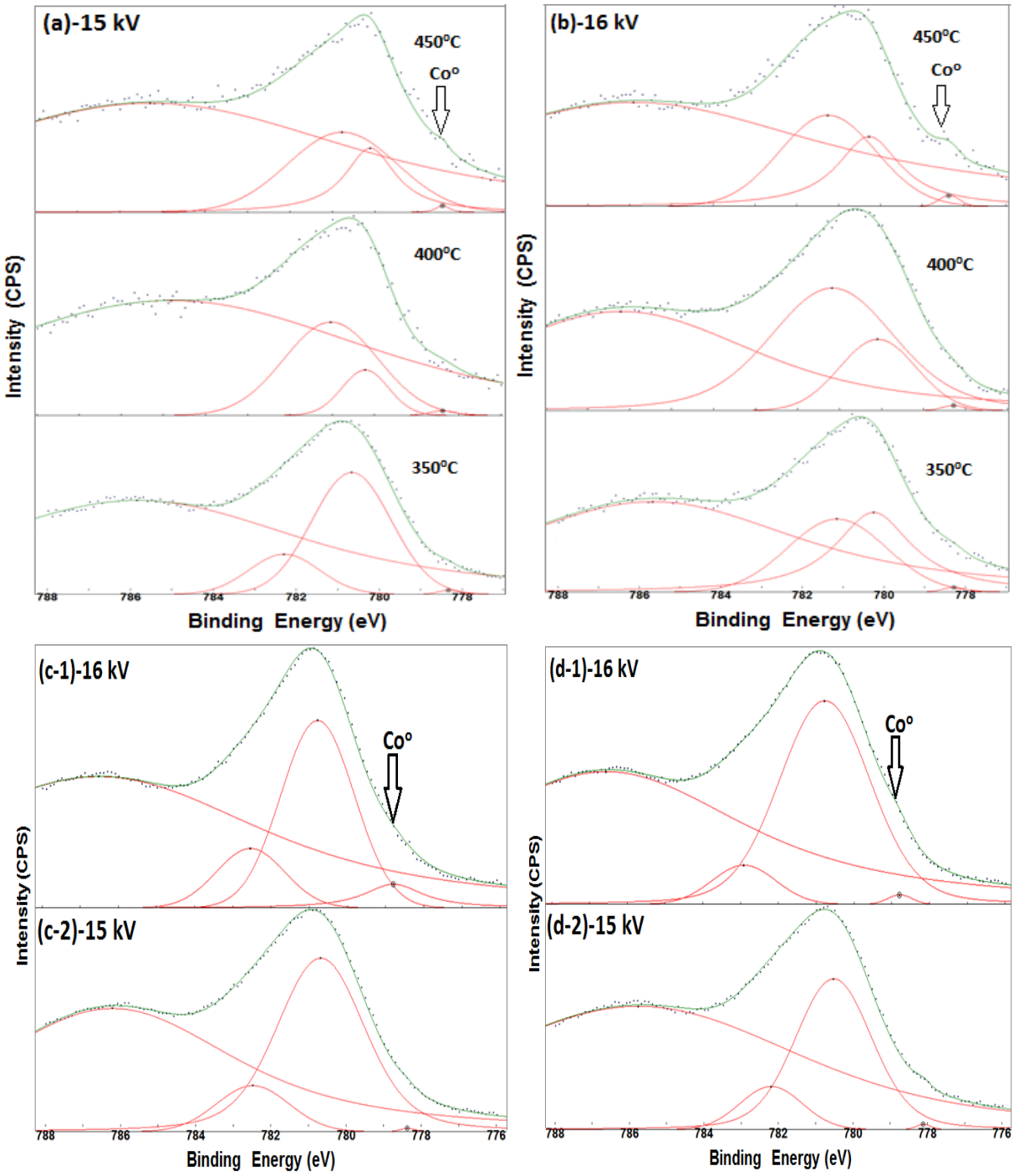

Figure 5.3: Typical XPS chemical binding spectra of Co $2p_{3/2}$ peaks (and their deconvolutions) of as-grown films (a, b) at various temperatures and electron beam accelerating voltages; the films grown and annealed at 400°C (c-1, c-2), and the films grown at 450°C and annealed at 600°C (d-1, d-2). The accelerating voltage is indicated in the inset.

of oxidation of Co^{+2} to Co^{+3}. The exact nature of the cobalt defect in the structure cannot be unequivocally determined with XPS measurements (Zhou et al., 2008). The co-existence of Co^{+2} and Co^{+3} suggests the presence of CoO and Co_2O_3 phases in CZO films near the film surface (Vadiyar et al., 2016). Similarly, chemical oxidation state/bonding of CZO films has been assessed for the films annealed at 400^{o}C and 600^{o}C, and the corresponding Co $2p_{3/2}$ and their deconvolution are shown in Figure 5.3(c-1, c-2) and Figure 5.3(d-1, d-2), respectively. XPS results show that CZO films before and after annealing exhibits metallic Co, and a substantial portion of Co atoms is present in the films as +2 and +3 oxidation states near the surface. The concentration of metallic Co appears to be highest in the films deposited at 16 kV and annealed at 400^{o}C, as depicted in Figure 5.3(c-1). Therefore, it can be concluded that 400^{o}C is the optimum annealing temperature to enhance the growth of metallic Co in CZO films. The formation of metallic cobalt in the films can be explained either in terms of the presence of oxygen vacancies in ZnO wurtzite structure (which may be enhanced by post growth thermal treatment) or of the smaller incorporation of oxygen during film growth (Tortosa et al., 2008).

5.1.2 Film thickness

Typical transversal cross-sections of the films annealed at 400^{o}C and 600^{o}C are presented in Figure 5.4(a, b). The films annealed at 400^{o}C and 600^{o}C have an average thickness of ~80 nm and ~61 nm, respectively. Figure 5.4-c shows the reflectance response obtained from visible spectroscopy of CZO films deposited on Si substrate at 450^{o}C and annealed at 600^{o}C. Film thickness is indirectly measured by means of a modified Marquardt-Levenberg built-in algorithm through minimization of the difference between measured and calculated data. The estimated thickness of the film is 66 nm, in good accordance with the thickness, i.e., 61 nm, measured from SEM cross-section as depicted in Figure 5.4(b). The as-grown film at 450^{o}C and 16 kV has a thickness of ~ 67 nm. The thickness measurements indicate that annealing at 400^{o}C leads to a

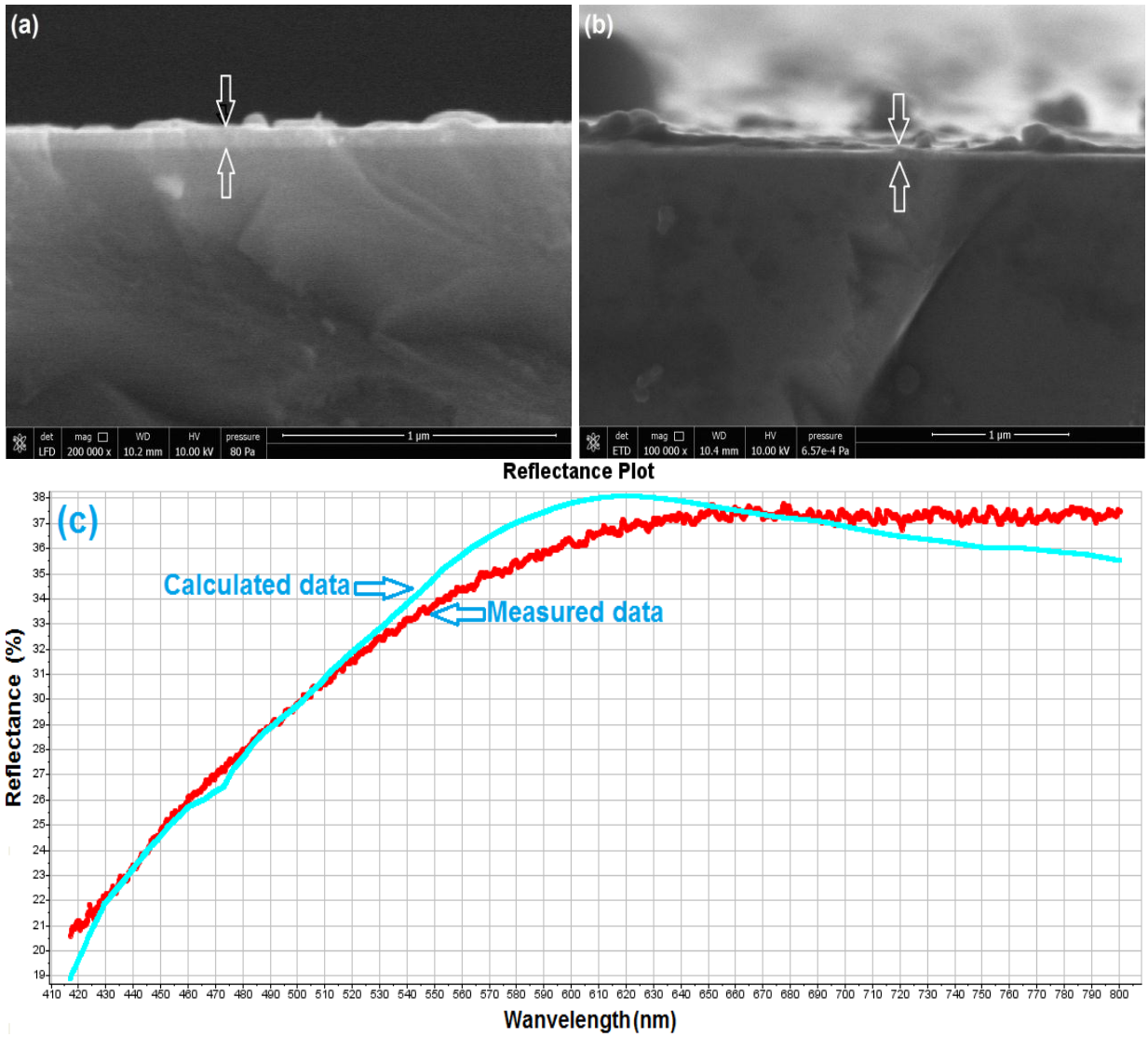

Figure 5.4: Typical transversal cross section of the film deposited at 16 kV, 450^{o}C and annealed at (a) 400^{o}C, (b) 600^{o}C; (c) Visible reflectance spectroscopic measurements of CZO films annealed at 600^{o}C.

significant increase in film thickness, whereas annealing at 600^{o}C (which results in films with a wrinkle-like structure) leads to a marginal decrease in film thickness relatively to as-grown films.

5.1.3 Morphology

Figure 5.5 depicts typical SEM images of CZO films deposited at various temperatures and electron beam accelerating voltages. It can be clearly observed that the films consist of nano-

sized globules (~10-400 nm) that are distributed uniformly on the films. The size of the globules does not appear to be much affected by the deposition temperature when the latter is varied from 350^{o}C to 450^{o}C, as shown in Figure 5.5(a-c) and Figure 5.5(d-f), at 15 kV and 16 kV, respectively. The density of the globules decreases as the temperature increases from 350^{o}C to 450^{o}C. The electron beam accelerating voltage does not seem to remarkably affect the size, shape and density of the globules in as-grown CZO films as shown in Figure 5.5(a-f). A closer inspection of SEM images, as shown in the insets of Figure 5.5, reveals that the globules are grown out of many fine nano-particulates. Significant morphological and structural changes have been observed in annealed films relatively to as-grown counterparts. Films annealed at 400^{o}C seem to consist of a greater number of globules that are larger in size, as shown in Figure 5.5(g, h), relatively to as-grown films, see Figure 5.5(b, e), at both accelerating voltage values. These morphological changes do not appear to be dramatically affected by the beam accelerating voltage as the latter is varied from 15 kV to 16 kV. At a higher annealing temperature, i.e., 600^{o}C, film morphology changes drastically whereby the globules seem to be surrounded by wrinkle-like features, as shown in Figure 5.5 (i, j). The effect of annealing on film morphology may be explained in terms of a) high surface energy favoring surface atoms migration and recrystallization/rearrangement, and resulting in large size globules, and, b) melting point of Zn/ZnO nanoparticles, viz., 419.5^{o}C (Gafiychuk et al., 2011; Gon et al., 2011). On the one hand, the formation of these nano-globules strongly depends on kinetic aspects, viz., high surface mobility of adatoms, deposition flux, nucleation rate, and surface diffusion, and on thermodynamic factors such as melting process. On the other hand, during post-growth thermal treatment, the nano-globules attain sufficient energy to initiate coalescence resulting in an increase in the globule size. When annealing temperature is raised to 600^{o}C, the surface

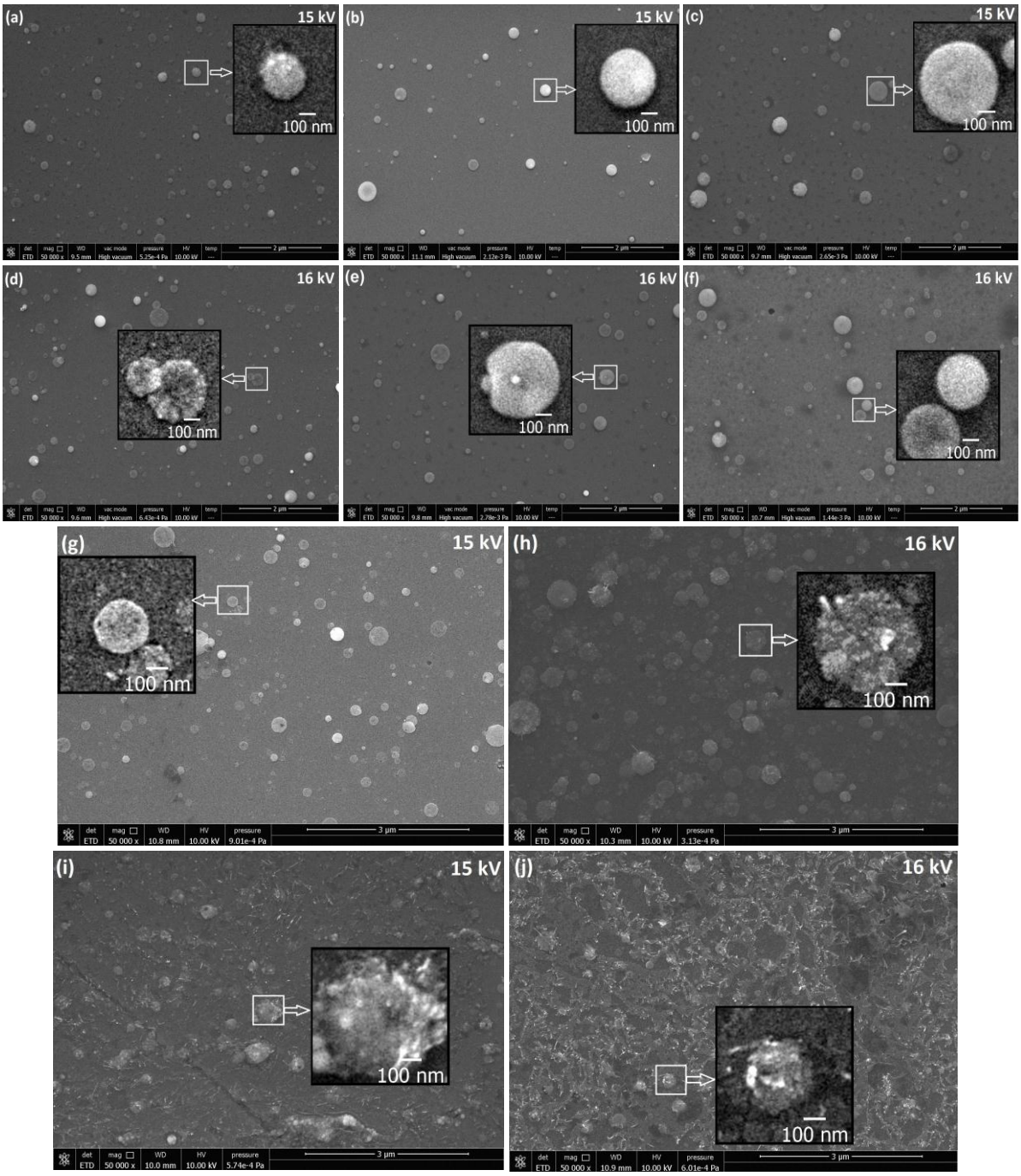

Figure 5.5: SEM images of as-grown films as a function of accelerating voltage (in the inset) at (a, d) 350^{o}C, (b, e) 400^{o}C, and (c, f) 450^{o}C. SEM images of heat-treated films as a function of accelerating voltage (in the inset) under the following conditions: deposited and annealed at (g, h) 400^{o}C, and (i, j) deposited at 450^{o}C and annealed at 600^{o}C. Square area is zoomed in and shown in the insets.

morphology of the films is significantly affected whereby the morphology changes from globular to nodular shape and is surrounded by wrinkle-like structures as shown in Figure 5.5 (i, j).

A typical distribution of nanoparticle size is shown in Figure 5.6 for films deposited at 450^{o}C. The particle size has been directly measured on SEM images shown in Figure 5.5 (c, f). The data reveal that beam accelerating voltages (15 kV, 16 kV) has no substantial effect on nanoparticle size distribution. The most frequent particle size lies in the range 6-10 nm at both accelerating voltages. The average particle size is ~12.4 nm and ~11.3 nm at 15 kV and 16 kV respectively, while the number of nanoparticles is only slightly larger at 16 kV relatively to 15 kV. Figure 5.7 depicts particle size distribution for the films deposited at 16 kV and annealed

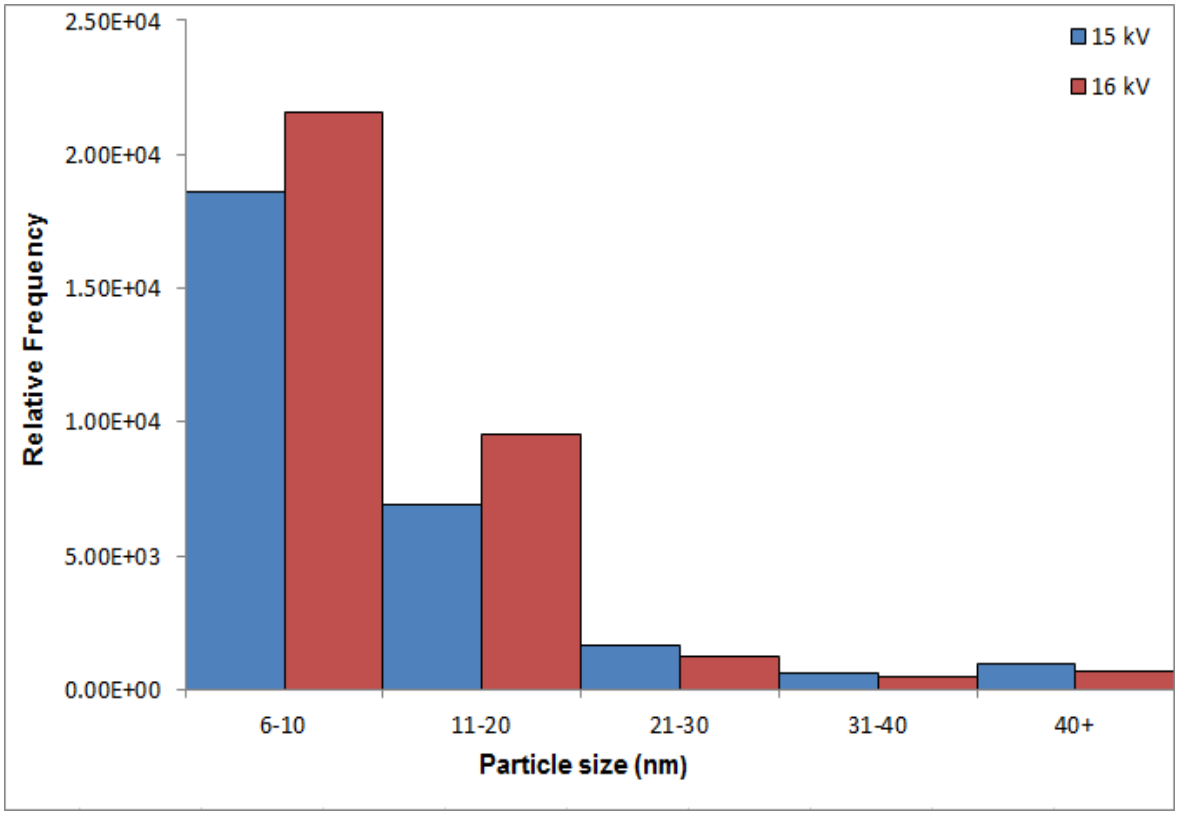

Figure 5.6: Particle size distribution in as-grown film deposited at 450^{o}C. The accelerating voltage is indicated in the inset.

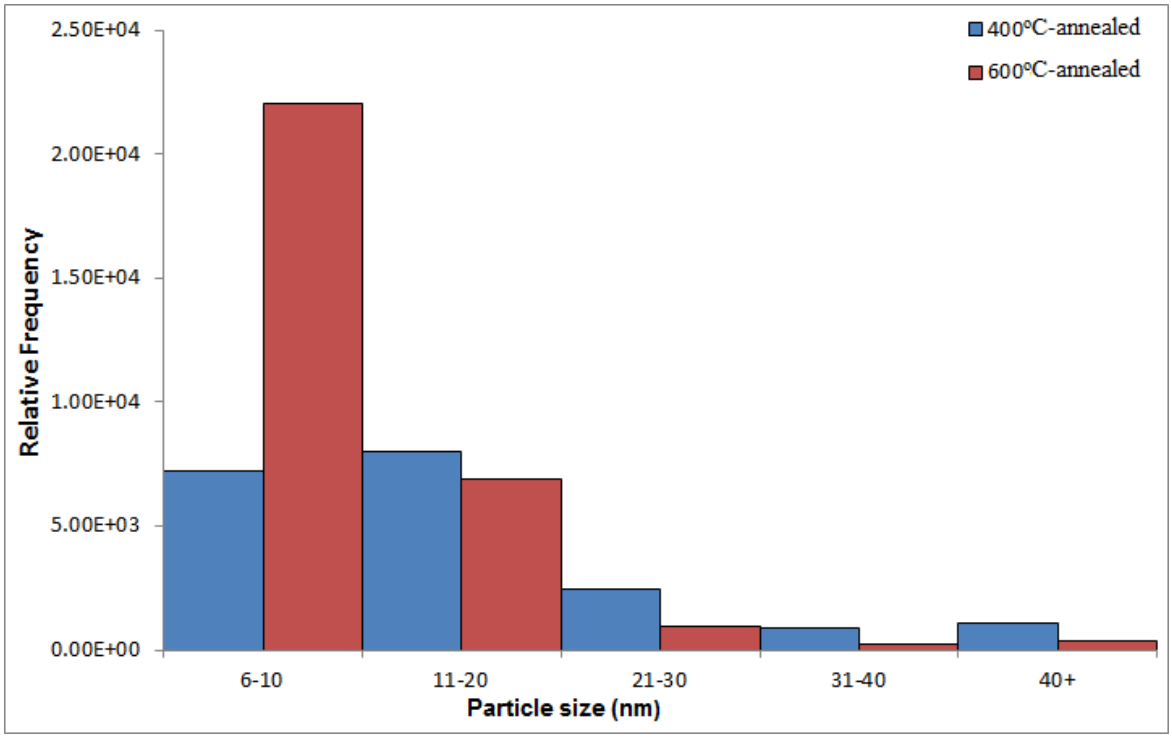

Figure 5.7: Particle size distribution in annealed film deposited at 450°C and 16 kV. The annealing temperature is indicated in the inset.

at 400°C and 600°C. The results are based on analysis of SEM images shown in Figure 5.5(h, j). The film annealed at 400°C has a significantly higher average particle size (~18 nm) relatively to the film annealed at 600°C (~10 nm). Moreover, the film annealed at 600°C has a higher proportion of particles whose diameter is in the range of ~6-10 nm.

Typical 2D AFM images of as-grown CZO films at various temperatures and beam accelerating voltages, and their corresponding 1D roughness profiles are presented in Figure 5.8. The findings do not indicate any drastic variations in surface average arithmetic roughness of as-grown films, whereby the roughness lies between ~3 nm and ~6 nm. The roughness profiles, as shown in Figure 5.8 (a-f), indicate that film roughness is due to Co-rich nano-globules distributed on the film surface. AFM (2D and 3D) scans of surface morphology of the films annealed at 400°C and 600°C are shown in Figure 5.9. The data reveal that surface roughness

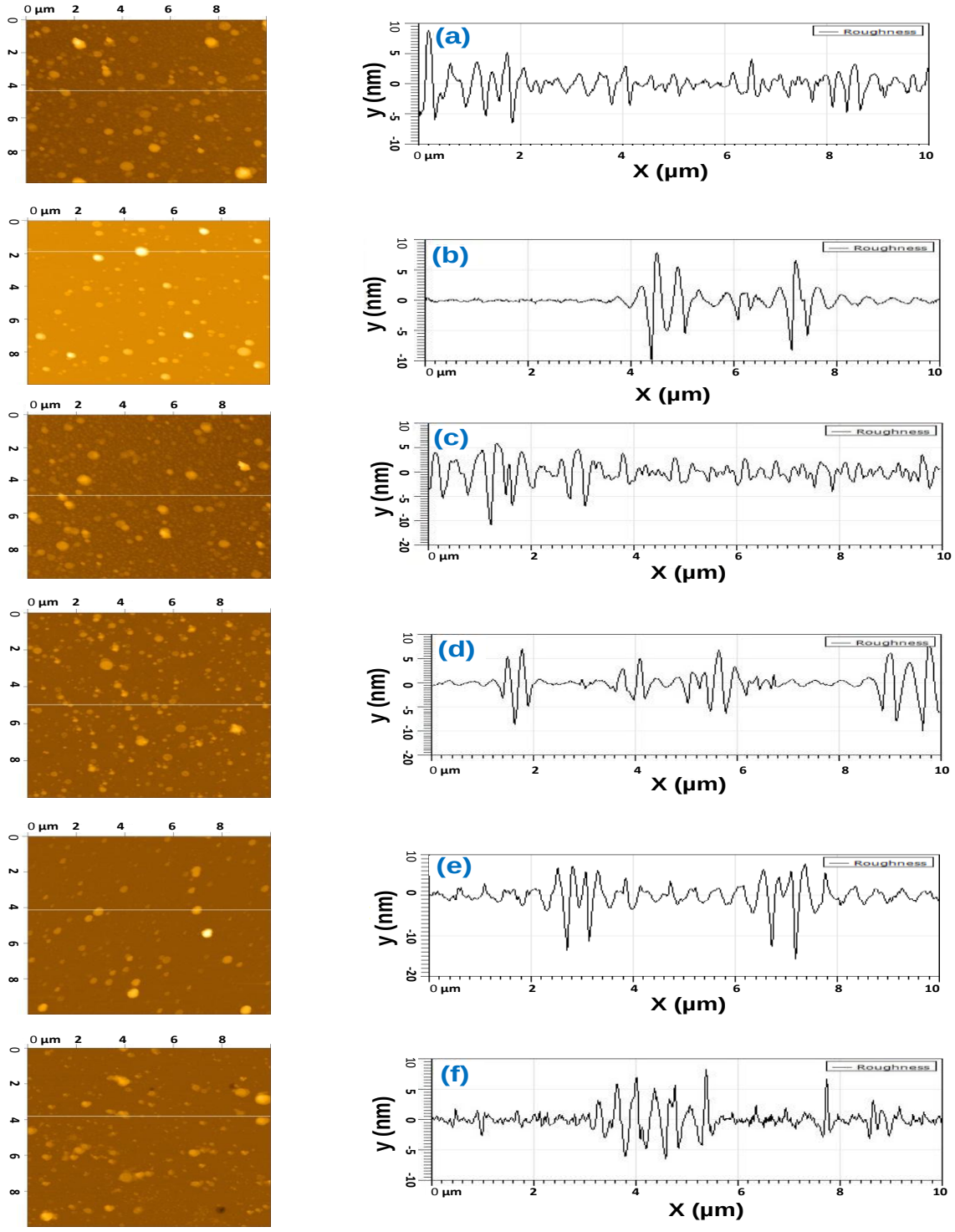

Figure 5.8: AFM images and one-dimensional surface roughness profiles of CZO thin films deposited at 15 kV (a) 350^{o}C, (b) 400^{o}C, (c) 450^{o}C, and at 16 kV (d) 350^{o}C, (e) 400^{o}C, (f) 450^{o}C.

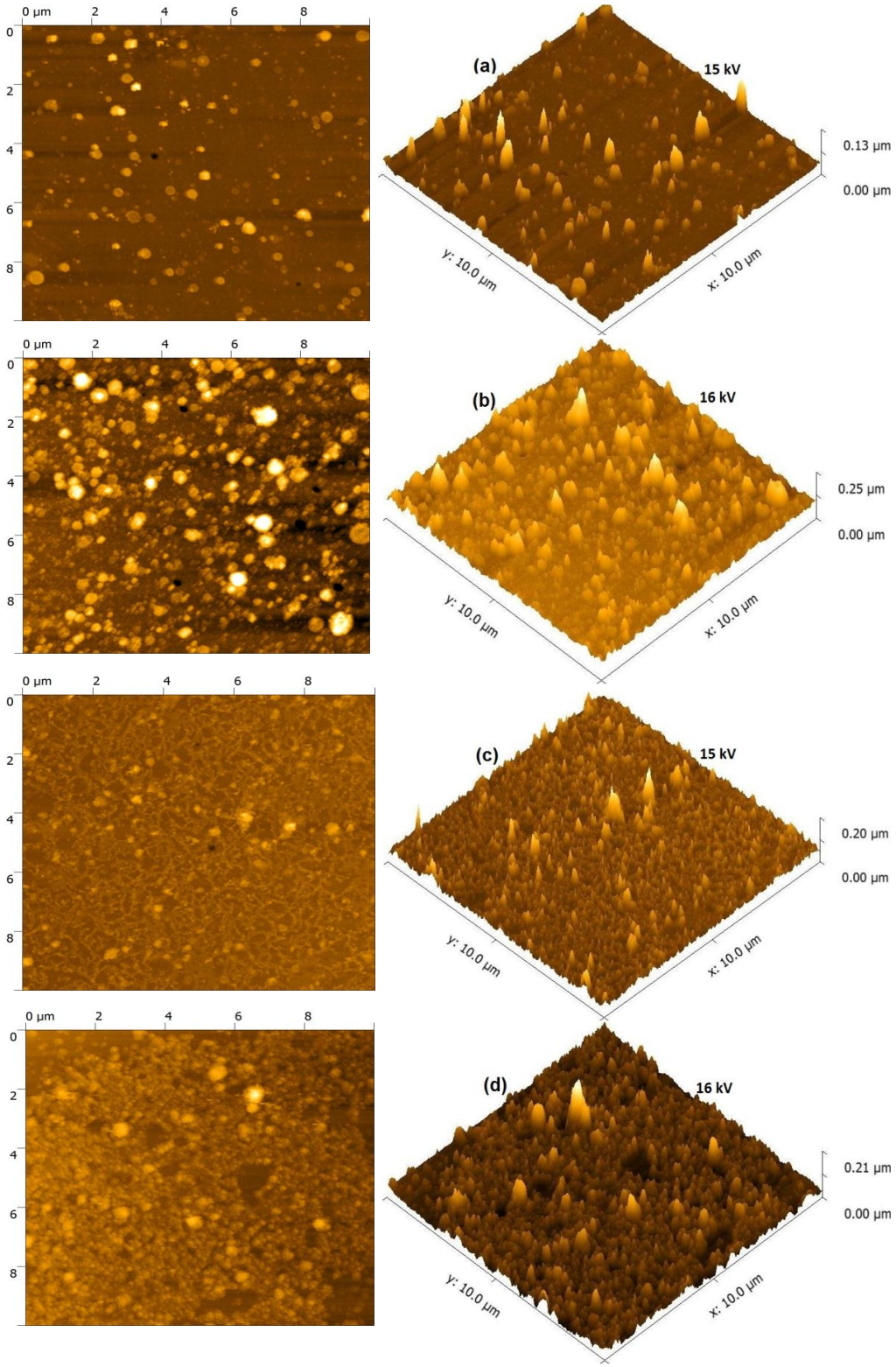

Figure 5.9: AFM images (2D, 3D) of films annealed at 400^{o}C (a, b) and 600^{o}C (c, d) versus accelerating voltage (indicated in the inset).

increase with post-annealing temperature. From Figure 5.9, the average arithmetic roughness increases from ~4 nm to ~11 nm (at 400^{o}C) and ~8 nm to ~15 nm (at 600^{o}C) as the electron beam accelerating voltage increases from 15 kV to 16 kV, respectively. The increase in surface roughness can be explained in terms of the increase in size of Co-rich globules followed by wrinkle-like agglomeration on the film surface, as explained earlier. Film roughening has also been reported to be caused by fluctuations of the vapor flux impinging on the substrate surface during deposition (Zangwill, 1996). Annealing results in voids and cracks in the films, as can be seen in Figure 5.5(g-j) and Figure 5.9(a-d). This is most likely owing to migration and re-arrangement of the surface atoms, a consequence of thermal treatment under reduced oxygen pressure as discussed earlier, and to thermal mismatch between Co (12.1 to 16.8x10^{-6} K^{-1}) (Donaldson and Beyersmann, 2012), ZnO (5 to 8x10^{-6} K^{-1}) (Pedersen et al., 2011) and the underlying substrate (2.6 to 4.3 x 10^{-6} K^{-1}) (Watanabe et al., 2004).

5.1.4 Structure

The crystal structure of CZO films has been determined by XRD using theta/2-theta Bragg-Brentano configuration. Figure 5.10-a shows XRD diffraction patterns in the 2θ range 30^{o}-80^{o} of the as-grown films on Si (100) at 450^{o}C and accelerating voltages of 15 kV and 16 kV. The diffractogram shows the characteristic peaks corresponding to 2Θ =34.43^{o} (002) and 36.26^{o} (101) indicative of the presence of ZnO in the films (PDF card no. 01-070-8070). The sharp and intense diffraction peak (002) reveals that the as-grown film has a preferential c-axis orientation. From Figure5.10-a, the structural analysis shows two peaks at 2Θ ~ 61.7^{o} (412) and 65.9^{o} (306) attributed to hcp metallic Co (PDF card no. 01-070- 2633). Figure 5.10-b reveals the XRD patterns of the films annealed at 400^{o}C. The films exhibit two diffraction peaks (002) and (101) corresponding to ZnO. The intensity of the peak (002) for the films annealed at 400^{o}C

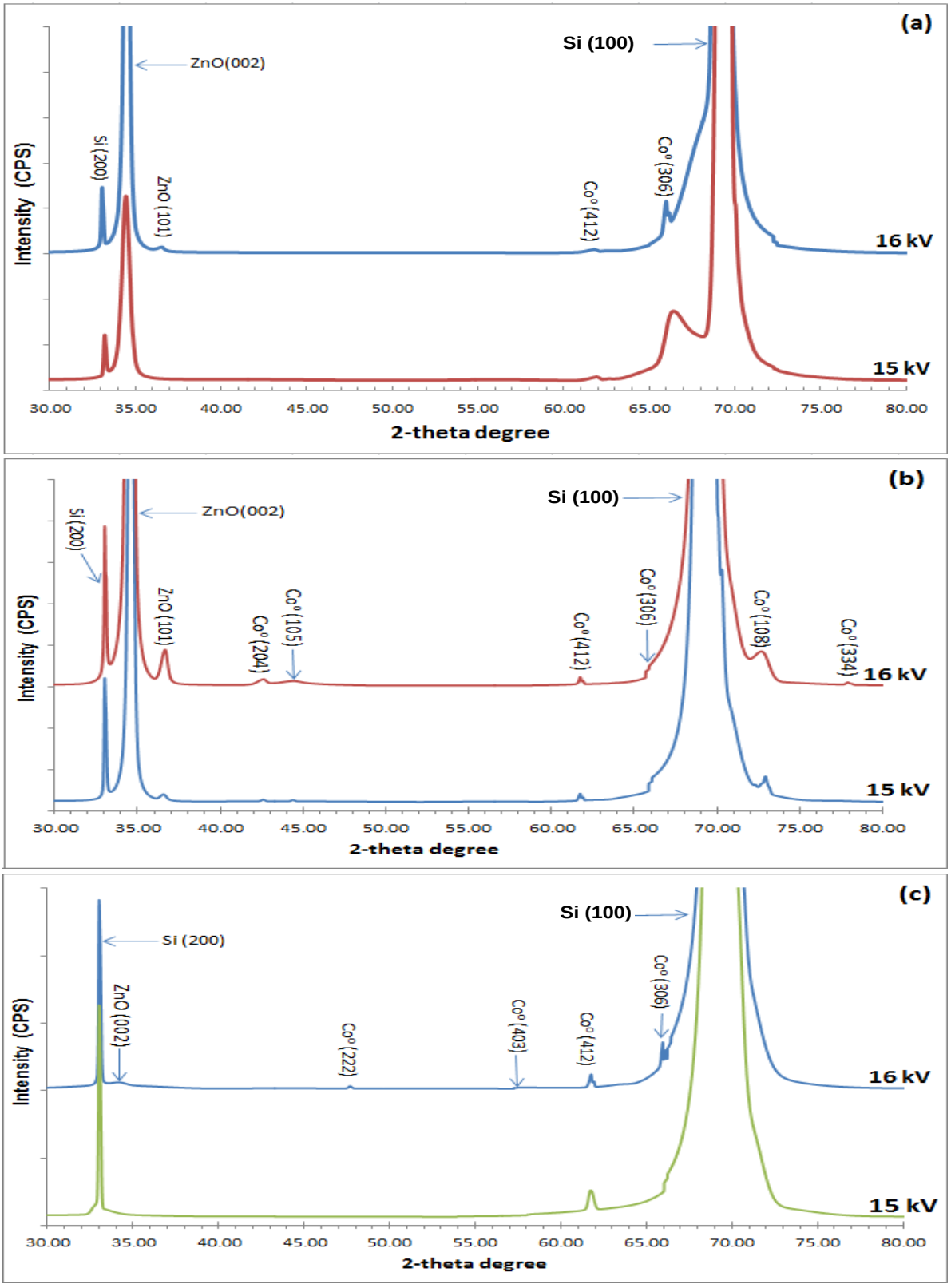

Figure 5.10: XRD diffraction pattern of as-grown film at 450°C (a), and annealed at 400°C (b), and (c) annealed at 600°C.

is much greater than that that of the as-grown films for both accelerating voltage values. This indicates that the films annealed at 400^{o}C have improved preferential c-axis orientation compared to the as-grown films. There are six diffraction peaks at 2Θ ~ 42.5^{o} (204), 44.8^{o} (105), 61.73^{o} (412), 65.9^{o} (306), 72.9^{o} (108) and 78.0^{o} (334) corresponding to hcp metallic Co phase for the films annealed at 400^{o}C (Hiu et al., 2002). Upon increasing the annealing temperature to 600^{o}C, the film produced at 16 kV exhibits one peak (002) only attributed to ZnO with very low intensity whereas for the film deposited at 15 kV, no ZnO phase could be detected due to the low concentration of Zn at higher annealing temperature in accordance with XPS (survey scan spectra) measurements. The very low intensity or absence of ZnO hexagonal wurtzite structure peak (see Figure 5.10-c) corresponding to the plane (002) can be explained in terms of higher annealing temperature (600^{o}C), which may result in significant distortion of ZnO hexagonal wurtzite structure, and, consequently, the diffractogram exhibits either only a weak reflection along the peak corresponding to (002) plane or does not reveal any signals diffracted from ZnO hexagonal wurtzite structure due to complete distortion of the wurtzite lattice as shown in Figure 5.10-c. The data also suggest that the degree of crystallinity of the films is improved at the lower annealing temperature and deteriorates at the higher annealing temperature (Zhang, et al., 2015; Joshi et al., 2014). The films grown at 16 kV and annealed at 600^{o}C exhibit four peaks at 2Θ ~ 47.1^{o} (222), 57.6^{o} (403), 61.70^{o} (412) and 65.9^{o} (306) corresponding to hcp metallic Co phase, whereas the film produced at a lower accelerating voltage (15 kV) and annealed at 600^{o}C shows one peak (412) only attributed to hcp metallic Co.

Chapter 6: Effect of substrate heat treatment on film properties and Fischer Tropsch synthesis

6.1 Introduction

In the sixth series of deposition experiments, $Co_xZn_{1-x}O$ thin-films have been deposited on c-sapphire and Si (100) substrates from the target containing different Co loadings viz., 5 w%, 10 w% and 20 w%. Prior to deposition, the substrates have been subjected to heat treatment (pre-annealing) at 1100^{o}C under reduced oxygen pressure. Other process parameters have been kept constant, viz., deposition temperature (450^{o}C), accelerating voltage (16 kV), pulse frequency (1Hz), number of pulses (3000) and background gas (Ar) pressure (~3 mTorr), see Chapter 3, Table 3.2. The corresponding results and discussion are given in section 6.1.1-4.

Based on characterization by complementary analytical techniques, the best quality films deposited on c-sapphire, Si and quartz have been evaluated as model nano-catalysts for Fischer-Tropsch synthesis (FTS) in a 3-phase continuously-stirred tank slurry reactor (3-φ-CSTSR) using a Robinson-Mahoney stationary basket (RMSB). The corresponding results are discussed in terms of catalytic activity and selectivity in section 6.1.5.

6.1.1 Structure

Figure 6.1 shows XRD patterns of CZO films deposited on c-sapphire and silicon substrates for different nominal Co loadings. Crystallographic phase analysis has been carried out using theta/2-theta Bragg-Brentano configuration to generate 30^o-80^o diffractograms. Diffraction peaks pertaining to the different phases in the deposited films can be observed. The characteristic peak of ZnO hexagonal wurtzite structure (002) can be observed at 2Θ ~34.43^o for the film corresponding to x = 0.05 and grown on c-sapphire, and the film exhibits two additional peaks corresponding to ZnO at 2Θ ~ 36.26^o (101) and 72.6^o (004), as shown in Figure 6.1(a). XRD pattern of the same film, i.e., with x = 0.05, shows a film that consists mainly of ZnO phase, with

a preferential c-axis orientation along plane (002). For the film with a Co loading of 0.1, the diffractogram does not show any presence of ZnO peaks corresponding to planes (101) and (004), and only reveals a weak reflection along the peak corresponding to plane (002), which is likely suggestive of a significant distortion of ZnO hexagonal wurtzite structure due to enhanced Co loading (Manouni et al., 2009). When the latter is further increased to x = 0.2, the corresponding diffractogram does not reveal any signals from ZnO phase due to complete distortion of the wurtzite structure. While no cobalt could be detected in $Zn_{0.95}Co_{0.05}O$ films deposited on c-sapphire, three peaks associated with metallic Co appear at $2\Theta \sim 37.6^{o}$ (300), 64.3^{o} (315), 79.8^{o} (317) for films with a cobalt loading of 0.1, and four peaks appear at $2\Theta \sim 37.6^{o}$ (300), 53.9^{o} (402), 64.3^{o} (315) and 79.8^{o} (317) corresponding to Co^{o} (PDF card no.: 01-070-2633) for films with x = 0.2. Similar trends with some salient differences have been observed in the phase analysis of films deposited on silicon, as shown in Figure 6.1-b. Zinc oxide phase is only detected for a Co loading of 0.05 but not for films with higher loading levels, i.e., 0.1 and 0.2. Metallic Co has been observed at $2\Theta \sim 61.7^{o}$ (412) for the film deposited on Si substrate even with a nominal Co loading of 0.05, as can be seen in Figure 6.1-b. The film with x = 0.1 exhibits two additional diffraction peaks associated with Co^{o}, viz., at $2\Theta \sim 41.4^{o}$ (302) and 35.7^{o} (203), whereas the diffractogram of the film with x = 0.2 reveals six additional peaks of Co^{o}, viz., at $2\Theta \sim 35.7^{o}$ (203), 41.4^{o} (302), 42.5^{o} (204), 50.1^{o} (205), 59.6^{o} (411) and 65.9^{o} (306). Overall, a higher intensity of metallic Co can be observed in films deposited on Si substrate, which suggests that Si (100) substrate is more favourable for the formation of hcp metallic Co in CZO films than c-sapphire substrate under the same deposition conditions. Diffraction peaks of CoO phase, which correspond to $2\Theta = 42.4^{o}$ (200) and 61.5^{o} (220) as per PDF card no. : 01 - 078- 0431, are not readily visible in the diffraction patterns shown in Figure

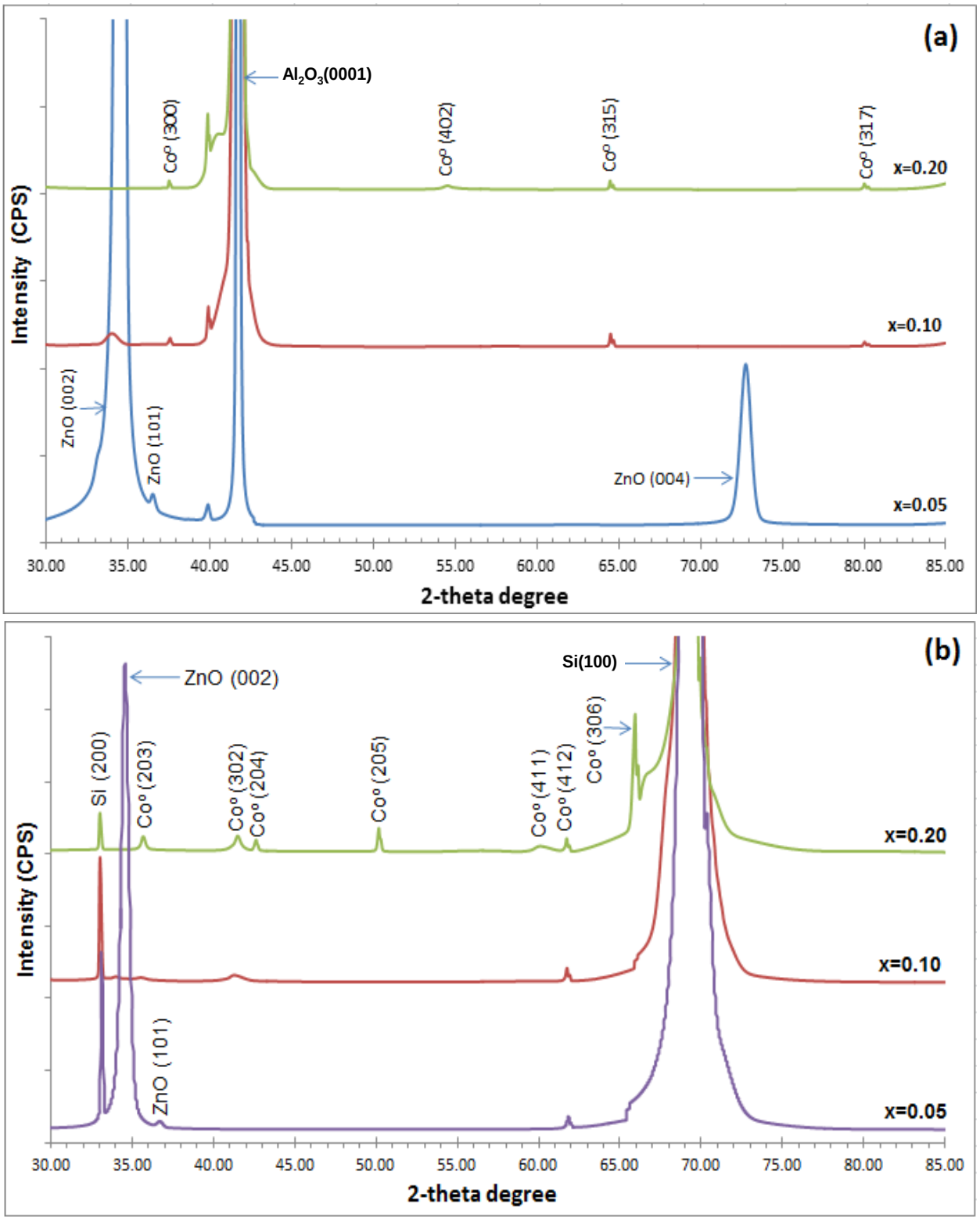

Figure 6.1: XRD patterns of $Zn_{1-x}Co_xO$ films with different loadings (as indicated) deposited on (a) c-sapphire, and (b) silicon substrates.

6.1(a, b). The most likely reason is that these peaks overlap with some of the peaks attributed to c-sapphire, viz., plane (006), and Co^{o}, viz., planes (204) and (412). Based on phase analysis, it seems that for low Co loading, i.e., x = 0.05, Co ions are largely incorporated into substitutional sites of ZnO lattice, while for CZO films with x = 0.1 and x = 0.2, Co ions are located in interstitial sites of zinc oxide structure.

6.1.2 Chemical composition and chemical states

Typical EDX line scan spectra, superimposed on corresponding SEM images, of CZO films deposited on c-sapphire are shown in Figure 6.2, which clearly confirm the presence of O, Zn and Co in the films. Line scans provide a quantitative analysis of material concentration along the dark green line ending with two blue circles indicated in Figure 6.2. The films consist of nano globules dispersed on the film surface. For a Co loading of 0.05, O, Zn and Co seem to be evenly distributed throughout the film, see Figure 6.2-a, whereas for Co loading of 0.1 and 0.2, as shown in Figure 6.2 (b, c), Co content is substantially higher in the nano globules relatively to the film matrix. It is worth noting that Co content in the globules increases as Co loading is increased, and, overall, oxygen content is relatively higher throughout the films. The high oxygen content in the films may be an artifact, which can be attributed to annealing the substrates under reduced oxygen pressure, whereby oxygen may have incorporated into the substrate surface. Quantitative EDX point analysis has been performed to further ascertain the chemical nature of globules and the matrix, and reveals that the deposited films are congruent with a composition close to that of the target material (with a relative error of ± 5%).

X-ray photoelectron spectroscopy is an efficient technique to elucidate the secondary phases near the surface of thin film. Figure 6.3-a depicts typical survey scan spectra of CZO films with different Co loadings deposited on silicon. Energy peaks in the scan reflect the

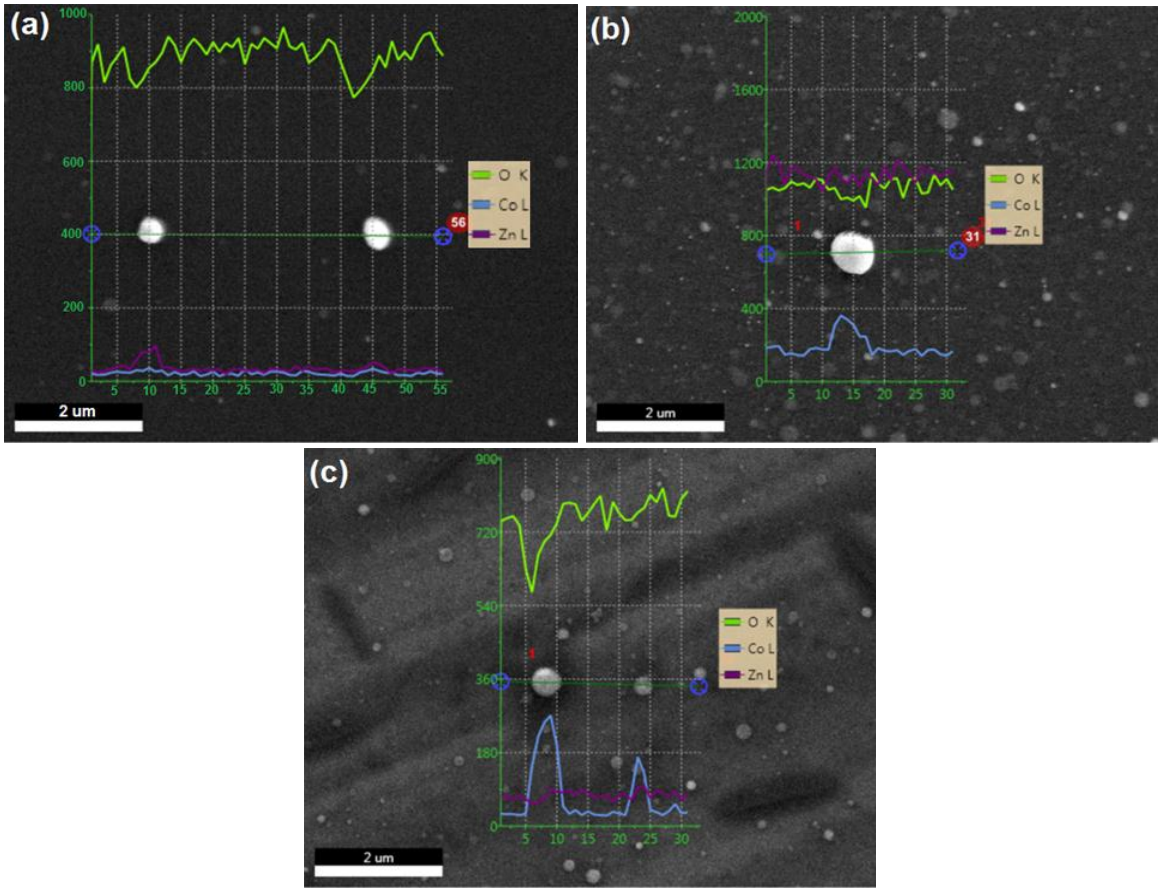

Figure 6.2: Typical EDX line scans along the dark green line on SEM image and the corresponding element profiles of $Zn_{1-x}Co_xO$ film deposited on c-sapphire (a) x = 0.05, (b) x = 0.1 and (c) x = 0.2.

presence of Co, Zn and O, in accordance with EDX data reported earlier. It can also be seen from CZO survey scan that the intensity of Zn signal decreases and Co intensity increases as Co loading increases. The presence of Zn signals in the films with x = 0.20 further confirms that Zn in the film is amorphous, which could not be detected by crystallographic analysis of the film (see Figure 6.1). XPS spectra of Co $2p_{3/2}$ peaks are presented in Figure 6.3(b, c).The deconvoluted Co $2p_{3/2}$ spectra indicate that cobalt is present in three chemical states, viz., Co^{o}, Co^{+2} and Co^{+3} valence states in the deposited films. The Co $2p_{3/2}$ peak at the binding energy around 780.5 eV is associated with oxidized Co (Co-O bonding) that is incorporated into ZnO

structure in Co^{+2} valence state configuration (Ivill et al., 2008). The smaller shoulder (peak) at the lower binding energy side at around 778–779 eV is attributed to metallic Co (Co-Co bonding) that is neither oxidized nor incorporated into ZnO structure ((Peng et al., 2005; Tortosa et al., 2008). The energy peak at around 782.8-783.3 eV is assigned to Co^{+3} oxidation state (Zhou et al., 2008; Alves et al., 2017). The intensity ratio of Co^{+2} and Co^{+3} signals in the films changes because of the possibility of oxidation of Co^{+2} to Co^{+3}. The exact nature of the cobalt defect in the structure cannot be unequivocally determined with XPS measurements (Zhou et al., 2008). XPS data reveal that a substantial fraction of Co is in an oxidized state (either Co^{+2} or Co^{+3} valence state) in the films. The concentration of metallic Co appears to be highest in the films with a Co loading of 0.20 on both substrates, which is in agreement with XRD results. The formation of metallic cobalt in CZO films can be explained either in terms of the presence of oxygen vacancies in ZnO wurtzite structure or smaller incorporation of oxygen during film growth (Tortosa et al., 2008).

6.1.3 Film thickness

Thickness of $Co_xZn_{1-x}O$ films deposited on pre-annealed (1100^oC) Si(100) and c-sapphire have been investigated by VRS. Figure 6.4 shows a typical reflectance response, obtained from visible spectroscopy of CZO (x=0.2) film deposited on Si substrate. The measured thickness is ~54 nm. The blue curve is the predicted (calculated) profile of the film, while the red curve is the measured one. The data reveal that the type of pre-annealed substrates and Co loading contents have no significant effect on the deposited film thickness. The thickness of all films (for series 6) have been estimated to range between 50 nm to 70 nm. It has been found that pre-annealing of substrate has a strong bearing on film thickness. The film deposited on pre-annealed Si substrate exhibit much higher film thickness (54 nm), see Figure 6.4, than as-grown film on Si

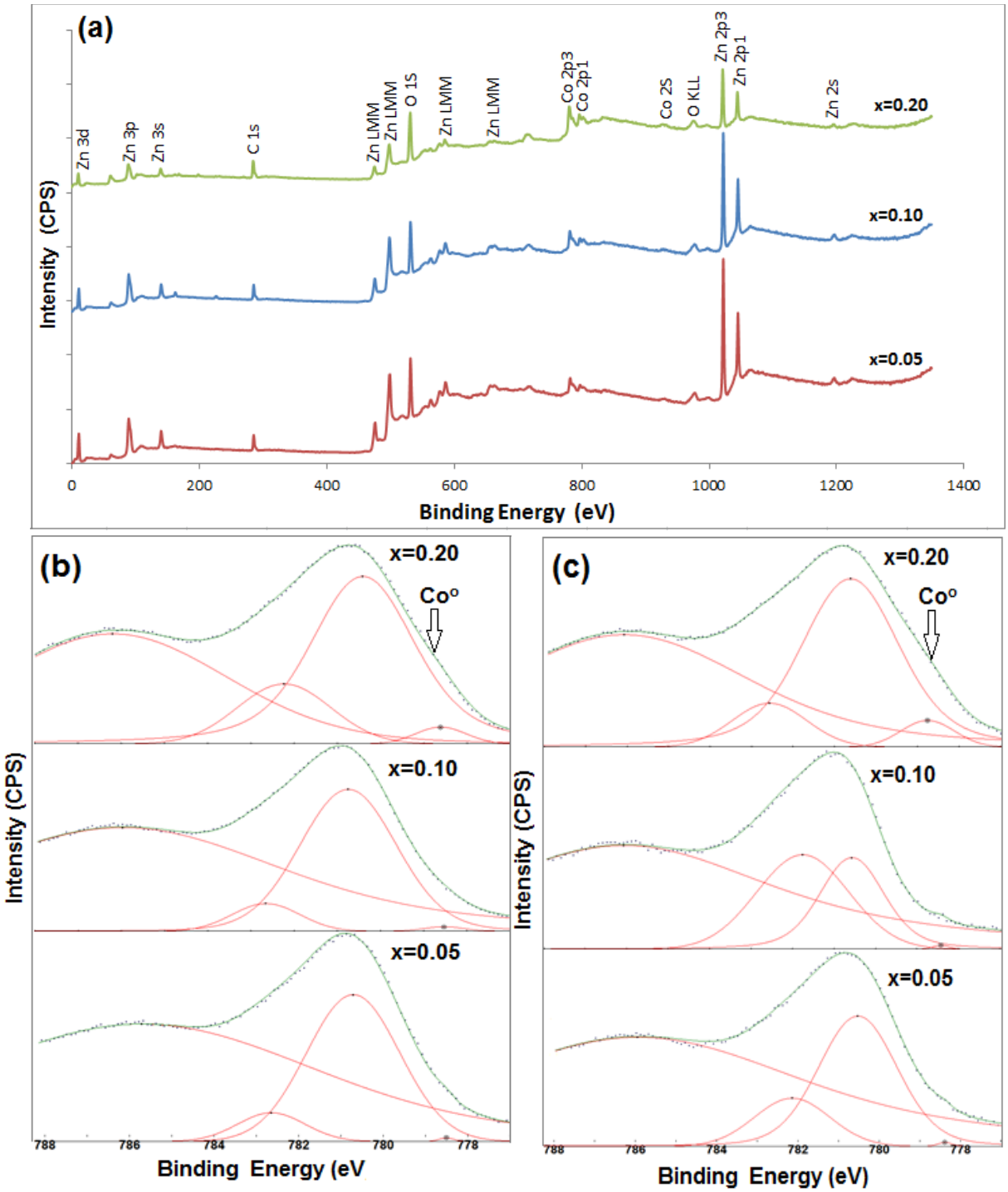

Figure 6.3: Typical XPS survey scan spectra of CZO films for various Co loadings on (a) silicon substrate ; XPS chemical binding spectra of Co $2p_{3/2}$ peaks (and their deconvolutions) for the films grown on (b) c-sapphire, and (c) silicon.

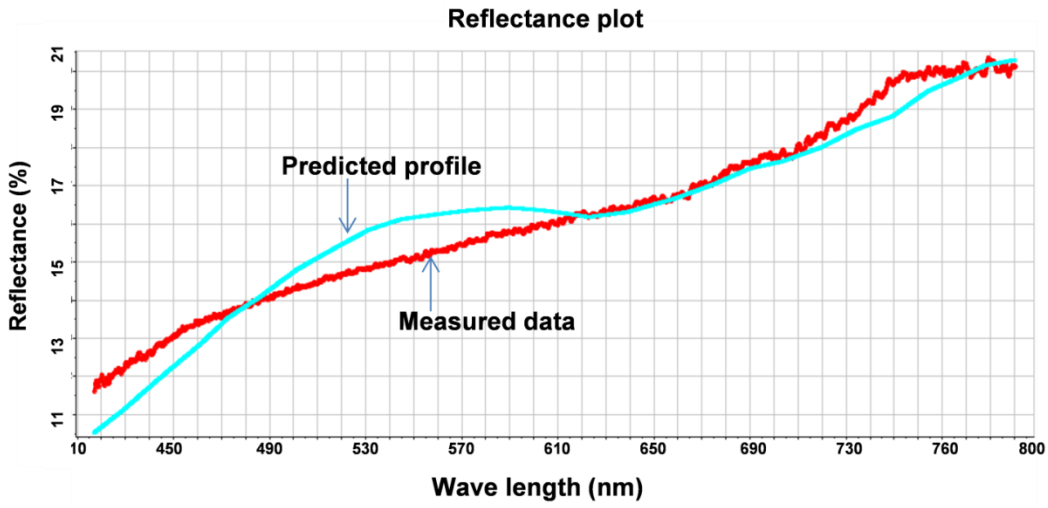

Figure 6.4: Visible reflectance response of $Co_xZn_{1-x}O$ (x=0.2) film on Si (100) annealed at 1100^oC resulting from sixth series.

(26 nm), see chapter 4, Figure 4.17-a under similar deposition conditions.

6.1.4 Morphology

SEM images of films deposited on c-sapphire and Si substrates are shown in Figure 6.5. Film morphology depends on kinetic and thermodynamic factors. Kinetic aspects include deposition flux (from plasma plume), nucleation rate, and surface diffusion (and interaction of atoms with neighbouring sites). Thermodynamic considerations require the Gibbs free energy to drop for the formation of a solid film to occur. Inspection of the images indicates that the films consist of nano globules of size in the range of ~10-300 nm. The level of Co loading strongly affects the surface morphology of the films, as can be observed in Figure 6.5. For a Co loading of 0.1, films deposited on both substrates consist of globules that are larger in size relatively to films with Co loadings of 0.05 and 0.2. Based on SEM observations, the growth of CZO films on c-sapphire seems to follow the Stranski-Krastanov growth model, i.e., layer plus islands, whereas films grown on silicon appear to follow the Volmer-Weber model, i.e., from 3D islands. In S-K model, a few layers are grown initially as the result of a larger decrease in free energy when the depositing atoms bond to the substrate relatively to bonding to one another and provided surface

diffusion is fast. Build-up of strain due to lattice mismatch, between the film and substrate, causes the formation of 3D islands on top of the initial layer to relax the strain. In V-W model, bonding between depositing atoms is energetically favorable and surface diffusion is slow, leading to a pile-up of atoms and subsequent formation of a film out of 3D island growth. A closer look at these globules reveals that each globule is made up of many smaller nanoparticulates, as illustrated in the insets of Figure 6.5. The formation of nanoparticulates is highly desirable to confer potential catalytic properties to CZO nano-composites films. Based on SEM measurements, the average nanoparticulate size is nearly 13.1 nm (x = 0.05), 14.9 nm (0.1) and 12.7 nm (0.2) on silicon, and 14.8 nm (x = 0.05), 20.0 nm (0.1) and 10.6 nm (0.2) on c-sapphire. The substrate material also seems to strongly affect the structural and morphological characteristics of the films. Films deposited on Si (100) consist of globules, which grow side-by-side and are characterized by the presence of voids and cracks, as shown in Figure 6.5 (a-c). The observed defects in the films are most likely due to thermal mismatch between Co (12.1 to 16.8×10^{-6} K^{-1}) (Donaldson and Beyersmann, 2012), ZnO (5 to 8×10^{-6} K^{-1}) (Pedersen et al., 2011) and the underlying substrate (2.6 to 4.3 x 10^{-6} K^{-1}) (Watanabe et al., 2004). Films deposited on c-sapphire consist of well-isolated globules dispersed in a matrix, as shown in Figure 6.5 (d-f). The films are continuous and free from cracks and voids, however, they exhibit some features of the underlying substrate, i.e., terraces and steps.

Film surface topography and roughness have been characterized by AFM in contact mode over a scan area of 3x3 μm^2. For catalytic applications, the surface morphology and roughness of CZO films are important properties as they affect the physico-chemical properties of the films (Yildirim et al., 2016). Figure 6.6 shows 3D topographs of the films deposited on silicon and c-sapphire. The bare pre-annealed substrates are very smooth with an average

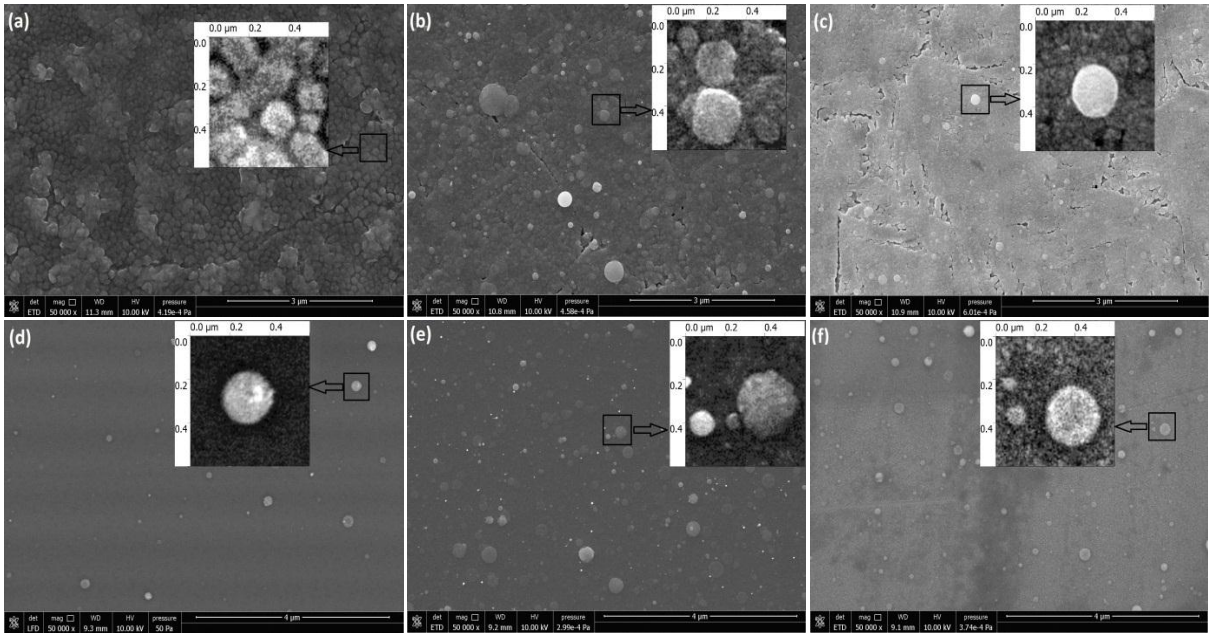

Figure 6.5: SEM images of CZO thin films with different Co loadings deposited on silicon: (a) x = 0.05, (b) x = 0.1, (c) x = 0.2, and on c-sapphire (d) x = 0.05, (e) x = 0.1, (f) x = 0.2. Square areas are zoomed in and shown in the inset.

arithmetic roughness (Ra) of less than 1 nm. Overall, films deposited on Si exhibit a higher Ra relatively to films deposited on c-sapphire. AFM data reveal that average arithmetic film roughness is nearly 19 nm (x = 0.05), 14 nm (0.1)and 10 nm (0.2) on silicon, and 1 nm (x = 0.05), 7 nm (0.1) and 2 nm (0.2) on c-sapphire. Noting that the higher the roughness is, the larger the surface area is, films deposited on pre-annealed Si should, in principle, yield an enhanced active area in catalytic applications. AFM images reveal that globules seem to grow side-by-side forming a continuous layer on silicon, see Figure 6.6 (a-c), whereas films on c-sapphire exhibit globules that are well isolated from each other, see Figure 6.6 (d-f). The foregoing AFM results are consistent with SEM results reported earlier.

6.1.5. Catalyst testing for Fischer-Tropsch synthesis

Catalyst activity has been evaluated in terms of decreasing pressure in the reactor during the batch operation period (of 3 h) due to the extremely low surface area of the catalyst, which

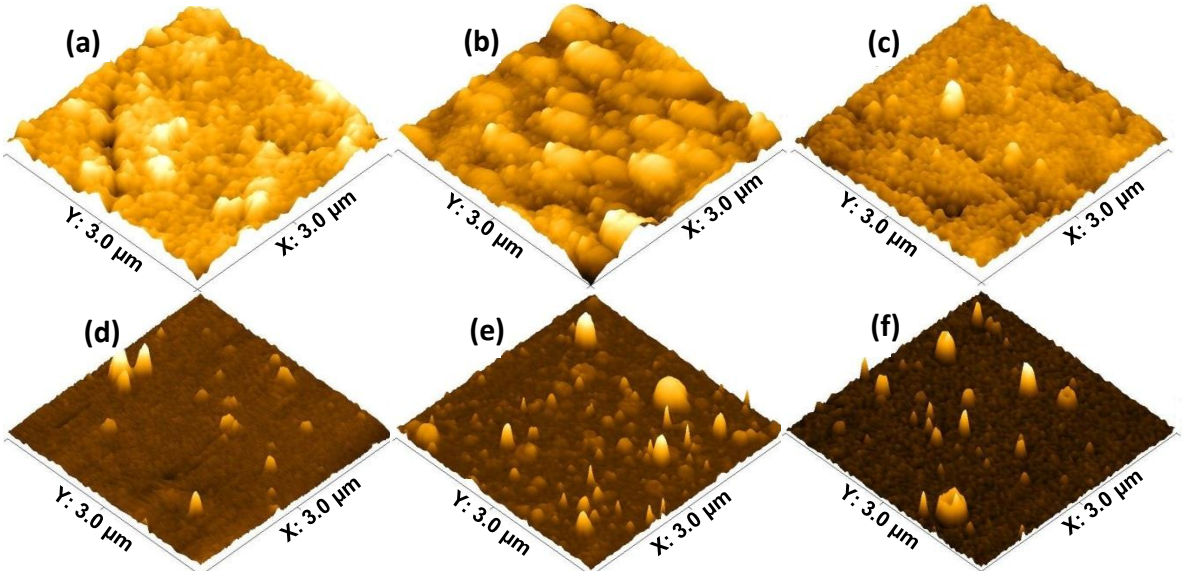

Figure 6.6: 3D AFM topographs of CZO films with different Co loadings grown on silicon (a) x = 0.05, (b) x = 0.1, (c) x = 0.2; and on c-sapphire (d) x = 0.05, (e) x = 0.1, (f) x = 0.2.

has been estimated at about 30 cm^2 for the 10 g of catalyst used in the test (or effectively given as 3 $cm^2.g^{-1}$). Figure 6.7 shows the evolution of the activity of Co-ZnO/SiO_2 catalyst tested at 500 K (227^oC) during batch operation after different times of continuous flow (on stream). It can be observed that for the first run conducted after 1 h of the catalyst on stream, the reaction shows a CO conversion of 20% at the end of the batch mode period. The second run, conducted after 6 h on stream, shows 16% CO conversion, while the third run carried out after 24 h on stream shows a 27% CO conversion. The CO conversion (%) has been calculated using equation 1.10 (see chapter 1, section 1.7.4). In comparing the activity of the catalysts under similar reaction conditions, it has been observed that catalyst activity decreases in the order of Co-ZnO/SiO_2 >> Co-ZnO/Al_2O_3 > Co-ZnO/Si when tested at 500 K. This is illustrated in Figure 6.8, and seems to indicate that Co-ZnO films supported on the oxide substrates have a superior catalytic performance. This may be explained in terms of energy band gap of substrate material, whereby quartz (8.95 eV) and c-sapphire (6.95 eV) exhibit higher band gaps than Si (1.09 eV) (Miyazakia, 2012 ; Lin and Fua, 2011). In the case of Si, electrons in the lattice are able to

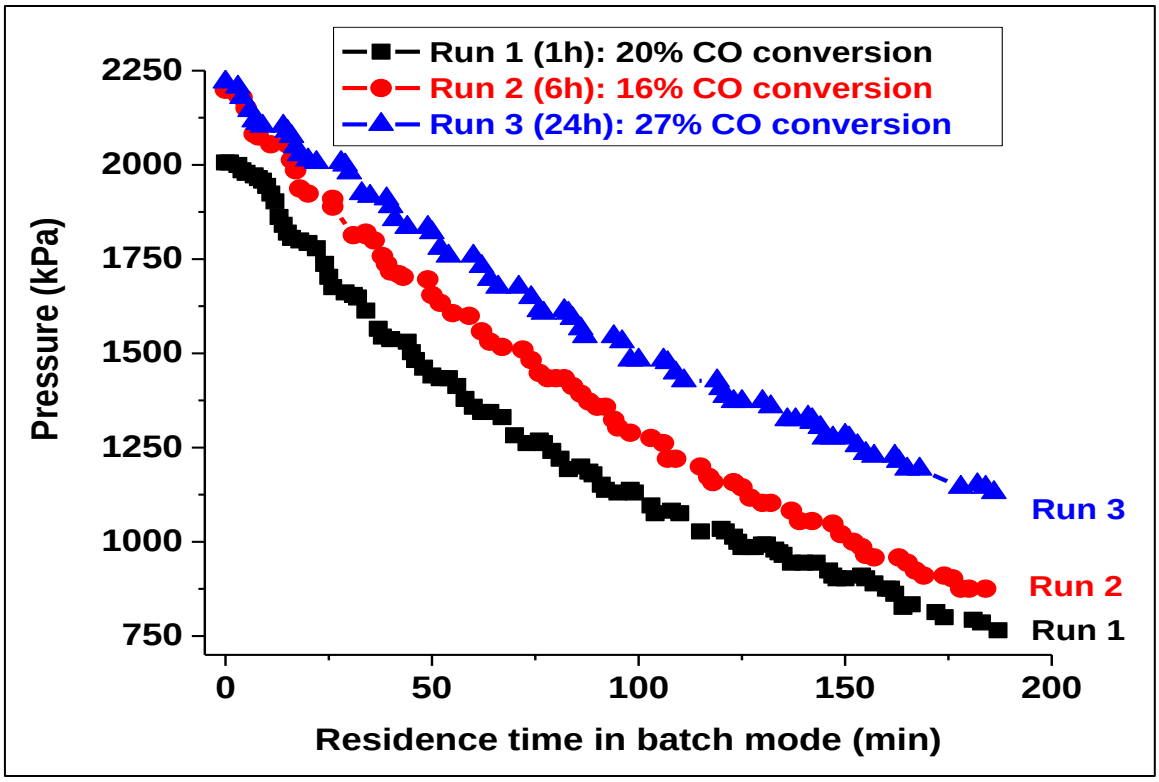

Figure 6.7: Catalyst activity plots of Co-ZnO/SiO_2 tested at 500 K shown by pressure drop in batch mode, with total online time and the corresponding conversion (at the end of each batch reaction) indicated in the inset.

overcome the band gap and, eventually, may couple with electrons in the lattice of Co resulting in either electronic saturation of cobalt or inducing its oxidation (Kariper and Özpozan, 2013). Figure 6.9 shows the activity of Co-ZnO/Al_2O_3 at two different temperatures, viz., 500 K and540 K. Interestingly, very similar pressure versus batch time profiles are obtained at the two different temperatures, albeit CO conversion is somewhat higher at 540 K (22%) than at 500 K (14%). Since Co-ZnO/Si catalyst has shown dismal performance (has required about 5 days to collect enough product for GC analysis), it has not been considered in the selectivity analysis in this work. The other two catalysts, i.e., Co-ZnO/Al_2O_3 and Co-ZnO/SiO_2, show high selectivity towards the production of longer-chain hydrocarbons with fuel fractions that contain less gasoline ($C_5 – C_{12}$), but richer in diesel ($C_{13} – C_{20}$) and waxes (C_{21+}), as demonstrated in

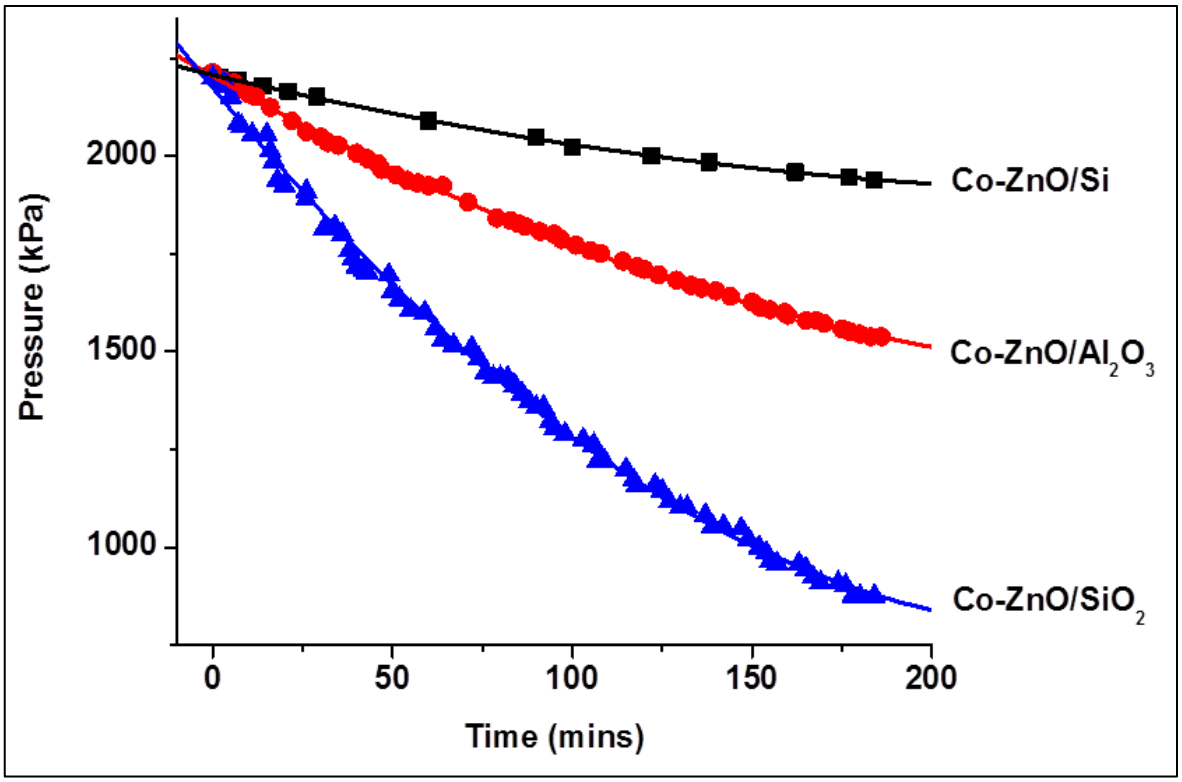

Figure 6.8: Plot showing decreasing catalyst activity in the order of Co-ZnO/Si_2 >> Co-ZnO/Al_2O_3 > Co-ZnO/Si tested at 500 K (227^{o}C).

Figure 6.10. Table 6.1 shows detailed selectivity data for different products under the conditions of Figure 6.10. The data indicate that Co-ZnO/Al_2O_3 catalyst has a selectivity of ~4% towards gasoline, 31% for diesel, and 65% for waxes, while Co-ZnO/SiO_2 catalyst shows a selectivity of ~12% towards gasoline, 51% for diesel, and 37% for waxes. In addition, Co-ZnO/SiO_2 catalyst favors the production of a substantial amount of carbon, which was deposited in the basket

Table 6.1: Catalyst selectivity of Co-ZnO/Al_2O_3 and Co-ZnO/SiO_2 tested at constant pressure of 2 MPa and temperature of 540 K in the continuous flow mode for 120 h.

Catalyst	Carbon dioxide	Light gases			Gasoline	Diesel	Waxes
Formula	CO_2	CH_4	C_2	C_3-C_4	(C_5-C_{12})	(C_{13}-C_{20})	(C_{21+})
Co-ZnO/Al_2O_3	0.10	0.30	0.06	0.00	3.72	30.94	65.34
Co-ZnO/SiO_2	0.08	0.10	0.00	0.00	12.40	50.94	36.67

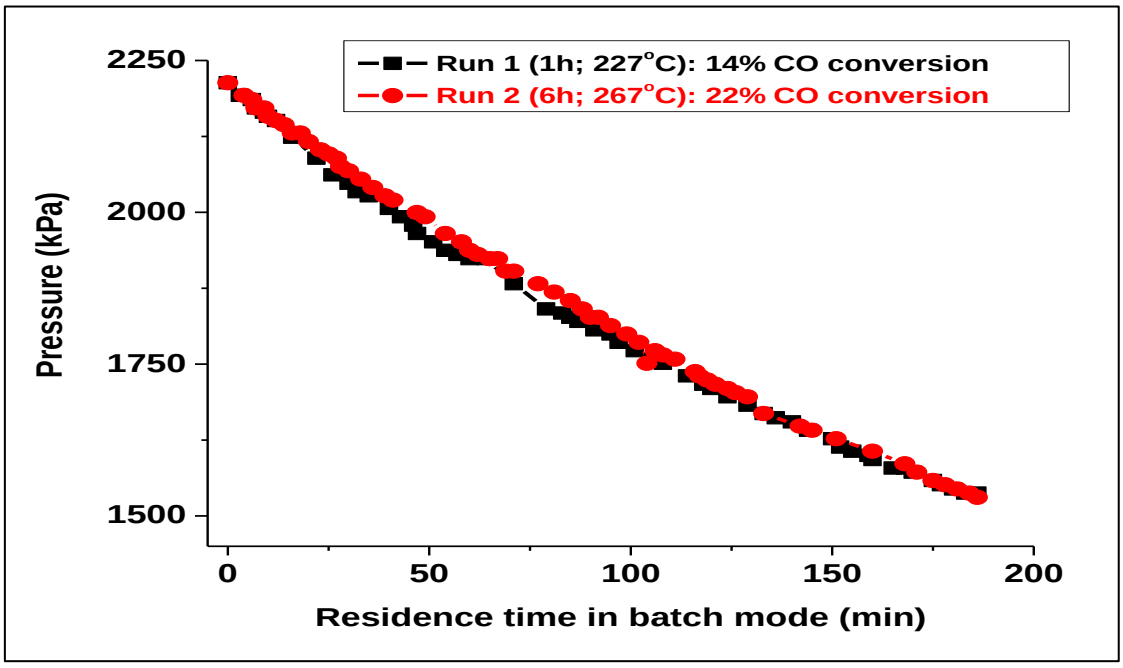

Figure 6.9: Catalyst activity of Co-ZnO/Al_2O_3 tested at 500 K and 540 K, with total online time and the corresponding conversion (at the end of each batch reaction) indicated in the inset.

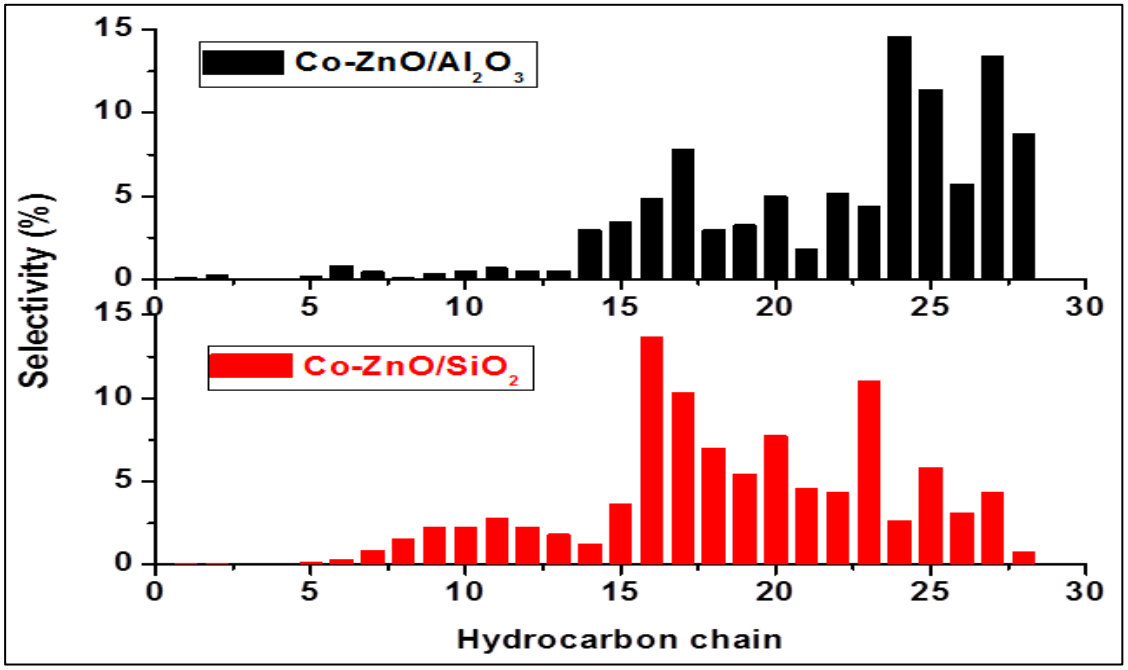

Figure 6.10: Catalyst selectivity of Co-ZnO/Al_2O_3 and Co-ZnO/SiO_2 tested at constant Pressure of 2 MPa and temperature of 540 K in the continuous flow mode for 120 h.

reactor, and about 10 cm^3 of H_2O after 120 h on stream, a feature that has not been observed when Co-ZnO/Al_2O_3 catalyst is used. The selectivity of nano-catalysts has been calculated using equation 1.12 (see chapter 1, section 1.7.4).

Chapter 7: Conclusions and future directions

7.1 Conclusions

The present work is a feasibility study towards the deposition of $Co_xZn_{1-x}O$ thin-film NCs via pulsed electron beam ablation. The main goals of this study are a) to access the potential of PEBA as an alternative thin film deposition technique for the preparation of CZO thin films, and, b) to exploit the deposited film, as model nano-catalysts in Fischer Tropsch synthesis. To this end, various operation conditions of PEBA, viz., deposition temperature, accelerating voltage and pulse frequency and substrate materials have been systematically investigated. The effects of substrate materials, Co loadings and heat treatment on the films properties have also been assessed. Discussion of the experimental data revolves around three main aspects of the films to have the potential as a model nanocatalyst, viz., presence of elemental cobalt, cobalt crystal phase (hexagonal-close packed), and size of nanoparticles. Finally, the potential of the films as model nano-catalysts has been evaluated in the context of the Fischer-Tropsch process in a 3-phase continuously-stirred tank slurry reactor (3-φ-CSTSR) using a Robinson-Mahoney stationary basket (RMSB) and the results are discussed in terms of catalytic activity and selectivity. The most important findings obtained throughout this work are summarized hereafter.

In the first series of deposition runs, CZO thin film NCs have been prepared from ablation of a single Co:ZnO target (containing 20 w% cobalt) on Si(100) at 14 kV, 2 Hz and at three different substrate temperatures (350^{o}C, 400^{o}C, 450^{o}C). The analytical data confirm the presence of O, Co and Zn in the deposited films and that the deposition process is congruent whereby the deposited films have a stoichiometry (20±5 w% Co) close to that of the target material. The films consist of nano-globules, which are cobalt rich-regions with ~20-70 w% Co. The size of the

globules increases and their number decreases as the temperature increases. It has been found that a substantial portion of Co atoms in the films are present as CoO as well as in elemental Co form. The hcp metallic cobalt phase also exists in the films, and whose contents increases with deposition temperature. It has been observed that the films produced at 14 kV exhibit a substantial number of particles whose size is below a threshold value of 4 nm. Generally, the activity of nano-catalyst for FTS decreases very sharply below the threshold value of the particle size. Therefore, the deposition runs have been carried out at higher voltage values (15 kV, 16 kV) in the remained of the experimental campaigns.

In the second series, CZO films have been grown via ablation of a CZO target (containing 20 w% Co) on Si (100) at deposition temperature of 350^{o}C to 800^{o}C, accelerating voltage of 15 kV and 16 kV, and a pulse frequency of 2 Hz. Films deposited at a temperature between 350^{o}C and 450^{o}C, and for both accelerating voltage values, appear to follow the Stranski-Krastanov growth model, while films deposited at 600^{o}C follow the Volmer-Weber model. The films obtained at 800^{o}C are the thickest (~120 nm). The films exhibit Co-rich globules (~20 nm to 300 nm) containing ~15–43 wt.% Co. At both accelerating voltages, films exhibit a higher proportion of particles whose diameter is in the range of ~6-10 nm, and no particles are found to be less than 5 nm in diameter. For films deposited in the temperature range 350^{o}C–450^{o}C, the temperature appears to have no considerable effect on globule size and to only moderately affect the density of the globules. When deposition temperature is further increased to 600^{o}C, the globule size is drastically decreased and the density of the globules increases. At higher beam accelerating voltage (16 kV), the overall globule size and globule density slightly increase. The roughness significantly increases (~19–23 nm) for the films produced at higher deposition temperatures (600^{o}C and 800^{o}C). The films exhibit Co in three chemical states, i.e., Co^{o}, Co^{2+},

and Co^{3+}, in the films, suggesting the coexistence of oxidized and non-oxidized valence states of cobalt near the film surface. The Co content in the films seems to be unaffected by accelerating voltage while it increases with temperature in the range 350°C–450°C. At higher deposition temperatures (600°C and 800°C), the films exhibit faceted particles and are relatively rough. The films deposited at 800°C consist of a predominantly Co phase. In term of higher hcp metallic Co content in the films, 600°C appears to be the optimum deposition temperature. The findings hint at the potential of the deposited films as model nano-catalysts in a variety of chemical processes.

In the third series, the films have been grown on c-sapphire and Si(100) via ablation of CZO target (containing 20 w% Co) at 450°C, 16 kV and at four different pulse frequencies (I Hz, 2 Hz, 4 Hz, 8 Hz). The beam frequency, overall, can substantially affect the structural and morphological characteristics of the deposited films. The film thickness increases as the beam frequency is increased. The beam frequency of 4 Hz seems to be a critical value as it corresponds to the maximum (minimum) globule size (density). The reduced globule size in films deposited at lower beam frequency results in smoother films. The average arithmetic roughness of the films increases with beam frequency. The beam frequency does not appear to substantially affect metallic Co concentration in the films. The films exhibit Co in three chemical states, i.e., Co^{o}, Co^{2+}, and Co^{3+}, in the films, suggesting the coexistence of oxidized and non-oxidized valence states of cobalt near the film surface. The deposited films exhibit hcp metallic Co hinting at the potential of CZO thin films model nano-catalysts, albeit to a lesser extent than the films deposited in series 2.

In fourth series, CZO thin film nano-catalysts have been deposited on three different crystalline substrates, viz., quartz (SiO_2), c-sapphire(Al_2O_3), and Si(100), and on one amorphous (pyrex) substrate at 2 Hz, 450°C and 16 kV. The growth of Co-ZnO thin films on the four

substrates seems to follow the Stranski-Krastanov (S-K) growth model. The type of substrate material does not seem to affect the thickness, average particle size, density of Co-rich nano-globules, and the average arithmetic roughness of the films. The films exhibit Co in three chemical states, i.e., Co^{o}, Co^{2+}, and Co^{3+}, in the films, suggesting the coexistence of oxidized and non-oxidized valence states of cobalt near the film surface. The substrate material seems to affect the content of hcp metallic Co in the films. The films deposited on crystalline substrates, viz., c-sapphire and quartz, contain a higher hcp metallic Co content relatively to the films deposited on amorphous pyrex substrate. In this series, CZO thin films have the potential to be used model nano-catalysts but to lesser extent than film prepared in series 2.

In the fifth series, CZO films have been deposited from a CZO target (containing 20 w% Co) within the temperature range 350^{o}C-450^{o}C, at electron beam acceleration voltages of 15 kV and 16 kV and beam frequency of 4 Hz. The films have been subjected to thermal annealing at either 400^{o}C or 600^{o}C for one hour. Post annealing of CZO film at 400^{o}C leads to a significant increase in film thickness, whereas annealing at 600^{o}C (which results in films with a wrinkle-like structure) leads to a marginal decrease in film thickness relatively to as-grown films. The morphological changes do not appear to be dramatically affected by the beam accelerating voltage as the latter is varied from 15 kV to 16 kV. The films exhibit Co in three chemical states, i.e., Co^{o}, Co^{2+}, and Co^{3+}, in the films, suggesting the coexistence of oxidized and non-oxidized valence states of cobalt near the film surface. Overall, post-annealing treatment significantly affects the structural and morphological properties of the films. Metallic Co content increases marginally in as-grown CZO films as the deposition temperature is raised from 350^{o}C to 450^{o}C. Annealing at 400^{o}C and 600^{o}C seem to improve the metallic Co signals in the films. Films annealed at 400^{o}C have higher average particle size and degree of crystallinity of ZnO hexagonal

wurtzite structure relatively to films annealed at 600^{o}C. Films annealed at 400^{o}C exhibit larger content in hexagonal closed pack (hcp) metallic Co (Co^{o}) compared to films annealed at 600^{o}C and to as-grown films. Thus, the quality and properties of CZO thin films can be improved by judiciously selecting growth conditions and post-growth annealing at appropriate temperature.

In the sixth series, CZO films have been grown at 1 Hz, 450^{o}C via ablation of three different targets, i.e., containing 5 w%, 10 w% and 20 w% cobalt on pre-annealed (1100^{o}C) Si (100) and c-sapphire substrates. The globule size is highest for a Co loading of 0.10. The globules are made up made up of nanoparticulates whose size is in the range of 11 nm-20 nm for both substrates. The type of pre-annealed substrate seems to strongly affect film morphology. The films on c-sapphire seem to follow the Stranski-Krastanov growth model, whereas films grown on silicon appear to follow the Volmer-Weber model. Co loading does not seem to have any significant effects on the film thickness, while the thickness increases on pre-annealed substrates in comparison with films deposited on un-annealed substrates. The films on both substrates exhibit a prominent ZnO hexagonal wurtzite structure for x = 0.05, whereas higher Co loading (x = 0.1, 0.2) results in a strong deformation of ZnO wurtzite lattice and in a higher content of hexagonal close-packed (hcp) metallic Co in CZO films. The hcp metallic Co is present in CZO films on Si for all Co loadings, whereas the films on c-sapphire show metallic cobalt signals only for Co loadings of 0.1 and 0.2. It seems that for low Co loading, i.e., x = 0.05, Co ions are largely incorporated into substitutional sites of ZnO lattice, while for Co loadings of 0.1 and 0.2 Co ions are located at interstitial sites of zinc oxide structure. The films exhibit Co in three chemical states, i.e., Co^{o}, Co^{2+}, and Co^{3+}, in the films, suggesting the coexistence of oxidized and non-oxidized valence states of cobalt near the film surface. Overall, metallic Co seems to be highest for a Co loading of 0.2 on both substrates.

Based on characterization of the deposited CZO thin films by complementary analytical techniques, the best quality films, viz., thin films prepared in series 4 and series 6 on crystalline substrates, have been selected for testing in a reactor setting. The films have been evaluated as model nano-catalysts for FTS in a 3-phase continuously-stirred tank slurry reactor (3-φ-CSTSR) using a Robinson-Mahoney stationary basket (RMSB). Films deposited on oxide substrates (SiO_2, Al_2O_3, pyrex) show good activity and high selectivity toward the longer chain hydrocarbons, while films on Si show poor performance in FTS tests. Fuel fractions, which have been observed in FT liquid products, are rich in diesel and waxes. Catalyst activity decreases in the order of Co-ZnO/SiO_2 >> Co-ZnO/Al_2O_3 > Co-ZnO/Si when tested at 500 K. The produced fuel fractions contain less of gasoline components (C_5–C_{12}) and more of the diesel fraction (C_{13}–C_{20}), alongside a significant production of waxes (C_{21+}). Specifically, Co-ZnO/Al_2O_3 nano-catalyst shows a selectivity of ~4%, 31%, and 65% towards gasoline, diesel, and waxes, respectively, while Co-ZnO/SiO_2 nano-catalyst shows a selectivity of ~12%, 51%, and 37%, for gasoline, diesel, and waxes, respectively.

7.2 Future directions

There are several directions along which this research can be further perused and improved. Based on the findings of the present work, a few suggestions are presented hereafter that can either be helpful to further tune film deposition process parameters, thin film catalyst morphology and FT reactor configuration and/or confer new physico-chemical properties to CZO thin film nano-catalysts. The future work could possibly focus on:

- Films can be deposited on both sides of the substrate in order to increase the catalyst active sites on the substrate surface. Higher concentration of the active sites will potentially results in higher activity and selectivity of the catalysts.
- Porous substrates can be used in order to increase the surface to volume ratio of thin film

- nano-catalyst.
- Various transition metals such as Cr, Mn, Mo, Ta, V, W and Zr, etc. can be added to Co based FT thin film nano-catalysts in order to improve activity and selectivity of the catalysts.
- Different dopants, viz, Fe, Ru, Ni (active metals for FTS) can be used instead of Co in order to evaluate these metals as this film nano-catalyst in FT reactor settings.
- Fixed bed tubular (FBT) reactor configuration can be used to test CZO thin film nano-catalyst. FBT might be a more suitable reactor configuration relatively to the slurry reactor in order to evaluate this kind of catalysts for FTS.
- Microstructured reactors may be more suitable to evaluate thin film nano-catalysts for FTS. Many advantages of microreactors have been reported over the conventional FT reactors settings viz., process efficiency, process intensification, load flexibility and product efficiency (Piermartini et al., 2017).
- Post (pre) thermal treatment of films (substrate) can be done under vacuum, which may enhance the metallic Co content in the films (Wang et al., 2013).
- The prepared CZO thin films can be employed as model nano-catalysts in many other energy intensive processes viz., hydrogenation of unsaturated organic feed stocks, steam reforming, hydrogen production and photocatalysis.

References

Acosta, D.R., Castaneda, L., Suarez, A.L., Santiago, A.G., 2009. Cobalt-doped zinc oxide thin solid films deposited by chemical spray techniques on silicon (100) substrates: The effects of the [Co]/[Zn] ratio on the morphological and physical properties. *Physica B* 404, 1427–431.

Adams, A., Calif, G., 1990. Thin film thickness measuring method. United States patents, 19. number 4,899,055. 1–8.

Adesina, A.A., 1996. Hydrocarbon synthesis via Fischer-Tropsch reaction: travails and triumphs. *Applied catalysis A: General* 138, 345–367.

Adegbuyi, P.A.O.A., 2009. The Effect of Annealing on the Microstructure of Mechanical Properties of a rolled steel product. *P. J. Sic. Tech*. 10, 149–162.

Aga, R.S., Cox, C., Ueda, A., Jackson, E, Collins, W.E., Mu, R., 2006. Influence of background gas pressure charging potential and target distance on the spot size ablated by single pulsed electron beam. *J. Vac. Sci. Technol. A* 24,11–14.

Ali, A., Henda, R., Fagerberg, R., 2017. Effect of temperature and discharge voltage on the properties of Co-doped ZnO thin films deposited by pulsed electron beam ablation. *Appl. Surf. Sci.* 422, 1082–1092.

Ali, A., Morrow, P., Henda, R., Fagerberg, R., 2016. Deposition of Cobalt Doped Zinc Oxide Thin Film Nano-Composites Via Pulsed Electron Beam Ablation. *MRS Adv.* 1, 433–439.

Ali, A.M., Shafeeq, A., Asghar, H.M.A., Hussain, S.N., Sattar, H., 2012. Doped Metal Oxide (ZnO) and Photocatalysis: A Review. *J.P.I.Ch.E.* 40, 11–19.

Aliofkhazraei, M., Ali N., 2014. Chapter 7: AFM Applications in Micro/Nanostructured Coatings, in Comprehensive Materials Processing. Ed. in chief Hashmi, S., *Elsevier Inc.*, vol.7, 191–241.

Alves, T.M.de.L., Amorim, B.F., Torres, M.A.M., Bezerra, C.G., Medeiros, S.N.de., Gastelois, P.L., Outon, L.E.F., Macedo, W.A.de.A., 2017. Wasp-waisted behavior in magnetic hysteresis curves of $CoFe_2O_4$ nanopowder at a low temperature: experimental evidence and theoretical approach. *RSC Adv.* 7, 22187–22196.

Aluha, J., Boahene, P., Dalai A., Hu Y., Bere K., Braidy N., Abatzoglou N., 2015. Synthesis and Characterization of Co/C and Fe/C Nanocatalysts for Fischer−Tropsch Synthesis: A Comparative Study Using a Fixed-Bed Reactor. *Ind. Eng. Chem. Res.* 54, 10661–10674.

Aluha, J., Braidy, N., Dalai A., Abatzoglou, N., 2016. Low-temperature Fischer-Tropsch

synthesis using plasma-synthesized nanometric Co/C and Fe/C catalysts. *Can. J. Chem. Eng.* 94, 1504–1515.

Aravind, A., Hasna, K., Jayaraj, M.K., Kumar, M.,Chandra, R., 2014. Magnetic and Raman scattering studies of Co-doped ZnO thin films grown by pulsed laser deposition. *Appl Phys A.* 115, 843–849.

Ashrafi, A., Jagadish, C., 2007. Review of zincblende ZnO: Stability of metastable ZnO phases, *J. Appl. Phys*. 102, 071101–12.

Baijense, C.R., Rekkel, T., 2009. Fischer Tropsch Catalyst. United States patents, Patent # US 7,563,747 B2, pp.1–10.

Barbier, A., Tuel, A., Arcon, I., Kodre, A., Martin, G.A., 2001. Characterization and catalytic behavior of Co/SiO_2 Catalysts: Influence of Dispersion in the Fischer–Tropsch Reaction. *J. Catal.* 200, 106–116.

Bardeleben, H.J., Jedrecy, N., Cantin, J.L., 2008. Ferromagnetic resonance signature of metallic Co clusters in ferromagnetic ZnCoO thin films. *Appl. Phys. Lett.* 93,142503–5.

Belghazi, Y., AitAouaj, M., Yadari, M. E., Schmerber, G., Bouillet, C.U., Leuvrey, C., Colis, S., Abd-lefdil, M., Berrada, A., Dinia, A., 2009. Elaboration and characterization of Co-doped ZnO thin films deposited by spray pyrolysis technique. *Microelectron. J*. 40, 265–267.

Benramache, S., Benhaoua, B., Chabane, F., 2012. Effect of substrate temperature on the stability of transparent conducting cobalt doped ZnO thin films. *J. Semicond*. 33, 093001–4.

Benramache, S., Temam, H.B., Arif, A., Guettaf, A., Belahssen, O., 2014. Correlation between the structural and optical properties of Co-doped ZnO thin films prepared at different film thickness. *Optik* 125,1816–1820.

Bezemer, G. L., Bitter, J.H., Kuipers, H.P.C.E., Oosterbeek, H., Holewijn, J.E., Xu, X., Kapteijn, F., Dillen, A.J.V., Jong K.P.de., 2006. Cobalt Particle Size Effects in the Fischer-Tropsch Reaction Studied with Carbon Nanofiber Supported Catalysts. *J. Am. Chem*. Soc.128, 3956–3963.

Boerrigter, H., Uil, H., 2002. Green Diesel from Biomass via Fischer-Tropsch synthesis: New Insights in Gas Cleaning and Process Design, Pyrolysis and Gasification of Biomass and Waste. *Expert Meeting*, pp.1–13.

Brabazon, D., Raffer, A., 2015. Chapter 3: Advanced characterization techniques for nanostructures; in Emerging Nanotechnologies for Manufacturing (Second Edition), ed., Ahmed, W. Jackson, M.J. *Elsevier Inc.*, pp.53–85.

Breejen, J.P.D., Sietsma, J.R.A., Friedrich, H., Bitter, J.H., Krijn, P., DeJong, K.P.D., 2010.

Design of supported cobalt catalysts with maximum activity for the Fischer-Tropsch synthesis. *J. Catal.* 270,146–152.

Bryant, W.A., 1977. Review; The fundamentals of chemical vapour deposition. *J. mat. Sci.* 12, 1285–1306.

Caglar, Y., 2013. Sol-gel derived nanostructure undoped and cobalt doped ZnO: Structural, optical and electrical studies. *J. Alloys Compd.* 560, 181–188.

Carlsson, J.O., Martinn P.M., 2010. Chapter 7: Chemical vapor deposition, in Handbook of deposition technologies for films and coatings (Third Edition); Science, Applications and Technology. Ed. Peter M. Martin P.M. William Andrew *Elsevier Inc.* pp. 314–363.

Callister, J.W.D., 2007. Materials science and engineering: An introduction, *John Wiley & Sons, Inc.* pp. 39–74.

Chaturvedi, S., Dave, P.N., Shah, N.K., 2012. Applications of nano-catalyst in new era. *J. Saudi Chem. Soc.*16, 307–325.

Christen., H.M., Eres, G., 2008. Recent advances in pulsed-laser deposition of complex oxides. *J. Phys. Condens. Matter*. 20, 264005–16 .

Christiansen , J., Schultheiss, C., 1979. Production of high current particle beams by low pressure spark discharges. J. Z. Phys. A 290, 35–41.

Chusuei, C.C., Goodman D.W., 2003. X-Ray Photoelectron Spectroscopy, Encyclopedia of Physical Science and Technology (Third Edition). pp.921–938.

Clarkson, J.S., Gamlin, T.D.,Hardy L.T., 2012. Fischer Tropsch Process. Patent number US 8,329,765 B_2, pp.1–10.

Collins, A.M., 2012. Nanotechnology Cookbook; Practical, Reliable and Jargon-free Experimental Procedures. *Elsevier Ltd.* pp.17–73.

Dalai, A.K.,Davis, B.H., 2008. Fischer-Tropsch synthesis: A review of water effects on the performances of unsupported and supported Co catalysts. *Appl. Catal., A* 348, 1–15.

Davis, B. H., 2002. Overview of reactors for liquid phase Fischer– Tropsch synthesis. *Catal Today*, 71, 249–300.

Davis, J.R., 1992. Asm Materials Engineering Dictionary, Technology & Engineering. New York, USA.

Donaldson, J.D., Beyersmann, D., 2012. Cobalt and Cobalt Compounds. Ullmann's

Encyclopedia of Industrial Chemistry, vol. 9, *Wiley-VCH Verlag GmbH & Co.KGaA, Weinheim*, 430–432.

Dorneles, L., Venkatesan, S. M., Gunning, R., Stamenov, P., Alaria J., Rooney M., Lunney, J. G., Coey J. M. D., 2007. Magnetic and structural properties of Co-doped ZnO thin films. *J. Magn. Magn. Mater.* 310, pp. 2087–2088.

Dry, M.E., 2002, High quality diesel via the Fischer–Tropsch process – a review. *J. Chem.*

Technol. Biotechnol. 77, 43-50.

Ellmer, K., Klein, A., Rech, B., 2008. Transparent Conductive Zinc Oxide, *Springer-Verlag Berlin,* pp.1–118.

Fadley, C.S., 2010. X-ray photoelectron spectroscopy: Progress and perspectives. *J. Electron. Spectrosc. Relat. Phenom.* 178, pp.2–32.

Fan, J.C., Sreekanth, K.M., Xie, Z., Chang, S.L., Rao, K.V., 2013. p-Type ZnO materials: Theory, growth, properties and devices. *Prog. Mater Sci.* 58, 874–985.

Ferreira, M.G.S., Zheludkevich, M. L., Tedim J., 2011. Chapter 9: Advanced protective coatings for aeronautical applications. In Nanocoatings and ultra-thin films; Technologies and applications. Eds. Makhlouf, A.S.H., Tiginyanu, I,. *Woodhead Publishing Limited*, pp. 235–270.

Fouchet, A., Prellier, W., Mercey, B., 2006. Influence of the microstructure on the magnetism of Co-doped ZnO thin films. *J. Appl. Phys.*100, pp. 013901–6.

Freide, J.J.H.M.F., Hardy, L.T., 2009. Modified catalyst and use of this catalyst for the conversion of synthesis gas to hydrocarbons. patent No.: US 7, 566,678 B2, pp.1–6.

Gacic, M., Jakob, G., Herbort, C., Adrian, H., 2007. Magnetism of Co-doped ZnO thin films, Physical review B 75. pp. 205206–8.

Gafiychuk, V.V., Ostafiychuk, B.K., Popovycha, D.I, Popovych, I.D., Serednytski, A.S., 2011. ZnO nanoparticles produced by reactive laser ablation. *Appl. Surf. Sci.* 257, 8396–8401.

Gnanamani, M.K., Jacobs, G., Shafer, W.D., Davis, B.H., 2013. Fischer-Tropsch synthesis: Activity of metallic phases of cobalt supported on silica. *Catal. Today* 215, 13-17.

Gomati, M.M.E, Walker, C.G.H., 2014. Chapter 1: Toward Quantitative Scanning Electron Microscopy, in Advances in imaging and electron physics. Ed. Hawkes P.W., *Elsevier*, vol.183, pp.1–40.

Gon, J.L.W., Huang, K., Zhu, J., Meng, F., Song, X., Sun, Z., 2011. Effect of annealing temperature on photocatalytic activity of ZnO thin films prepared by sol-gel method. *Superlattices Microstruct*. 50, 98–106.

Gual, A., Godard, C., Castillon, S., Ferre, D.C., Claver, C., 2012. Colloidal Ru, Co and Fe-nanoparticles. Synthesis and application as nanocatalysts in the Fischer Tropsch process. *Catal. Today* 183, 154–171.

Gürbüz, O., Güner, S., Büyükbakkal, Ö., Çalışkan, S., 2015. Structural, optical, and conducting properties of crystalline ZnO:Co thin films grown by reactive electron beam deposition. *J. Magn. Magn. Mater.* 373, 90–95.

Hind, A.R., Chomette, L., 2011. The determination of thin film thickness using reflectance spectroscopy, *J. Agilent Technology*, SI-A-1205.

Hirano, T., Kozuka, H., 2003. Photoanodic properties of ZnO thin films prepared from zinc acetate solutions containing cobalt acetate and polyvinylpyrrolidone. *J. Mat. Sci.* 38, 4203–4210.

Hiu, S.R., Wu, M., Ge, S., Yan, D., Zhang, Y.D., Xiao, T.D., Yacaman, M.J., Miki-Yoshida, M., Hines, W.A., Budnick, J.I., 2002. Synthesis and characterization ofstructure controlled nano-cobalt particles. *MRS Proc.* 755, 20–26.

Hobel, M., Greek, J., Linker, G., Schultheiss, C. 1990, Deposition of superconducting YBaCuO thin films by pseudospark ablation. *J. Applied Physics Letters*, 56, pp. 973–975.

Homma, Y., Kobayashi, Y., Ogino, T., 2003. Role of transition metal catalysts insingle-walled carbon nanotube growth in chemical vapor deposition, *J. Phys.Chem. B* 107, 12161–12164.

Hullavarad, S., Hullavarad, N., Look, D., Claflin, B., 2009. Persistent Photoconductivity Studies in Nanostructured ZnO UV Sensors. *Nanoscale Res Lett.* 4, 1421–1427.

Ivill, M., Peartonm, S.J., Rawal, S., Leu, L., Sadik, P., Das, R., Hebard, A.F., Chisholm, M., Budai, J.D., Norton, D.P., 2008. Structure and magnetism of cobalt-doped ZnO thin films. New *J. Phys.* 10. 065002–21.

Jahangiri, H., Bennett, J., Mahjoubi, P., Wilson, K., Gua, S., 2014. A review of advanced catalyst development for Fischer-Tropsch synthesis of hydrocarbons from biomass derived syn-gas. *Catal. Sci. Technol.* 4, 2210–2229.

Jalili, N., Laxminarayana, K., 2004. A review of atomic force microscopy imaging systems: application to molecular metrology and biological sciences. *Mechatron.*14, 907–945.

Jaramillo, T.F., Baeck, S.H., Shwarsctein, A.K., Choi, K.S., Stucky, G.D., McFarl, E.W., 2005. Automated Electrochemical Synthesis and Photoelectrochemical Characterization of $Zn_{1-x}Co_xO$ Thin Films for Solar Hydrogen Production. *J. Comb. Chem.,* 7, 264–271.

Jayakrishnan ,D.S., 2012. Chapter 5: Electrodeposition: the versatile technique for

nanomaterials. In Corrosion protection and control using nanomaterials; A volume in Woodhead publishing series in metals and surface engineering. Eds. Saji, V.S., Cook, R.M., 86–125.

Jayakumar, O.D., Gopalakrishnan, I.K., Kulshreshtha, S.K., 2005. The structural and magnetization studies of Co-doped ZnO co-doped with Cu: Synthesized by co-precipitation method. J. *Mater. Chem.*15, pp.3514–3518.

Jess, A., Popp, R., Hedden, K., 1999. Fischer Tropsch Synthesis with nitrogen rich syngas fundamentals and reactor design aspects. *Applied Catalysis A: General* 186, 321–342.

Jiang, Q.D., Matacotta, F.C., Konijnenberg, M.C., Mueller, G., Schultheiss, C. 1994. Deposition of YBa_2 Cu_3 O_{7-x} thin films by channel-spark pulsed electron beam ablation. *Thin Solid Films* 241, 100–102.

Joshi, S., Nayak, M.M., Rajannaa, K., 2014. Effect of post-deposition annealing on transverse piezoelectric coefficient and vibration sensing performance of ZnO thin films. *Appl. Surf. Sci.* 296,169–176.

Harshavardhan, K.S., Strikovski, M., 2005. Pulsed electron-beam deposition of high temperature superconducting films for coated conductor applications, in Second Generation HTS Conductors, ed. Goyal, A., *Springer, Berli*n, pp. 109–133.

Hilal, N., Bowen, W.R., Alkhatib, L., ogunbiyi, O., 2006. A review of atomic force microscopy applied to cell interactions with membranes. *Chem. Eng. Res. Des.* 84, 282–292.

Kaiser, N., 2002. Review of the fundamentals of thin-film growth. *Applied Optics* 41, pp. 3053–3060.

Karaca, H., Safonova, O.V., Chambrey, S., Fongarland, P., Roussel, P., Constant, A.G., Lacroix, M., Khodakov, A.Y., 2011. Structure and catalytic performance of Pt-promoted alumina-supported cobalt catalysts under realistic conditions of Fischer-Tropsch synthesis. *J.Catal.* 277, 14–26.

Karamat, S., Rawat, R.S., Tan, T.L., Lee, P., Chen, R., Sun, H.D., Zhou, W., 2010. Ferromagnetism in ZnCoO thin films deposited by PLD. *Appl Phys A* 101, 717–722.

Karamat, S., Rawat, R.S., Lee, P., Tan, T.L, Springham, S.V., Ramanujan, R.V., 2013, Synthesis and characterization of bulk cobalt-doped ZnO and their thin films. *J. Supercond Nov. Magn.* 26, 3115–3123.

Kariper, E.A., Özpozan, T., 2013. Cobalt xanthate thin film with chemical bath deposition. *J. Nanomater* 2, 1–9.

Kelly, P.J., Arnell, R.D., 2000. Magnetron sputtering: a review of recent developments and

applications. Vacuum 56, 159–172.

Khare, N., Kappers, M.T., Wei, M., Blamire, M.G., MacManus-Driscoll J.L. 2006. Defect-induced ferromagnetism in Co-doped ZnO. *Adv. Mater.*,18, pp. 1449–1452.

Khodakov, A.Y., Chu, W., Fongarland, P., 2007. Advances in the Development of Novel Cobalt Fischer-Tropsch Catalysts for Synthesis of Long-Chain Hydrocarbons and Clean Fuels. *Chem. Rev.*, 107, pp.1692–1744.

Kim, J.H., Kim, H., Kim, D., Ihm, Y.E., Choo, W.K., 2004.The origin of room temperature ferromagnetism in cobalt-doped zinc oxide thin films fabricated by PLD. J. Eur. Ceram. Soc. 24, 1847–1851.

Kim, S. G., Kim, J. Y., Kim, H.J., 2000. Deposition of MgO thin films by modified electrostatic spray pyrolysis metho. *Thin Solid Films,* 376, pp. 110–114.

Kittilstved, k.R., Liu, K.W., Gamelin, D.R., 2006. Electronic structure origins of polarity-dependent high-TC ferromagnetismin oxide-dilutedmagnetic semiconductors. *Nat. Mater.* 5, 291–297.

Koren, G., Gupta, A., Baseman, R.J., Lutwyche, M.I., Laibowitz, R.B., 1989. Laser wavelength dependent properties of $YBa_2Cu_3O_{7-\S}$,thin films deposited by laser ablation. *Appl. Phys. Lett.* 55, 2450–2452.

Lee, D.Y., Kang, Y.C., Park, H.D., Ryu, S. K., 2003. V UV characteristics of BaAl O :Mn phosphor particles prepared from aluminum polycation solutions by spray pyrolysis. *J. Alloys Compd.* 353, pp. 252–256.

Lee, H.J., Jeong, S.Y., Cho, C.R., Park, C.H., 2002. Study of diluted magnetic semiconductor: Co-doped ZnO. *Appl. Phys. Lett.*, 81, pp. 4020–3.

Liming, H., Haque, E., Barg, S., 2008. Public policy discourse, planning and measures toward sustainable energy strategies in Canada. *Renewable and Sustainable Energy Reviews*, 12, 91–115.

Lim, S.W.; Hwang, D.K., Myoung, J.M., 2003. Observation of optical properties related to room-temperature ferromagnetism in co-sputtered $Zn_{1-x}Co_xO$ thin films. *Solid State Commun.* 125, 231–235.

Lin, B., Fua, Z., 2011. Green luminescent center in undoped zinc oxide films deposited on silicon substrates. *Appl. Phys. Lett.* 11, 943–945.

Liu, S.-Y., Chen, T., Wan, J., Ru, G.-P, Li, B.-Z., Qu, X.-P., 2009. The effect of pre-annealing of sputtered ZnO seed layers on growth of ZnO nanorods through a hydrothermal method. *Appl Phys A* 94, 775–780.

Liu, X., Li, X., Fujimoto, K., 2007. Effective control of carbon number distribution during Fischer-Tropsch synthesis over supported cobalt catalyst. *Catal. Commun*. 8, 1329–1335.

Liu, X.C., Shi, E.W., Chen, Z.Z., Zhang, H.W., Xiao, B., Song, L.X., 2006. High-temperature ferromagnetism in (Co, Al)-co-doped ZnO powders. *Applied physics letters*, 88, 252503–3.

Liu, Y., Yang, S., Wei, G., Pan, J., Yuan, Y., Cheng C., 2013. Influence of Substrate Temperature on Stress and Morphology Characteristics of Co-Doped ZnO Films Prepared by Laser-Molecular Beam Epitaxy. *J. Mater. Sci. Technol.* 29, 1134–1138.

Liu, Z., Xing, Y., Xue, Y., Wu, D., Fang, S., 2015. Synthesis, characterization, and Fischer-Tropsch performance of cobalt/zinc aluminate nanocomposites via a facile and corrosion-free co-precipitation route. *J. Nanopart Res.*17, 1–11.

Llorca, J., Homs, N., and Piscina P.R.D.L., 2004. In situ DRIFT-mass spectrometry study of the ethanol steam-reforming reaction over carbonyl-derived Co/ZnO catalysts. *J. Catal.* 227, 556–560.

Losey, M.W., Kelly J.J., 2008. Chapter: 1.10, Electrodeposition. In Comprehensive microsystems. Eds. Gianchandani Y., Tabata O., Zappe H. vol. 1, pp. 271–292.

Lu, Z.L., Bian, X.F., Zou, W.Q., Xu, M.X., Zhang, F.M., 2010. The origin of ferromagnetism in Co-doped ZnO single crystalline films upon reducing annealings. *J. Alloys Compd*. 492, 31–34.

Mabee, W.E., Fraser, E.D.G., McFarlane, P.N., Saddler, J.N., 2006. Canadian Biomass Reserves for Biorefining. *Applied Biochemistry and Biotechnology* 129, 22–40.

Machlin, E.S., 2006. Materials Science in Microelectronics II; The Effects of Structure on Properties in Thin Films. Second edition. *Elsevier Ltd.* pp. 1–56.

Manouni, A.E., Tortosa, M., Manjon, F.J., Mollar, M., Mari, B., Royo, J.F.S., 2009. Effect of annealing on $Zn_{1-x}Co_xO$ thin films prepared by electrodeposition. *Microelectron. J*. 40, 268–271.

Mannsfeld, S.C.B., Virkar, A., Reese C.,Toney, M.F., Zhenan, Bao Z.,2009. Precise Structure of Pentacene Monolayers on Amorphous Silicon Oxide and Relation to Charge Transport. *Adv. Mater.* 21, 2294–2298.

Martin, L.W., Chu, Y.H., Ramesh, R., 2010. Advances in the growth and characterization of magnetic, ferroelectric, and multiferroic oxide thin films. *Mater. Sci. Eng., R.* 68, 89–133.

Mathis, J. E. and Christen, H.M. 2007. Factors that influence particle formation during pulsed electron deposition of YBCO precursors. *Physica C.* 459, 47–51.

Michler, G.H., 2008. Electron microscopy of polymers. *Springer-Verlag Berlin Heidelberg.* pp. 87– 42.

Miyazakia, S., 2001. Photoemission study of energy-band alignments and gap-state density distributions for high-k gate dielectrics. *J. Vac. Sci. Technol. B.* 19, 2212–2216.

Mohamed, R.M., McKinney, D.L, Sigmund, W.M., 2012. Enhanced nanocatalysts. *Mater. Sci. Eng., R.* 73, 1–13.

Morales, F., Weckhuysen, B.M., 2006. Promotion Effects in Co-based Fischer–Tropsch Catalysis. *Catalysis*,19, 2006, 1–40.

Muller, G., Konijnenberg, M., Kraft, G., Schultheiss, C., 1995. Deposition by means of pulsed electron beam ablation, in Science and Technology of Thin Films, eds. Matacotta, F.C.,Ottaviani, G., *World Scientific, Singapore*, pp. 89–119.

Narayanan, R., El-Sayed, M.A., 2005. Catalysis with Transition Metal Nanoparticles in Colloidal Solution: Nanoparticle Shape Dependence and Stability. *J. Phys. Chem. B*, 109, 12663–12676.

Negi D.S., Royc A., Loukya B., Dileep K., Shetty S., Kumar N., Kumar P.S.A., Datta R., 2014. Epitaxial Co metal thin film grown by pulsed laser deposition using oxide target. *J. Cryst. Growth.* 394, 112–115.

Neogi, S.K., Ghosh, R., Paul. G.K., Bera, S.K., Bandyopadhyay, S., 2009. Effects of Co doping on structural, morphological and transport properties of sol-gel AZO thin films. *J. Alloys Compd.* 487, 269–273.

Nistor, M., Gherendi, F., Mandache, N. B. 2011. Fast Imaging of Ablation Plasma Produced by a Pulsed Electron Beam. *IEEE Transaction On Plasma Science*. vol. 39, issue 11, pp. 2800–2801.

Nistor, M., Mandache, N.B., Perriere, J., 2008. Pulsed electron beam deposition of oxide thin films, *J. Phys. D: Appl.* 41,165205.

Norbeck, J.M., Park, C.S., 2008. Operation of a steam hydro-gasifier in a fluidized bed reactor, Patent application, U.S. patent number US 2008/0021120 A1, pp. 1–4.

Ohring, M. 2002. The materials science of thin films: deposition and structure, 2nd ed. *Academic Press, New York*, pp.375–414.

Okabe, K., Li, X., Wei, M., Arakawa, H., 2004. Fischer–Tropsch synthesis over Co–SiO_2 catalysts prepared by the sol-gel method. *Catal. Today* 89, 431–438.

Opel, M., Nielsen, K.W., Bauer, S.. Goennenwein, S.T.B., Cezar, J.C., Schmeisser, D., Simon, J., Mader, W., 2008. Nanosized superparamagnetic precipitates in cobalt-doped ZnO. *Eur. Phys. J. B*, 63, 437–444.

Palma, R.J.M., Lakhtakia, A., 2013. Chapter-15: Vapour deposition techniques. In Engineered biomimicry. Ed. Lakhtakia, A., *Elsevier Inc.*, pp. 383–398.

Pan, Z., Bukur, D.B., 2011. Fischer–Tropsch synthesis on Co/ZnO catalyst-Effect of pretreatment procedure. *Appl. Catal., A.* 404, 74–80.

Patil, P.S.,1999. Review: Versatility of chemical spray pyrolysis technique. *Mater. Chem. Phys.* 59, 185–198.

Peng, Y.Z., Liew, T., Song, W.D., An, C.W., Teo, K.L., Chong, T.C., 2005. Structural and optical properties of Co-doped ZnO thin films. *J. Supercond. Novel Magn*., 1, 97–103.

Perednis D., Gauckler, L.J., 2005. Thin film deposition using spray pyrolysis, *J. Electroceram.* 14,103–111.

Perez L.M., Aguirre N.M., Aguirre S.M., Angel O.Z., 2015. Nanometric structure of highly oriented zinc blende ZnO thin films, *Mater. Lett.*139, 63–65.

Poongodi, G., Anandan, P., Kumar, R.M., Jayavel, R., 2015. Studies on visible light photocatalytic and antibacterial activities of nanostructured cobalt doped ZnO thin films prepared by sol-gel spin coating method. *Spectrochim. Acta, Part A.*148, 237–243.

Prepelita, P., Medianu, R., Sbarcea, B., Garoi, F., Filipescu, M., 2010. The influence of using different substrates on the structural and optical characteristics of ZnO thin films. *Appl. Surf. Sci.* 256, 1807–1811.

Ptak, A.J. 2015. Chapter 4: Principles of Molecular Beam Epitaxy, in Handbook of Crystal Growth; thin film and epitaxy (second edition). Ed. Kuech, T., pp. 161–192

Radzimska, A.K., Jesionowski, T., 2014. Zinc Oxide-From Synthesis to Application: A Review. *Mater.* 7, 2833-2881.

Rampino, S., Pattini, F., Malagù, C., Pozzetti, L., Stefancich, M., Bronzoni, M., 2014. Application of a substrate bias to control the droplet density on Cu(In,Ga)Se_2 thin films grown by pulsed electron deposition. *Thin Solid Films* 562, 307–313.

Reuel, R.C., Bartholomew, C.H., 1984. Effects of Support and Dispersion on the CO Hydrogenation Activity/Selectivity Properties of Cobalt. *J. Catal.* 85, 78–88.

Ribic, P. R., Bratina, G., 2007. Behavior of the (0001) surface of sapphire upon high-temperature annealing. *Surf. Sci.* 601, pp. 44–49.

Rong, F.X., 1995. Liquid target pulsed laser deposition. *Appl. Phys. Lett.* 67, Pp. 1022–1024.

Rytter, E., Holmen A., 2016. On the support in cobalt Fischer–Tropsch synthesis—Emphasis on alumina and aluminates. *Catal. Today* 275, 11–19.

Paredes, A., 2014. Scanning electron microscopy, in Encyclopedia of food microbiology (second edition). Ed. In chief, Batt, C.A., pp. 693–701.

Park, C.H., Chadi D.J., 2005. Hydrogen-Mediated Spin-Spin Interaction in ZnCoO. *Phys. Rev. Lett.* 94, pp. 127204–4.

Park, J.H., Kim, M.G., Jang, H.M., Ryu, S., 2004. Co-metal clustering as the origin of ferromagnetism in Co-doped ZnO thin films. *Appl. Phys. Lett.*, 84,1338–1340.

Pearton, S.J., Norton, D.P., Ip, K., Heo, Y.W.,Steiner, T., 2005. Recent progress in processing and properties of ZnO. *Prog. Mater Sci.* 50, 293–340.

Pedersen, J.D., Esposito, H.J., Siong, K., 2011. Direct Synthesis and Characterization of Optically Transparent Conformal Zinc Oxide Nanocrystalline Thin Films by Rapid Thermal Plasma CVD. *Nanoscale Res. Lett.* 6, 1–12.

Piermartini, P., Boeltken, T., Selinsek, M., Pfeifer, P., 2017. Influence of channel geometry on Fischer-Tropsch synthesis in microstructured reactors. *Chem. Eng. J.* 313, 328–335.

Sadeqzadeh, M., Karaca, H., Safonova, O.V., Fongarland, P., Chambrey, S.,Roussel, P., Constant, A.G., Lacroix, M., Ferre, D.C., Luck, F.,Khodakov, A.Y., 2011. Identification of the active species in the working alumina-supported cobalt catalyst under various conditions of Fischer–Tropsch synthesis. *Catal. Today* 164, pp. 62–67.

Sakka, S., 2013. Chapter: 11.1.2, Sole-gel process and applications. In Handbook of advanced ceramics; Materials, applications, processing and properties. Ed., Somiya, S., pp. 883–910.

Salman, H.S.A., Abdullah, M.J., 2013. Structural, optical, and electrical properties of Schottky diodes based on undoped and cobalt-doped ZnO nanorods prepared by RF-magnetron sputtering. *Mater. Sci. Eng., B* 178, 1048–1056.

Samanta, K., Bhattacharya, P., Katiyar, R.S., 2006. Raman scattering studies in dilute magnetic semiconductor Zn1-xCoxO. *Phys. Rev. B* 73, pp. 245213–5.

Saravanan, R., Rani, M.P., 2012. Metal and Alloy Bonding: An Experimental Analysis ; Charge Density in Metals and Alloys, *Springer, London, UK*, pp. 22–64.

Sati, P., Deparis, C., Morhain, C., Schafer, S., Stepanov, A., 2007. Magnetic properties of single crystalline Zn1-xCoxO thin films. *Superlattices Microstruct.* 42, 191–196.

Sbrockeya, N.M.,Tompa, G.S., Kalkur, T.S., Zhang, J., Alpay, S.P., Cole, M.W., 2012. Voltage induced acoustic resonance in metal organic chemical vapor deposition SrTiO3 thin film. *J. Vac. Sci. Technol. B* 30, 061202–5.

Schultheiss, C., Hoffmann, F., 1990. Observation of directed bremsstrahlung from a hollow cathode plasma. *Nucl. Instrum. Methods Phys. Res., Sect. B* 51,187–191.

Schmidt, H., Diaconu, M., Hochmuth, H., Benndorf, G., Wenckstern, H.V., Biehne, G., Lorenz, M.,Grundmann, M., 2007. Electrical and optical spectroscopy on ZnO:Co thin films. *Appl. Phys. A* 88,157–160.

Serpone, N., 2006. Is the Band Gap of Pristine TiO_2 Narrowed by Anion- and Cation-Doping of Titanium Dioxide in Second-Generation Photocatalysts? *J. Phys. Chem. B* 110, 24287–24293.

Semaltianos, N.G., 2001. Thermally evaporated aluminum thin films. *Appl. Surf. Sci.* 183, 223–229.

Seyama, H., Soma, M., Theng, B.K.G., 2013. Chapter 2.5 – X-Ray Photoelectron Spectroscopy in Hand book of clay, Developments in Clay Science, *Elsevier Ltd* , vol. 5, pp. 161–176.
Siefert, W., 1984. Corona spray pyrolysis: A new coating technique with an extremely enhanced deposition efficiency. *Thin Solid Films,*120, 261–214.

Song, C.; Geng, K.W.; Zeng, F.; Wang, X.B.; Shen, Y.X. and Pan, F. 2006. Giant magnetic moment in an anomalous ferromagnetic insulator: Co-doped ZnO. *PhysiIcal Review B*, 73, 024405–6.

Song, C., Pan, S.N., Liu, X.J., Li, X.W., Zeng, F., Yan, W.S., He, B.,Pan, F., 2007. Evidence of structural defect enhanced room-temperature ferromagnetism in Co-doped ZnO. *J. Phys.: Condens. Matter*. 19, pp. 176229–8.

Song, D., Li, J., 2006. Effect of catalyst pore size on the catalytic performance of silica supported cobalt Fischer-Tropsch catalysts. *J. Mol. Catal. A: Chem*. 247, 206–212.

Strikovski, M., Kim, J.,Kolagani, S., 2010. Plasma energetics in pulsed laser and pulsed electron deposition. Springer Handbook of crystal growth, eds. Dhanaraj, G., Byrappa, K., Prasad, V., Dudley, M., *Springer-Verlag, Berlin Heidelberg*, pp. 1193–1211.

Stucki, J.W., Banwart, W.L. (eds.) (1980). Advanced Chemical Methods for Soil and Clay Minerals Research. Reidel, D., pp.169–203.

Su, X., Wang, L., Chen, J., Wan, X., Zhang, X., Wang, R.P., 2011. Role of cobalt in ZnO:Co thin films. *J. Phys. D: Appl. Phys*. 44, 265002–4.

Taabouche, A., Bouabellou, A., Kermiche, F., Hanini F., Bouachiba, Y., Grid, A., Kerdjac, T., 2014. Properties of cobalt-doped zinc oxide thin films grown by pulsed laser deposition on glass substrates. *Mater. Sci. Semicond. Process.* 28, 54–58.

Tavasoli, A., Abbaslou, R.M.M., Trepanier, M., Dalai, A.K., 2008. Fischer-Tropsch synthesis over cobalt catalyst supported on carbon nanotubes in a slurry reactor. *Appl. Catal*., A 345, 134–142.

Tillotson T.M., Gash, A.E., Simpson, R.L., Hrubesh, L.W., Satcher, Jr. J.H., Poco, J.F., 2001.

Nanostructured energetic materials using sol-gel methodologies. *J. Non-Cryst. Solids* 285,338–345.

Tortosa, M., Mollar, M., Manjón, F. J., Marí, B., Sánchez-Royo, J. F., 2008. Cathodic electrodeposition of ZnCoO thin films. *Phys. Stat. Sol.* 5, 3358–3360.

Tricot, S., Nistor, M., Millon E., Leborgne, C.B., Mandache, N.B., Perrière. J., Seiler, W., 2010. Epitaxial ZnO thin films grown by pulsed electron beam deposition. *Surf. Sci.* 604, 2024–2030.

Tsakoumis, N.E., Rønninga, M., Borg, Ø., Rytter, E., Holmen, A., 2010. Deactivation of cobalt based Fischer–Tropsch catalysts: A review. *Catal. Today* 154, 162–182.

Tuan, A.C., Bryan, J.D., Pakhomov, A.B., Shutthanandan, V., Thevuthasan, S., McCready, D.E., Gaspar, D., Engelhard, M.H., Rogers, J.W.J., Krishnan, K., Gamelin, D.R., Chambers, S.A., 2004. Epitaxial growth and properties of cobalt-doped ZnO on a-Al_2O_3 single-crystal substrates. *Phys. Rev. B* 70, 054424–9.

Ueda, K., Tabata, H., Kawaj, T., 2001. Magnetic and electronic properties of transition metal doped ZnO films. *Appl. Phys. Lett.* 79, 988–990.

Ullah, R., Dutta, J., 2008. Photocatalytic degradation of organic dyes with manganese-doped ZnO nanoparticles. *J. Hazard. Mater.* 156, 194–200.

Vadiyar, M.M., Kolekar S.S., Chang, J.-Y., Kashalec, A.A., Ghulec, A.V., 2016. Reflux Condensation Mediated Deposition of Co_3O_4 Nanosheets and $ZnFe_2O_4$ Nanoflakes Electrodes for Flexible Asymmetric Supercapacitor. *Electrochim. Acta* 222,1604–1615.

Vanalakar, S.A., Mali, S.S., Agwane, G.L., Kamble, A., Kim, L.Y., Patil, P.S., Kim, J.Y., Kim, J.H., 2016. Influence of laser repetition rate on the $Cu_2ZnSn(SSe)_4$ thin films synthesized via pulsed laser deposition technique. *Sol. Energy Mater. Sol.* 157, 331–336.

Vasireddy, S., Campos, A., Miamee, E., Adeyiga, A., Armstrong, R. Allison, J.D., Spivey, J.J., 2010. Study of attrition of Fe-based catalyst supported over spent FCC catalysts and their Fischer–Tropsch activity in a fixed bed reactor. *Appl. Catal., A* 372, pp. 184–190.

Venkatesan, T., Harshavardhan, K.S., Strikovski, M., Kim, J., 2005. Recent advances in the deposition of multi-component oxide films by pulsed energy deposition. In Thin Films and Heterostructures for Oxide Electronics, eds. Ogale, S.B. *Springer, Berlin Heidelberg*, pp.385–413.

Viart, N., Richard-Plouet, M., Muller, D., Pourroy, G., 2003. Synthesis and characterization of Co/ZnO nanocomposites: towards new perspectives offered by metalypiezoelectric composite materials. *Thin Solid Films* 437, 1–9.

Wadhwa, A. S., Dhaliwal, E. H. S., 2008. A Textbook of Engineering Material and Metallurgy,

University Science Press, New Delhi, India, pp.152–165.

Wan, H.J., Wu, B.S., Zhang C.H., Xiang H.W., Li, Y.W., Xu, B.F., Yi, F., 2007. Study on Fe-Al_2O_3 interaction over precipitated iron catalyst for Fischer–Tropsch synthesis. *Catal. Commun.* 8, 1538–1545.

Wang, A., Zhong, Z., Lu, C., Lv, L., Wang, X., Zhang, B., 2011, Study on field-emission characteristics of electrodeposited Co-doped ZnO thin films. *Physica B* 406, 1049–1052.

Wang, X., Ning, W., Hu, L., Li, Y., 2012. Influences of Al_2O_3 on the structure and reactive performance of Co/ZnO catalyst. *Catal. Commun.* 24, 61–64.

Wang, Z., Zhao, H., Yao, Q., Xu, J., Kimura, H., 2013. The influence of layer thickness and post annealing on magnetism of pulsed laser deposited ZnO/Co multilayers. *J. Magn. Magn. Mater.* 345, 41–47.

Wasa, K., 2012. Chapter 3: Sputtering Systems, in Handbook of sputter deposition technology; Fundamentals and applications for functional Thin films, nanomaterials, and MEMS, (second edition). Eds., Wasa, K., Kanno, I., Kotera, H., *William Andrew, Elsevier Inc.*, pp. 77–139.

Wasa, K., Kitabatake, M., Adachi, H., 2004. Thin film materials technology : sputtering of compound materials. *Springer-Verlag GmbH & Co. KG and William Andrew*, Inc. pp. 17–66.

Watanabe, H., Yamada, N., Okaji, M., 2004. Linear thermal expansion coefficient of silicon from 293 to 1000 K. *Int. J. Thermophys.* 25, 221–236.

Wei, H., Yao, T., Pan, Z., Mai, C., Sun, Z., Wu, Z., Hu, F., Jiang, Y., Yan, W., 2009. Role of Co clusters in wurtzite Co:ZnO dilute magnetic semiconductor thin films. *J. Appl. Phys.* 105, 043903–6.

Witanachchi, S., Ahmed, K., Sakthivel, P., Mukherjee, P., 1995. Dual-laser ablation forparticulate-free film growth. *Appl. Phys. Lett.* 66, 1469–1471.

Xiaoping, D.I.A., Changchum, Y.U., Ranjia, L.I., 2007. Deactivation of CeO_2-Promoted Co/SiO_2 Fischer–Tropsch Catalysts. *Chin. J. Catal.* 28, 1047–1052.

Xin, Z., Qi, W.S., Jun, L.G., Cheng, X.G., 2006. Growth of n-type ZnO thin films by using mixture gas of hydrogen and argon. *Chin. Phys.* 5, 199–202.

Xu, C., Cao, L., Su, G., Liu, W., Qu, X., Yu, Y., 2010. Preparation, characterization and photocatalytic activity of Co-doped ZnO Powders. *J. Alloys Compd*. 497, 373–376.

Yang, H., Nie, S., 2009. Preparation and characterization of Co-doped ZnO nanomaterials. *Mater. Chem. Phys.* 114, 279–282.

Yang, H.N., Zhao,Y.P., Wang,G.C., Lu, T.M., 1996. Noise-induced roughening evolutionof amorphous Si films grown by Thermal Evaporation. *Phys. Rev. Lett.* 76, 3774–3777.

Yang, S., Lv, R., Wang, C., Liu, Y., Song, Z., 2013. Structural and magnetic properties of cobalt-doped ZnO thin films on sapphire (0001) substrate deposited by pulsed laser deposition *J. Alloys Compd.* 579, pp. 628–632.

Yang, Z., 2013. A perspective of recent progress in ZnO diluted magnetic semiconductors. *Appl. Phys. A* 112, 241–254.

Yildirim, O.A., Arslan, H., Sönmezoglu, S., 2016. Facile synthesis of cobalt-doped zinc oxide thin films for highly efficient visible light photocatalysts. *Appl. Surf. Sci.* 390, 111–121.

Yoo, Y.Z., Fukumura, T., Jin, Z., Hasegawa, K., Kawasaki, M., Koinuma, H., 2001. ZnO–CoO solid solution thin films, *J. Appl. Phys.*, 90, pp. 4246–4250.

Yuanyuan, S., Kongyong, L., Jinlin, L.I., 2009. Effect of Silylation of SBA-15 on Its Supported Cobalt Catalysts for Fischer-Tropsch Synthesis. *Chin. J. Catal*. 30, 1091–1095.

Zangwill, A., 1996. Some causes and a consequence of epitaxial roughening. *J. Cryst. Growth* 163, 8–21.

Zhang, X.L., Hui, K.S., Binc, F., Hui, K.N., Lei Li, Cho, Y.R., Mane, R.S., Zhou, W., 2015. Effect of thermal annealing on the structural, electrical and optical properties of Al–Ni co-doped ZnO thin films prepared using a sol–gel method. *Surf. Coat. Technol.* 261, 149–155.

Zhang Z., Lagally M.G., 1997. Atomistic Processes in the Early Stages of Thin-Film Growth. *Sci.* 276. 377-383.

Zhou, Z., Zhang, Y., Wang, Z., Wei, W., Tang, W., Shi, J., Xiong, R., 2008. Electronic structure studies of the spinel $CoFe_2O_4$ by X-ray photoelectron Spectroscopy. *Appl. Surf. Sci.* 254, 6972–6975.

Znaidi L., 2010. Review: Sol–gel-deposited ZnO thin films: A review, *Mater. Sci. Eng*., B. 174, 18–30.

Zukova, A., Teiserskis, A., Kazlauskiene, V., Gunko Y.K., Dijken, S.V., 2007. Structural and magnetic properties of Co-doped ZnO films grown by pulse-injection MOCVD. J. *Magn. Magn. Mater.* 316, 203–206.